Study of charmless three-body decays of neutral B mesons with the LHCb spectrometer

Krzysztof Grzegorz Sobczak

Numéro d'ordre : 2202 PCCF T 1109
EDSF : 703

UNIVERSITÉ BLAISE PASCAL
U.F.R. Sciences et Technologie

ÉCOLE DOCTORALE DES SCIENCES FONDAMENTALES

THÈSE

présentée pour obtenir le grade de

DOCTEUR D'UNIVERSITE
(SPECIALITE: PHYSIQUE DES PARTICULES)

par

Krzysztof Grzegorz SOBCZAK

STUDY OF CHARMLESS THREE-BODY DECAYS OF NEUTRAL B MESONS WITH THE LHCB SPECTROMETER

Soutenance publique le 15 décembre 2011, devant la commission d'examen :

Président :	M.	T.	GERSHON	
Examinateurs :	M.	O.	DESCHAMPS	
	Mme.	MN.	MINARD	Rapporteur
	M.	S.	MONTEIL	
	M.	P.	PERRET	
	M.	V.	VAGNONI	Rapporteur

Abstract

This thesis describes an exploratory work on three-body charmless neutral B mesons decays containing either a K_S or a π^0. The events are reconstructed with the LHCb spectrometer installed at Cern (Geneva, CH) recording the proton-proton collisions delivered by the Large Hadron Collider (LHC). The phenomenology of such modes is rich and covers the possibility to measure all angles of the unitarity triangle linked to the Cabibbo-Kobayashi-Maskawa (CKM) matrix. The single example of the γ measurement is explored in this document.

The LHC accelerator and the most relevant sub-detector elements of the LHCb spectrometer are described in details. In particular, emphasis is given to the calorimetry system for which the calibration and alignment of the PreShower (PRS) of the electromagnetic calorimeter has been performed. We used particles at minimum ionisation deposit for such a task. The calibration results until year 2011 are reported as well as the method of the PS alignment with respect to the tracking system of the spectrometer.

A method to discriminate high energy π^0 and photon is introduced, based on electromagnetic cascade information combined into a multivariate analysis. The strategy to evaluate the performance is given and the tool is applied to the exploratory search of $B \to hh\pi^0$ final states.

Additionally, we conducted a similar search for the modes $B_{d,s} \to K_S hh$, where h can be either a charged kaon or a pion. The physics reach of such modes lies in the possibility of measuring the β and β_s CKM angles to be compared to their charmonia extraction. Differences in between these two determinations can be the sign of New Physics. The first step of this search is to establish the unobserved modes $B_s \to K_S hh$. We report in a fifth of the data 2011 statistics the first observation of the decay channel $B_s \to K_S K\pi$.

Keywords

LHCb, CKM Matrix, CP violation, B mesons decays, Flavour Physics, Calorimetry and Preshower.

Résumé

Ce document de thèse décrit la recherche des désintégrations en trois corps des mésons beaux neutres qui contiennent un K_S ou un π^0 dans l'état final. Ces événements sont reconstruits au moyen du spectromètre LHCb installé auprès du collisionneur proton-proton LHC, sis au Cern à Genève. La phénoménologie des ces modes est riche et couvre la possibilité de mesurer tous les angles du triangle d'Unitarité de la matrice Cabibbo-Kobayashi-Maskawa (CKM) qui décrit les amplitudes de transition par courant chargé faible entre quarks. Une illustration portant sur la mesure de l'angle γ est développée dans ce document plus en détail.

L'accélérateur LHC et les éléments utiles du spectromètre LHCb sont rapportés en mettant l'accent sur le travail conduit au cours de cette thèse sur l'étalonnage et l'alignement du détecteur de pieds de gerbe du calorimètre électromagnétique. Nous avons construit une méthode de calibration du détecteur au moyen de particules qui le traversent au minimum d'ionisation. Les résultats et les performances de ces calibrations sont discutées.

Une méthode de discrimination des π^0 et des photons de haute énergie est présentée, bénéficiant des mesures des caractéristiques des cascades électromagnétiques dans le PreShower et le calorimètre. Ces informations sont combinées dans une analyse multivariable. La stratégie de contrôle des performances du discriminateur directement à partir des données est discutée et cet outil est appliqué à la recherche des états finals $B \to hh\pi^0$.

Une recherche similaire des modes de désintégration $B_{d,s} \to K_S hh$, où h peut être un pion ou un kaon chargé a été conduite. Ce mode de désintégration permet de mesurer la phase faible du mélange des mésons B_d ou B_s et la comparaison de ces déterminations avec celles extraites des modes charmonia peut permettre de mettre en évidence une phase faible au-delà du Modèle Standard dans l'amplitude de désintégration. La première étape de cette analyse consiste à établir les signaux des modes non encore observés $B_s \to K_S hh$. Ce travail exploratoire présente la première observation du mode $B_s \to K_S K\pi$.

Mots clés

LHCb, LHC, Matrice CKM, violation de CP, désintégration et mélange des mésons beaux, Calorimétrie, Preshower.

Acknowledgements

I would like to thank several people for their support during my PhD. It is impossible to mention all of them here. It is also impossible to express all my gratitude in a few words only. Nevertheless, I would like to present in this short part all the names that I have in my mind, and I will never forget.

I have to begin from my supervisor, Stéphane Monteil, whose importance in my PhD cannot be overestimated. A tutor, who perfectly knows, how to guide students into the world of high energy physics. A brilliant researcher, who shares his experience generously. A friendly, patient, helpful, and strongly motivating man.

I would like to thank the jury. The president, Timothy Gershon, the leader of the LHCb group from the University of Warwick, with which I had a pleasure of preparing the $K^0_S hh$ analysis. Marie-Nöelle Minard, the referee, a calorimeter expert, who has impressed me with her knowledge and commitment. Vincenco Vagnoni, the referee, the coordinator of the "Gamma with loops" working group. And the examiners. Pascal Perret, the leader of the Clermont-Ferrand LHCb group and the coordinator of the LHCb calorimeter project. Olivier Deschamps, a calorimeter software guru, who has given me many advices on the complicated computing environment of the LHCb.

I also want to express how much I appreciate the atmosphere of the local LHCb group. These are: Ziad Ajaltouni, Hervé Chanal, Eric Cogneras, Olivier Deschamps, Marwa Jahjah, Pierre Henrard, Régis Lefèvre, Luigi Li Gioi, Stéphane Monteil, Valentin Niess, and Diego Roa Romero. Among them, there are such different personalities, but together they create a group which cooperates perfectly. I want to say to all of them a big "Thank you!". Even if it is not listed here, I am certain, that they will know for what.

I would like to thank my family for motivating me and showing how to be ambitious.

Last but not least, I can never thank enough my wife, Jagoda. Everything was possible only because of her presence.

Moim kochanym Babciom i Dziadkom,
Krystynie i Henrykowi,
Łucji i Kazimierzowi.

Contents

Abstract **3**

Résumé **5**

Acknowledgements **7**

Contents **11**

Introduction **17**

1 Introduction to CKM matrix and γ angle measurements **19**
1.1 CKM matrix . . . 21
1.1.1 Introduction . . . 21
1.1.2 CKM matrix properties . . . 22
1.2 CKM matrix parameters . . . 24
1.2.1 Magnitudes of the matrix elements . . . 24
1.2.2 Angles . . . 28
1.3 γ measurements at the LHCb . . . 29
1.3.1 γ from tree processes . . . 29
1.3.2 γ from loop processes . . . 32
1.4 Charmless three-body B decays . . . 33
1.4.1 BGM method . . . 33
1.4.2 CPS and GPSZ method . . . 36
1.5 $B_s^0 \to K\pi\pi$ . . . 42

2 LHCb – the detector at the LHC **45**
2.1 Large Hadron Collider . . . 47
2.1.1 Accelerator overview . . . 47
2.1.2 Experiments at the LHC . . . 47
2.1.3 Luminosity . . . 49
2.1.4 $b\bar{b}$ quark pair production . . . 49
2.2 LHCb detector . . . 50
2.2.1 Overview . . . 50
2.2.2 Vertexing and tracking . . . 52
2.2.3 Operations . . . 67

3 Preshower detector **69**
3.1 Introduction . . . 71
3.2 Scintillating cell . . . 71
3.3 Modular structure . . . 73
3.4 Photomultipliers . . . 73
3.4.1 Linearity . . . 75
3.4.2 Uniformity . . . 75
3.4.3 Magnetic field . . . 77
3.4.4 Gain and high voltage . . . 78
3.5 Building the detector . . . 78
3.6 Electronics . . . 78
3.7 Pion and electron separation . . . 83

4 Preshower calibration **85**
4.1 Minimum ionising particles . . . 87
4.1.1 Particle energy loss formalism . . . 87
4.1.2 Assumption on dependency on $\beta\gamma$ . . . 88
4.1.3 Digitalised signal from MIPs . . . 89
4.2 Multianode photomultipliers and electronics in the calibration . . . 89
4.2.1 Multianode photomultipliers . . . 89
4.2.2 Signal shape . . . 90
4.2.3 Spill-over correction . . . 91
4.2.4 Bunch crossing parity . . . 91
4.2.5 Pedestal correction . . . 92
4.2.6 Magnetic field correlation . . . 93
4.2.7 Detector stability . . . 96
4.3 Calibration strategy . . . 96
4.3.1 Inter-calibration and global uniformisation . . . 96
4.3.2 Inter-calibration procedure . . . 96
4.3.3 Timeline . . . 100
4.4 Inter-calibration with cosmic rays . . . 100
4.4.1 Introduction . . . 100
4.4.2 Event selection . . . 103
4.4.3 Track length correction used . . . 106
4.4.4 Track length correction systematic error . . . 107
4.4.5 Results . . . 108
4.4.6 Numeric gains . . . 109
4.5 Inter-calibration with collisions . . . 109
4.5.1 Calibration used in 2010 . . . 109
4.5.2 Software corrections used in reconstruction of 2010 data . . . 117
4.5.3 Calibration used in 2011 . . . 120
4.6 High voltage settings . . . 123
4.6.1 Cosmic rays settings . . . 124
4.6.2 Settings used in 2009 for collisions . . . 124
4.6.3 Settings used in 2010 . . . 125
4.6.4 Settings used in 2011 . . . 126

4.7 Energy flow calibration . . . 126
4.7.1 Method description . . . 126
4.7.2 Results for calibration used in 2010 . . . 126
4.7.3 Results for calibration used in 2011 . . . 129
4.8 Problematic channels . . . 132
4.9 Monte Carlo studies . . . 132
4.9.1 Kinematic distributions . . . 132
4.9.2 Rounding in track length correction . . . 137
4.10 Alignment . . . 141
4.10.1 Introduction to alignment . . . 141
4.10.2 Realignment method description . . . 141
4.11 Summary . . . 150

5 Exploratory work: $B^0_{(s)} \to hh\pi^0$ observation with 2010 data 151
5.1 Monte Carlo . . . 153
5.2 Neutral pion reconstruction . . . 155
5.3 Trigger . . . 157
5.4 Stripping . . . 158
5.5 Efficiency study . . . 160
5.5.1 Limitations . . . 160
5.5.2 Expected yields formula . . . 161
5.5.3 Monte Carlo efficiencies . . . 162
5.5.4 Reconstruction ability . . . 164
5.5.5 Difference in kinematic and topology . . . 165
5.5.6 Yields before selection . . . 165
5.6 Signal selection . . . 165
5.6.1 Selection design . . . 165
5.6.2 Signal and background modelling . . . 166
5.6.3 Merged π^0 results . . . 166
5.6.4 Resolved π^0 selection . . . 170
5.7 $KK\pi^0$ mode . . . 170
5.8 $\pi\pi\pi^0$ mode . . . 172
5.9 Summary . . . 174

6 π^0/γ separation 175
6.1 $B \to X\gamma$ physics . . . 177
6.2 K$\pi\pi^0$ and K$^*\gamma$ case . . . 178
6.3 Discriminant construction . . . 179
6.3.1 ECAL variables . . . 179
6.3.2 PRS variables . . . 182
6.4 Discriminant optimisation . . . 183
6.4.1 Basics . . . 183
6.4.2 Optimisation with ECAL variables only . . . 185
6.4.3 Optimisation with PRS variables only . . . 185
6.4.4 ECAL and PRS optimisation comparison . . . 188
6.4.5 Performance of optimisation with ECAL and PRS variables combined together . . . 188

6.5 Real data check with D^0 sample . . . 191
6.5.1 Stripping . . . 191
6.5.2 Selection . . . 192
6.5.3 Merged π^0 from $D^0 \to K\pi\pi^0$ . . . 192
6.5.4 Resolved π^0 from $D^0 \to K\pi\pi^0$ . . . 192
6.5.5 Discriminant response . . . 194
6.6 K$\pi\pi^0$ and K$\pi\gamma$ . . . 197
6.7 $K\pi\pi^0$ with π^0/γ separation . . . 197
6.7.1 Statistics . . . 197
6.7.2 Application of the discriminant . . . 198
6.7.3 Selecting K*(892) . . . 199
6.7.4 Tightening the selection . . . 202
6.7.5 Tight $K^*\gamma$ . . . 204
6.7.6 Dalitz plot of $K\pi\pi^0$ . . . 204
6.8 KKπ^0 with π^0/γ separation . . . 205
6.9 Summary . . . 205

7 Charmless 3-body decays with a K^0_S in the final state 209
7.1 Introduction . . . 211
7.2 K^0_S reconstruction . . . 212
7.3 Exploratory work with 2010 data . . . 212
7.4 Data samples . . . 216
7.5 Background . . . 216
7.5.1 Modes identified from the data . . . 218
7.5.2 MC background studies . . . 220
7.5.3 Combinatorial background . . . 224
7.6 Selection design . . . 224
7.6.1 Concepts . . . 224
7.6.2 Data sets . . . 224
7.6.3 Variables . . . 225
7.6.4 Working point selection . . . 226
7.7 PID cuts . . . 228
7.8 Fit model . . . 229
7.9 $K^0_S\pi\pi$ channel . . . 230
7.9.1 2010 data fit . . . 230
7.9.2 2011 data fit . . . 230
7.10 $K^0_SK\pi$ channel . . . 233
7.11 K^0_SKK channel . . . 233
7.12 Perspectives . . . 235

Summary 239

A Photomultiplier β parameter determination 241

B Track momentum maps 247

C B2HHPi0 stripping control plots **253**
C.1 Merged π^0 . . . 255
C.2 Resolved π^0 . . . 257
C.3 Merged π^0, $\mu_1 = 0.6$, 10 TeV and $\mu_2 = 2.3$, 7 TeV comparison . . . 259
C.4 Resolved π^0, $\mu_1 = 0.6$, 10 TeV and $\mu_2 = 2.3$, 7 TeV comparison . . . 261

D π^0/γ discriminant optimisation control plots **263**
D.1 Inner distributions . . . 265
D.2 Middle distributions . . . 267
D.3 Outer distributions . . . 269
D.4 ECAL optimisation . . . 271
D.5 PRS optimisation . . . 273
D.6 ECAL + PRS optimisation . . . 275

E $K^0_S hh$ additional plots **277**
E.1 K^0_S DD . . . 279
E.2 K^0_S LL . . . 281

Bibliography **283**

Introduction

The Nobel Prize in Physics in 2008 was awarded to Makoto Kobayashi and Toshihide Maskawa "for the discovery of the origin of the broken symmetry which predicts the existence of at least three families of quarks in nature". The impact of their work on the modern physics, and particularly particle physics, cannot be overestimated. Their construction is now one of the solid foundations of the Standard Model, supported by the results of the B-factories, in run for the 2000 decade. The LHCb experiment is taking over and also concentrates on the CKM (Cabibbo-Kobayashi-Maskawa) matrix parameter measurements and CP violation observations. It is currently the spectrometer of the highest energy, and it will hopefully bring many fascinating results. It searches for any deviations from the predictions of the Standard Model, which can be a signature of the New Physics, enlarging the laboratories of interest to B_s and B_c mesons as well as beautiful hadrons.

Among the CKM parameters, the γ angle is one of the least precisely measured. The current value is $68^\circ\ ^{+13^\circ}_{-14^\circ}$ [2]. It has been constrained more precisely lately, but still there is a space for improvement. The objective of the efforts described in this book was to prepare basics of a γ measurement from a Dalitz analysis of $B^0_s \to K^-\pi^+\pi^0$ and $B^0_s \to K^0_S\pi^+\pi^-$ decays. The integrated luminosity recorded by the LHCb until summer 2011 does not allow to perform such complicated analysis. However, it is sufficient for branching fraction measurements of unobserved modes, like different $B \to K^0_S hh$ decays. The modes with one K^0_S in the final state are very appealing in another respect: the β angle measurement. In a time dependent analysis of $B^0 \to K^0_S\pi\pi$ and $B^0_s \to K^0_S KK$, the very same weak phase as the one in $B^0 \to J/\psi K^0_S$ exhibits. Its measurement and the comparison of the latter extraction is a test of the New Physics in the decay.

The first chapter of this document is dedicated to the CKM matrix, and the measurements of its parameters. A short presentation of the current results is given. It describes shortly γ measurements at the LHCb, and focuses on the methods based on the charmless decays of $B \to K\pi\pi$.

The next two chapters describe briefly the LHCb spectrometer, and more precisely the preshower detector of the electromagnetic calorimeter.

Any measurement involving neutral pions requires calibrated calorimeter. A part of the calorimeter system in the LHCb is the preshower detector of the electromagnetic calorimeter. A process of calibration of the preshower is presented in the Chapter 4. It is a comprehensive description of the efforts, which were made to commission the detector for the first collisions in the LHC, and then to improve the performance of it, to reach the initial objective which was the calibration at the level of 5%. The procedure of the (re-)alignment of the preshower is also included in this part.

The Chapter 5 displays then the exploratory work on the charmless decays of neutral B mesons into the final state of $hh\pi^0$. It starts from the Monte Carlo studies, description of the trigger, the stripping and the selection. Then the first observation with the statistics obtained in the year 2010 is made, which suggests a possible, significant contamination of radiative B decays. Hence, an instrument – a π^0/γ discriminant – is introduced. The construction of it is described in the Chapter 6. Additionally, the method of the evaluation of this tool performance on the data with the sample of $D^0 \to K\pi\pi^0$ is presented. Finally, the first results from 2011 are given.

The last chapter summarises the achievements on the analysis of charmless neutral B decays into $K^0_S hh$ up to October 2011. It focuses on the preparations for the relative measurement of the branching fraction of $B^0_s \to K^0_S K\pi$, for which, a first observation is reported here. Moreover, the other $K^0_S hh$ modes are discussed. The analysis, is progressing fast and the final result on branching fraction measurements and observation of new B_s modes is expected soon.

Chapter 1

Introduction to CKM matrix and γ angle measurements

The construction of the Standard Model is globally well-proven by precise measurements in two types of experiments: precise tests of the gauge sector (Z pole observables and m_W at LEP, m_{top} at Tevatron), and the measurements of the CKM parameters, mostly constrained so far by $\Upsilon(4s)$ e^+e^- colliders. However, there are parameters, which cannot be called precisely measured. The γ angle is an example of that kind of parameters. Reaching γ experimentally is a challenging task. In this part we will describe some possible approaches to the subject.

The chapter starts from a short introduction to the CKM matrix, followed by an extraction of its parameters, with the most up to date results on their values. Then an overview of LHCb plans of measuring γ is presented. Finally, we describe the methods which are based on $B \to K\pi\pi$, and $B_s^0 \to K\pi\pi^0$ decays. The last method, unreachable by B-factories, but available to the LHCb, allows to extract γ in an electroweak-penguin-free way, with theoretical uncertainty below 1°.

In the process of this thesis, the selection of π^0 final states happened to be very difficult to achieve and my efforts concentrated at some point into the charmless decay modes $B \to K_S^0 hh$. It is a major ingredient of the gamma extraction with $K\pi\pi^0$, but it has a physics interest on its own: the measurement of the angle β. A chapter will be dedicated to it.

1.1 CKM matrix

1.1.1 Introduction

We start this description classically, from the Standard Model (SM) [3, 4] as renormalisable quantum field theory, constructed under the principle of local gauge invariance with $SU(3)_C \otimes SU(2)_L \otimes U(1)_Y$ symmetric group. In this group the strong interaction symmetry group of colour rotations, denoted by $SU(3)_C$, is present, as well as the electroweak interaction group $SU(2)_L \otimes U(1)_Y$. The second is spontaneously broken to $SU(2)_L \otimes U(1)_Y \rightarrow U(1)_{em}$, where $U(1)_{em}$ is the group of the electromagnetic interaction.

In the SM a limited number of particles is present. There are twelve gauge bosons. Among them, the first eight are the gluons – massless, electrically neutral, color carrying mediators of the strong interactions. The ninth is photon, a massless particle without electric charge, which mediates the electromagnetic interaction. The last three are the bosons, which carry the weak interactions, W^+, W^- and Z^0. They acquire masses through spontaneous symmetry breaking, and they can interact with each other. The very last, special, gauge boson of the SM is the unobserved so far Higgs boson. (One should call it BEH boson [5], Brout and Englert bringing the decisive treatment of the Goldstone bosons.)

The next category of particles in the SM is consisted of fermions. In this group there are quarks, which are able to interact with all the types of interactions just introduced. The other subgroup are leptons, which are sensitive to weak and electromagnetic interactions only. All fermions are organised into three families. They interact the same way with different fields, but they have different quantum numbers and masses. The field associated with fermions has left chirality components, transforming as $SU(2)_L$ doublets, and right chirality transforming as singlets. The weak interaction operates on left chirality components only.

The $SU(3)_C \otimes SU(2)_L \otimes U(1)_Y$ symmetry group prevents the masses of leptons and quarks to appear in the Lagrangian directly. The electroweak symmetry is broken since both fermions and weak bosons Z and $W^\pm$ do have masses. It is possible to generate the masses in the SM by considering a doublet of complex scalar fields, out of which a single massive scalar object is exhibited (the so-called Higgs boson). The other three degrees of freedom from the complex doublet are absorbed to give rise to the $W^\pm$ and Z masses. The Lagrangian of the interaction with the Higgs condensate can be written as [2]:

$$\mathcal{L}_Y = -\lambda^d_{ij} \bar{Q}^{I_3}_{Li} \phi D^{I_3}_{Rj} - \lambda^u_{ij} \bar{Q}^{I_3}_{Li} \phi^* U^{I_3}_{Rj} + h.c, \tag{1.1}$$

where $\lambda^{u,d}$ are 3×3 complex matrices, ϕ is the Higgs field, i, j denotes the generations. $Q^{I_3}_{Li} = (U, D)^{I_3}_L$ are left-handed quark doublets, while $D^{I_3}_{Rj}$ and $U^{I_3}_{Rj}$ are right-handed down and up quark singlets.

When ϕ acquires a vacuum expectation value $v = \langle 0|\phi|0\rangle$, the equation (1.1) yields mass terms for the quarks. The quark mass spectrum is obtained by diagonalisation of the mass matrices. The λ^u_{ij} matrix can be diagonalised with two unitary matrices:

$\mathcal{U}_L^{u(d)}$ and $\mathcal{U}_R^{u(d)}$.

$$\mathcal{U}_L^{u(d)} \frac{\lambda_{ij}^u . v}{\sqrt{2}} \mathcal{U}_R^{u(d)} = \begin{pmatrix} m_{u(d)} & 0 & 0 \\ 0 & m_{c(s)} & 0 \\ 0 & 0 & m_{t(b)} \end{pmatrix} . \tag{1.2}$$

This is where the masses of fermions m_i are input into the SM.

The currents of the weak interaction transform from the base of the weak interaction eigenstates to the base of mass eigenstates, and this transformation is done directly with the elements of the matrix defined as

$$V_{CKM} = \mathcal{U}_L^u \mathcal{U}_L^{d\dagger} = \begin{pmatrix} V_{ud} & V_{us} & V_{ub} \\ V_{cd} & V_{cs} & V_{cb} \\ V_{td} & V_{ts} & V_{tb} \end{pmatrix} . \tag{1.3}$$

This is the well known Cabibbo, Kobayashi, Maskawa (CKM) matrix [1].

The charged current Lagrangian is written initially:

$$\mathcal{L}_W = i \frac{g_1}{2} \bar{Q}_{Li}^{I_3} \gamma^\mu (\vec{\tau} . \vec{W})_\mu Q_{Li}^{I3} , \tag{1.4}$$

where g_1 is the weak coupling constant, $\vec{\tau}$ are the Pauli matrices, the generators of the $SU(2)$ group, γ^μ are the Dirac γ-matrices, and $\vec{W}$ are the three vector fields. This Lagrangian written in terms of the mass eigenstates becomes:

$$\mathcal{L}_W = i \frac{g_1}{\sqrt{2}} (\bar{U}_{Li} \gamma^\mu \mathcal{U}_{ik}^u \mathcal{U}_{kj}^{d\dagger} D_{Lj} {W_\mu}^+ + \bar{D}_{Li} \gamma^\mu \mathcal{U}_{ik}^d \mathcal{U}_{kj}^{u\dagger} U_{Lj} {W_\mu}^-) + \frac{i g_1}{2} \bar{Q}_{Li} \gamma^\mu \tau^3 {W_\mu}^3 Q_{Li} . \tag{1.5}$$

The two explicitly written fields W^+ and W^- are the linear combinations of W^1 and W^2: $W^\pm = \frac{1}{\sqrt{2}}(W^1 + iW^2)$. There is also the third term in this equation, which is responsible for the interactions mediated by the neutral current, which is not changed by the application of the transformation. A remarkable consequence is the absence of flavour changing neutral currents in the first order in the SM.

1.1.2 CKM matrix properties

We are used to the CKM matrix which dimension is 3×3. The number 3 stands for 3 quark families. But generally this matrix does not have to be the size of 3, but any number N. Such $N \times N$ matrix has to be unitary, as it is the product of two unitary matrices. Not all parameters of the matrix are meaningful, as $2N - 1$ of the phases can be absorbed in the quark fields by phase redefinition (global phase invariance). Additionally, the unitarity states that it can be parametrised with $N(N-1)/2$ Euler angles. It means that there are $(N-1)(N-2)/2$ independent phases. Thus, in case of $N = 2$ families, the matrix is real and there can not be any CP violation. To explain the CP violation we need at least three quark families. In case of $N = 3$, the CKM matrix can be parametrised with three rotation angles θ_{12}, θ_{23}, θ_{13} and one phase δ. All the information about CP violation is contained in this phase. This masterpiece is due to Kobayashi and Maskawa, awarded by the Nobel Prize in 2008. The typical choice of the parametrisation is:

$$V_{\text{CKM}} = \mathcal{R}_{23}(\theta_{23}, 0) \otimes \mathcal{R}_{13}(\theta_{13}, \delta_{13}) \otimes \mathcal{R}_{12}(\theta_{12}, 0) . \tag{1.6}$$

The matrix in this parametrisation is [6]:

$$V_{\rm CKM} = \begin{pmatrix} c_{12}c_{13} & s_{12}c_{13} & s_{13}e^{-i\delta_{13}} \\ -s_{12}c_{23} - c_{12}s_{23}s_{13}e^{i\delta_{13}} & c_{12}c_{23} - s_{12}s_{13}s_{23}e^{i\delta_{13}} & s_{23}c_{13} \\ s_{12}s_{23} - c_{12}c_{23}s_{13}e^{i\delta_{13}} & -c_{12}s_{23} - s_{12}c_{23}s_{13}e^{i\delta_{13}} & c_{23}c_{13} \end{pmatrix}, \qquad (1.7)$$

where $c_{ij} = \cos\theta_{ij}$, $s_{ij} = \sin\theta_{ij}$, and $i, j = 1, 2, 3$.

The experimental observations of the parameters of the CKM matrix, and their hierarchy, led Wolfenstein [7] to propose an expansion of the matrix in terms of four parameters: λ, A, ρ, and η. The expansion parameter is the Cabibbo angle $\lambda \approx 0.22$. The definition of the parameters is given below:

$$\begin{aligned} s_{12} &= \lambda\ , \\ s_{23} &= A\lambda^2\ , \\ s_{13}e^{-i\delta} &= A\lambda^3(\rho - i\eta)\ , \end{aligned} \qquad (1.8)$$

which ensures a parametrisation unitary exact at each order of the development [8]. In this parametrisation η contains the CP violation information. The matrix looks like at $\mathcal{O}(\lambda^4)$:

$$V_{\rm CKM} = \begin{pmatrix} 1 - \lambda^2/2 - 1/8\lambda^4 & \lambda & A\lambda^3(\rho - i\eta) \\ -\lambda & 1 - \lambda^2/2 - 1/8\lambda^4(1 + 4A^2) & A\lambda^2 \\ A\lambda^3(1 - \rho - i\eta) & -A\lambda^2 + A\lambda^4(1 - 2(\rho + i\eta))/2 & 1 - A^2\lambda^4/2 \end{pmatrix} + \mathcal{O}(\lambda^5). \qquad (1.9)$$

A phase-convention-independent measure of CP violation, known as Jarlskog invariant [9] J, can be written as:

$$J \sum_{\sigma\gamma=1}^{3} \epsilon_{\mu\nu\sigma}\epsilon_{\alpha\beta\gamma} = {\rm Im}(V_{\mu\alpha}V_{\nu\beta}V^*_{\mu\beta}V^*_{\nu\alpha})\ , \qquad (1.10)$$

where ϵ are the Levi-Civita completely antisymmetric tensors.

The CKM matrix unitary implies various relations among its elements. Three of them can be represented with triangles in a complex plane can be written as:

$$V_{ud}V^*_{ub} + V_{cd}V^*_{cb} + V_{td}V^*_{tb} = 0, \qquad (1.11)$$

$$V_{td}V^*_{ud} + V_{ts}V^*_{us} + V_{tb}V^*_{ub} = 0, \qquad (1.12)$$

$$V_{ud}V^*_{us} + V_{cd}V^*_{cs} + V_{td}V^*_{ts} = 0. \qquad (1.13)$$

The areas of the triangles are the same, and equal to the half of the Jarlskog invariant.

The most common choice of the representation of the unitarity triangle is presented in the figure 1.1. In this representation, in the $\bar\rho - \bar\eta$ plane, defined by

$$\bar\rho + i\bar\eta = -\left(\frac{V_{ud}V^*_{ub}}{V_{cd}V^*_{cb}}\right), \qquad (1.14)$$

the length of the basis of this triangle is equal to 1. The other two are:

$$R_u = \left|\frac{V_{ud}V^*_{ub}}{V_{cd}V^*_{cb}}\right| = \sqrt{\bar\rho^2 + \bar\eta^2}, \qquad (1.15)$$

$$R_t = \left|\frac{V_{td}V^*_{tb}}{V_{cd}V^*_{cb}}\right| = \sqrt{(1 - \bar\rho)^2 + \bar\eta^2}. \qquad (1.16)$$

The internal angles of the unitarity triangle, denoted by α, β and γ are:

$$\alpha = \arg\left(-\frac{V_{td}V_{tb}^*}{V_{ud}V_{ub}^*}\right), \beta = \pi - \arg\left(\frac{V_{td}V_{tb}^*}{V_{cd}V_{cb}^*}\right), \gamma = \arg\left(-\frac{V_{ud}V_{ub}^*}{V_{cd}V_{cb}^*}\right). \quad (1.17)$$

Nothing is said about A, λ, $\bar{\rho}$ and $\bar{\eta}$ within the SM. In order to perform a global consistency check of the KM paradigm, it is necessary to measure or constrain the parameters in a redundant way. The measurements which allow to extract the parameters of the unitarity triangle will be described shortly in the next sections. The current constraints on these parameters collected by the CKMfitter group are presented in the figure 1.2 and exhibit an amazingly correct agreement among all observables.

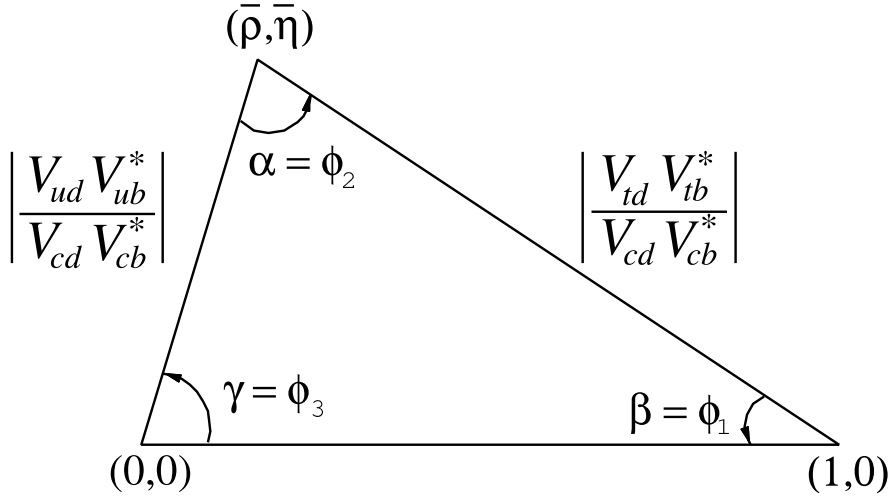

Figure 1.1: *Sketch of the unitarity triangle*

1.2 CKM matrix parameters

1.2.1 Magnitudes of the matrix elements

1.2.1.1 $|V_{ud}|$

The best determination of this matrix element is achieved by measuring nuclear beta decays [10], with an error dominated by theoretical uncertainties from nuclear Coulomb distortions and from radiative corrections. An additional measurement comes from the neutron lifetime. Currently, the world best average is [8]:

$$|V_{ud}| = 0.97425 \pm 0.00022 \quad (1.18)$$

1.2.1.2 $|V_{us}|$

The $|V_{us}|$ element traditionally has been measured from semileptonic decays of $K_L^0 \to \pi e \nu$. Recently the experimental results have allowed to pin down the statistical errors,

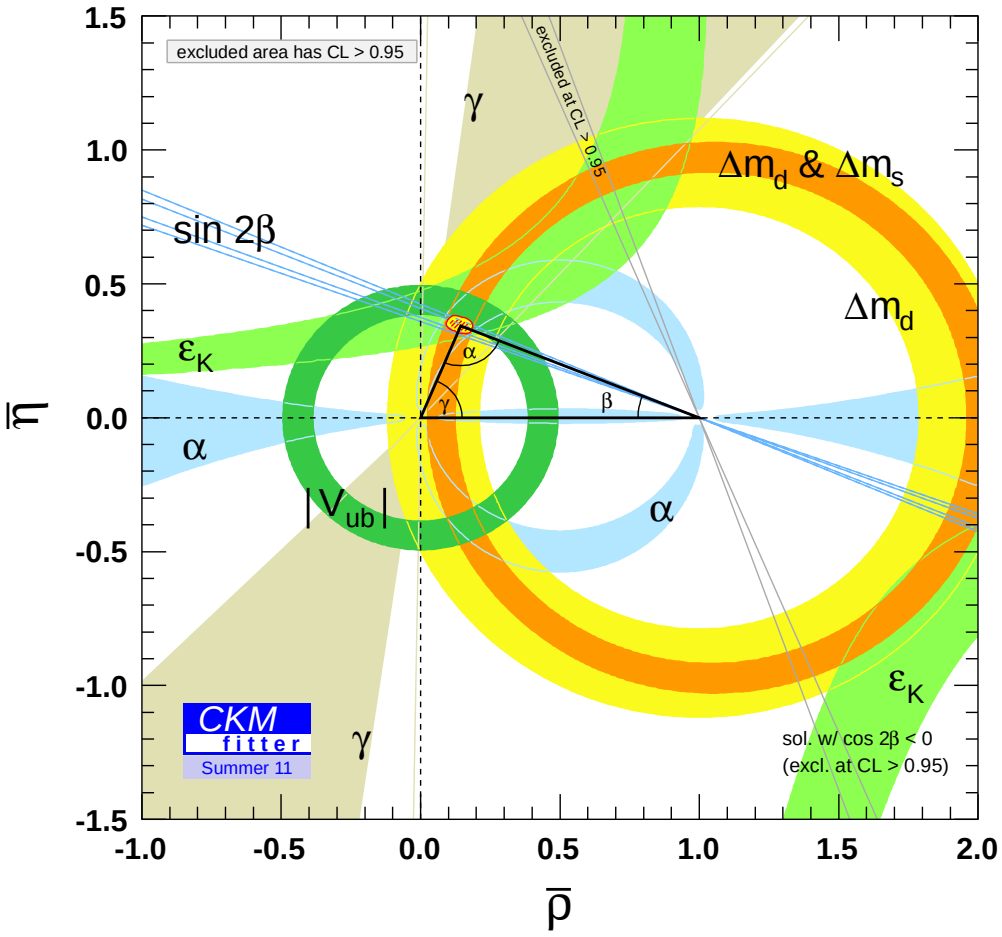

Figure 1.2: *Constraint on the unitarity triangle parameters at CL > 95% [8].*

thus allowing a comparison to similar modes burden by larger systematic errors: $K_L^0 \to \pi\mu\nu$, $K^\pm \to \pi^0 e^\pm \nu$, $K^\pm \to \pi^0 \mu^\pm \nu$ and $K_S^0 \to \pi e \nu$.

An additional constraint comes from the ratio of the decay widths of $K \to \mu\nu(\gamma)$ and $\pi \to \mu\nu(\gamma)$, where (γ) denotes that radiative decays are included. The ratio is given by $|V_{us}/V_{ud}|$, thus knowing precisely $|V_{ud}|$, one can compute $|V_{us}|$ also.

The average value determination and the measurements are described in [11]. The PDG [2] value is;

$$|V_{us}| = 0.2255 \pm 0.0024 \tag{1.19}$$

1.2.1.3 $|V_{cd}|$

The magnitude of the parameter $|V_{cd}|$ can be extracted from semileptonic charm decays [12], like $D \to Kl\nu$ and $D \to \pi l\nu$, but the form factors have to be theoretically mastered. The other possibility of determination of this parameter is available via neutrino and antineutrino interactions. Here the difference of the ratio of double-muon to single-muon production by neutrino beams is proportional to the charm cross section of valence quarks d, which means that it is proportional to $|V_{cd}|$ times the average semileptonic branching ratio of charm mesons $\mathcal{B}_\mu$ [13].

The average calculation is more complicated in this case, as it requires assumptions about the scale of the QCD corrections, and because the $\mathcal{B}_\mu$ parameter depends on the specific neutrino beam parameters. The current best value is [2]:

$$|V_{cd}| = 0.230 \pm 0.011 \tag{1.20}$$

1.2.1.4 $|V_{cs}|$

The direct determination of this parameter is possible with semileptonic decays of D or leptonic decays of D_s, however one has to use unquenched lattice QCD calculations for the proper semileptonic form factors for D. It is also possible to use flavour tagged W decays – this kind of measurement was performed at LEP, however the statistical error was large [14].

The world average is [2]:

$$|V_{cs}| = 1.023 \pm 0.036 \tag{1.21}$$

1.2.1.5 $|V_{cb}|$

This parameter can be determined from exclusive and inclusive semileptonic decays of B mesons into charm. The inclusive cases use the semileptonic decay rate measurement, accompanied by the leptonic energy and the hadronic invariant mass spectra. The exclusive determinations are based on B decays to D and D^*. The exclusive determination is less precise than the inclusive one, because of the theoretical uncertainty coming from the poor knowledge ot the form factors

An average of the inclusive and exclusive gives [8]:

$$|V_{cb}| = 0.04089 \pm 0.00038^{(\text{exp.})} \pm 0.00059^{(\text{theo.})}. \tag{1.22}$$

1.2.1.6 $|V_{ub}|$

The determination of this parameter from inclusive $B \to X_u l\bar{\nu}$ is burden with large $B \to X_c l\bar{\nu}$ background. Thus the first evidence of this parameter came from the decay at the end point of the lepton spectrum, where $b \to cl\bar{\nu}$ events are kinematically forbidden due to the c quark mass. However such regions are dominated by the so-called shape function, a non-perturbative object that reflects the Fermi motion of the b quark inside the B meson. In addition, exclusive determination of $|V_{ub}|$comes from the study of $B \to \pi l\bar{l}$. Again, it is dominated by the knowledge of the form factors.

The value of the parameter is [8]:

$$|V_{ub}| = 0.000392 \pm 0.000009^{(\text{exp.})} \pm 0.000045^{(\text{theo.})}. \tag{1.23}$$

Let us notice that $|V_{ub}|$ and $|V_{cb}|$ measurement from exclusive and inclusive determinations are only in marginal agreement [15]. The interested reader can look at HFAG [16].

1.2.1.7 $|V_{td}|$ and $|V_{ts}|$

$|V_{td}|$ and $|V_{ts}|$ are not accessible from tree-level decays of the top quark. However, they can be measured in the oscillations of $B - \bar{B}$, where top quark appears in box diagrams, or in rare decays, where top can be found in loops. The precision is limited by theoretical uncertainties in hadronic effects, but it can be improved by determining ratio $|V_{td}/V_{ts}|$. Assuming $|V_{tb}| = 1$, PDG [2] values are:

$$|V_{td}| = 0.0084 \pm 0.0006 \tag{1.24}$$

$$|V_{ts}| = 0.0387 \pm 0.0021 \tag{1.25}$$

Some uncertainties can be reduced by the ratio $\xi = (f_{B_s}\sqrt{\hat{B}_{B_s}})/(f_{B_d}\sqrt{\hat{B}_{B_d}})$, where $f_{B_{s,d}}$ are the decay constants and $\hat{B}_{B_{s,d}}$ are the Bag parameter. It allows to calculate the ratio $|V_{td}/V_{ts}|$ from $\Delta m_d/\Delta m_s$ in theoretically better controlled way [2]:

$$|V_{td}/V_{ts}| = 0.211 \pm 0.001^{(\text{exp.})} \pm 0.005^{(\text{theo.})}. \tag{1.26}$$

Another possibility of determining this ratio comes from the ratio of $B \to \rho\gamma$ and $B \to K^*\gamma$, which is yet limited by the statistics [16].

1.2.1.8 $|V_{tb}|$

The determination of $|V_{tb}|$ currently is possible only from the decays of t quark at single top production at Tevatron [17], by using the ratio of branching fractions

$$R = \frac{\mathcal{B}(t \to Wb)}{\mathcal{B}(t \to Wq)} = \frac{|V_{tb}|^2}{\sum_q |V_{tq}|^2} = |V_{tb}|^2. \tag{1.27}$$

The average from both Tevatron experiments is [2]:

$$|V_{tb}| = 0.88 \pm 0.07 \tag{1.28}$$

1.2.2 Angles

Since CP violation involves phases of CKM elements, many of measurements of observables, which are CP-violating, can be used to constrain the CKM angles and the parameters $\bar{\rho}$, $\bar{\eta}$. Currently, the most precise measurements are provided by Belle and BaBar experiments.

1.2.2.1 α angle

Because α is the phase between $V_{tb}^* V_{td}$ and $V_{tb}^* V_{ud}$, there is only one time-dependent CP asymmetry in $b \to u\bar{u}d$ decay dominated modes, which allows to measure $\sin 2\alpha$. Practically, the measurements are taken on the decays [18]: $B \to \pi\pi$, $B \to \rho\pi$ and $B \to \rho\rho$.

The decay of $B^0 \to \rho^+\rho^-$ contains two vector mesons in the final state. This fact usually means that the state is a mixture of CP-even and CP-odd components. However, it was measured that the longitudinal polarisation fractions of $B^0 \to \rho^+\rho^-$ and $B^+ \to \rho^+\rho^0$ to be close to unity, which means that the final states are almost purely CP-even, actually like the $B \to \pi\pi$ system. The analysis requires to measure the time-dependent CP asymmetries for $B^0 \to \rho^+\rho^-$, together with the branching fractions and polarisation measurements of the other $B \to \rho\rho$ decays.

In the $B \to \pi\pi$ decays the penguin $b \to d$ amplitudes have different phase than $b \to u\bar{u}d$ tree amplitude. Including the fact that they are of the same order in λ, it means, that the penguin contribution are sizable. Thus, the time-dependent $B^0 \to \pi^+\pi^-$ analysis does not measure $\sin 2\alpha$, but $\sin(2\alpha + 2\Delta\alpha)$, where $2\Delta\alpha$ is the phase difference between $e^{2i\gamma}\bar{A}_{\pi^+\pi^-}$ and $A_{\pi^+\pi^-}$. The value of $\Delta\alpha$ can be constrained using the isospin relations, and hence accompanied modes $\pi\pi^0$ and $\pi^0\pi^0$

The last type: $B^0 \to \rho^+\pi^-$ is not a CP eigenstate. However, both B^0 and $\bar{B}^0$ can decay to the same final state, which means that mixing-induced CP violations can occur, allowing to measure the angle. It is the least precisely constrained measurement from the mentioned here.

The combined result of the measurements gives [2]:

$$\alpha = 89.0^\circ \, {}^{+4.4^\circ}_{-4.2^\circ} \tag{1.29}$$

1.2.2.2 β angle

The β angle, the mixing angle of the B^0 mesons, is measured through time-dependent CP asymmetry to a final state f, common to both B^0 and $\bar{B}^0$, given by:

$$\mathcal{A}_f = \frac{\Gamma(\bar{B}^0(t) \to f) - \Gamma(B^0(t) \to f)}{\Gamma(\bar{B}^0(t) \to f) + \Gamma(B^0(t) \to f)} = S_f \sin(\Delta m_d t) - C_f \cos(\Delta m_d t), \tag{1.30}$$

where

$$S_f = \frac{2\mathrm{Im}\lambda_f}{1 + |\lambda_f|^2}, \quad C_f = \frac{1 - |\lambda_f|^2}{1 + |\lambda_f|^2}, \quad \lambda_f = \frac{q}{p}\frac{\bar{A}_f}{A_f}. \tag{1.31}$$

By q/p we represent he CP violation in $B^0 - \bar{B}^0$ mixing, approximated by:

$$\frac{q}{p} = \frac{V_{tb}^* V_{td}}{V_{tb} V_{td}^*} = e^{-2i\beta + \mathcal{O}(\lambda^4)}. \tag{1.32}$$

A_f and $\bar{A}_f$ denotes the amplitudes of $B^0 \to f$ and $\bar{B}^0 \to f$. If f is a CP eigenstate, and amplitudes with one CKM phase dominate the decay, then we can write that $|A_f| = |\bar{A}_f|$, $C_f = 0$, and $S_f = \sin(\arg \lambda_f) = \eta_f \sin 2\beta$, where η_f is the CP eigenvalue of f, and 2ϕ is the phase difference between normal and charge conjugate decays.

The decays of $b \to c\bar{c}s$, where B^0 decays to CP eigenstates ($B^0 \to J/\psi K^0$ and similar charmless modes) are the cleanest from the theoretical point of view to extract β, by measuring $S_f = -n_f \sin 2\beta$. The penguin amplitudes which phase is different from $b \to c\bar{c}s$ are λ^2-suppressed, and hence the measurements is clear of any polluting phase contribution. Also penguin-dominated decays $b \to s\bar{q}q$ have the same CKM phase as tree level $b \to c\bar{c}s$, providing an access to $\sin 2\beta$ (e.g. $B^0 \to \phi K$ and $B^0 \to \eta' K^0$). Those measurements are used to probe the new physics in the decay $\Delta F = 1$. A chapter of this thesis will be dedicated to the observation with the LHCb of some of these decay modes.

The angle β is the most precisely measured angle among all in the CKM matrix. The averaged value is [16]:

$$\sin 2\beta = 0.673 \pm 0.023 \tag{1.33}$$

1.2.2.3 γ angle

The least precisely measured angle is γ, where the uncertainties from direct measurements are beyond 15% [8]:

$$\gamma = 68^\circ \, {}^{+13^\circ}_{-14^\circ}. \tag{1.34}$$

The following sections will described the methods of measuring this angle, focusing mostly on the possibilities available to the LHCb. In details we will investigate also the decays of $B_{(s)} \to K\pi\pi$, which observations with the real data are described later in the experimental part. Just before we move to the extended description of the possible measurements of γ, we can take a look at the constraints on the value of this angle – the plot is shown in the figure 1.3.

1.3 γ measurements at the LHCb

The γ angle can be measured from processes containing tree or loop diagrams. The LHCb experiment allows to explore both ways. The first is a theoretically clean way to measure γ. The second one requires strong interaction theoretical assumptions In the following paragraphs we will look briefly at the most important approaches to this subject. The description refers to a short review [19], and the key measurement at the LHCb roadmap [20]. Another introduction to the subject, which focuses not only at LHCb methods, can be found in [21].

1.3.1 γ from tree processes

1.3.1.1 $B^\mp \to D^0 K^\mp$ and $\overline{B}^0 \to D\overline{K}^{*0}$

The sensitivity to γ at tree level is present in time-integrated measurement of the modes $B^\mp \to D^0 K^\mp$ and $\overline{B}^0 \to D\overline{K}^{*0}$, since these modes are self-tagged through D decay. The charged B decay diagram is shown in the figure 1.4. One of these

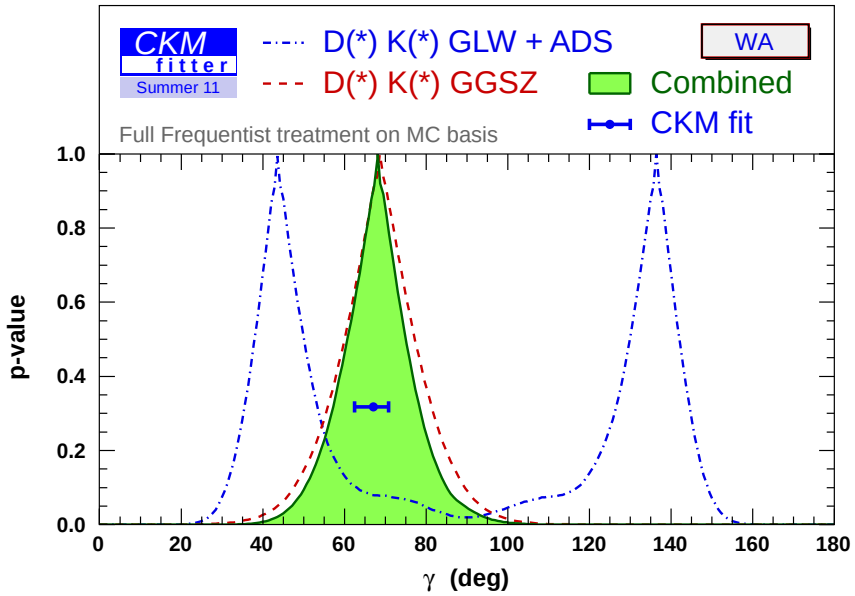

Figure 1.3: *Constraints on γ from world average $D^{(*)}K^{(*)}$ decays (GLW and ADS) and Dalitz analyses (GGSZ).*

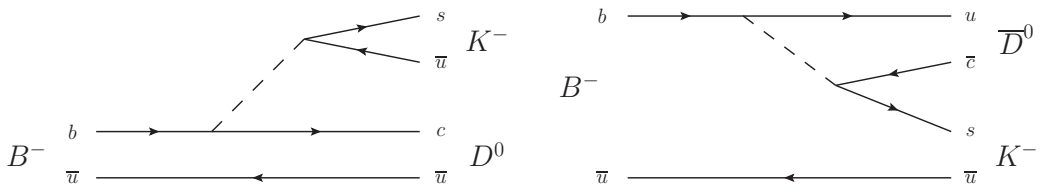

Figure 1.4: *Feynman diagrams for $B^- \to D^0 K^-$ (left) and $B^- \to \overline{D}^0 K^-$ (right).*

diagrams depends on the CKM matrix element V_{cb}, while the other on V_{ub} (which is CKM suppressed, and in addition it is colour suppressed). The sensitivity to γ is controlled by the ratio of the amplitudes:

$$R_B = \frac{b \to u}{b \to c} \tag{1.35}$$

The weak-phase difference between the two is $-\gamma$, so when D^0 and $\overline{D}^0$ interfere while decaying to the same final state, the access to γ is available. The method is not polluted by penguin loops, which mediate flavour changing neutral current processes, that can be influenced by new physics. The largest correction is due to $D^0\overline{D}^0$ mixing [16, 22]. The observed rate of mixing influences γ by less than 1°.

The first proposal of the γ angle measurement with this decay is known as the GLW method (Gronau, London, Wyler) [23], where D decays into CP eigenstates. In the LHCb the CP-even final states $\pi^+\pi^-$ and K^+K^- have been studied. Additionally the decays into flavour specific final state $K^+\pi^-$ can be used, which allows to equally reach the very same final state. This method is known as ADS (Atwood, Dunietz, Soni) [24].

For the neutral case, $B^0 \to D\overline{K}^{*0}$ (figure 1.4), both diagrams are colour suppressed, which reduces the branching fraction. On the other hand it increases the interference importance.

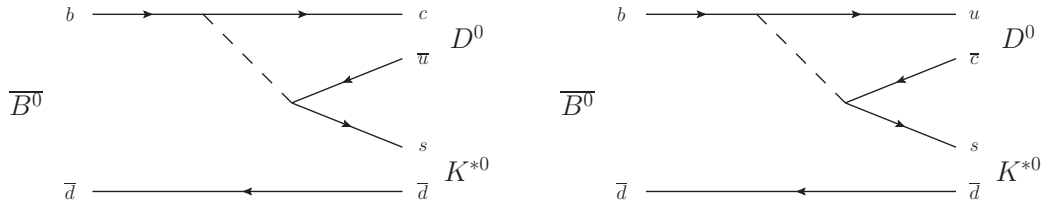

Figure 1.5: *Feynman diagrams for $\overline{B}^0 \to D^0K^{*0}$ (left) and $\overline{B}^0 \to \overline{D}^0K^{*0}$ (right).*

Another method involves an analysis of three body self-conjugate D decays. It was proposed by Grossman, Soffer and Zupan [25] and Bondar [26]. The sensitivity to γ comes from differences in the Dalitz plot of the D decay from $B^+ \to DK^+$ and $B^- \to DK^-$. The most favourable method is based on a Dalitz analysis of the decay $D \to K^0_S\pi^+\pi^-$, because of a large branching fraction and a rich resonances structure.

1.3.1.2 $B^0_s \to D^\pm_s K^\mp$

It is possible to extract $\gamma - \phi_M$ (ϕ_M is the B^0_s mixing phase) from time-dependent asymmetries in the decay of $B^0_s \to D^\mp_s K^\pm$ [27]. The tree level (figure 1.6) sensitivity to γ arises from the interference between the direct decay of B^0_s and $\overline{B}^0_s$ to $D^-_s K^+$ and decay after mixing. The ratio of the magnitudes of the two interfering amplitudes is expected to be approximately 0.4. The value of ϕ_M used to retrieve γ from $\gamma - \phi_M$ can be aqquired from the measurement of $B^0_s \to J/\psi\phi$ decays [20]. Let us notice that it is uniquely accessible at the LHCb.

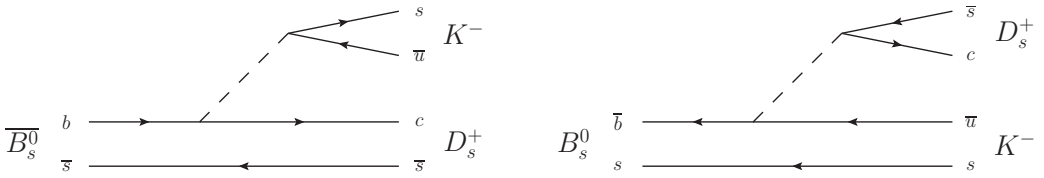

Figure 1.6: *Feynman diagrams for $\overline{B}_s^0 \to D_s^+ K^-$ (left) and $B_s^0 \to D_s^+ K^-$ (right)*

1.3.1.3 $B^0 \to D^{\pm}\pi\mp$

The time dependent CP asymmetries in $B^0 \to D^{\pm}\pi\mp$ allow to measure $\gamma + 2\beta$ [28], because β is already well measured. The formalism of the measurement is similar to the one introduced in $B_s^0 \to D_s^{\mp} K^{\pm}$. The ratio of the magnitudes of the interfering amplitudes is small. Hence the measurement requires large statistics.

1.3.2 γ from loop processes

1.3.2.1 $\mathrm{B}^0 \to \pi\pi$ and $\mathrm{B_s}^0 \to \mathrm{KK}$

Another interesting method [29, 30] is related to neutral B mesons transitions into two light pseudoscalar mesons: $\mathrm{B}^0 \to \pi\pi$ and $\mathrm{B_s}^0 \to \mathrm{KK}$ receive contributions from both tree and penguin topologies. The key point of this method is the usage of the U-spin symmetry [31], which is a subgroup of the $SU(3)$ flavour symmetry of strong interactions. It connects the strange and down quarks in the same way through $SU(2)$ transformations as the isospin symmetry connects the up and down quarks. This approach has two differences over the conventional $SU(3)$ flavour symmetry usage:

- There are no additional dynamical assumptions, for example annihilation topologies are not neglected.
- The electroweak penguins, which are not invariant under the isospin symmetry, can be included.

The two modes are related to each other through an interchange of all down and strange quarks (figure 1.7). The U-spin symmetry allows to derive relations between their hadronic parameters, and the experimental observables include sufficient information to extract the γ angle. The observables are the CP-averaged branching ratios as well as the direct and mixing-induced CP asymmetries. The theoretical accuracy of this method is limited by U-spin-breaking effects, which can be obtained experimentally to a certain extent.

1.3.2.2 $B \to K\pi\pi$ and $B_s^0 \to K^-\pi^+\pi^0$

The measurement of γ with $B_{d,u} \to K\pi\pi$ was already proposed at the LHCb, while the measurement involving $B_s^0 \to K^-\pi^+\pi^0$ is a new method. Both of them are related to the measurements presented in the next chapters of this document and will be described briefly theoretically in the next sections.

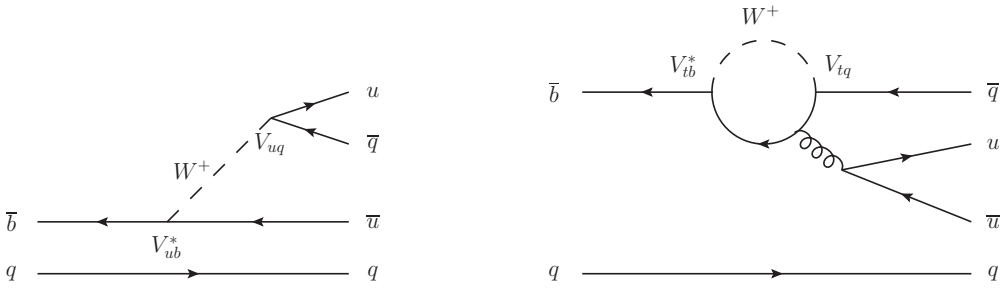

Figure 1.7: *Feynman diagrams for* $\mathrm{B}^0 \to \pi\pi$ *and* $\mathrm{B_s}^0 \to \mathrm{KK}$ *processes.*

1.4 Charmless three-body B decays

The history of $B \to K\pi\pi$ starts in 1991, when Lipkin, Nir, Quinn and Snyder [32] performed an isospin analysis of $K\pi\pi$ and obtained the relations among the amplitudes for various $B \to K\pi\pi$ decays, which led them to the extraction of the clean weak-phase. However, their analysis neglected the electroweak penguin (EWP) contribution. Twelve years later, in 2003, Deshpande, Sinha and Sinha [33] published the analysis for the case of symmetric $\pi\pi$ isospin states, which included EWP contributions. In their approach they assumed that the EWPs can be related to the tree diagrams, similarly as in [34, 35]. However, as presented in [36], these relations are incorrect in $K\pi\pi$. This situation last until 2011, when a new approach was published by Imbeault, Rey-Le Lorier and London [37]. This is a complex and comprehensive analysis of $B \to K\pi\pi$, which seems to put the γ extraction from these decays back to game.

Here we will review the methods proposed to extract γ from $B \to K\pi\pi$. We will start from the simplest approach proposed in the Gamma from Loops workgroup from Bediaga, Guerrer and Miranda (BGM) [38] at the LHCb. Then we will move to the analysis of Ciuchini, Pierini, Silvestrini (CPS) [39], and Gronau, Pirjol, Soni, Zupan (GPSZ) [40]. Recently, a paper with a very general analysis of three-body decays by Imbeault, Rey-Le Lorier and London (IRLL) [37] was published. As it does not contain an immediate practical application, we will not discuss it here.

1.4.1 BGM method

This method [38] is based on a time-independent analysis of a quasi two-body decays. It uses the decay of charged $B^\pm$ to compute the penguins amplitude, which is then put into the calculation of B^0 amplitude, fixing the amplitudes of decays of both B into $K\chi_{c0}$. The method is based on three hypothesis:

1. The contribution to $B^\pm \to K^{*0}\pi^\pm$ is penguin only.
2. The penguin components in $B^\pm \to K^{*0}\pi^\pm$ and $B^0, \bar{B}^0 \to K^{*\pm}\pi^\mp$ are equal.
3. χ_{c0} has the same amplitude for $B^\pm \to K^\pm\chi_{c0}$ and $B^0, \bar{B}^0 \to K^0_S\chi_{c0}$.

Although there are experimental measurements which can be used as hints that the first two assumptions are correct, the method states, that the second and third can

be tested on the tree magnitudes measured from the intermediate process $B^0, \bar{B}^0 \to K^{*\pm}\pi^{\mp}$. On the other hand the method neglect completely annihilation diagrams contribution, which by some models are expected to be eventually significant [41]. The method also puts under the carpet the EWPs contribution. Hence it requires additional corrections, which effectively will lead to the analysis similar to the CPS/GPSZ. However it is described here, because it was the first analysis of charmless three-body decays with one kaon of B^0 proposed inside the LHCb collaboration, and it contains elements used also in the other analyses presented in the next sections.

1.4.1.1 $B^{\pm} \to K^{\pm}\pi^{+}\pi^{-}$ charmless mode

The first part of the method is Dalitz analysis of the auto-tagged decay $B^{\pm} \to K^{\pm}\pi^{+}\pi^{-}$, which aims at extraction of amplitudes of various intermediate resonances, such as $K^*(890)^0$, $K^*(1430)^0$, $\rho(770)^0$, $f_0(980)$ and χ_{c0}. It is based on the Isobaric model, where the two-body resonant intermediate state amplitudes are represented by Breit-Wigner functions multiplied by angular distributions associated with the spin of the resonance. The contributions from different resonances are combined with complex coefficients, which are then extracted from a maximum likelihood fit to the data. The total Isobaric amplitude, given as a function of Dalitz plot variables s_{12} and s_{13} is:

$$A_T = a_{NR}e^{i\delta_{NR}}A_{NR}(s_{12}, s_{13}) + \Sigma_{n=1}^{N} a_n e^{i\delta_j} A_n(s_{12}, s_{13}). \tag{1.36}$$

The fit parameters are the coefficient magnitudes a_{NR}, a_n, and the phases δ_{NR}, δ_j. The NR states for the non-resonant part, which amplitude (A_{NR}) is usually represented by a constant. The resonant amplitude (A_n) is given with:

$$A_n = {}^{J}F_n \times {}^{J}\mathcal{M}_n \times BW_n, \tag{1.37}$$

where ${}^{J}F_n$ are the Blatt-Weisskopf damping factors [42], ${}^{J}\mathcal{M}_n$ are spin-depend terms which account for angular-momentum conservation, and BW_n is a relativistic Breit-Wigner function:

$$BW_n = \frac{m_n\Gamma_n}{m_n^2 - s_{ij} - im_n\Gamma_n(s_{ij})}. \tag{1.38}$$

${}^{J}\mathcal{M}_n$ in case of a resonance formed by a pair of particles noted with subscripts **1** and **3** are given by:

- 1, for spin 0 resonance.
- $-2|\mathbf{p_3}||\mathbf{p_2}|\cos\theta$ for spin 1 resonance.
- $\frac{4}{3}(|\mathbf{p_3}||\mathbf{p_2}|)^2(3\cos^2\theta - 1)$ for spin 2 resonance.

In these equations $\mathbf{p_2}$ and $\mathbf{p_3}$ are the 3-momentum of the particles **2** and **3** accordingly, and θ is the angle between **2** and **3**. All are measured in the rest frame of the resonance.

As it was already mentioned, it is assumed that $B^{\pm} \to K^{*0}\pi^{\pm}$ is only penguin. It also applies to further K^{*0} resonances. In addition, it is expected from $SU(3)$ flavour symmetry, that the penguin amplitudes for all $B \to K^*\pi$ processes are the same. From the analysis of $B^{\pm} \to K^{\pm}\pi^{+}\pi^{-}$ the amplitude of penguin $B^{\pm} \to K^{*0}\pi^{\pm}$ is extracted, with a_P as the magnitude and δ_P as the phase.

1.4.1.2 $B^0, \bar{B}^0 \to K^0_S\pi^+\pi^-$ step

Now let's move to the $B^0, \bar{B}^0 \to K^0_S\pi^+\pi^-$ decay. We are again interested in the decay through the intermediate resonance $K^{*\pm}$. The amplitudes can be written as: $A_{K^{*+}\pi^-} = a_P e^{i\delta_P} + a_T e^{i\theta^+}$ for $B^0 \to K^{*+}\pi^-$, and $A_{K^{*-}\pi^+} = a_P e^{i\delta_P} + a_T e^{i\theta^-}$ for $\bar{B}^0 \to K^{*-}\pi^+$, where $\theta^\pm = (\delta_T \pm \gamma)$, and $\delta_{P,T}$ denotes phases of penguin and tree transitions. We put a_P and δ_P from the previous point, and extract a_T and $\theta^\pm$ from the Dalitz analysis of $B^\pm \to K^\pm\pi^+\pi^-$. Once we have $\theta^\pm$, we can calculate the weak phase γ with:

$$\gamma = \frac{\theta^+ + \theta^-}{2}. \tag{1.39}$$

This mode is, opposite to $B^\pm \to K^\pm\pi^+\pi^-$, not auto-tagged. The typical approach in such case is to use the other b for the tagging purposes. Thus, the precision depends on the precision of the tagging. In the LHCb experiment, one has to deal with an effective tagging efficiency of few percent. Fortunately a method of the analysis is possible: it is a joint fit of B^0 and $\bar{B}^0$. We follow the authors of the method with the expression for the probability of observation the final state $K^0_S\pi^+\pi^-$, independent from its origin: $|M(\Delta t)|^2 + |\bar{M}(\Delta t)|^2$, where:

$$\begin{aligned} M(\Delta t) &= e^{-(\Gamma/2 - iM)\Delta t}\left[A\cos(\Delta m\Delta t/2) - i\frac{q}{p}\bar{A}\sin(\Delta m\Delta t/2)\right], \\ \bar{M}(\Delta t) &= e^{-(\Gamma/2 - iM)\Delta t}\left[\bar{A}\cos(\Delta m\Delta t/2) - i\frac{q}{p}A\sin(\Delta m\Delta t/2)\right], \end{aligned} \tag{1.40}$$

are the matrix elements for observing the original B^0 and $\bar{B}^0$. The A and $\bar{A}$ time-independent amplitudes are for $B^0 \to K^0_S\pi^+\pi^-$ and $\bar{B}^0 \to K^0_S\pi^+\pi^-$ decays. When the production rates for B^0 and $\bar{B}^0$ are the same, and $|p/q| = 1$, in the sum the mixing dependence disappear:

$$|M(\Delta t)|^2 + |M(\Delta t)|^2 = e^{-\Gamma t}(|\mathcal{A}^0|^2 + |\bar{\mathcal{A}}^0|^2). \tag{1.41}$$

Similarly to the equation 1.36, A^0 and $\bar{A}^0$ are written as:

$$\begin{aligned} A^0 &= a_\chi e^{i\delta_\chi}A_\chi + \Sigma_i a_i e^{i\delta_i}A_i, \\ \bar{A}^0 &= \bar{a}_\chi e^{i\bar{\delta}_\chi}A_\chi + \Sigma_i \bar{a}_i e^{i\bar{\delta}_i}A_i. \end{aligned} \tag{1.42}$$

The maximum likelihood fit with free parameters a, δ, $\bar{a}$, $\bar{\delta}$ for a joint sample of untagged, time integrated B^0 and $\bar{B}^0$ events is made to the probability density function given by:

$$PDF = \frac{|A^0|^2 + |\bar{A}^0|^2}{N^0 + \bar{N}^0}, \tag{1.43}$$

where $N^0 = \int |A^0|^2 ds_{ij} ds_{jk}$, and $\bar{N}^0 = \int |\bar{A}^0|^2 ds_{ij} ds_{jk}$.

In the convention which assigns to K^0_S, π^+, π^- indexes **1**, **2**, **3** respectively, the charge conjugation operation is equivalent to swapping the Dalitz variables $s_{12} \leftrightarrow s_{13}$. The schematic of the Dalitz plot with these variables is presented in the figure 1.8. The resonances of K^{*0} are aligned in different axis for A^0 and $\bar{A}^0$, which can be understood as a kind of signature for the event originating from B^0 and $\bar{B}^0$ respectively. Although the $\pi\pi$ resonances for B^0 and $\bar{B}^0$, the regions of interference between $K\pi$ and $\pi\pi$ are separated. The result of the fit, combined with the information extracted in the previous step, and fixation of the phase from $K^0_S\chi_{c0}$, allows to compute γ.

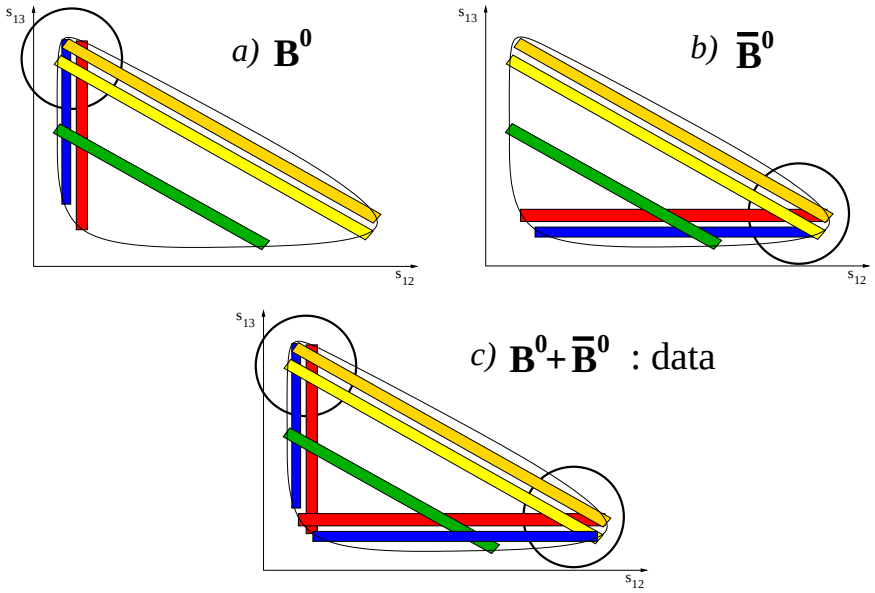

Figure 1.8: *Schematic Dalitz plot of $B^0 \to K^0_S\pi^+\pi^-$ (a), $\bar{B}^0 \to K^0_S\pi^+\pi^-$ (b), and a joint one (c). The colour stripes represent resonances regions. The circles display the regions of interference. There is no interference between the horizontal and the vertical red and blue stripes (K^{*0}). s_{12} is the square invariant mass of $K^0_S\pi^+$ and s_{13} is the square invariant mass of $K^0_S\pi^-$.*

1.4.2 CPS and GPSZ method

This method was initially described in [39], and then extended in [40]. In this review we will focus on the selected parts of the analyses concentrating on γ extraction from $B \to K^*\pi$, referring for more details to the mentioned publication.

1.4.2.1 Isospin decomposition

We start from a decomposition of $B \to K^*\pi$ decays (K^* states for any K resonance), by applying the isospin symmetry. Writing the decays explicitly, we have for possibilities: $B^+ \to K^{*+}\pi^0$, $B^+ \to K^{*0}\pi^+$, $B^0 \to K^{*0}\pi^0$, $B^0 \to K^{*+}\pi^+$. The amplitudes can be written as:

$$\begin{aligned} -A(K^{*+}\pi^-) &= B_{1/2} - A_{1/2} - A_{3/2}, \\ A(K^{*0}\pi^+) &= B_{1/2} + A_{1/2} + A_{3/2}, \\ -\sqrt{2}A(K^{*+}\pi^0) &= B_{1/2} + A_{1/2} - 2A_{3/2}, \\ \sqrt{2}A(K^{*0}\pi^0) &= B_{1/2} - A_{1/2} + 2A_{3/2}. \end{aligned} \tag{1.44}$$

The minus sign is associated with a $\bar{u}$ quark in a meson. The amplitudes B and A correspond to $\Delta I = 0$ and $\Delta I = 1$ transitions respectively, while their subscripts denote the isospin of the final state $K^*\pi$. The amplitudes marked with B are connected with QCD penguins, while by A we denote other amplitudes. By summing with correct coefficients the first and the last equations, or the second and the third equations, we

obtain:

$$\begin{aligned} 3A_{3/2} &= A(K^{*+}\pi^-) + \sqrt{2}A(K^{*0}\pi^0) \\ &= A(K^{*0}\pi^+) + \sqrt{2}A(K^{*+}\pi^0). \end{aligned} \tag{1.45}$$

With another combinations (first, second, fourth, and first, second, and third) we can extract $A_{1/2}$:

$$\begin{aligned} 6A_{1/2} &= A(K^{*+}\pi^-) + 3A(K^{*0}\pi^+) - 2\sqrt{2}A(K^{*0}\pi^0) \\ &= 3A(K^{*+}\pi^-) + A(K^{*0}\pi^+) - 2\sqrt{2}A(K^{*+}\pi^0). \end{aligned} \tag{1.46}$$

The similar decomposition is done for the charge conjugate decays, with amplitudes denoted by $\bar{A}$.

The two $\Delta I = 1$ amplitudes, $A_{3/2}$ and $A_{1/2}$, do not contain QCD penguin contributions. If there was no EWP contribution, they would carry only a single weak phase equal γ. First, let us proceed with this assumption of no EWP contributions, as it is presented in the original publications. We define two ratios:

$$\begin{aligned} R_{1/2} &\equiv \frac{\bar{A}_{1/2}}{A_{1/2}}, \\ R_{3/2} &\equiv \frac{\bar{A}_{3/2}}{A_{3/2}}, \end{aligned} \tag{1.47}$$

and the phase γ given with:

$$\begin{aligned} \Phi_{1/2} &\equiv -\frac{1}{2}\arg(R_{1/2}), \\ \Phi_{3/2} &\equiv -\frac{1}{2}\arg(R_{3/2}), \\ \gamma &= \Phi_{3/2} = \Phi_{1/2}. \end{aligned} \tag{1.48}$$

The conclusion is, that if there was no EWP contribution, the γ angle can be calculated easily with the equations above.

1.4.2.2 Electroweak penguins inclusion

To include EWPs we will start from the basic equations of electroweak interactions. We can write the general representation of the electroweak effective hamiltonian for quark-level $\bar{b}$ decays [43]:

$$H_{\text{eff}} = \frac{G_F}{\sqrt{2}} \sum_{q=d,s} \left(\sum_{p=u,c} \lambda_p^{(q)} (C_1(\mu) Q_1^{qp}(\mu) + C_2(\mu) Q_2^{qp}(\mu)) - \lambda_t^{(q)} \sum_{i=3}^{10} C_i(\mu) Q_i(\mu) \right), \tag{1.49}$$

where $\lambda_p^{(q)} = V_{pb}^* V_{pq}$, and μ is the renormalisation point. All physical quantities must be independent of μ. C_i are the Wilson coefficients, which include gluons (QCD corrections) whose energy is above μ, while the operators Q_i include QCD corrections

of energy less than μ. We are interested only in transitions in which we have s in the final state, and we don't have any c, so the hamiltionian reduces to:

$$H^s_{\text{eff}} = \frac{G_F}{\sqrt{2}} \left(V^*_{ub} V_{us} (C_1(\mu) Q^{su}_1(\mu) + C_2(\mu) Q^{su}_2(\mu)) - V^*_{tb} V_{ts} \sum_{i=3}^{10} C_i(\mu) Q_i(\mu) \right). \quad (1.50)$$

For the rest of this chapter we will skip the superscript of Q^{su}_i. The operators Q_i are divided into groups:

- Current-current operators:

$$Q_1 = (\bar{b}_\alpha u_\beta)_{\text{V-A}} (\bar{u}_\beta s_\alpha)_{\text{V-A}}, \quad (1.51)$$
$$Q_2 = (\bar{b}_\alpha u_\alpha)_{\text{V-A}} (\bar{u}_\beta s_\beta)_{\text{V-A}}. \quad (1.52)$$

- QCD-penguins operators:

$$Q_3 = (\bar{b}_\alpha s_\alpha)_{\text{V-A}} \sum_q (\bar{q}_\beta q_\beta)_{\text{V-A}} \quad (1.53)$$
$$Q_4 = (\bar{b}_\alpha s_\beta)_{\text{V-A}} \sum_q (\bar{q}_\beta q_\alpha)_{\text{V-A}}, \quad (1.54)$$
$$Q_5 = (\bar{b}_\alpha s_\alpha)_{\text{V-A}} \sum_q (\bar{q}_\beta q_\beta)_{\text{V+A}}, \quad (1.55)$$
$$Q_6 = (\bar{b}_\alpha s_\beta)_{\text{V-A}} \sum_q (\bar{q}_\beta q_\alpha)_{\text{V+A}}. \quad (1.56)$$

- Electroweak-penguins operators:

$$Q_7 = \frac{3}{2} (\bar{b}_\alpha s_\alpha)_{\text{V-A}} \sum_q e_q (\bar{q}_\beta q_\beta)_{\text{V+A}}, \quad (1.57)$$
$$Q_8 = \frac{3}{2} (\bar{b}_\alpha s_\beta)_{\text{V-A}} \sum_q e_q (\bar{q}_\beta q_\alpha)_{\text{V+A}}, \quad (1.58)$$
$$Q_9 = \frac{3}{2} (\bar{b}_\alpha s_\alpha)_{\text{V-A}} \sum_q e_q (\bar{q}_\beta q_\beta)_{\text{V-A}}, \quad (1.59)$$
$$Q_{10} = \frac{3}{2} (\bar{b}_\alpha s_\beta)_{\text{V-A}} \sum_q e_q (\bar{q}_\beta q_\alpha)_{\text{V-A}}. \quad (1.60)$$

The forms are summed over α and β, which are colour indexes. $\bar{q}q$ denotes a pair of light quarks $q = u, d, s, c$. e_q stands for the electric charges of the quarks. The quark current $(\bar{q}^{(1)} q^{(2)})$ denotes $\bar{q}^{(1)} \gamma^\mu (1 \pm \gamma_5) q^{(2)}$. Typical diagrams of the operators are shown in the figure 1.9: the current-current in the subfigure (a), the QCD-penguins in (b), and the electroweak-penguins in (c).

Now the key points are the observations in $\Delta S = 1$ decays. The first is that the EWP operators Q_7 and Q_8 are associated with small Wilson coefficients C_7 and C_8 respect to C_9 and C_{10}:

$$|C_{9,10}| \gg |C_{7,8}|, \quad (1.61)$$

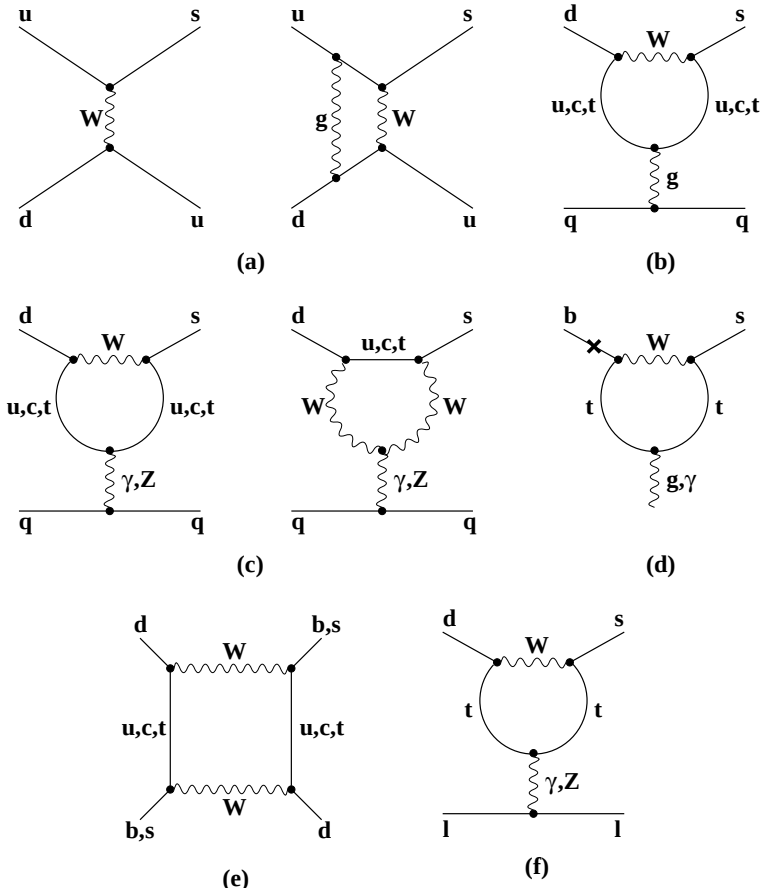

Figure 1.9: *Typical diagrams in the full theory from which the operators (1.51)-(1.60) originate [43]. Note that there is no correspondence between the diagrams and the operators – illustration only.*

which means that we can neglect them. The second comes from the operator relations, which allow to eliminate $Q_{9,10}$:

$$Q_{9,10} = \frac{3}{2}Q_{2,1} + [\text{operators with } \Delta I = 0]. \tag{1.62}$$

Now the effective hamiltonian for $\Delta I = 1$, $\Delta S = 1$ becomes:

$$H^s_{\Delta I=1} = \frac{G_F}{\sqrt{2}}\left[V^*_{ub}V_{us}\left(C_1Q_1 + C_2Q_2\right) - \frac{3}{2}V^*_{tb}V_{ts}\left(C_9Q_2 + C_{10}Q_1\right)\right] \tag{1.63}$$

Defining new operators and coefficients as:

$$\begin{aligned} Q_\pm &\equiv \frac{1}{2}\left(Q_1 \pm Q_2\right), & (1.64)\\ C_\pm &\equiv C_1 \pm C_2, & (1.65)\\ C^{EWP}_\pm &\equiv C_9 \pm C_{10}, & (1.66) \end{aligned}$$

one can write the hamiltonan as:

$$\begin{aligned} H^s_{\Delta I=1} &= \frac{G_F}{\sqrt{2}}\left[\left(V^*_{ub}V_{us}C_+ - \frac{3}{2}V^*_{tb}V_{ts}C^{EWP}_+\right)Q_+\right.\\ &+ \left.\left(V^*_{ub}V_{us}C_- + \frac{3}{2}V^*_{tb}V_{ts}C^{EWP}_-\right)Q_-\right]. \end{aligned} \tag{1.67}$$

We observe that the relation between Wilson coefficients:

$$\frac{C^{EWP}_+}{C+} = \frac{C^{EWP}_-}{C-}, \tag{1.68}$$

holds up to 1% correction [43]. That allows us to write:

$$H^s_{\Delta I=1} = \frac{G_F}{\sqrt{2}}\left[V^*_{ub}V_{us}(1+\kappa)\left(C_+Q_+ + \frac{1-\kappa}{1+\kappa}C_-Q_-\right)\right], \tag{1.69}$$

where

$$\kappa \equiv -\frac{3}{2}\frac{C^{EW}_+}{C_+}\frac{V^*_{tb}V_{ts}}{V^*_{ub}V_{us}}. \tag{1.70}$$

Therefore the ratios (1.47) can be rewritten with EWP inclusion:

$$R_I = e^{2i[\gamma + \arg(1+\kappa)]}\frac{1 + \frac{1-\kappa^*}{1+\kappa^*}r_I}{1 + \frac{1-\kappa}{1+\kappa}r_I}, \tag{1.71}$$

where

$$r_I \equiv \frac{\langle(K^*\pi)_I|C_-Q_-|B\rangle}{\langle(K^*\pi)_I|C_+Q_+|B\rangle}, \tag{1.72}$$

and I denotes the isospin of the final state.

The parameter κ depends only on the calculable Wilson coefficients and on the CKM parameters. We can estimate the shift in Φ_I (equation 1.48) caused by this

parameter alone, using the central values of the CKM parameters [8], and next to leading order values of Wilson coefficients at $\mu = m_b = 4.8$ GeV:

$$\kappa = -0.35 + 0.56i. \tag{1.73}$$

This translates into $\arg(1+\kappa) = 41^\circ$.

The case of r_I is more complicated. While for $B \to K\pi$ decays the $SU(3)$ symmetry guarantees that $\langle (K^*\pi)_{3/2}|C_-Q_-|B\rangle$ vanishes, the same argument, based on the symmetry of the final state does not apply to $K^*\pi$ final states. We restrict ourselves here to $(K^*\pi)_{3/2}$ case only. Calculations based on $SU(3)$ flavour symmetry presented in [40] result in the representation of $r_{3/2}$ given by:

$$r_{3/2} = \frac{A(\rho^+\pi^0) - A(\rho^0\pi^+) - \sqrt{2}[A(K^{*+}\bar{K}^0) - A(\bar{K}^{*0}K^+)]}{A(\rho^+\pi^0) + A(\rho^0\pi^+)}. \tag{1.74}$$

The expression can be simplified by neglecting the $\Delta S = 0$ QCD penguin amplitude given by $\sqrt{2}[A(K^{*+}\bar{K}^0) - A(\bar{K}^{*0}K^+)]$, and by assuming that the strong phase between the two amplitudes in the remaining term is small. With these assumptions the results is:

$$r_{3/2} = 0.054 \pm 0.045 \pm 0.023, \tag{1.75}$$

where the first error comes from the experimental errors in $B \to \rho\pi$ branching ratios, the second is due to allowed $SU(3)$ symmetry breaking in the calculations. For the discussion on the errors caused by the assumptions taken in the calculation of $r_{3/2}$ one has to refer to [40].

Combining the results together, the path to extract γ theoretically is clear:

$$\gamma = \frac{1}{2}\arg\left(\frac{\overline{A_{3/2}}}{A_{3/2}}\frac{1+\frac{1-\kappa}{1+\kappa}r_{3/2}}{1+\frac{1-\kappa^*}{1+\kappa^*}r_{3/2}}\right) - 2\arg(1+\kappa), \tag{1.76}$$

where all parameter have been already expressed in terms of measurable amplitudes.

1.4.2.3 Measurements

Experimentally we have to find the amplitudes from the equation (1.45). To do it we need to perform a Dalitz analysis on different decay samples. The analysis itself is the same as in the BGM case. Let us look at the decays and information that we can retrieve from their analyses.

- $B^+ \to K^+\pi^+\pi^-$
  This self-tagging process give information about the magnitudes of amplitudes $B^+ \to K^{*0}(892)\pi^+$, $B^+ \to K_0^{*0}(1430)\pi^+$, and eventually the other K^* resonances, as well as their relative phase. The same for charged conjugate. However, this decay provides no information on a relative phase between $K^{*0}\pi^+$ and $K^{*0}\pi^-$.

- $B^0 \to K^+\pi^-\pi^0$
  This decay is also self-tagged, and allows to fit $A(B^0 \to K^{*+}\pi^-)$ and $A(B^0 \to K^{*0}\pi^0)$. It is possible to extract two magnitudes for $K^*(892)$ and $K_0^*(1430)$, with three relative phases between these amplitudes. The study of this process permits a measurement of the magnitude of $R_{3/2}$, but not its phase.

- $B^0 \to K^0_S\pi^+\pi^-$
  This mode is not self-tagged, however very useful to relate the phases of $A(K^{*+}\pi^-)$ and $\bar{A}(K^{*-}\pi^+)$. The analysis here is similar to the one described in the BGM section.

- $B^+ \to K^0_S\pi^+\pi^0$
  Again a flavour specific process, which allows to determine the magnitudes of four amplitudes: $A(K^{*0}\pi^+)$, $A(K^{*+}\pi^{0)}$, $A(K^{*0}_0\pi^+)$, and $A(K^*_0\pi^0)$, with their relative phases. The decay not measured previously.

- $B^0 \to K^0_S\pi^0\pi^0$
  This decay seems to be not accessible experimentally now, as it involves two π^0, and it is not flavour specific. If it was possible, then it would allow to measure the phase difference between $A(K^{*0}\pi^0)$ and $\bar{A}(K^{*0}\pi^0)$.

1.5 $B^0_s \to K\pi\pi$

The method of extraction γ from $B^0_s \to K\pi\pi$ decays was initially proposed by Ciuchini, Pierini, and Silvestrini (CPS) in [44], following the scheme of $B \to K\pi\pi$ analysis. Then it was reviewed by Gronau, Pirjol, Soni, and Zupan (GPSZ) in [40]. This method is unavailable for the B-factories. Moreover it is based on the decays which are predicted, but never observed yet. The virtue of this approach is that it is much lower influenced by EWPs than $B \to K\pi\pi$.

The isospin decomposition for this mode gives us (for the diagrams see figure 1.10):

$$\begin{aligned} A_s(K^{*+}\pi^-) &= A^s_{3/2} - \sqrt{2}B^s_{1/2}, \\ A_s(K^{*0}\pi^0) &= \sqrt{2}A^s_{3/2} + B^s_{1/2}, \end{aligned} \tag{1.77}$$

where again $B^s_{1/2}$ denotes the amplitude which contains a QCD penguin contribution, and $A^s_{3/2}$ denotes the other amplitudes. Since this is $\Delta S = 0$ transition, the QCD penguin operator behaves as $\Delta I = 1/2$, and it is contained only in $B^s_{1/2}$, what allows us to construct a QCD-penguin-free amplitude:

$$3A^s_{3/2} = A_s(K^{*+}\pi^-) + \sqrt{2}A_s(K^{*0}\pi^0). \tag{1.78}$$

Neglecting EWP contributions, the amplitude $A_{3/2}$ is pure tree. We can define a ratio similar to the equation (1.47):

$$R^s_{3/2} \equiv \frac{\bar{A}^s_{3/2}}{\bar{A}^s_{3/2}}, \tag{1.79}$$

and $\Phi^s_{3/2}$, which is equal to γ:

$$\Phi^s_{3/2} \equiv -\frac{1}{2}\arg(R^s_{3/2}) = \gamma. \tag{1.80}$$

In the process of estimating the impact of EWP inclusion we can find, that the value of $r_{3/2}$ given in the equation (1.72) in $B^0_s \to K^*\pi$ vanishes, $r^s_{3/2} = 0$, because for $\Delta S = 0$ part of Q_- is pure $\Delta I = 1/2$. Hence only the κ^s parameter can influence

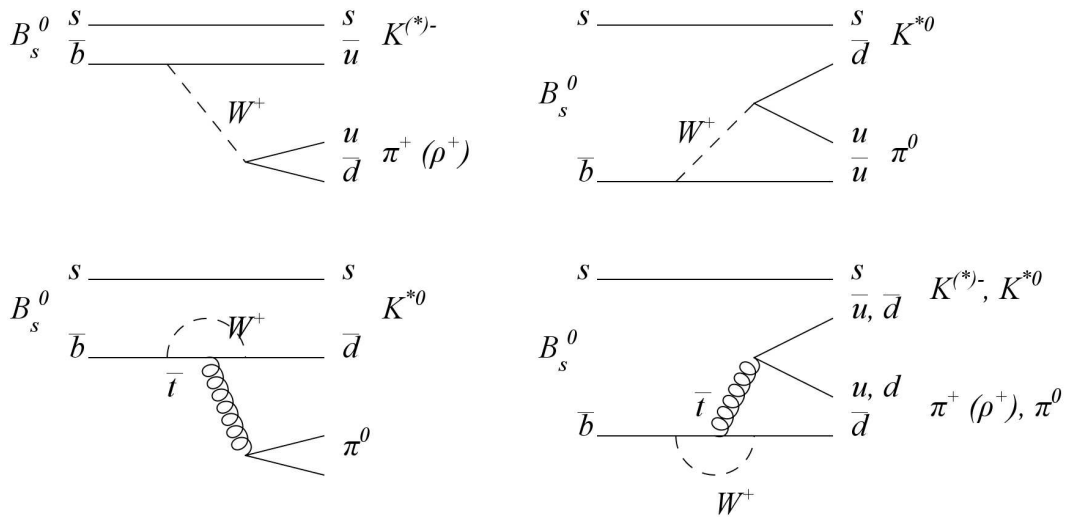

Figure 1.10: *Tree and QCD penguin diagrams contributing to* $B_s^0 \to K^-\pi^+\pi^0$.

γ value. The estimation from [44] gives $\kappa^s = (0.4 + 2.8i) \cdot 10^{-2}$, which means that the impact of EWPs is negligible. The main conclusion is that the theoretical error for calculating γ with (1.80) is below one degree. Additionally, the measurement is unaffected by the new physics entering at the loop level. It places it at the same level as gamma from pure tree decays, even if this is not a purely tree decay itself.

Experimentally the procedure is divided into two steps. The amplitudes $A^s_{3/2}$ can be determined by looking at the decay chains: $B_s^0 \to K^{*-}(\to K^-\pi^0)\pi^+$ and $B_s^0 \to K^{*0}(\to K^-\pi^+)\pi^0$ from the Dalitz analysis of auto-tagged sample of $B_s^0 \to K^-\pi^+\pi^0$.. Similarly for the charge conjugate amplitudes. As K^* any measurable resonance can be used. Still we miss the phase difference between $A^s_{3/2}$ and $\bar{A}^s_{3/2}$.

This information can be extracted from the second Dalitz analysis, this time the $K^0_S\pi^+\pi^-$ which is not flavour specific. We consider the decay chain $B_s^0 \to K^{*-}(\to \bar{K}^0\pi^-)\pi^+$ and its charge conjugate. These two decays (it means: the normal one and the charge conjugate) do not interfere directly, but they both interfere with the decays of $B_s^0, \bar{B}_s^0 \to \rho^0(\to \pi^+\pi^-)K^0_S$, or any other $\pi^+\pi^-$ resonance, such as for example f^0. In the untagged case, such as the LHCb case, the analysis can be performed similarly to $B^0 \to K^0_S\pi^+\pi^-$ (described previously). The physics behind these modes is rich, but it is experimentally extremely challenging, since it relies on both K^0_S and π^0 final states reconstruction.

Chapter 2

LHCb – the detector at the LHC

The Large Hadron Collider (LHC) is the highest energy accelerator ever built by humankind. It is a very complicated machine, which needs as well complicated infrastructure. Usually people build accelerators which serve for multiple experiments. The same applies for the LHC. One of the experiments is the LHCb.

This chapter describes shortly the design of the LHC and LHCb. It starts from basic information on the accelerator, and it is followed by the second part devoted to the LHCb construction. A short description of each subdetector is given, focused on the properties important for the analyses presented in the rest of the chapters.

2.1 Large Hadron Collider

The Large Hadron Collider is an opposite, circulating beams collider of very high energies. It is localised at CERN and occupies the same 27 km length tunnel as its predecessor – the Large Electron Positron Collider (LEP). More precisely it shares the same tunnel and some of the same experiment locations as the LEP. The first circulations of beams took place on September 10th, 2008. A technical accident in one of superconducting magnetic dipoles damaged a part of the infrastructure, which forced an unscheduled stop of one year. Again, a stable beam was present in the LHC on November 20th, 2009. It may be understood as the beginning of the new era in high energy physics collider researches and measurements.

2.1.1 Accelerator overview

The LHC was designed as a cold machine mainly for the acceleration and collision of proton beams, however a heavy-ion mode was also foreseen. The primary aim was to reach the energy of 7 TeV per particle, which is the energy of 14 TeV in the mass centre system. Then it was realised that in the first years it would be very difficult to reach that energy, and the energy was reduced in two steps: first to 10 TeV and then to 7 TeV in the mass centre. The last working point, with beams at 3.5 TeV per particle was used for 2010 and 2011 collisions. The production and the acceleration of protons is realised in a few steps and presented in the figure 2.1: the process starts from the LINAC2 which gives protons the first energy of 50 MeV, then they are accelerated to 1.4 GeV in the Booster, transferred to the Proton Synchrotron where they reach the energy of 25 GeV. The final step before the injection to the LHC is the Super Proton Synchrotron which is designed to accelerate to 450 GeV per particle.

The beams are driven by superconducting magnets in cryostats cooled with superfluid helium to keep the magnets below 2 K. The nominal magnetic field for energy per proton equal to 7 TeV is equal to 8.33 T. There are 1232 magnets, additionally 392 quadrupole magnets are installed, which focus the beams, accompanied by radio frequency cavities which accelerate the particles.

2.1.2 Experiments at the LHC

Several experiments are placed around the LHC. They vary in size and complexity. The three largest proton-proton detectors (ATLAS, CMS, LHCb) are accompanied by one heavy ion detector: ALICE. ATLAS (A Toroidal LHC ApparatuS) [46] and the CMS (Compact Muon Solenoid) [47] are 4π (surrounding the collision point) detectors, designed to be used as general purpose apparatus, mainly focused at searches for new physics by looking for new particles, especially the famous Higgs boson as well as supersymmetric particles. ALICE (A Large Ion Collider Experiment) ([48],[49]) aim is to search for and explore quark-gluon plasma. The LHCb (LHC beauty) will be described in the following sections. Finally there are smaller experiments: TOTEM (TOTal Elastic and diffractive cross section Measurement) ([50],[51]) which measures the total cross-section in proton-proton collisions at the LHC, and LHCf (LHC forward) [52] designed to measure forward neutral particle production.

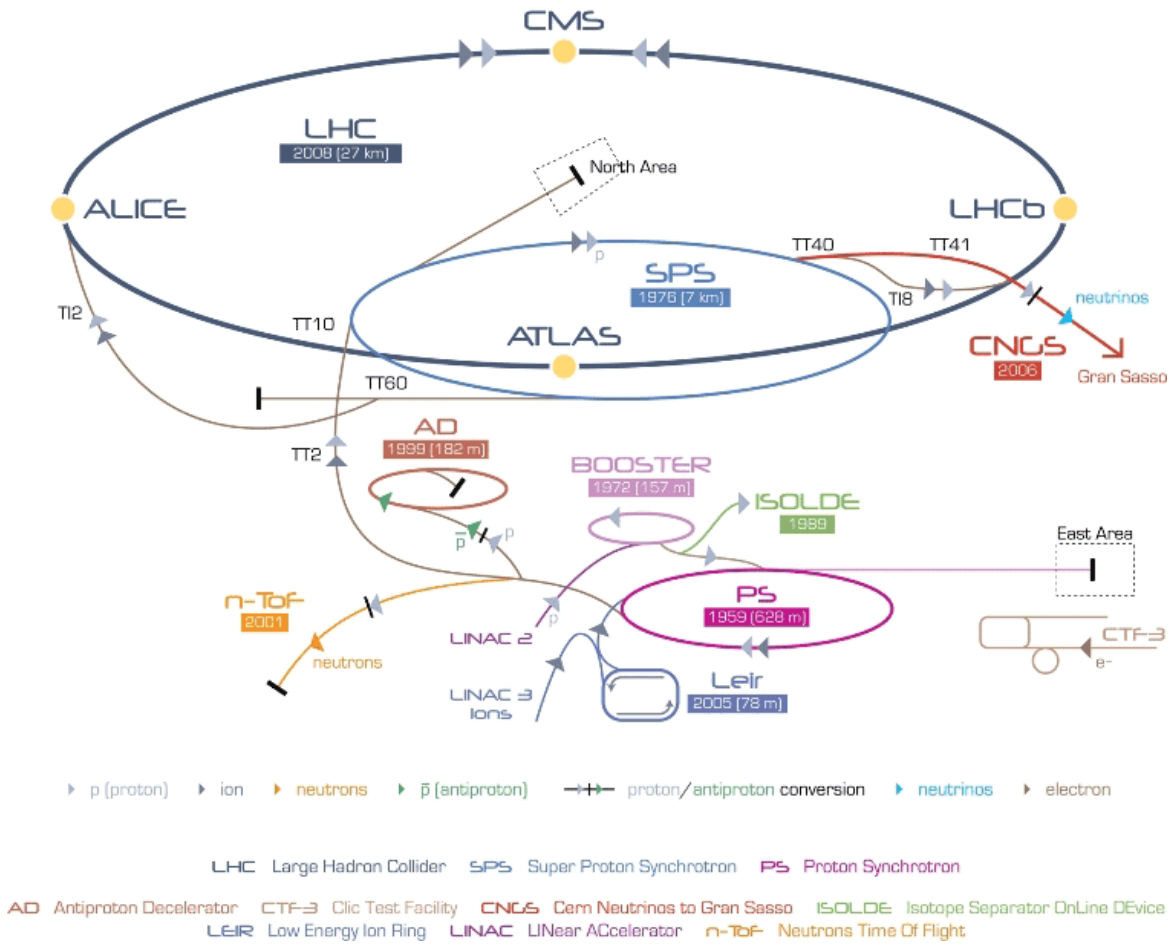

Figure 2.1: *Schematic representation of the accelerators system at CERN [45]. Proton path starts from LINAC2, leads through the Booster, the Proton Synchrotron (PS), the Super Proton Synchrotron (SPS) and ends in the Large Hadron Collider).*

2.1.3 Luminosity

There are different requirements for the luminosity from the experiments. ATLAS and the CMS are interested in the highest luminosity, because the expected cross-section for Higgs production is as low as a few femtobarns. On the other hand, the LHCb aims for precise measurements which require lower luminosity – to limit number of vertices.

The luminosity of the machine at a point of interaction is given with [53]:

$$\mathcal{L} = \frac{N_1 \, N_2 \, k_b \, f \gamma \, F}{4\pi\beta^* \epsilon}, \tag{2.1}$$

where N_i is the number of protons in each packet, k_b is the number of bunches, f is the revolution frequency, γ is the relativistic factor, β^* is the value of the betatron function at the interaction point, ϵ is the emittance, and F is the reduction factor caused by the crossing angle between the beams. The values of these are given in the table 2.1.

Parameter	Nominal Value	2010 Value	Aug 2011 Value
N_1, N_2	$1.05 \cdot 10^{11}$	$1.2 \cdot 10^{11}$	$(1.2 - 1.3) \cdot 10^{11}$
k_b	2835	368	1380
f [Hz]	11245.5	11245.5	11245.5
γ	7460.6	3730.3	3730.3
$\epsilon[\mu\,\mathrm{mrad}]$	3.75	2.0-3.5	2.0
β^* [m]	0.5	3.5	1.5 - 3.0
$\sqrt{S}$ [TeV]	14	7	7

Table 2.1: *Parameters of the LHC accelerator for the nominal luminosity of* $10^{34}\mathrm{cm}^{-2}\mathrm{s}^{-1}$*, and for conditions of 2010 (peek luminosity* $2 \cdot 10^{32}\mathrm{cm}^{-2}\mathrm{s}^{-1}$*) and August 2011 (*$2.37 \cdot 10^{33}\mathrm{cm}^{-2}\mathrm{s}^{-1}$*) [54].*

The LHC can give different luminosities at each interaction point. The design way is the refocusing the proton beams close to the experiment locations. Practically, luminosity changes for the LHCb were achieved by changing how the beams overlap at the interaction point. This is called *beam levelling*. This way ATLAS and the CMS can benefit from large luminosity, while the LHCb can use lower luminosity. The figure 2.2 shows the probability of different numbers of interactions per bunch crossing as a function of the luminosity. The collaboration decided that the luminosity of $3.5 \cdot 10^{32}$ $\mathrm{cm}^{-2}\mathrm{s}^{-1}$ should be the value used by the experiment, resulting in approximately 1.2 proton-proton interaction per bunch crossing. However for the years 2010 and 2011 higher luminosities were used from a range reaching the luminosity equivalent to about 2.5 visible interaction per bunch crossing in 2010 and 1.5 in 2011.

2.1.4 $b\bar{b}$ quark pair production

The dominant mechanism of b-quark pair production from collisions of protons is gluon-gluon fusion (figure 2.3) and quark-antiquark pair annihilation. The diagrams

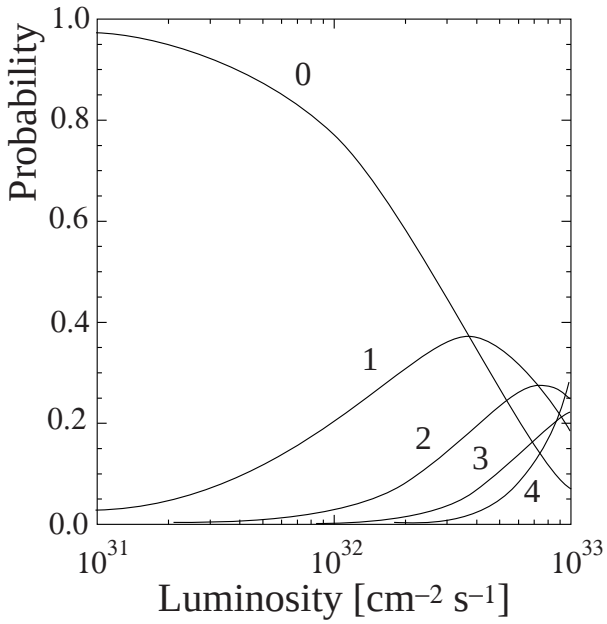

Figure 2.2: *Probability of different numbers of interactions per bunch crossing as a function of the luminosity for nominal filling scheme.*

involve vector particles and that leads to the fact that $b\bar{b}$ pairs are produced in the centre of mass rest frame mostly in forward and backward directions. This is additionally enhanced by the boost, and the observed angular distribution of the quark pair in the experiment is the one presented in the figure 2.4. The design of the LHCb as a single-arm spectrometer was chosen on the basis of this angular property.

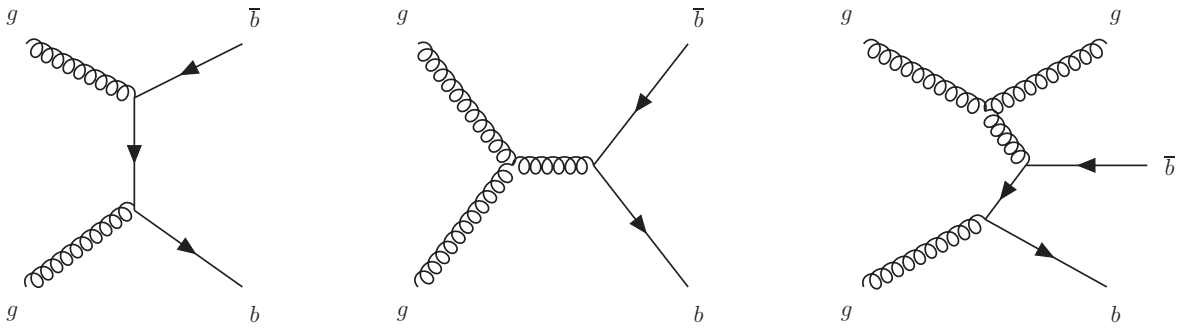

Figure 2.3: *Examples of gluon-gluon fusion production of $b\bar{b}$ pairs.*

2.2 LHCb detector

2.2.1 Overview

The LHCb concept was proposed such that the detector can use the large $b\bar{b}$ statistics available at the LHC in the forward region, and the fact, that differently from the

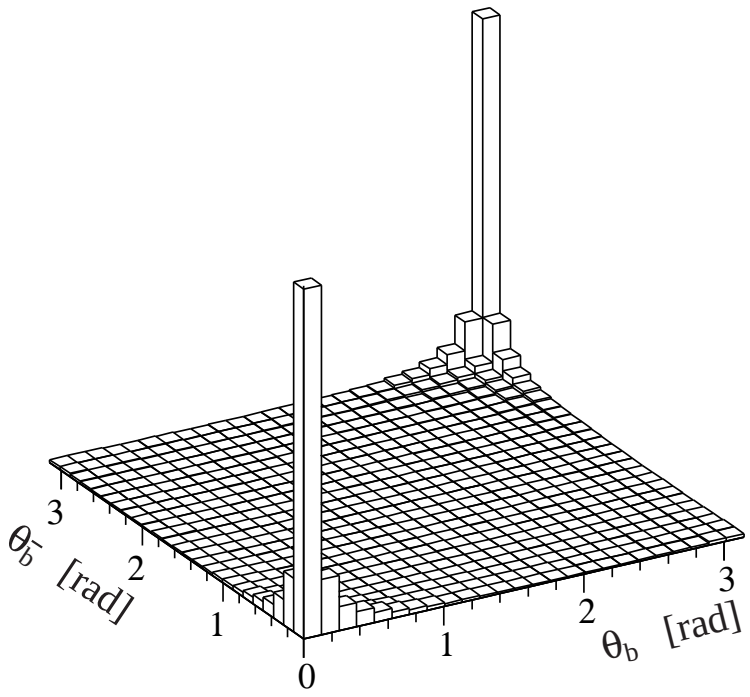

Figure 2.4: *Distribution of the polar angles of production of $b\bar{b}$ pairs in the LHCb calculated with PYTHIA [55] for collisions of p-p at $\sqrt{s} = 14$ TeV.*

B factories, all b-hadrons are produced. Among other measurements presented by the LHCb collaboration, the experiment has measured the ratio of hadronisation fraction into B_s^0 quark combination and B_d^0 quark combination [56] with the result of:

$$f_s/f_d = 0.253 \pm 0.017^{stat} \pm 0.017^{syst} \pm 0.020^{theor}. \tag{2.2}$$

It is in good agreement with the values determined at the LEP and the Tevatron [57].

The LHCb is a spectrometer with angular coverage stretched out from 10 mrad to 300 mrad in the bending[1] plane and to 250 mrad vertically. This concept is well-grounded by the forward-backward production of $b\bar{b}$ pairs presented in the figure 2.4.

The detector is localised at Interaction Point 8 of the LHC, which is also the cavern previously occupied by DELPHI detector. The schematic overview of the LHCb spectrometer with positions of the subdetectors is shown in the figure 2.5. During normal LHC operations beams collide inside the vertex locator (VELO). The products of the interactions which fly in the positive z-axis orientation, within the detector acceptance region, pass then the second detector of the tracking system : the trigger tracker (TT). Next is the first ring imaging Cherencov counter RICH1. Then there is the empty space but filled with the magnetic field. That space is surrounded by the dipole magnet – the source of the field. Then the strong magnetic field inside the magnet is found. Moving forward we cross the further tracking stations (T1, T2, T3), RICH2 and the first muon station (M1). Then the calorimeters have their kingdom, with an order (in terms of location in the direction from the interaction

[1]The bending plane is the horizontal plane, perpendicular to the magnetic field.

point) of: the scintillator pad detector (SPD), a layer made of lead, the preshower (PRS), the electromagnetic calorimeter (ECAL) and hadron calorimeter (HCAL). The LHCb last part is the rest of muon stations (M2-M5).

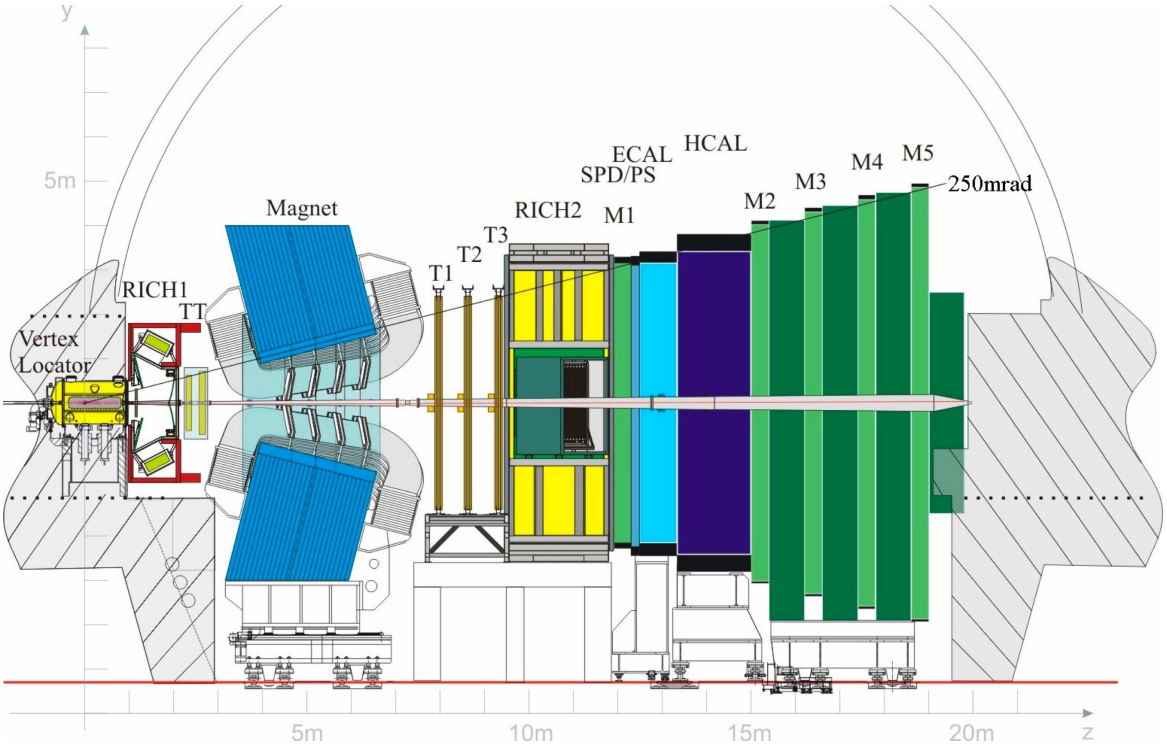

Figure 2.5: *LHCb schematic overview.*

From the point of view of calorimeter system that empty space is an original and very useful concept. It means that in front of the first detector (SPD) average material which a particle has to pass is about 60% of radiation length [58].

The detector is divided into two halves: left and right, or rather the C side (the cryogenics side) and the A side (the cavern access side). The halves (except of RICH detectors) can be moved independently horizontally which gives access for maintenance.

In the next sections a more detailed description of each subdetector will be presented. Again we will try to follow the natural path of particles produced in the collisions. Thus we begin from vacuum inside the beam pipe made of beryllium[59] and we will continue our travel up to the muon system.

2.2.2 Vertexing and tracking

2.2.2.1 Vertex locator

The closest detector to the beams intersection point is the VErtex LOcator (VELO), which aims for measuring the position of the primary vertices and to reconstruct the secondary vertices of weakly decaying hadrons (B mesons $c\tau$ is about $440 - 500$ μm). Additionally it has a function in the L0 trigger initially for *pile-up veto system*. Data

are taken in the detector in closed position. For all other operations like injection of the beams, the detector is in opened position to protect it from an eventual larger flux of particles.

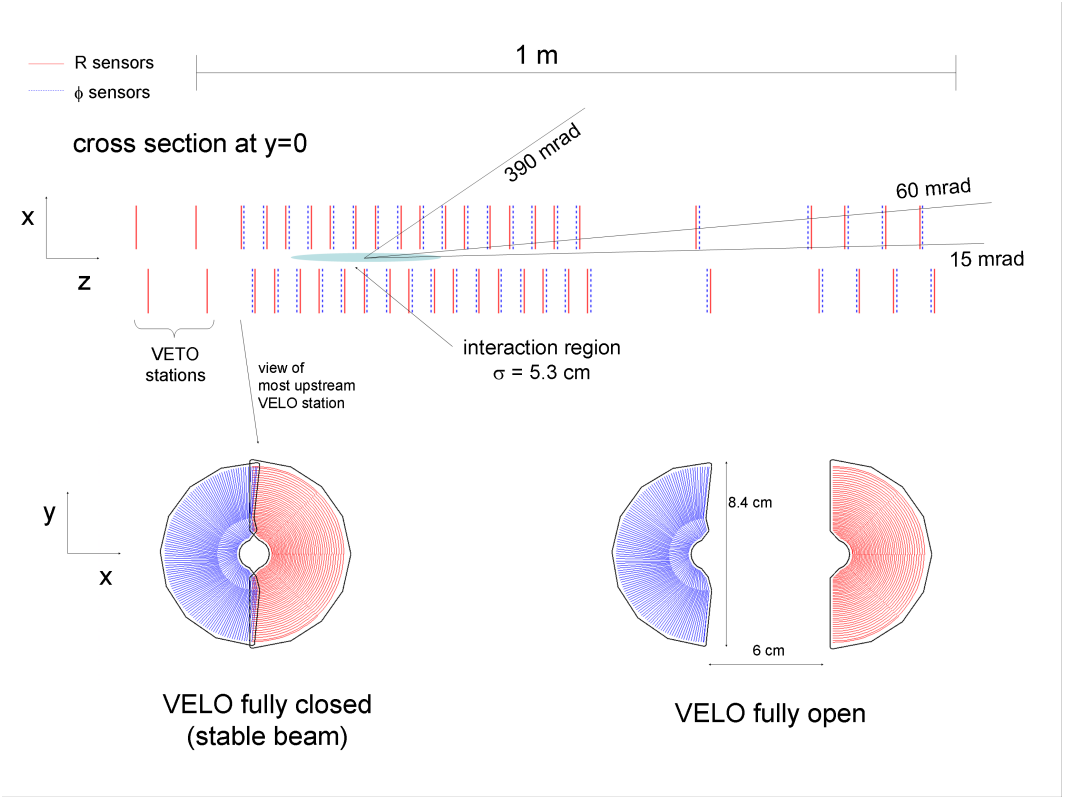

Figure 2.6: *Cross-section at $y = 0$ of closed VELO from above (top) and the schematic sketch of a pair of VELO sensors in closed and open positions (bottom). The bottom pictures also present the conception of two types of sensors: quasi radial measuring ϕ – marked with blue, and circular measuring r – marked with red.*

The detector construction is a masterpiece. It is built of 42 semicircular silicon detector modules (figure 2.6) (21 each side). Each one is perpendicular to the beam pipe and has two types of sensors. One have a circular shape, patterned with azimuthal, measures the radial coordinate r, while the other – quasi radial strips – the angular ϕ [60]. Both types of sensors are constructed from 2048 strips for each station. This structure also defines the local, cylindrical coordinates. Additionally, there are 4 stations (2 each side) in the backward hemisphere, which have to improve the primary vertex and track multiplicity measurements.

VELO measures charged particles as close to the beam pipe as possible. It was already remarked that the b-hadrons are produced mostly at low small angles, that explains why the detector has to be so close to the beam line. VELO starts at $r = 5$ mm, but the sensitive part of it displaced by 3 mm and starts at $r = 8$ mm. However this is to close for the LHC operating in injection or unstable mode. For that reason VELO is by default in retracted position, at a radius of 35 mm. It is closed when the beams are declared stable. Additionally the design of VELO consists of a

RF foil, which serves in shielding the detector from radio frequency from the beams. That prevents fast degradation of VELO sensors. The detector in closed state with sensors positioning is presented in the figure 2.7. Let us mention that this beautiful design makes it a fantastic tool for $b-$hadron selection and lifetime measurements. A justification of this can be found in the figure 2.8, where the vertex resolution is presented, and in the figure 2.9, which presents the resolution of impact parameter measured for 2011 data.

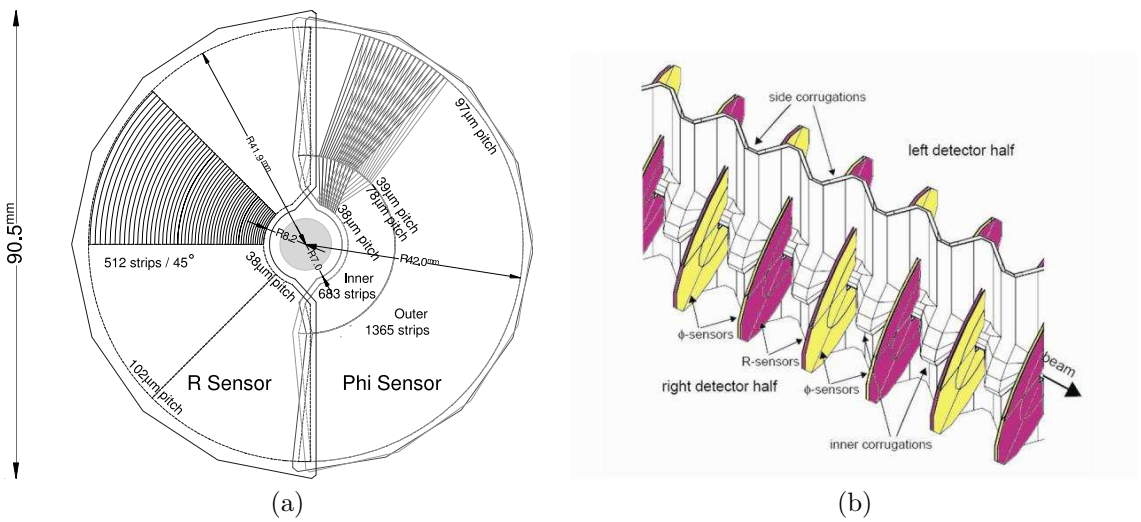

(a) (b)

Figure 2.7: *a) The sketch which illustrates the $r\phi$ geometry of VELO. b) The detector halves in closed position with RF foil isolating the sides and the detector from the beams.*

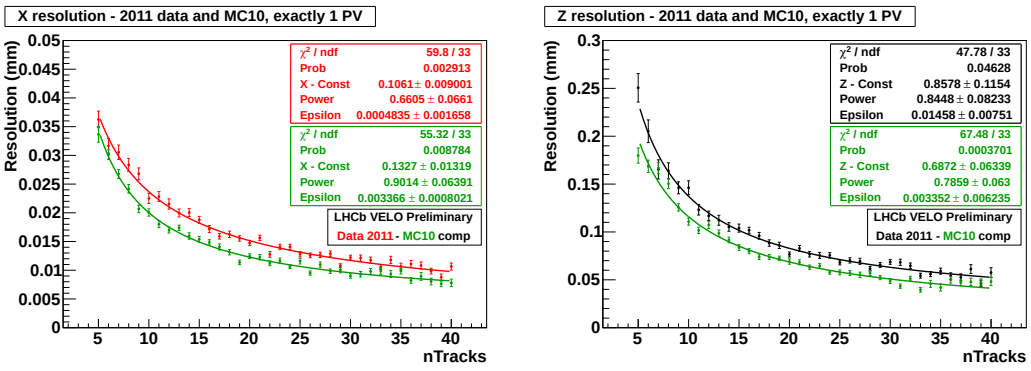

Figure 2.8: *Vertex reconstruction resolution as a function of number of tracks. Results for 2011 data (black) and MC10 (green). Differences between the two comes from the alignment and material description in the simulation.*

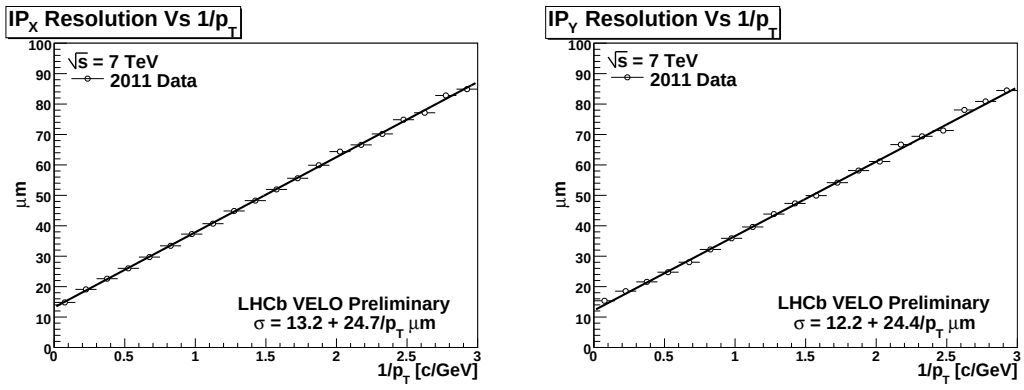

Figure 2.9: *Impact parameter (IP) in x and y for 2011 data. Measured from minimum bias sample of tracks with respect to z of fitted primary vertex. Events with one reconstructed primary vertex only.*

2.2.2.2 Magnet

The detector would not be called spectrometer if there was no magnet. The magnet of the LHCb is a warm (it means that it is not a superconducting magnet), dipole magnet, which was designed to deliver an integrated magnetic field of 4 T · m for particles travelling 10 m (an approximate distance from the interaction point to the RICH2) through the field. The field ranges up to 1 T and it was precisely mapped with an array of Hall probes (figure 2.10 for both polarities). The magnetic field is swapped regularly to collect the same amount of data for each polarity.

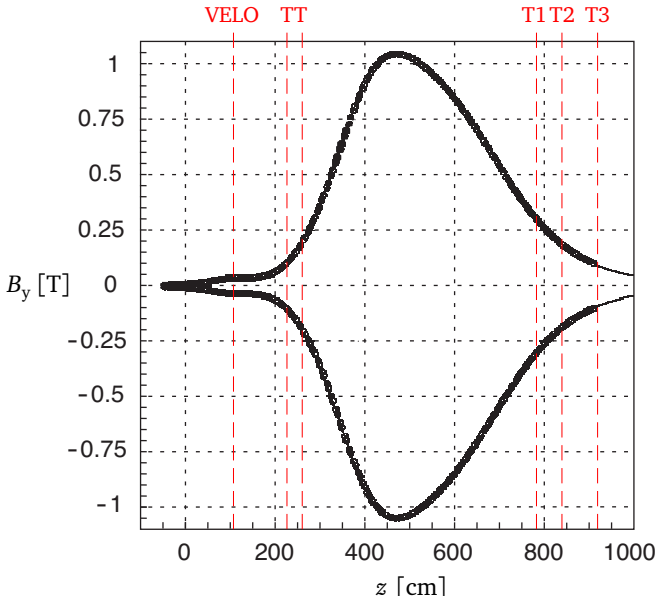

Figure 2.10: *Magnetic field variation along the z axis for both polarities. x and y are equal to 0. The z positions of tracking subdetectors are marked.*

The total weight of the yoke is 1500 tons and the two coils are together 54 tons.

The construction is presented in the figure 2.11.

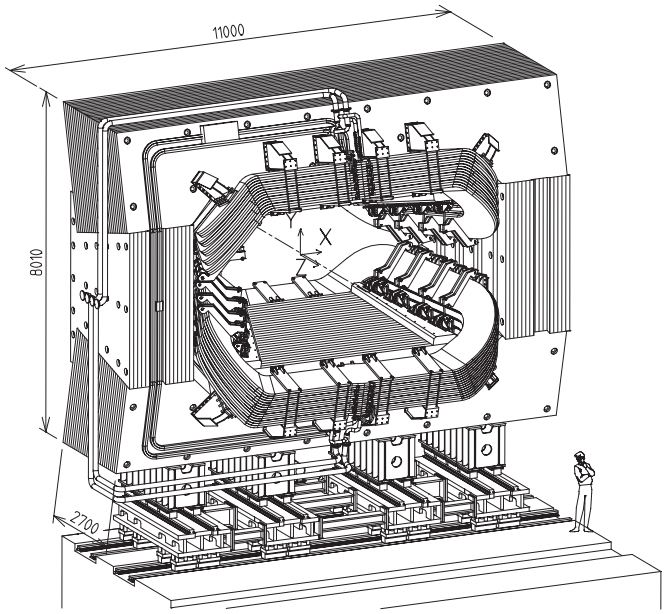

Figure 2.11: *Perspective view of the magnet. The interaction point is located behind the magnet.*

From the figure 2.10 it is possible to learn that at the locations of the RICH and calorimeters the magnetic field is not negligible. These two detectors use photomultipliers, so their performance is decreased by presence of magnetic field. Thus a dedicated shielding had to be designed.

2.2.2.3 Silicon trackers

The silicon trackers aim at measurements allowing to reconstruct tracks close to the beam pipe. That is the region where the occupancy is the largest. There are two silicon detector in the LHCb. The first is located in front of the magnet and is called the TT, while the other (IT) is positioned after the magnet. The IT is split into three stations: T1, T2 and T3. All of above use silicon microstrip sensors of a size of about 200 μm. The TT is about 150 cm wide and 130 cm tall. The IT is 120 cm wide and 40 tall, shaped like a cross and it is located in the centre of three tracking stations, just in the inner of the outer tracker. The schematic is shown in the figure 2.12. Each of the ST stations has four detection layers, arranged with vertical strips in the first and the last layer and the strips rotated by a stereo angle of -5° and $+5^\circ$ in the second and the third layer respectively. The TT is built of 143360 readout strips, and the IT is built of 129024 strips. The sensor overall active areas are 8.4 m^2 and 4.0 m^2 respectively.

2.2.2.4 Outer tracker

The outer tracker (OT) is a drift-time detector, designed as an array of individual straw-tube modules. It is located in the outer part of the three stations: T1, T2 and

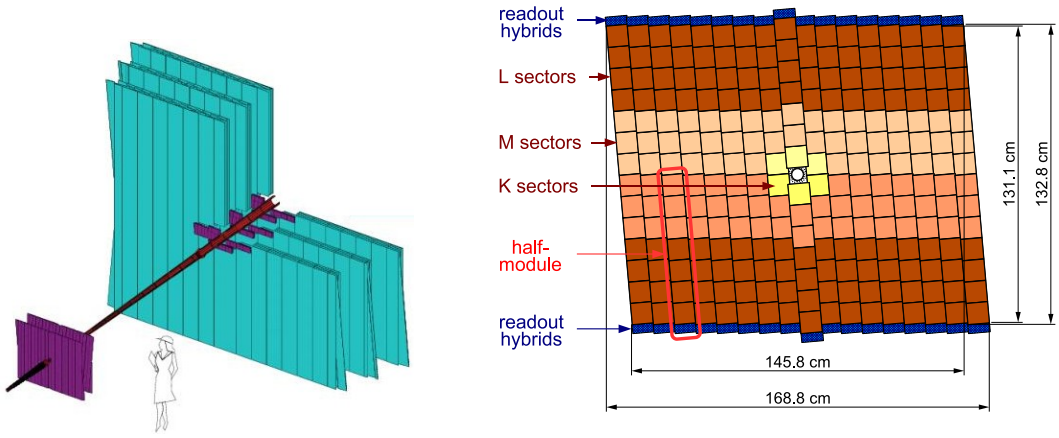

(a) (b)

Figure 2.12: *a) The schematic of tracking detectors (VELO excluded). The violet parts are the silicon trackers, the light blue areas are the outer tracker drift tubes. The violet detector with the lowest z location is the TT. b) The layout of the third TT detection layer.*

T3, covering the rest of not covered by the IT, 300 mrad horizontally and 250 mrad vertically acceptance. Each module contains two staggered layers of drift tubes. The tubes are filled with a mixture of 70% of argon and 30% of CO_2. The drift time is shorter than 50 ns. Each station contains similarly to the silicon trackers four layers, and each layer contains 4608 straw tubes.

2.2.2.5 RICH systems

The two RICH detectors are the basis of charged particle identification at LHCb, and the particle identification is crucial for any flavour physics experiment [61]. The first station RICH1 is located between VELO and the TT. The second station RICH2 lies between the T3 and the first muon station. The schematic of RICH detectors is presented in the figure 2.13. Three types of Cherenkov radiators are used: RICH1 uses aerogel and C_4F_{10}, RICH2 has CF_4. The Cherenkov angles of emitted light for these medias are given in the figure 2.14. A combination of spherical and flat mirrors is used to focus and reflect light on phtotodetection planes located outside the angular acceptance of LHCb. Hybrid photon detectors (figure 2.15) are used to detect the Cherenkov photons. These detectors are placed in MuMetal cylinders and covered by external iron shielding to allow operation in the magnetic field.

The two stations are complementary in terms of particle momentum coverage. RICH1, the upstream detector, legitimately has to discern low momentum particles of the range 1-60 GeV/c. RICH2, the downstream detector, is able to cover the high momentum range which starts from values of $\tilde{1}5$ GeV/c and goes beyond 100 GeV/c. The fact that the momentum ranges of the two detector are different explains also their angular acceptances. RICH1 has a wide acceptance of ± 25 mrad to ± 300 mrad horizontally nad ± 250 mrad vertically. RICH2 acceptance is lower and is limited from about ± 15 mrad to ± 120 mrad horizontally and ± 100 mrad vertically. However such

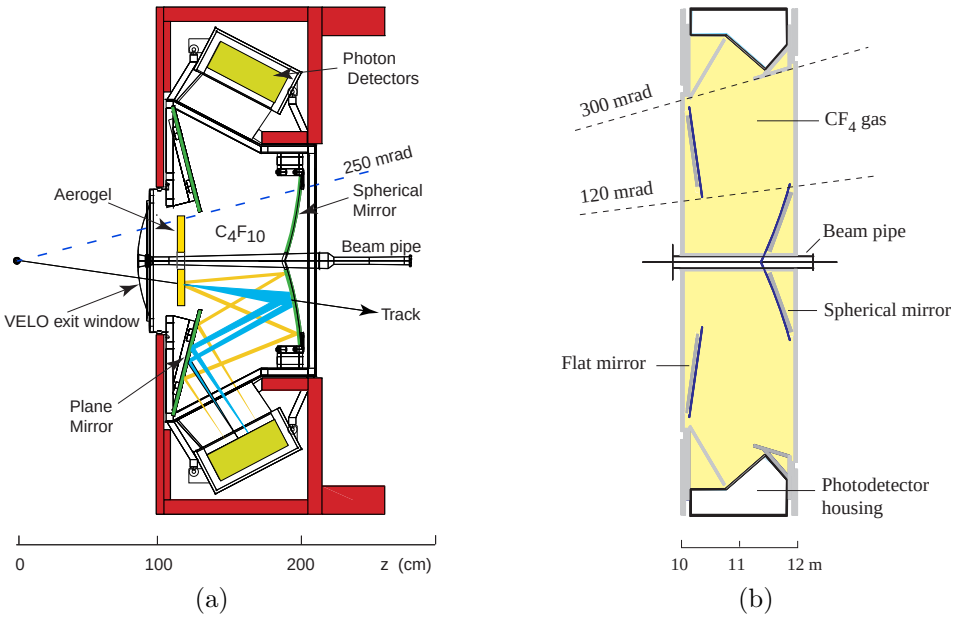

Figure 2.13: *a) RICH1 schematic from side. b) RICH2 schematic from above.*

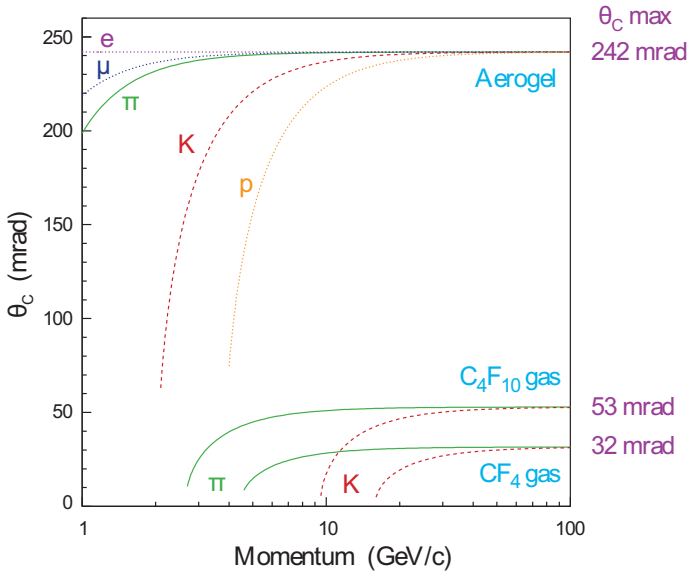

Figure 2.14: *Cherenkov angle versus particle momentum for radiator medias used in RICH detectors.*

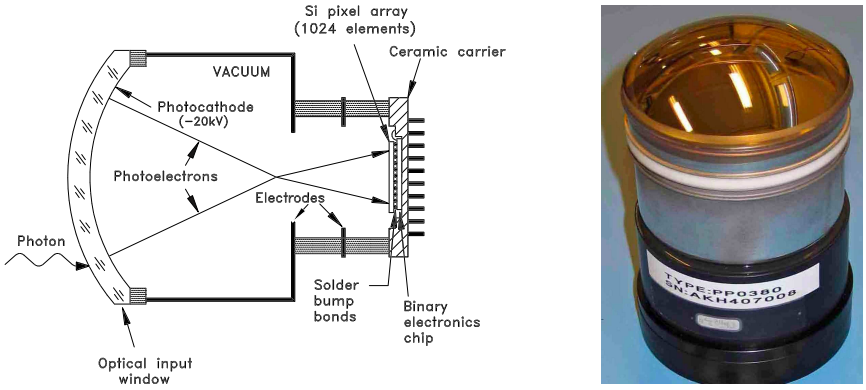

Figure 2.15: *Schematic and the photograph of hybrid photon detector.*

limitations are not biasing, because large momentum particles are well focused around the beam pipe and large acceptance is not needed. An example can be found in the figure 2.16, where the polar angle against the momentum of pions coming from the simulation of $B^0 \to \pi^+\pi^-$ is given – the low momentum pions accessible angle range spreads widely, while high momentum pions are well contained within the angular limitation of RICH2.

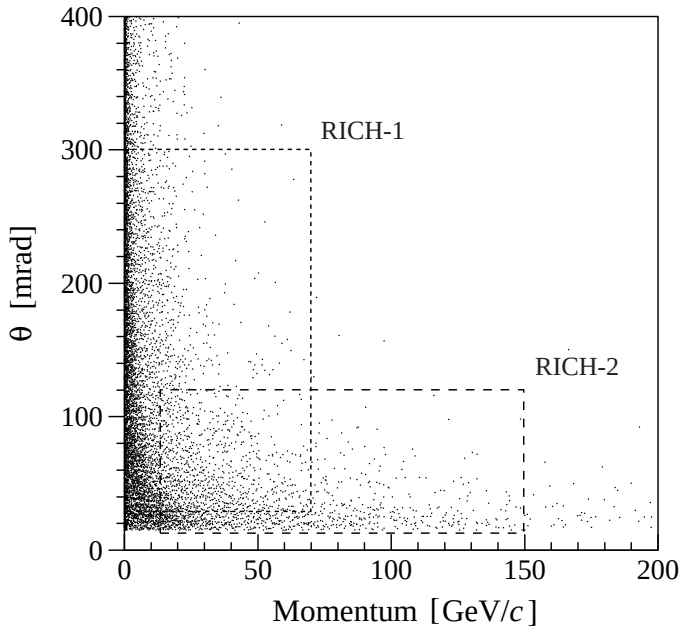

Figure 2.16: *Polar angle versus the momentum of pion track from simulated* $B^0 \to \pi^+\pi^-$ *decays. The angular acceptances of RICH1 and RICH2 are marked.*

Having the knowledge about the construction of the detectors it is worth to look at the usefulness of them. In the figure 2.17 one can find two plots of a reconstructed invariant mass of $\pi^+\pi^-$ combinations from the simulation [61]. The experimentally interesting mode in that case is $B^0 \to \pi^+\pi^-$. The plots prove that the addition of RICH allows to purify the peak of B^0 impressively. The result of the analysis of charged

two-body decays of B mesons with 2010 LHCb data, which include $B^0 \to \pi^+\pi^-$, but also $B_s^0 \to K^+K^-$ and $B^0 \to K\pi$ are presented in the figure 2.18.

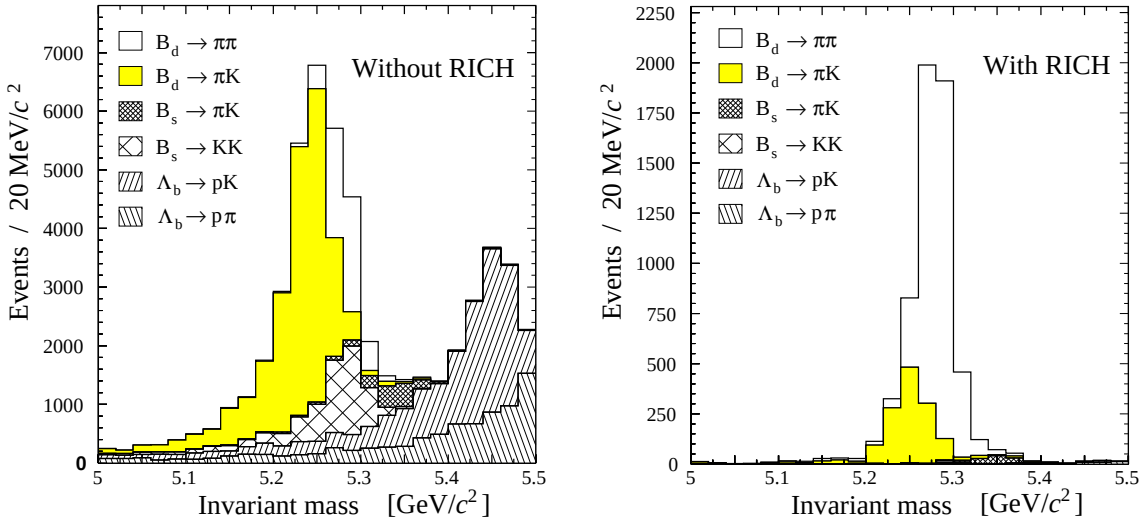

Figure 2.17: *Reconstructed invariant mass for several two-body decays with and without RICH information in use.*

2.2.2.6 Calorimeters

The calorimeter system of the LHCb is divided into four subdetectors. Going downstream the detector, these are scintillating pad detector (SPD), preshower (PRS) including lead layer in front of it, electromagnetic (ECAL) and hadronic (HCAL) calorimeters. The calorimeter purpose is to measure the energy of particle by stopping it and collecting the signal produced. The calorimeter system is also the basic tool for the trigger and particle identification in the trigger.

The SPD is a 15 mm thick layer of scintillator which aims at registering passage of charged particles. Downstream the SPD there is a 12 mm thick layer made of lead (2.5 X_0), followed by another layer of scintillator tiles – the PRS. The PRS has the same construction as the SPD and the only difference is in the readout of the detectors. The SPD gives a binary response while the PRS output is with 10-bit precision (but 8-bit word length). The PRS uses the difference in interaction lengths for electrons and pions in lead to distinguish them – electrons deposit significantly more energy than pions.

ECAL and HCAL are both sampling calorimeters with a structure which is composed from alternately scintillating pads and a dense material which encourages showering (figure 2.19). In case of ECAL, the scintillators are 2 mm thick, and the material between them is 4 mm thick lead. The sheets are aligned along z direction. ECAL integrated thickness was chosen to be 25 radiation lengths [63]. HCAL is made of 4 mm scintillators and 16 mm thick sheets of iron, arranged differently than ECAL – the short axes of the elements are perpendicular to the z axis which has to improve lateral sampling of hadronic showers. Along z the structure of HCAL is made of 200 mm by 200 mm pads of iron and scintillator.

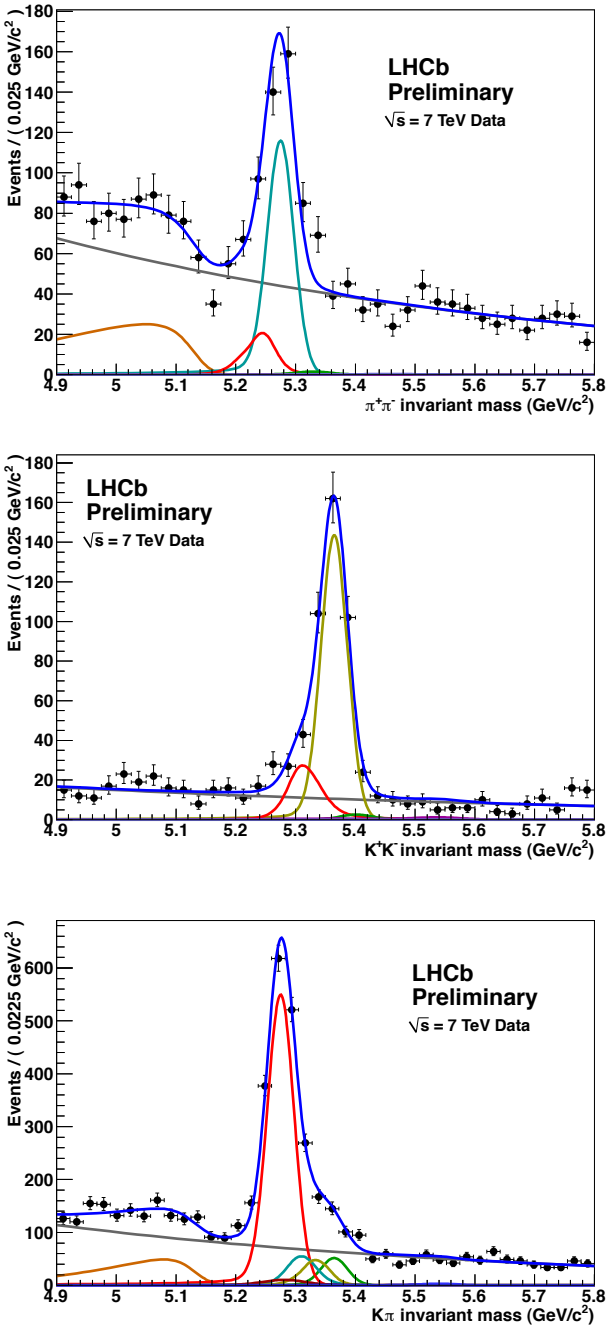

Figure 2.18: *$\pi^+\pi^-$ (top), K^+K^- (middle), and $K^+\pi^-$ with charge conjugate (bottom) invariant mass spectra obtained with 2010 statistics [62]. The result of the unbinned maximum likelihood fit. The main components contributing to the fit model: $B^0 \to \pi^+\pi^-$ (light blue), $B_s^0 \to K^+K^-$ (dark yellow), $B^0 \to K\pi$ (red), $B_s^0 \to K\pi$ (green), combinatorial background (grey), 3-body partially reconstructed decays (orange).*

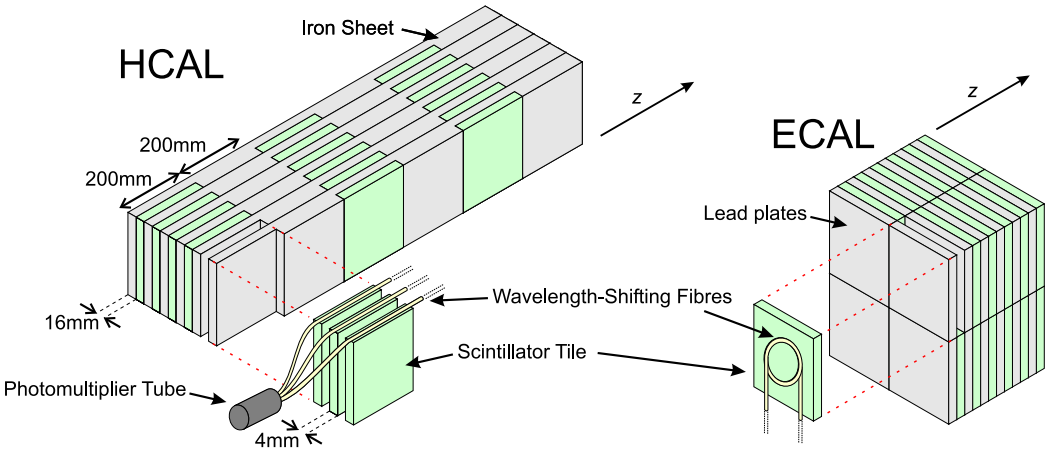

Figure 2.19: *Fine structure of the LHCb calorimeters. The single-edge readout of the iron-scintillator HCAL on the left. The shashlik readout of the lead-scintillator ECAL on the right [64].*

The density of particles varies by about two orders of magnitude over the calorimeter surface, hence, to limit the flux in each cell, the calorimeters have variable lateral segmentation (figure 2.20). The SPD, the PRS and ECAL follow the same structure: they are divided into three regions (inner, middle and outer), and they are projective detectors. The size of square cells in one region is constant and equal to: ∼40 mm in the inner region, ∼60 mm in the middle and ∼120 mm in the outer. There are small differences between the cell size of the SPD, the PRS and ECAL which is due to requirement to match the projective geometry from the interaction point. HCAL has two zones: the inner with the square cells of ∼130 mm diameter and the outer with ∼260 mm cells.

ECAL uses a shashlik calorimeter technology, the sampling scintillators and lead segments are impaled by plastic wavelength shifting (WLS) fibres. This well known technology [65, 66, 67] combines modest energy resolution, low response time and radiation resistance[2]. The design energy resolution:

$$\frac{\sigma_E}{E} = \frac{10\%}{\sqrt{E}} \oplus 1\%, \tag{2.3}$$

where E is the energy in GeV, results in a resolution of B mass reconstruction from Monte Carlo equal to 65 MeV/c^2 for the decay B $\to$ K$^*\gamma$ and of 75 MeV/c^2 for B $\to \rho\pi$. The resolution measured on the data with B $\to$ K$^*\gamma$ is equal to 86 MeV/c^2. The energy resolution of ECAL modules was measured with electron beams. The parametrisation used:

$$\frac{\sigma_E}{E} = \frac{a}{\sqrt{E}} \oplus b \oplus \frac{c}{E}, \tag{2.4}$$

[2]The most recent measurements suggest that ECAL degrades faster than it was designed and measured before.

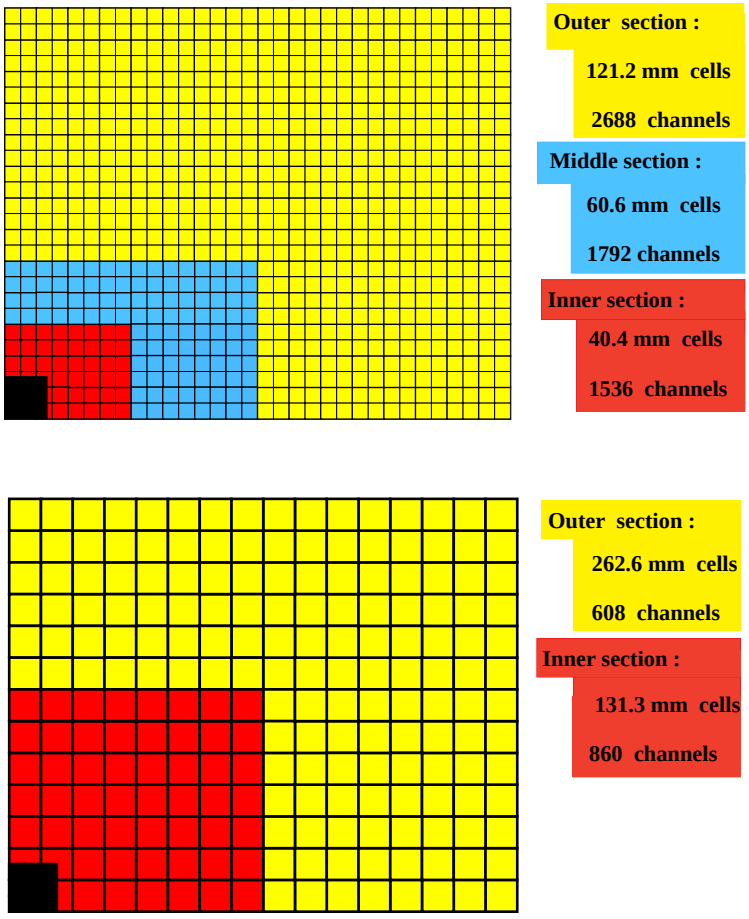

Figure 2.20: *Lateral segmenation of the SPD, the PRS and ECAL (top) and HCAL (bottom). Only the one fourth of each detector is represented.*

where E is given in GeV is used. The parameters a, b, and c stand for the stochastic, constant and noise terms respectively. The measurement results for the outer region is presented in the figure 2.21. The values of these parameters depend on the type of module. They were measured with the test beam to be $8.5\% < a < 9.5\%$ and $b \approx 0.8\%$.

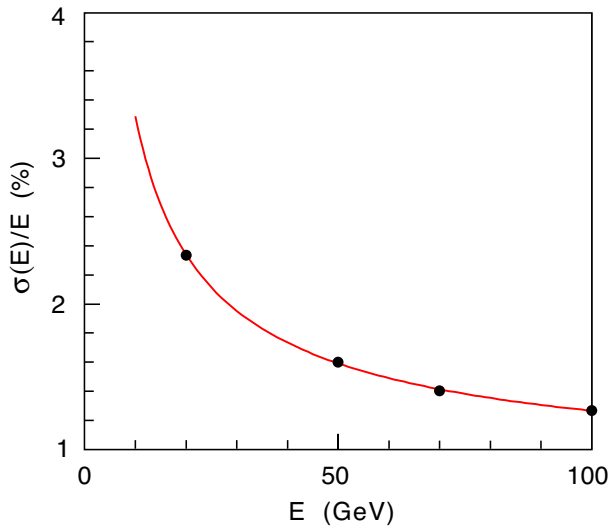

Figure 2.21: *Energy resolution of ECAL measured with electron beams over a surface of* ± 15 *mm and* ± 33 *mm for the outer region [68].*

The ratio of active to passive material for HCAL is 0.18, which is a low value. The energy response to 50 GeV pions is given in the figure 2.22. The leakage of showers from the calorimeter can be observed with tails towards low energies. The energy resolution fir is also presented in the same figure. The result is found to be [68]

$$\frac{\sigma_E}{E} = \frac{(69 \pm 5)\%}{\sqrt{E}} \oplus (9 \pm 2)\%. \tag{2.5}$$

2.2.2.7 Muon system

The muon detectors are important for trigger purposes and offline muon identification. The layout of the system is presented in the figure 2.23. It is made of five rectangular stations: one in front of the calorimeter (M1), and four downstream the calorimeter (M2-M5). They are mainly multiwire proportional chambers (M2 to M5), with triple-GEM (gas electron multiplier) technology used in the inner region of M1 (which is more resistant to radiation). The stations M2 to M5 are separated by 80 cm thick iron absorbers which should block hadrons. The total thickness of absorbing materials (including the calorimeter) is approximately 20 interaction lengths [69]. This allows triggering on muons, which have crossed all five stations, of the minimum momentum of approximately 6 GeV/c.

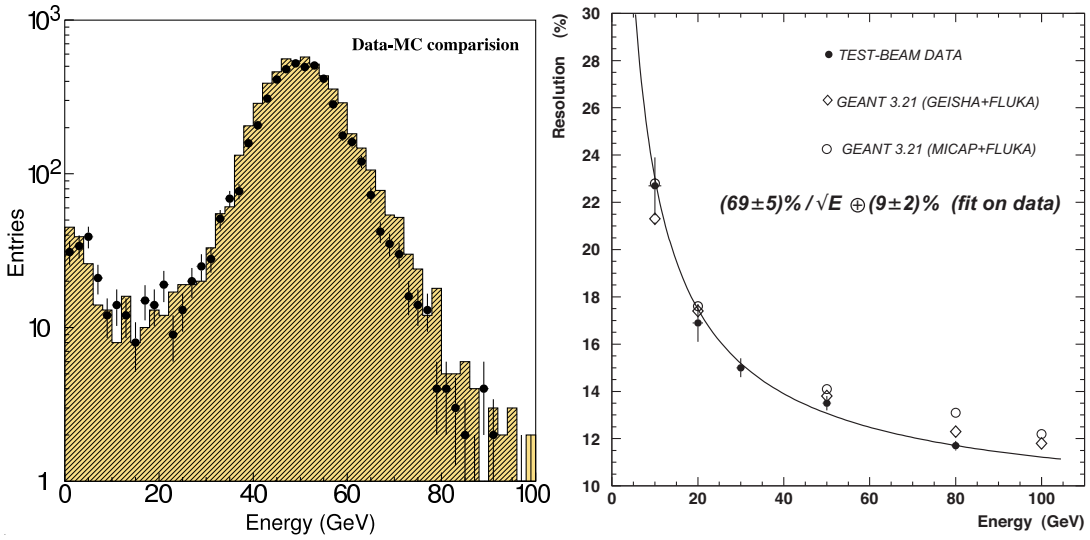

(a) (b)

Figure 2.22: *a) The energy response for pions from of energy equal to 50 GeV. The hatched histogram is for the test beam and the dots are for the simulation. b) The energy resolution of HCAL [68].*

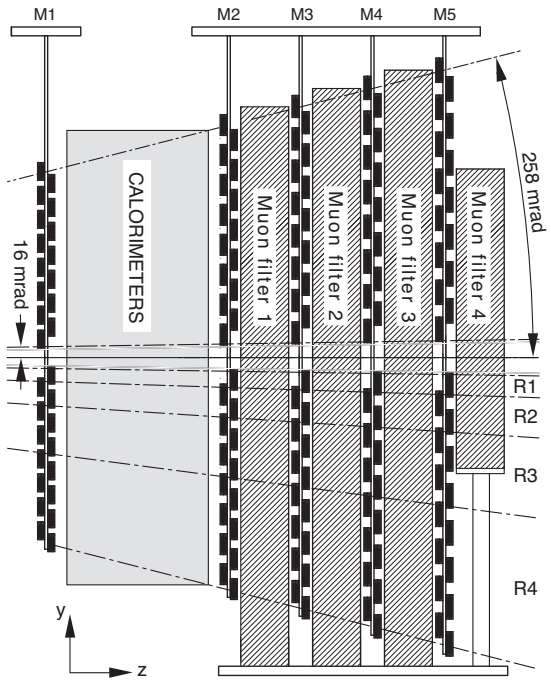

Figure 2.23: *Side view of the muon system positions.*

2.2.2.8 Trigger

About 1% of visible proton-proton interactions contain $b\bar{b}$ pairs. But only a fraction from few percent to 20% can be found within the acceptance of the detector. Moreover the interesting physics is characterised typically by branching ratios lower or much lower than 10^{-3}. On the other hand there are technical limitations of amount of data that can be written into a data storage in a certain period. In fact the bandwidth available for writing is about 2 kHz, while the LHC operating at designed luminosity will produce interactions at LHCb with frequency close to 10 MHz. That large disproportion between writing abilities and operational frequency of the detector requires very efficient selection of events that are the most interesting from the physical point of view.

As in many other experiments, the LHCb trigger system is a multi-stage process [70, 71]. The first phase is the hardware L0 trigger. The second stage is the software based high level trigger (HLT).

The L0 trigger works synchronously with the 40 MHz bunch crossing frequency and is designed to reduce the output to 1 MHz, which is the frequency at which the entire detector can be read. The trigger has to make the decision in 2 μs, which in addition of the time of flight of the particles, cable and electronic delays gives 4 μs from the bunch crossing to the moment when the readout supervising system receives the decision to store the event.

The L0 trigger consists of three subsystems, each based on a different subsystem: pile-up (currently not used), calorimeter and muon. The pile-up has to distinguish between bunch crossings with single and multiple visible interactions, and aimed for removing the multiple one. We will see that it has not been the choice of operation. One of the main signatures of B meson decays is the presence of particles with large transverse momentum. The data from muon detectors and the calorimeter are analysed. The L0 takes in account the transverse momentum of muon candidates, and the transverse energy of hadron, electron and photon candidates from the calorimeter. An event is accepted when at least one of the alleys gives a positive answer.

The HLT runs on events which passed the L0 trigger. It is split into two stages for the reason of timing: HLT1 and HLT2 [72]. The HLT1 performs a partial event reconstruction and selection and aims to reduce the rate by a factor of around 20. It is based on the concept of selecting one very good quality track with high transverse momentum. The selection is split into lines, which allow to tune (by changing transverse momentum threshold) the efficiency of selecting inclusively different decay types by daughters type (electron, photon, muon).

The HLT2 algorithms are performed on all the events passing the HLT1, no matter of the type of the candidate type. The HLT2 first makes a complete pattern recognition to find all particle tracks in the event. Then a set of selections is applied. The selections can be inclusive (for generic B decays or resonances like J/ψ), or exclusive to provide the highest possible efficiency on specific channels. An example of the exclusive selection is the HLT2 line for $\mathrm{B}^0_{\mathrm{d/s}} \to hh\pi^0$ decays developed by Clermont-Ferrand group [73].

2.2.3 Operations

The LHCb operates in cycles following the LHC cycles. Once the machine is are ready, the beams are injected into the LHC – the fill starts. Then stabilised beams are accelerated to the nominal energy of 3.5 TeV per particle. After the injection, the high voltages are turned on on the most of the detectors, and VELO is moved into closed position when stable beams are declared. The run begins, and lasts until the beams are dumped, or any problem appear. Once the beams are dumped, the machine has to prepare for another fill, and then the process may restart.

The LHC started with beams of low intensity, where number of bunches per beam were as low as three, effectively resulting in two collisions of beams at the LHCb interaction point per one revolution. The number of bunches has increased, and reached 1380per beam, with 1320 colliding in the LHCb accordingly in July 2011. Average number of visible interactions per bunch crossing, denoted by μ, varied, and was essentially close to 2.5 in 2010 and close to 1.5 in 2011.

Cumulatively, the LHC provided the integrated luminosity equal to 42.2 pb^{-1} in 2010, and 1161.8 pb^{-1} up to October 20^{th} 2011. All detectors and the data acquisition system are required to register the data. This results in reduced registered luminosity respect to the luminosity delivered by the LHC. The LHCb was able to register 37.7 pb^{-1} in 2010, and 1052.3 pb^{-1} in 2011. It means that the experiment was ready for registering the data for approximately 90% of the integrated luminosity provided by the accelerator. The plots of the integrated luminosity over time for 2010 and 2011 are presented in the figure 2.24.

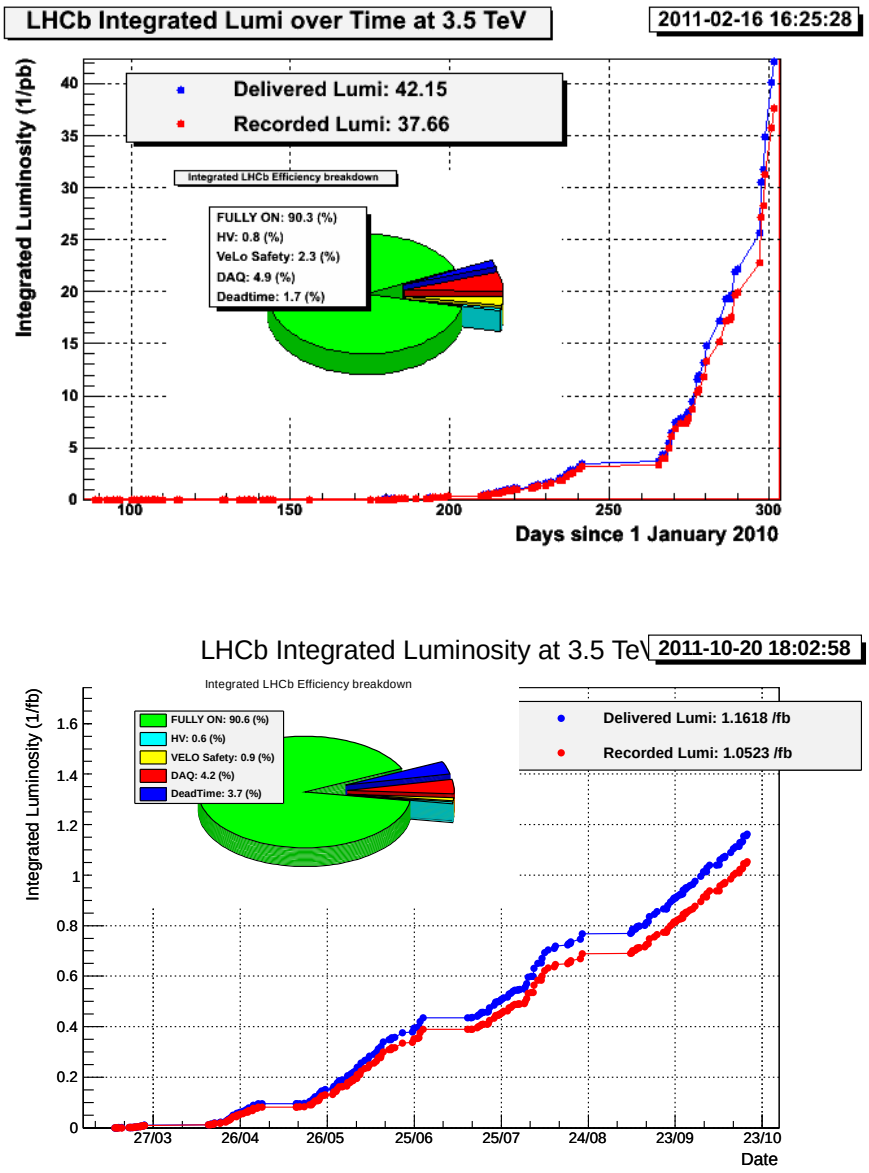

Figure 2.24: *Integrated luminosity over time in 2010 (top) and 2011 (bottom). Pie charts for the LHCb data taking efficiency are also plotted.*

Chapter 3

Preshower detector

A brief overview of calorimeters used in the LHCb experiment was already presented in the previous chapter. Here we will focus at only one part of the calorimeter system: the preshower detector. The Clermont-Ferrand group is in charge of the entire readout of the PRS, from the photodetector to the front-end electronics. This is a very complex subject and hence beyond the scope of this work. A perfect source describing the PRS and it electronics is [68], where the detector and its commissioning is described in details.

The following sections are a short description of the PRS. We will concentrate only on those subjects which are the most important from the point of view of the calibration of the detector. The process of calibration will be described in the next chapter.

3.1 Introduction

In the LHCb calorimeter system there are two detectors which are like brothers – the SPD and the PRS. In fact they look very alike, but they have different readout. They both use scintillating cells, where particles passing the detector deposit parts of their energy. The emitted light is then transported via wavelength shifting fibres and clear plastic fibres to multi-anode photomultipliers (Ma-PMT). The electronics is different and the result is binary in case of the SPD and analog of 8-bit precision in case of the PRS. That kind of construction allowed to build fast, multi-channel pad detectors, with an affordable cost

Between the SPD and the PRS there is a layer made of lead. It is 15 mm thick corresponding to 2.5 X_0. That encourages electron and photon to interact and start electromagnetic cascades.

The information that each scintillating pad detectors give is different. The SPD allows to spot fast charged particles, while the PRS is able to distinguish between pions and electromagnetic showers. That discrimination is very useful for the L0 trigger, where no other data allowing to identify the particle specie is available. But it also gives valuable information for the offline reconstruction as the detectors increase the z granularity.

3.2 Scintillating cell

The basic active element of the preshower is a square, polystyrene cell [74]. The sketch of a cell is presented in the figure 3.1 and a photo of one cell can be found in the figure 3.2. The detector is made of 6016 cells of three different sizes. The cells of the same size are grouped together and their location depends on the distance from the centre of the detector. The exact parameters of the cells are given in the table 3.1. It is worth to notice that the cell size is not equal to the size of the polystyrene cuboid, which is about 3-4 mm lower. That should have some consequences when one considers the cell efficiency of a particle registration at the borders. The cell sizes in the regions are like 1:1.5:3. The depth of each cell is equal to 15 mm.

Region	Dimension (cm)	Cell size (mm)	Scintillator size (mm)	Cells
Inner	191.4 x 143.5	39.84	39.5	1536
Middle	382.7 x 239.0	59.76	59.4	1792
Outer	765.5 x 622	119.5	119.1	2688

Table 3.1: *Characteristic parameters of the preshower: the total dimension of the region, the cell size, the size of the active scintillator and the total number of cells in each region.*

In each cell, a circle-shaped groove is cut in which a WLS fibre is placed. There are 3.5 loops of WLS fibre in a cell. The number of loops was optimised to achieve the best light collection efficiency [75] and the signal formation [76]. The WLS fibre is made of polystyrene with paraterphenyl (1.5%) and POPOP (0.04%) dopants added. The fibres are glued with a dedicated device which provides the binding of the fibre and a

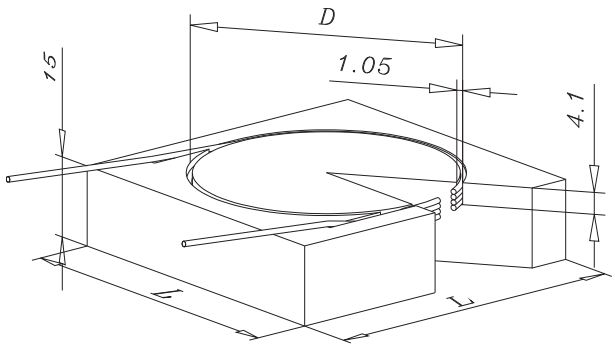

Figure 3.1: *Scintillator cell design. D parameter is the diameter of the WLS fibre groove. It is equal to: 37 mm, 56 mm, and 100 mm for the inner, the middle, and the outer respectively.*

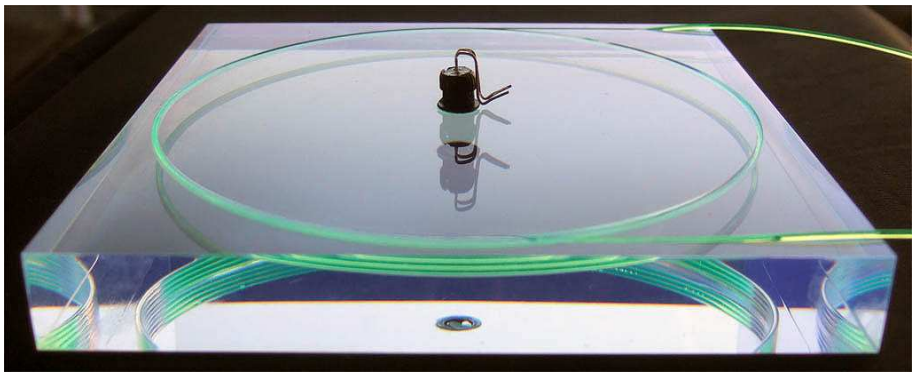

Figure 3.2: *Photography of an individual scintillator pad with the WLS fibre. At the top of the cell a LED is located which is used for monitoring the cell response.*

uniform glue filling. The scintillator surface is polished to obtain better optical quality and enveloped with 0.15 mm TYVEK paper, which has to improve light reflection. The paper instead of a solid structure is used to reduce the spacing between pads. The WLS fibre exits the cell from two sides and both ends joins separate clear fibres. The clear fibres lead to the same pixel of the photomultiplier.

3.3 Modular structure

The scintillating pads are organised [74] in groups which are packed together inside square boxes (478 mm by 478 mm), called module. The size of the modules is the same for all regions, so it forces different packing of the cells in each area. In the inner there are 144 cells inside a module. The middle modules contain 64 cells, and the outer contain 16 cells. The boxes are made of fibreglass material which was designed to minimise spacing between modules and thus between the neighbouring cells from two adjacent modules. On the top cover of the module there are output ports allowing optic fibres to exit from the box. The sketch of modules and fibre routing is presented in the figure 3.3, while the actual plot of an exemplary module can be found in the figure 3.4.

Modules are grouped together in supermodules – columns of height of 7.7 m (the entire detector height) and width of about 96 cm. The supermodules are mounted to a support plate.

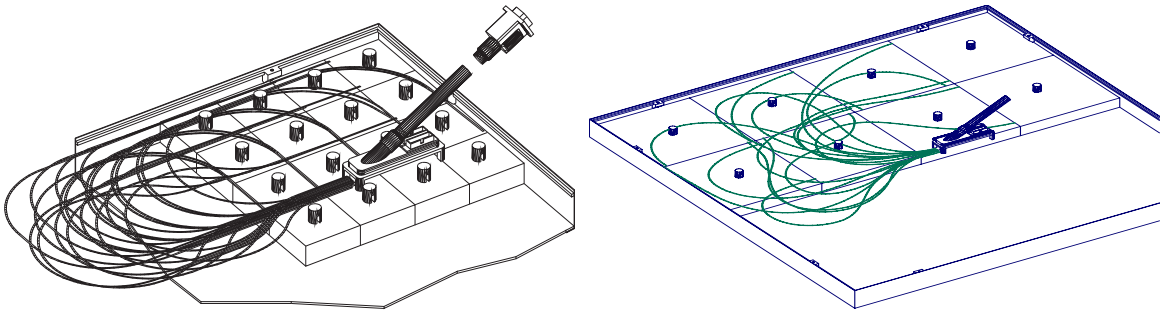

Figure 3.3: *Fibre routing inside the inner (left) and the outer (right) module box.*

3.4 Photomultipliers

The clear fibres conduct light to the photomultipliers. The PRS uses multi-anode photomultipliers (Ma-PMT) manufactured by a commercial company Hamamatsu to convert light into an electric signal. The schematic of the Ma-PMT is given in the figure 3.5. Each Ma-PMT consists of a single photo-cathode, behind which focusing electrodes guide photo-electrons to one of 64 anodes (pixels). A pixel is a square of 2 mm by 2 mm, and distances between pixels are equal to 0.3 mm. The set of focusing wires keeps the electrons inside the correct pixel. Among the available technologies at that time, the 8-stages amplification was chosen. Each Ma-PMT output is connected to one front-end board of the electronics.

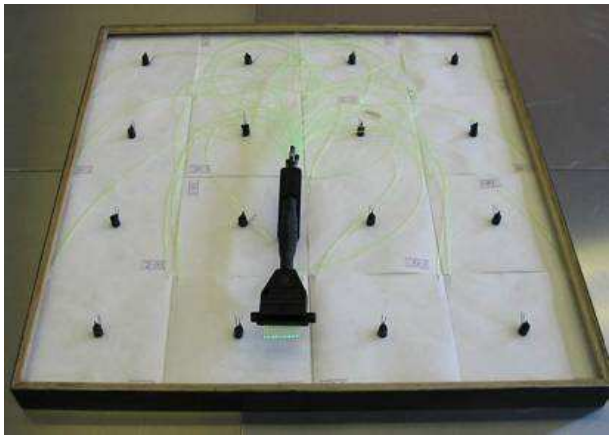

Figure 3.4: *Photography of a single module from the outer region.*

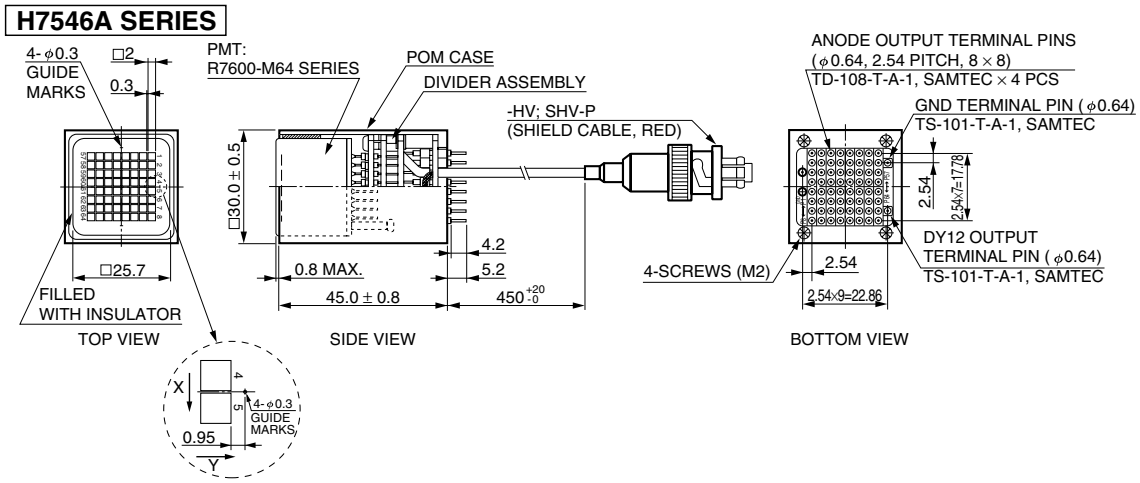

Figure 3.5: *Schematic of the multi-anode photomultiplier produced by Hamamatsu [77].*

The Ma-PMT can be characterised by many parameters. The complete analysis of the photomultiplier can be found in [68]. Among them three properties are important for the next chapter. These are: the linearity of the response, the gain uniformity and the gain change with the high voltage supply.

3.4.1 Linearity

The measurements were performed to find a range of light yield for which the photomultiplier response is linear (figure 3.6). The upper limit of the deviation from the linearity is at the level of 5% for the Ma-PMT working at the current of a few μA. However the final design predicts that the Ma-PMT should not be used with the current higher than 200 μA to reduce the ageing effects. Thus the linearity of the response requirement if fulfilled by the photomultiplier.

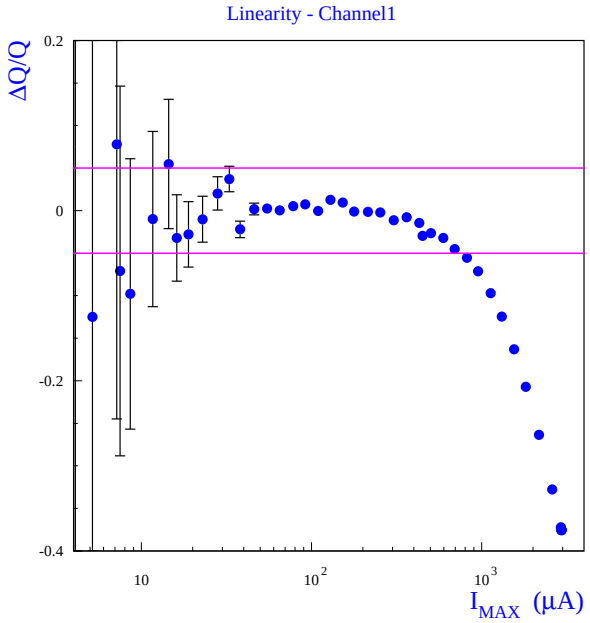

Figure 3.6: *Deviation from the linear response of a channel of a Ma-PMT as a function of the maximum current delivered.*

3.4.2 Uniformity

For the proper measurements of the energy of particles it is necessary that each channel of the Ma-PMT has the same gain. If the gain is different, then a correction has to be applied at the electronics level to equalise all channels responses. A test performed on a photomultiplier (figure 3.7) shows that a maximum relative spread of gains can reach the value of 2.

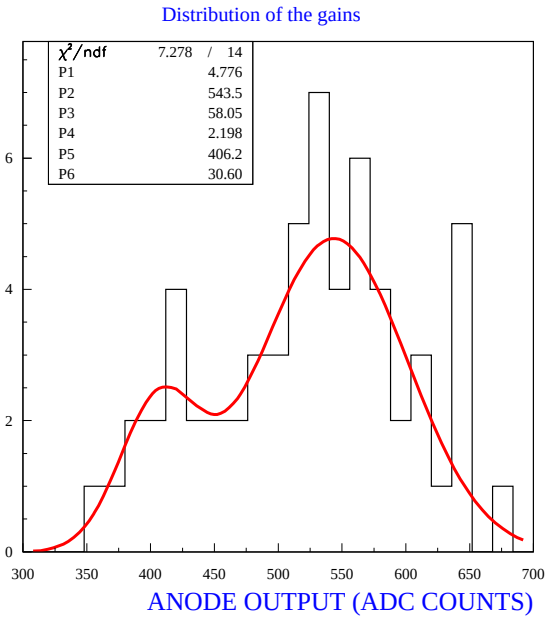

Figure 3.7: *Maximum response of each instrumented anode of the Ma-PMT.*

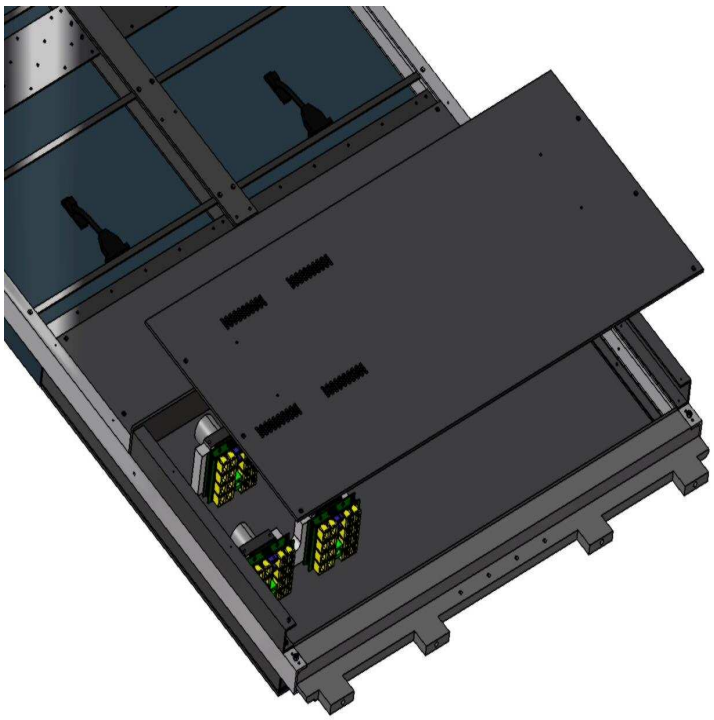

Figure 3.8: *Sketch of the housing of the tubes inside the stainless steel box [68].*

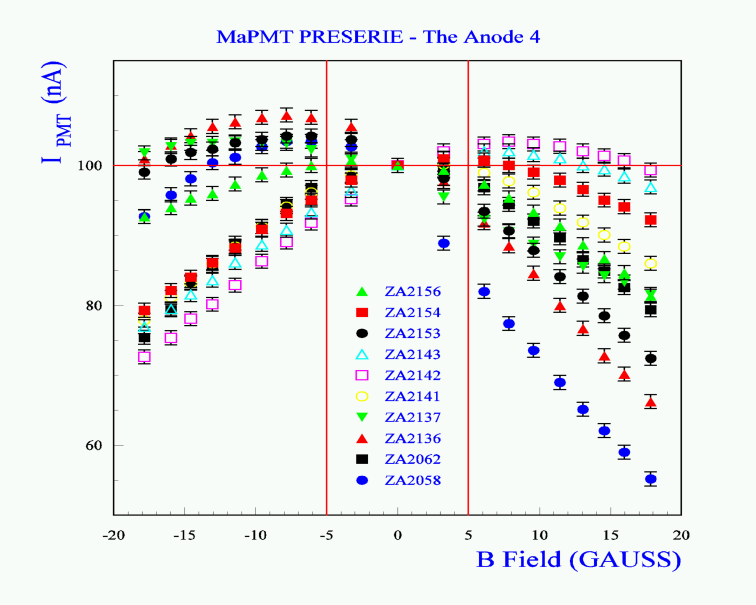

Figure 3.9: *Effectiveness of the photomultiplier as a function of the magnetic field. Different prototype units proposed to the experiment by the manufacturer were tested [68].*

3.4.3 Magnetic field

A photomultiplier is an equipment sensitive to magnetic field. The LHCb environment is soaked with magnetic field and one can predict that this fact will influence photomultiplier effectiveness, thus the calibration of the preshower. A proper magnetic field shielding is essential as well as measurements of the impact of the irreducible magnetic component on the detector operations. The first requirement was designed and manufactured by Clermont-Ferrand team. All details of that magnificent job are described in [68]. The second part was checked with 2010 data and will be described here, but first a few words about how magnetic field can disturb the detector calibration.

In 1997 the photomultipliers manufacturer performed series of measurement investigating how significant is the impact of magnetic field on the performance of the photomultipliers. It reported that for fields not larger than 40 G in transverse component and not larger than 20 G in longitudinal component, the tube answer should not be decreased more than by 5%. The Clermont group has made independent test and has obtained results significantly different from the company (figure 3.9). That motivated the group to prepare even stronger than predicted magnetic field shielding to protect the tubes. A special box made of stainless steel was designed to keep the tubes with all their connections, and each tube was additionally protected by a dedicated cylinder made of μ-metal (figure 3.8). The size of the cylinder (4 cm diameter, 6 cm long, 1 mm depth) was optimized with a dedicated software. The design was a compromise between protection versus weight and space restrictions. A prototype was tested in the magnetic field just after the installation of the magnet in the LHCb cavern. The results are in the table 3.2. The goal was reached, the shielding reduced the magnetic field of 150 G without any protection to the level of $1 - 2$ G.

Position	B without cover (G)	B with cover (G)	cover + μ-metal (G)
1	62	37	1
2	63	42	1
3	65	37	1
4	55	35	2
5	53	36	1.5

Table 3.2: *Measurements of the magnetic field inside the shielding box made of stainless steel designed as a magnetic field protection. Five positions in the box were investigated. Three measurements of the total B field, expressed in Gauss, at PMT locations are performed : without the cover of the box, with the cover of the box installed and with the full shielding (cover + μ-metal cylinder) [68].*

3.4.4 Gain and high voltage

The gain was measured with varying high voltage supplying the Ma-PMT. The attenuation of the light corresponded to the linear range of the response for the whole range of the scanned high voltage values. The response in terms of the integrated charge as a function of the high voltage for a typical channel is presented in the figure 3.10. The result can be fit by:

$$< Q >= \alpha V^{\beta}, \tag{3.1}$$

where $< Q >$ is the integrated charge, α and β are the constant values for a given channel. The β parameter is important for the high voltage operations, especially for the calibration purpose. This parameter measurement for all boards will be described in the calibration part.

3.5 Building the detector

It was already mentioned that the preshower is divided into three regions. A supermodule is the building block important from the structural point of view. From the logical point of view, the division into front-end boards (photomultipliers) is more important. Each front-end board, following the Ma-PMT pattern, collects 64 channels. The front-end boards are grouped inside electronic crates, building eight preshower regions numbered from the PRS0 to the PRS7. The organisation of the regions is summarised in the table 3.3. The numeration of the regions and the numeration of the boards in regions used in this document is given in the figure 3.11. A picture taken during the assembly of the PRS presenting the detector is displayed in the figure 3.12.

3.6 Electronics

The electronics of the preshower is also a complex subject and hence too wide to be presented here in details. Again we refer to [68] for a complete review and tests of it.

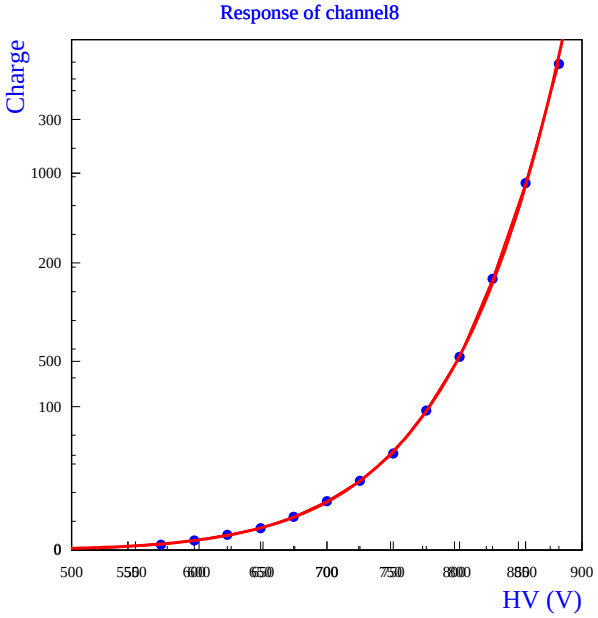

Figure 3.10: *Integrated charge averaged over 500 measurements as a function of the high voltage applied to the Ma-PMT. A fit of* $< Q >= \alpha V^{\beta}$ *is performed.*

PRS	Region	Boards	Half-boards
PRS0	Outer C	12	2
PRS1	Outer C	8	0
PRS2	Middle C	14	0
PRS3	Inner C	10	4
PRS4	Inner A	10	4
PRS5	Middle A	14	0
PRS6	Outer A	8	0
PRS7	Outer A	12	2

Table 3.3: *Organisation of the regions of the preshower with the number of boards and the number of half-boards for each region.*

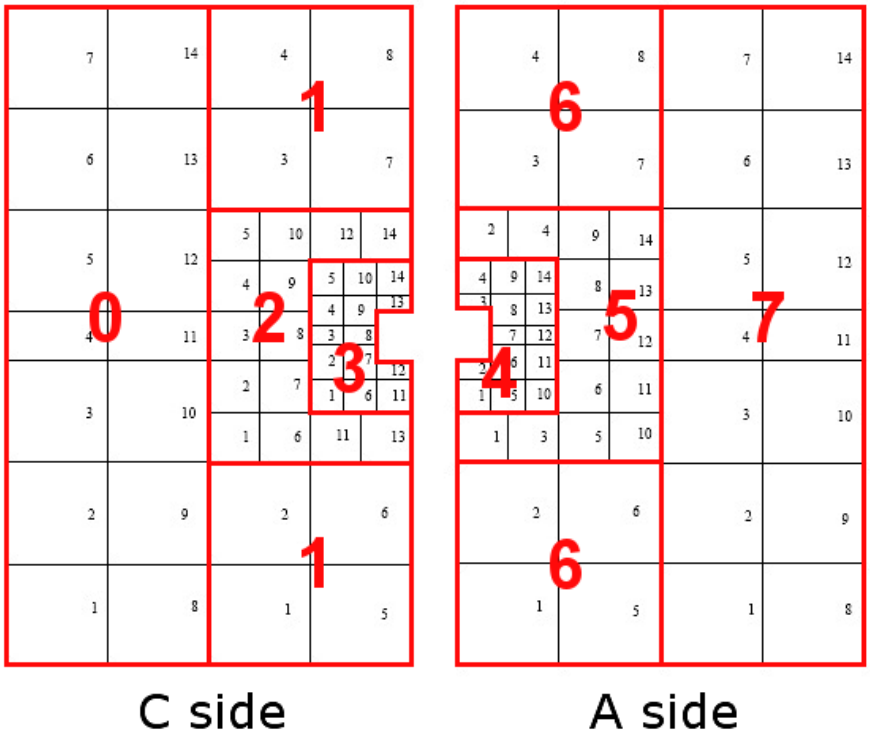

Figure 3.11: *Numbering scheme and the organisation of the preshower regions and the front-end boards. The reader has to be aware that this numbering is slightly different from the numbering based on the position inside crates given in [78].*

Figure 3.12: *Front view of one half of the SPD/PRS.*

The very-front-end (VFE) boards receive electronic signals from the Ma-PMT of the PRS but also of the SPD. They process them and allow reading out. Additionally they have to provide correct timing and synchronisation with the LHC clock. Finally they produce the data which is sent to the L0 trigger.

The electronics works in 25 ns time gap regime, synchronised with the LHC. For each channel of the preshower there are two parallel paths in the VFE board, and each one corresponds to one parity of the current bunch crossing number. This double structure is needed because of the construction of the electronics (figure 3.13). Let's start with from the moment when a new time gap of an odd number starts, so from the time of 0 s. Then until the time of 25 ns the integrator of the first path integrates the charge collected by the Ma-PMT. At the time of 25 ns the integration stops and the result after processing is available for reading. Because the process of resetting the integrator also last some time, the integration has to be frozen for the first path. To avoid the dead time, the integration of the charge starts in the second path, and lasts until reaching the time of 50 ns, when the systems swap again. Two paths mean, that for the same input, the output can be different because of the difference in the amplification between the paths. This difference is due to spread of output of chips used in the electronics. The spread has been measured in the lab to be not larger than 5%. However, the spread was never measured for chips mounted in the VFE boards. As we will see in the calibration part, in that case, the spread can be larger than 5%.

At this stage also the signal is corrected for three factors. First the pedestal values are subtracted. Then the correction which has to uniformise the board is applied. We say that the numeric gains are applied, or that the signal is *gained*. They can be

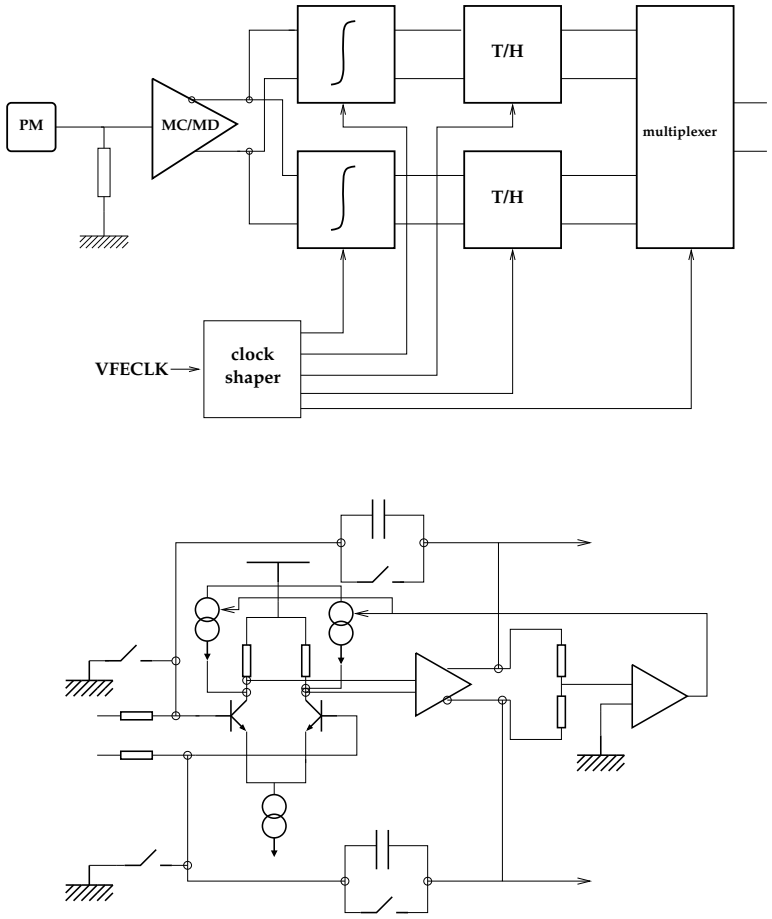

Figure 3.13: *Sketch of the building block of the very front-end (top) and the schematics of the integrator (bottom).*

applied independently for both paths in the electronics, it means that there can be one numeric gain for even bunch crossing numbers and one for odd bunch crossing numbers. That way it is possible to correct globally multiple effects like the Ma-PMT channels differences and the electronic amplification differences. The procedure inverted to the application of the numeric gains is called *degaining*.

The last correction that can be applied is called as *spill-over correction* (described with more details in the Section 4.2.3). It comes from the fact that about 15% of the signal collected during the 25 ns arrives in the next 25 ns, and in consequence it leaks to the next time gap. It is possible to subtract on a statistical basis a fraction α of the charge integrated during the previous bunch crossing from the charge integrated in the current one. That way we should be able to reduce that leaking of the signal from one time gap to the following one.

The output from the front-end board is almost ready, just the conversion is left. The analog-digital converters output is 10-bit, but the readout from the board is expected to be 8-bit, thus a transcoding algorithm is run which reduces the precision for large values. The data are decoded back in the readout cards, but the precision is partially lost[1]. The transcoding algorithm is given in the table 3.4, while the inverse transcoding in the table 3.5. The transcoding is used to get the best dynamics from the 8-bit electronics.

	$d_{10} \leq 128$	$128 \leq d_{10} \leq 256$	$256 \leq d_{10} \leq 512$	$512 \leq d_{10}$
d_8	d_{10}	$128 + \frac{d_{10}-128}{2}$	$192 + \frac{d_{10}-256}{8}$	$224 + \frac{d_{10}-512}{16}$

Table 3.4: *Conversion from raw to trancoded data. d_{10} is the 10-bits original data value, whereas the d_8 is the transcoded value.*

	$d_8 \leq 128$	$128 \leq d_{10} \leq 192$	$192 \leq d_{10} \leq 224$	$512 \leq d_{10}$
d_{10}	d_8	$2 \cdot d_8 - 126$	$8 \cdot d_8 - 1276$	$16 \cdot d_8 - 3064$

Table 3.5: *Inverse transcoding algorithm*

3.7 Pion and electron separation

The preshower is the key element for the separation of electrons and pions. A test was performed on the X7 test beam at the CERN SPS with both electrons and pions of the momentum between 10 GeV/c and 50 GeV/c. The result is presented in the figure 3.14.

If we are interested in the electrons, we can remove the particles with deposits lower than 5 times the minimum ionising particle most probable value of the deposit[2].

[1] In fact for values larger than 128 ADC counts the absolute precision is reduced, however the relative precision (which is really meaningful) does not decrease.

[2] The 5 MIP MPV correspond to 50 ADC count. The PRS was designed to work at 10 ADC count for the MIP MPV for the best resolution and energy range. However it is possible to run at different values. That situation when the MIP MPV position was higher than 10 ADC count was present in 2010 data taking.

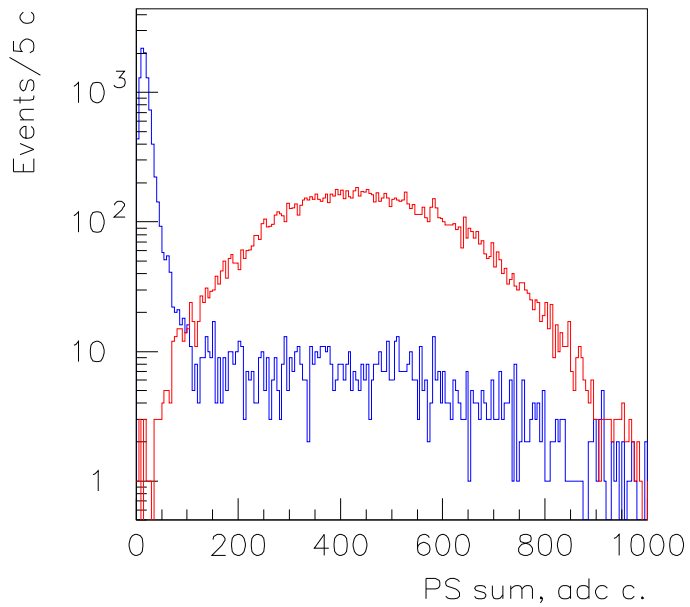

Figure 3.14: *Energy deposit in the PRS histograms for: a) 50 GeV electrons, b) 50 GeV pions. The measurement was performed on the X7 test beam.*

With that cut, the efficiency for the electrons is equal to 91%, 92% and 97% for the momentum of 10 GeV/c, 20 GeV/c and 50 GeV/c respectively. The appropriate rejection factors for the pions for these values are: 99.6%, 99.6% and 99.7% [75].

Chapter 4

Preshower calibration

This part describes the process of calibration of the preshower. It starts from a short introduction to minimum ionising particles and energy loss in a thin scintillator. It describes the properties of multianode photomultipliers and the electronics which are related to the calibration process. The calibration itself is a two step procedure. The first stage is an inter-calibration within each electronic board (one photomultiplier, 64 cells). The second step is the process of levelling the boards. In this chapter, the following calibration results are given: the initial calibration with cosmic rays, the calibration with the first collision data from 2009, and the calibration with 2010 data. Another method of calibration is the energy flow method [89], which is also referred in this chapter as a crosscheck. Finally, the procedure of re-alignment of the detector and its results are presented.

4.1 Minimum ionising particles

Let us begin from a short reminder of energy loss of particles in a thin scintillator, which focuses on minimum ionising particles. The preshower calibration procedure is based on this kind of particles.

The preshower, like any calorimeter, is able to measure energy deposits no matter what is the source of the deposit. It can be a charged particle, or a neutral. It can be a photon, an electron, or a pion, or anything else. For the calibration purposes only a specific group of particles is useful. These are the minimum ionising particles (MIP) – relativistic charged particle as pions, charged kaons, muons and protons. In a scintillator of the PRS they behave similarly so they are used all together.

4.1.1 Particle energy loss formalism

When one thinks about energy loss in a material, one usually has in mind the Bethe-Bloch equation [2]:

$$-\left\langle \frac{dE}{dx} \right\rangle = Kz^2 \frac{Z}{A} \frac{1}{\beta^2} \left[\frac{1}{2} \ln \frac{2m_e c^2 \beta^2 \gamma^2 T_{\max}}{I^2} - \beta^2 - \frac{\delta(\beta\gamma)}{2} \right], \tag{4.1}$$

which describes the mean rate of energy loss by moderately relativistic ($0.1 \lesssim \beta\gamma \lesssim 1000$) charged particles. In the equation K is a constant equal to $4\pi N_A r_e^2 m_e c^2$, where N_A is the Avogadro's number, r_e is the classical electron radius, m_e is the electron mass. The other terms in the equation (4.1) are: Z – the atomic number of the absorber, A is the atomic mass, T_{max} is the maximum kinetic energy which can be imparted to a free electron in a single collision, I is the mean excitation energy, $\delta(\beta\gamma)$ is the density correction, β with γ are kinetic parameters of the particle, and z is the charge of the particle. In the given range of $\beta\gamma$ (1-100) the accuracy of the law is better than few percent. Outside this range it starts to fail: for the low $\beta\gamma$ additional corrections from the electron structure of the material have to be applied, while above the upper limit radiative effects start to play important role. The energy loss for all ranges is presented in the figure 4.1. The figure presents the plot for muons in copper, however the shape should be similar for the scintillators, with an exception of the magnitude of the stopping power.

Here we have to define the range of $\beta\gamma$ for particles used in the calibration process. For calibration with cosmic rays we can not control the momentum, but for the calibration with real data, which will be described in the second part of this chapter, the momentum range (so $\beta\gamma$) is limited. The low limit is caused by the magnetic field which bends low momentum particles out of the calorimeter acceptance. For protons it is approximately $\beta\gamma \approx 1$, while for pions and muons it is about 10 times larger. The upper limit of $\beta\gamma$ is approximately few hundreds for pions (lower for protons). This limit is determined by the maximum kinematically allowed energy from proton-proton interaction. These limits fit the range in which the Bethe-Bloch formula stands. Furthermore, it was checked that for polystyrene, the minimum to maximum variation was contained within 20%, which makes the mean value as a proper estimate of the energy deposits. In practice the spread of dE/dx will be absorbed in the resolution of the photostatistics.

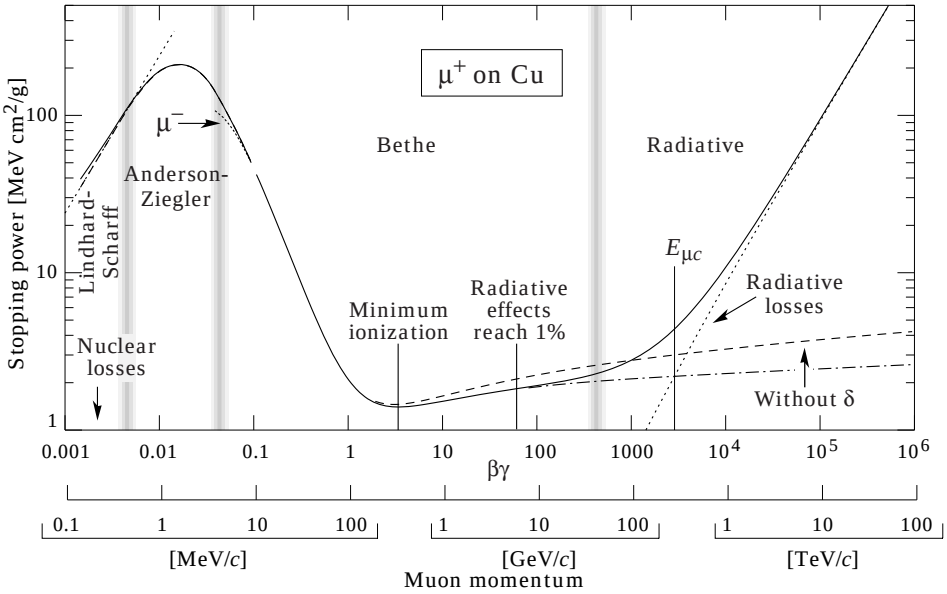

Figure 4.1: *Energy loss (dE/dx) of muons in copper [2]. The shape in a plastic scintillator is similar except of the magnitude.*

The usage of the mean energy loss is problematic, as the mean is weighted by very rare events with large single-collision energy deposits. Even with samples of hundreds of events a dependable value for the mean energy loss cannot be obtained [2]. Instead of the mean energy loss, one can use the most probable energy loss (MPV), defined as:

$$\mathrm{MPV} = \xi \left[\ln \frac{2mc^2\beta^2\gamma^2}{I} + \ln \frac{\xi}{I} + j - \beta^2 - \delta(\beta\gamma) \right], \tag{4.2}$$

where

$$\xi = \frac{K}{2} \left\langle \frac{Z}{A} \right\rangle \frac{x}{\beta^2}, \tag{4.3}$$

and x is the thickness in g cm^{-2}, and $j = 0.200$ [80]. The energy loss probability distribution $f(\mathrm{MPV}; \beta\gamma, x)$ is described by Landau distribution[1] [79].

4.1.2 Assumption on dependency on $\beta\gamma$

The statistics available for the calibration is not enough to perform analysis that depends on $\beta\gamma$. Thus we have to assume that the rise of the MPV with $\beta\gamma$ is not really significant in the accessible range of $\beta\gamma$. We construct an average minimum ionising particle, which is momentum-independent, and we assume that this average MIP s the same properties for all preshower cells, at least inside the regions. In fact this assumption in terms of the energy loss probability distribution is equal to a convolution of the Landau with a distribution of probability of occurrence of a given MPV, which comes from the relation between MPV and $\beta\gamma$.

[1]Landau distribution is defined as a complex integral: $p(x) = \frac{1}{2\pi\imath} \int_{c-\imath\infty}^{c+\imath\infty} e^{t \ln t + xt} dt$, where c is any positive real number. $x = R(E - E_{\mathrm{MPV}})$, where R is a constant related to the absorber and E is the particle energy.

4.1.3 Digitalised signal from MIPs

As a MIP passes a cell of the detector, it losses a fraction of its energy in the scintillating material. An amount of light proportional to the deposited energy is emitted. The light is then collected and amplified by the photomultiplier, and the outcome is an electric signal, processed by electronics. A registered output from the electronics, represented by a number, interpreted as an energy stored in a given cell of calorimeter is an outcome of all parts of the described process, and each part of it has an impact on the final result. First, the energy deposited by a particle of a given energy which crosses a thin scintillator with a certain angle is described by just introduced Landau distribution. The most probable value of the Landau distribution depends not only on $\beta\gamma$ of the particle, but also on a length of a path of the particle inside the scintillator. The scintillation and the light collection efficiency are the next processes which modify the outcome of the measurement. Then there is the photomultiplier with its photostatistics. The last part is a noise produced in the electronics. The output – digital signal of the energy deposit depositted by MIP is not a simple distribution, but a convolution of multiple distributions described above.

With an increase of the statistics one can fit more detailed models, which describe more effects playing role in the measurement of an energy stored by MIPs. However even the simple model, which takes in account only the Landau distribution, is correct enough to perform the first calibration of the detector.

The first extension to that model is a convolution of the Landau and a Gaussian. In this model all fluctuations (dE/dx dependency on $\beta\gamma$, scintillation, tubes photostatistics) are inside the Gaussian. This allows to uniformise the detector with the calibration within 20% with cosmic rays. With particles originating in proton-proton interactions the calibration can be as good as 10%. When a proper correction of a different track lengths of particles passing a cell from various angles is taken into account, it is possible to calibrate the detector at least at 5% level, which is required for proper particle energy measurements.

4.2 Multianode photomultipliers and electronics in the calibration

4.2.1 Multianode photomultipliers

The photomultipliers were already described in the section 3.4. Let us remind here, that each photomultiplier contains 64 anodes corresponding to 64 channels of the PRS. One high voltage is applied to the photomultiplier. The response for each channel in the board in ADC counts can be written as (derived from equation 3.1):

$$R_{ch} = g_{ch} \cdot \alpha_{ch} \cdot U^{\beta}, \tag{4.4}$$

where g_{ch} is the numeric gain applied in the electronics for the channel, α_{ch} is the parameter characterising channel uncorrected response. β is the parameter of high voltage scaling, assumed to be the same for all channels in the board. U is the high voltage value applied to the photomultiplier. g_{ch} is set in the electronics in the process of inter-calibration. β is extracted from the measurement (the measurement is

described in Appendix A). α_{ch} is not required in the calibration, because the calibration process always refers to the previous calibration, as in the equation:

$$R'_{ch} = \frac{g'_{ch}}{g_{ch}} \left(\frac{U'}{U} \right)^{\beta} R_{ch}, \tag{4.5}$$

where R'_{ch} is a required response after the calibration, g'_{ch} and U' are new parameters applied to obtain the response. From this equation we can find the new high voltage settings:

$$U' = U \left(\frac{R'_{ch}}{R_{ch}} \cdot \frac{g_{ch}}{g'_{ch}} \right)^{\frac{1}{\beta}}. \tag{4.6}$$

This formula was used whenever new high voltage settings were required.

4.2.2 Signal shape

The processes described in the section 4.1.3 (scintillation) last a certain time, longer than 25 ns. To measure the whole energy deposit, one have to integrate the signal over time. The signal shape measured on data [83] is displayed in the figure 4.2. The fact, that signal is longer than 25 ns means, that it lasts more more than a time gap between two bunch crossings in the nominal LHC filling scheme. Thus one have to align the detector in time [68] to maximise signal in a 25 ns time gap. When properly time-aligned, the integration has to start when signal reaches 30% of its maximum value.

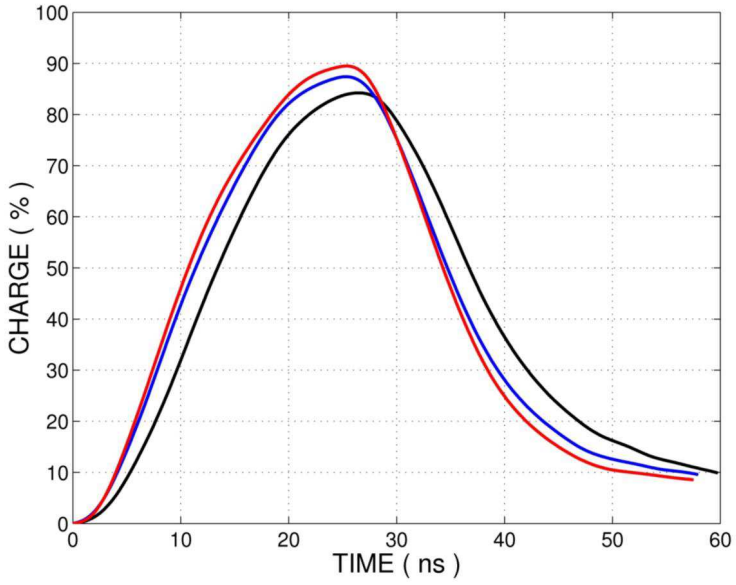

Figure 4.2: *Signal shape as a function of time from the nominal time of arrival of the particle. Red – inner, blue – middle, black – outer. Plot obtained from the collision data [83]. The detector is aligned in time such the signal integration starts at signal yield of 30%.*

4.2.3 Spill-over correction

The signal in T0+1 has to be corrected for the fraction of signal from the time gap T0 remaining in the time gap T0+1. This correction is called the *spill-over correction*. A certain fraction (α) of the integrated signal in T0 is subtracted from the integrated signal in T0+1. The fraction α is determined on the data [83] independently for each channel. The distribution of the α for different regions of the detector is given in the figure 4.3. The spill-over correction is important only when the intervals between collisions are small, at the level of ~ 50 ns. It means that this correction was unimportant in 2009 and 2010, thus it was not used in the data taking at that time. However, it was necessary in 2011. The α values were measured in the beginning of 2011.

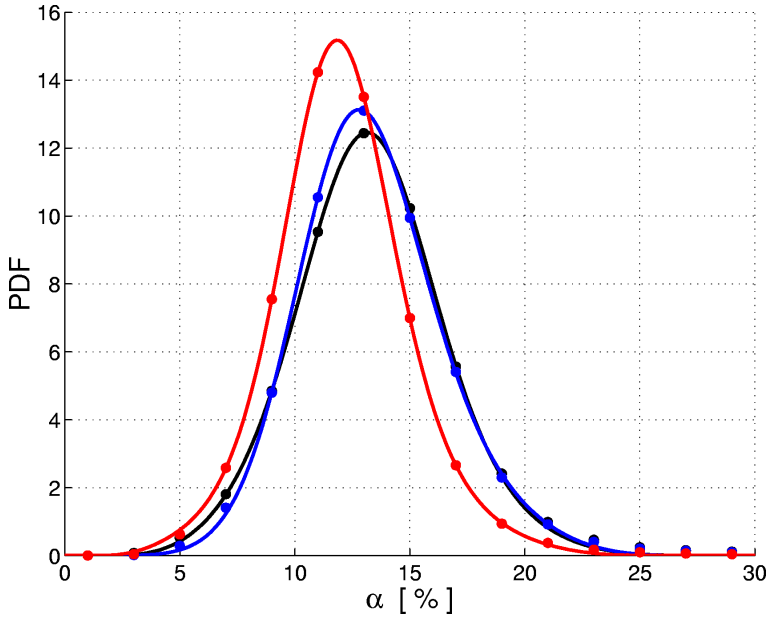

Figure 4.3: *Percentage of the total signal in time gap T0+1. Red – inner, blue – middle, black – outer. Plot obtained from the collision data [83].*

4.2.4 Bunch crossing parity

Each photomultiplier channel readout has two very-front-end (VFE) electronics integrators. In the same time gap of 25 ns, one channel is working in integrating mode (it integrates a charge collected by the photomultiplier), while the other channel is reset. Then their role change. They swap once per 25 ns, and the change is triggered by the LHCb clock to fit the machine bunch crossing time gaps. The system is designed such way, that for each photomultiplier one subsystem should work always for one bunch crossing number parity: one subsystem for odd and one for even.

It was measured that chips used in front-end boards may vary by $\pm 5\%$. However the real spread (e.g. the chips in thin electronic board environment) had been never checked before 2010. Keeping in mind that also pedestals are different for even and odd bunch crossing id, it appears to be something that has to be investigated and mastered for a correct calibration. Because of the design it one should split calibration by bunch

crossing number parities whenever it is possible. An example plot of a distribution of charged particles energy deposits in ADC counts for channel 3573 for two bunch crossing id parities is given in the figure 4.4.

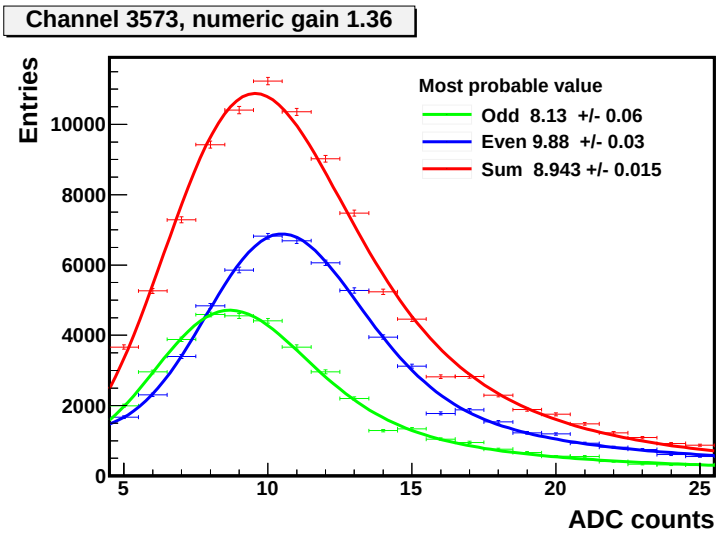

Figure 4.4: *Measured energy deposit of charged particles for channel 3573. Blue points represent measurements in even bunch crossing numbers, green points are for odds, while red points are for the sum of the evens and the odds. For each histogram a fit of the model (Gaussian convoluted with Landau and addition of exponential) is performed. The blue and the green points are fit well by the function, while the red fit is not as perfect for the most probable values region. The difference between even and odd most probable values of MIP is* 19% *for this channel. The differences between the even and the sum and between the odd and the sum are both equal to* 10%*. The difference in statistics comes from bunch filling scheme in the data sample used.*

4.2.5 Pedestal correction

Each channel electronics is instrumented by a hardware correction for offset. The correction can be applied independently for even and odd bunch crossings. Corrections up to 255 ADC count with the precision of 1 ADC count are allowed. Above 128 ADC count the transcoding is applied, which reduces the precision to 2 ADC count. Pedestal values are measured in dedicated runs and computed offsets are applied to the electronics. Additionally, residual pedestals are also measured every run. By residual pedestals we understand fractions of pedestals that are not corrected in the electronics. There are two reasons why residual pedestals are different from zero:

- Offsets drift from the values obtained in the measurement used in the electronics. For example power supply cuts may result in changes of pedestals.

- Limited offset correction precision in the electronics.

Region	Even (ADC count)		Odd (ADC count)	
	Mean	σ	Mean	σ
C side				
Outer	0.758 ± 0.014	0.492 ± 0.010	0.665 ± 0.014	0.515 ± 0.011
Middle	0.755 ± 0.018	0.513 ± 0.013	0.744 ± 0.020	0.567 ± 0.014
Inner	0.672 ± 0.019	0.510 ± 0.014	0.514 ± 0.022	0.566 ± 0.015
A side				
Outer	0.839 ± 0.016	0.564 ± 0.013	0.692 ± 0.016	0.535 ± 0.011
Middle	0.849 ± 0.020	0.584 ± 0.016	0.705 ± 0.019	0.549 ± 0.014
Inner	0.865 ± 0.020	0.532 ± 0.014	0.584 ± 0.021	0.556 ± 0.017

Table 4.1: *Parameters of the fits of Gaussian to the residual pedestal histograms for 2010 statistics used in calibration.*

While the first type can be solved by remeasuring the pedestals, the second can not be corrected in the electronics. Thus, we have to correct for them in the calibration process.

The residual pedestals measured for 2010 data used in the calibration are presented in the figure 4.5. It can be observed that the distributions can be fit by Gaussian function. The parameters of the fits are collected in the table 4.1. Typical values of the mean are about $0.5 - 0.9$ ADC count, which is a non-negligible fraction of MIP MPV value. The mean is always positive and shifted from zero, which is the result of the method used to compute offsets used in the electronics. The even and the odd values are not correlated (figure 4.6). It justifies the fact that independent calibration for both bunch crossing parities is mandatory and the residual pedestals have to be corrected.

4.2.6 Magnetic field correlation

In the section 3.4.3 the magnetic shielding was described. Even when the tubes are shielded, some of the magnetic field remain. Once the polarity of the magnetic field is set, the field itself is constant, thus the residual field inside the tubes is also constant. If the efficiency is slightly changed it should not vary with time, so it will be automatically corrected with the first calibration with the magnetic field on. However when magnetic field polarity is changed, then the efficiencies may change. It means that if we calibrate with magnetic field down configuration, then that calibration may be different from a calibration with magnetic field up polarity. This effect was checked with the first 2010 data, with the detector calibrated with 2009 data. For two samples: one magnetic field down (28 millions of tracks) and one magnetic field up (24 millions of tracks), a measurement of MIP MPV values was performed. The results are available in the figure 4.7. The check was performed by regions and globally. A global correlation between two opposite magnetic field polarisations is 96.9%. The conclusion is that the polarity has no effect on the detector calibration.

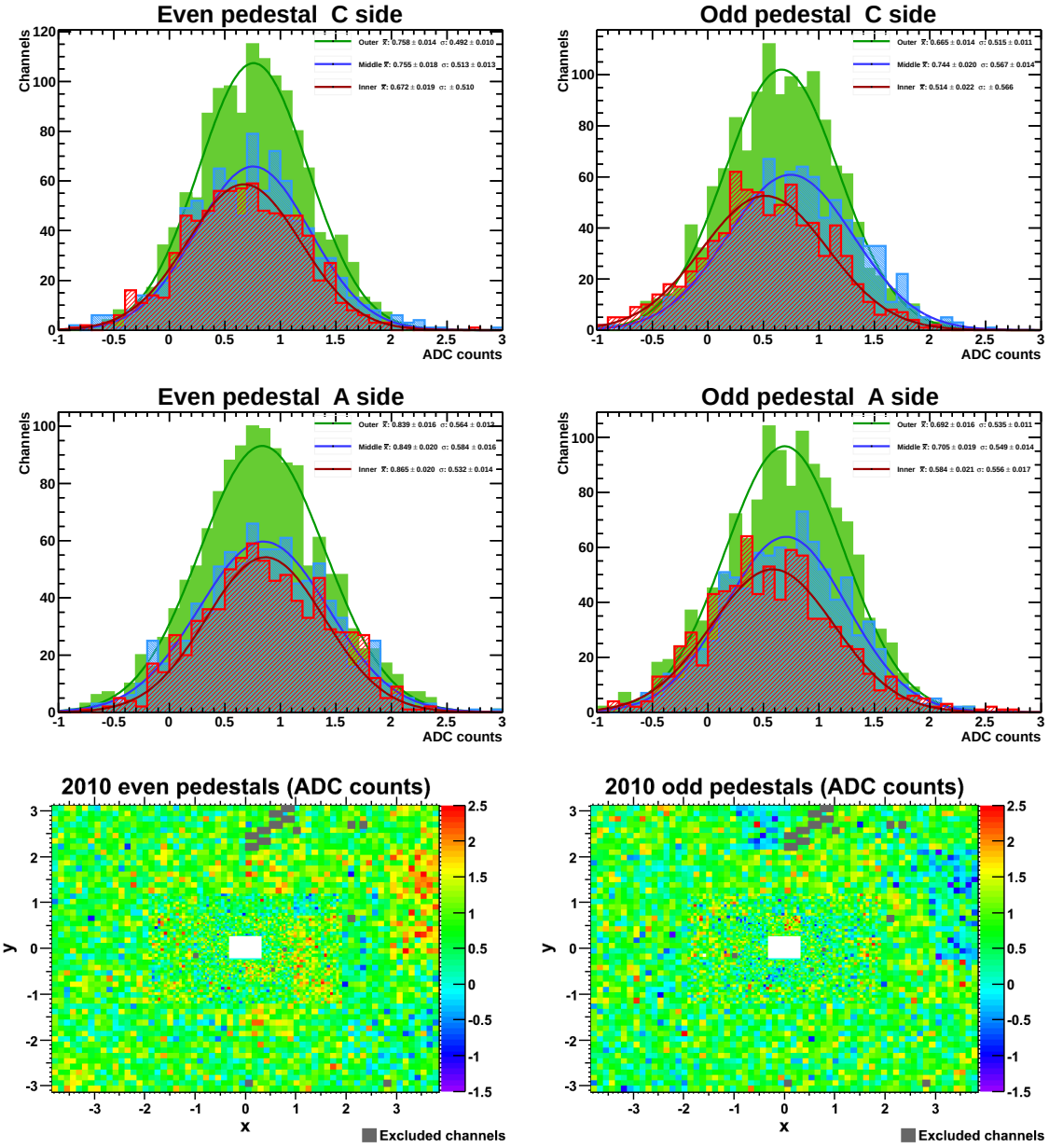

Figure 4.5: *Residual pedestal values by region and bunch crossing number parity for 2010 statistics used in calibration process.*

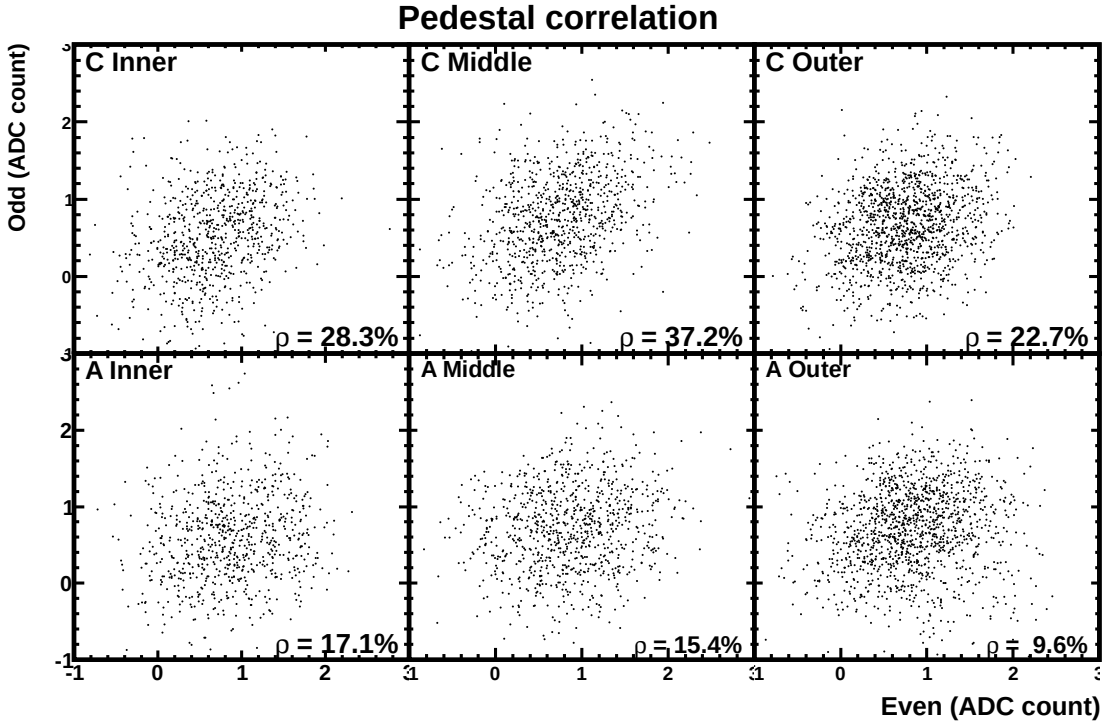

Figure 4.6: *Correlations between even and odd residual pedestal values for 2010 statistics used in calibration process.*

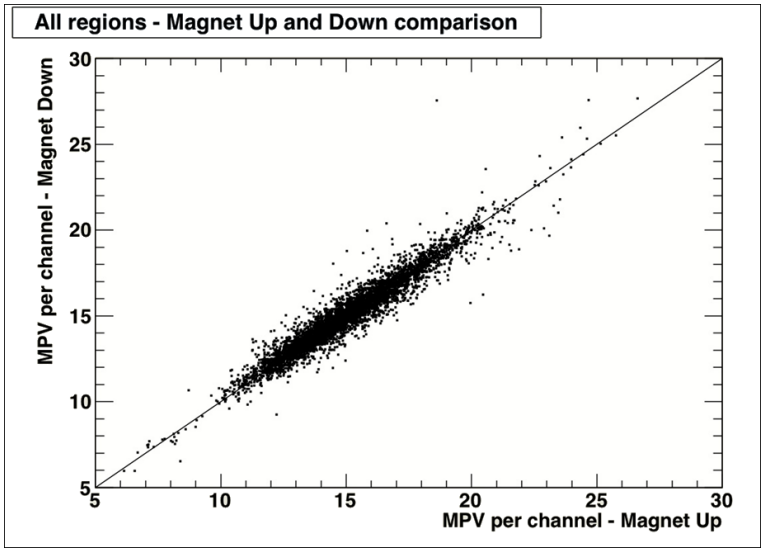

Figure 4.7: *Minimum ionising particle energy deposit most probable value in ADC counts magnetic field up and down polarities correlation. One point represents one channel.*

4.2.7 Detector stability

Detector response stability in time was checked in 2010. Two consecutive samples were prepared: one from April and one from May. Each sample was split by bunch crossing id. The available statistics was: 230 millions of tracks for April odd bunch crossing id, 310 millions for April even bunch crossing id, 700 millions for May odds, and 200 millions for May evens. Calibration fits were performed on all samples. The correlation between May and April results (figure 4.8) is greater than 99% for all regions except A side middle part, where it is equal to 97% for the evens. The results shows that at least in a scale of one month the detector was stable in terms of pedestals and the calibration.

4.3 Calibration strategy

4.3.1 Inter-calibration and global uniformisation

The calibration of the detector is performed in two steps. The first one is done inside each board (for each photomultiplier). For each channel one can assign two numeric gain corrective factors: one for even bunch crossing numbers, and one for odd bunch crossing number. Each numeric gain is from the range of [1,2]. Once the board is equalised over all channels, the global board response can be manipulated with high voltage applied to the photomultiplier.

Eventually, it is possible to correct the results during data reconstruction. For this reason one corrective factor per channel is stored in the database (no even/odd splitting). However, by construction this cannot improve the calibration for the trigger. This correction is sometimes called *software calibration*.

4.3.2 Inter-calibration procedure

The inter-calibration begins from the construction of a set of collected charge histograms. Two or one histograms per channel. Two, when even/odd subchannel splitting is used, and one histogram when splitting is not used. From those histograms, the most probable values (MPV) of MIP deposits are extracted. The next step is the assignment of new numeric gains.

4.3.2.1 Charge distribution construction and MIP deposit model fit

For each channel, a collected charge distribution is built. It is corrected event by event for track length inside cell, which depends on crossing angle. Different corrections have been used for cosmic data and collision data. They will be given later, when discussing each sample of the data (sections 4.4 and 4.5).

To each histogram a convolution of a normal distribution and a Landau distribution is fit. The Landau part represents the law of energy loss of a minimum ionising particle in a thin scintillator. The law was introduced by L. Landau in 1944[79]. The most probable value (MPV), is the characteristic parameter and for a perfectly calibrated detector should be the same for all cells. The σ_{Landau} is characteristic to

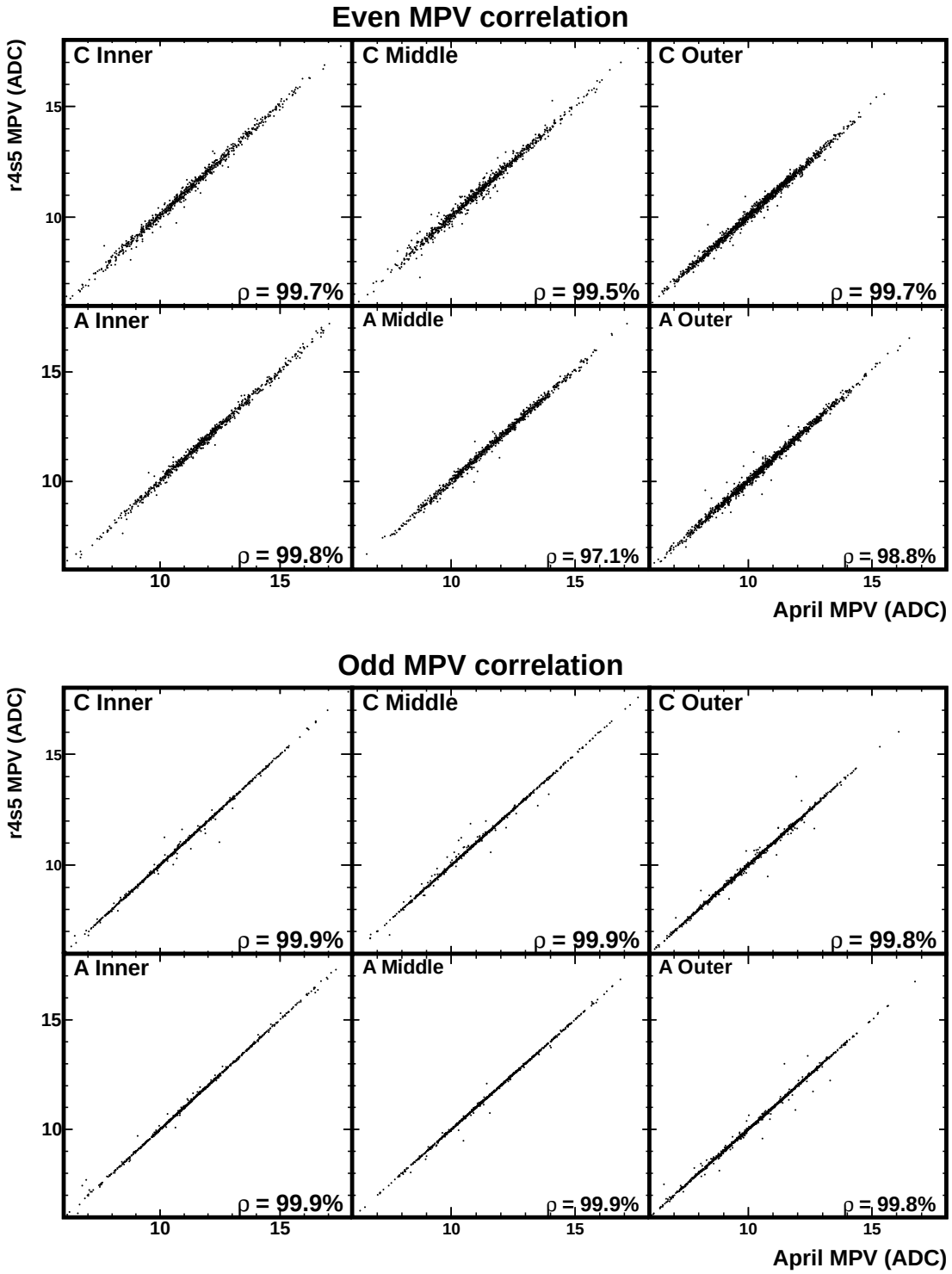

Figure 4.8: *Correlation between MIP MPV position measured in April (horizontally) and May (r4s5, vertically).*

the material used in the detector. The Gaussian part is used to describe various effects which fluctuate energy deposits, which main sources are variable photomultiplier photostatistics and track length correction errors. The presented convolution is not a physical probability density function because it is non-zero for deposits lower than 0, while energy deposit can not be negative physically. However the cumulative distribution for values lower than 0 for typical values of MIP MPV position (100 ADC count for cosmic data, and 15-20 ADC for collisions) and Gaussian widths ($\sim$ 20 ADC counts for cosmics and $\sim$ 1 ADC counts for collisions) is negligible for the purpose of the calibration.

An exponential component is added for collision data, which has to model mild electromagnetic background and eventual uncorrected pedestals.

An example of the distributions with fits, obtained with the cosmic data, can be found in the figure 4.9.

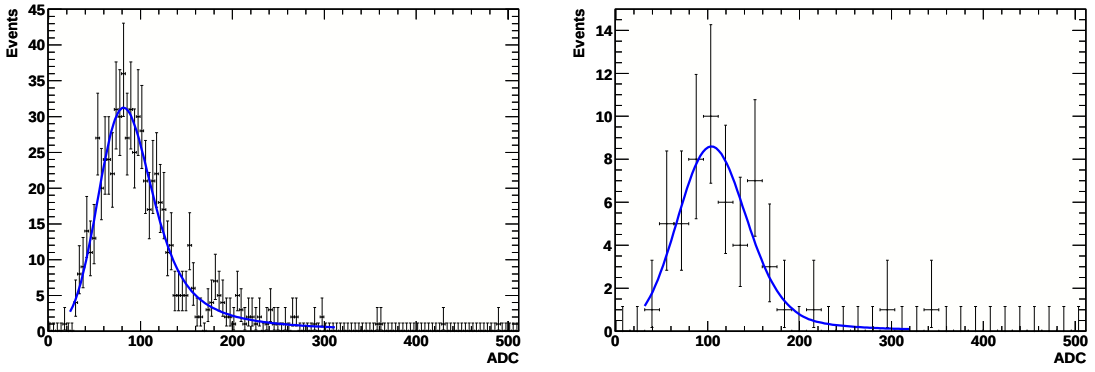

(a) Outer (b) Inner

Figure 4.9: *Example distributions of the energy deposits (charges collected by photomultipliers) with fits of the convolution of the normal distribution and the Landau distribution to the 2009 cosmic data statistics. One channel for outer (a) and inner (b) presented. Statistics used is 667 tracks for (a), and 53 for (b).*

4.3.2.2 Charge distribution degaining

Before assignment of new numeric gain corrective factors, one has to apply inverted corrective factors to the current numeric gains. This correction can be applied in two ways:

- by dividing the results of the fit by the numeric gains,
- or by converting the histograms accordingly to the inverted corrective factors.

The first solution is clear, so we will focus on the second one. As mentioned in the section 3.6, this procedure is call *degaining*.

To explain the advantage of the second procedure, we will use an example charge distributions presented in the figure 4.10. For this channel the numeric gain value

is 1.67. The raw output (gained) from the electronics is given in the histogram (a). The histogram (b) is obtained after degaining procedure application. Let us look first at the histogram (a). The very first observation is that there are series of bins with non-zero entries and empty bins. The holes can have the width of one or two bins. They are the result of the gaining procedure. This procedure operates on integers. It applies a multiplication by a number from the range [1,2], and the result are integers again. Rounding in the numerical operations results in the structure observed in the histogram (a). This rounding does not influence the precision of the measurements for large ADC count values, but is important for MIP sector.

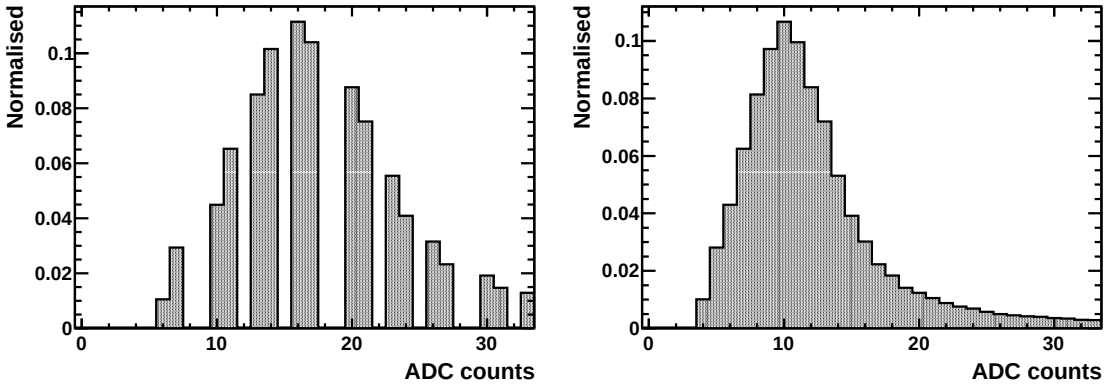

(a) Raw output (b) Degained output

Figure 4.10: *Example of raw charge distribution (a), which is the direct readout from the electronics. The reconstructed degained distribution (before applying numeric gain correction inside the electronics) is given for comparison (b). The numeric gain corrective factor used for this channel is 1.67.*

The rounding in gaining is a potential source of systematic errors in the fit results. For this reason, it is better to apply degaining to the histogram rather and then fit, than divide the fit result by the numeric gain.

4.3.2.3 Numeric gain assignment

After all MPV values of MIP energy deposits are obtained, procedure of assigning new correction starts. The first stage is the sorting of channels in each board by their MPV value. It means that the new indexes are assigned such that:

$$\forall(i \geq 1, j \geq 1, i > j) : \mu_i \geq \mu_j,$$

where μ_i and μ_j are the MPV values for channels i and j. The range of corrective factors (numeric gains) that the front-end electronics can afford is [1,2] with 8-bit precision. To fill the range the most efficiently a procedure of finding a channel k for which a numeric gain equal to 1 is applied. The channels is chosen such the highest number of the rest channel has values of the MPV not lower than the half of the MPV value μ_k of the channel k:

$$\mu_k \leq 2\mu_m \wedge (m = 1 \vee (m > 1 \wedge \mu_k > 2\mu_{m-1})),$$

such that $k - m$ is the largest from all possible choices of k. Once the best range is found, assigning new gains begins. The gain g_l for channel l is equal to:

$$g_l = \begin{cases} 1 & \text{if} \quad l > k \\ \frac{\mu_k}{\mu_l} & \text{if} \quad m \leq l \leq k \\ 2 & \text{if} \quad l < m \end{cases}$$

All channels which lie inside the range limited by channels m and k have assigned numeric gains that put them after correction to the value of MPV for channel k. All the rest, it means outside the range, are corrected as much as it is possible, but not fully.

4.3.3 Timeline

Before going into the details of the preshower calibration campaigns described in this documents, it is good to put them in a chronological order:

- We consider that the detector was initially precalibrated as described in [68].
- The initial calibration was performed with cosmic rays in autumn 2009. It resulted in new numeric gains (same for even and odd bunch crossing numbers) written in the electronics, and new high voltage settings applied to the photomultipliers. This calibration prepared the preshower for the first LHC collisions. The target value of MIP MPV was 20 ADC counts in 25 ns time gap (T0).
- The first calibration with beam data was performed with 2009 statistics. It allowed to produce new numeric gains (same for both bunch crossing parities) for most of the regions, except the most top and the most bottom rows of the outer region boards. New high voltage settings were also applied. The result (measured after) was $14 - 17$ ADC counts for MIP MPV. These settings were use in the detector for the whole period of the year 2010.
- In the late spring of 2010 a new measurement of MIP MPV was performed. The results were not included in the electronics. Instead, they were used as software corrections in the process of reprocessing of 2010 data. This calibration again did not split between even and odd bunch crossing numbers.
- During winter break of 2010/2011, the full process of calibration was performed again. New numeric gains were assigned, different for even and odd bunch crossing numbers. Also, new high voltage settings were applied. The target value of MIP MPV after this calibration was 10 ADC counts.

4.4 Inter-calibration with cosmic rays

4.4.1 Introduction

The preshower detector was already precalibrated, when the calibration with cosmic rays was performed. The precalibration set MIP MPV value at 100 ADC counts (total charge) within its precision.

The calibration with cosmic rays was performed at the time when the only information fully available for that purpose was coming from the calorimeters. It means that it was impossible to use the detector tracking system to reconstruct cosmic tracks. Instead of that an algorithm based on calorimeter signal only was introduced. The algorithm reconstructed particle tracks with two calorimeter elements (ECAL and HCAL) as an input for the track fit (an example is given in the figure 4.11).

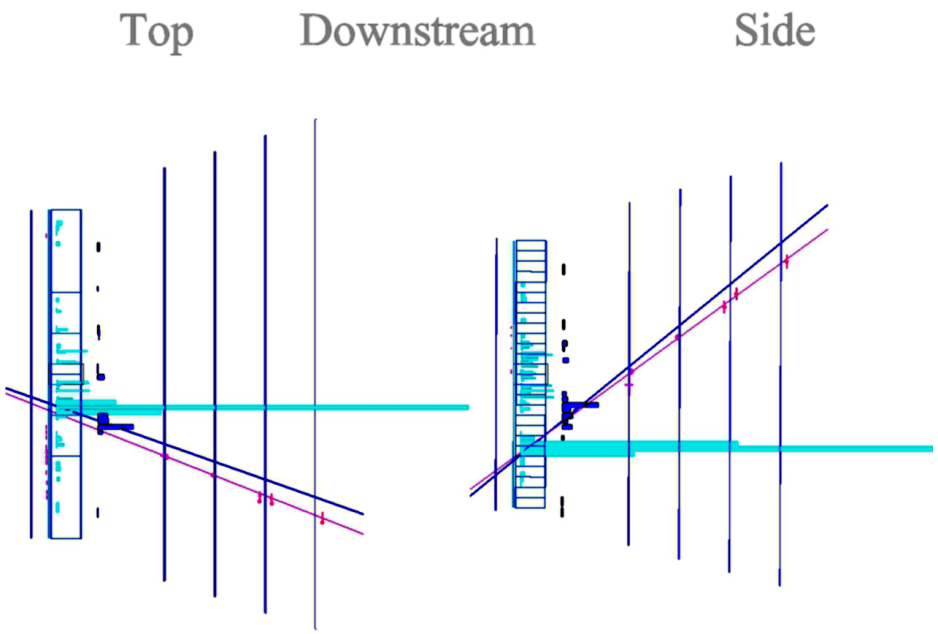

Figure 4.11: *An example of cosmic event from above (left), and from side (right). The calorimeters and the muon stations are visible. ECAL deposits are marked with cyan, HCAL with dark blue. Muon hits are in magenta. The track reconstructed with calorimeter hits (ECAL and HCAL) is drawn with dark blue line. For comparison, the track reconstructed with muon station hist is painted in magenta.*

About 4 millions of cosmic events were registered. The detector was set to store for each triggered cosmic ray event a table of data for consecutive 25 ns time gaps. Usually it was a range starting from two time gaps before triggered time gap, up to two time gaps after triggered one inclusively. That setup is called TAE±2.

During normal operations with beams the LHCb detector is aligned in time with the LHC machine to start integration of signal when particles from the *pp* interaction arrive to the detector. However cosmic rays arrive randomly, thus there is no possibility of starting the integration of signal from the PRS detector exactly at the time of arrival. Instead another approach is taken: the LHCb detector runs with its own internal clock, measuring out gaps of 25 ns; the time of arrival of a cosmic ray particle is calculated off-line *a posteriori* from the ratio of the charge collected from the consecutive time gaps. The signal charge stored in the histograms is the total charge integrated from the model.

The definition of local spherical coordinates used in the analysis is given in the

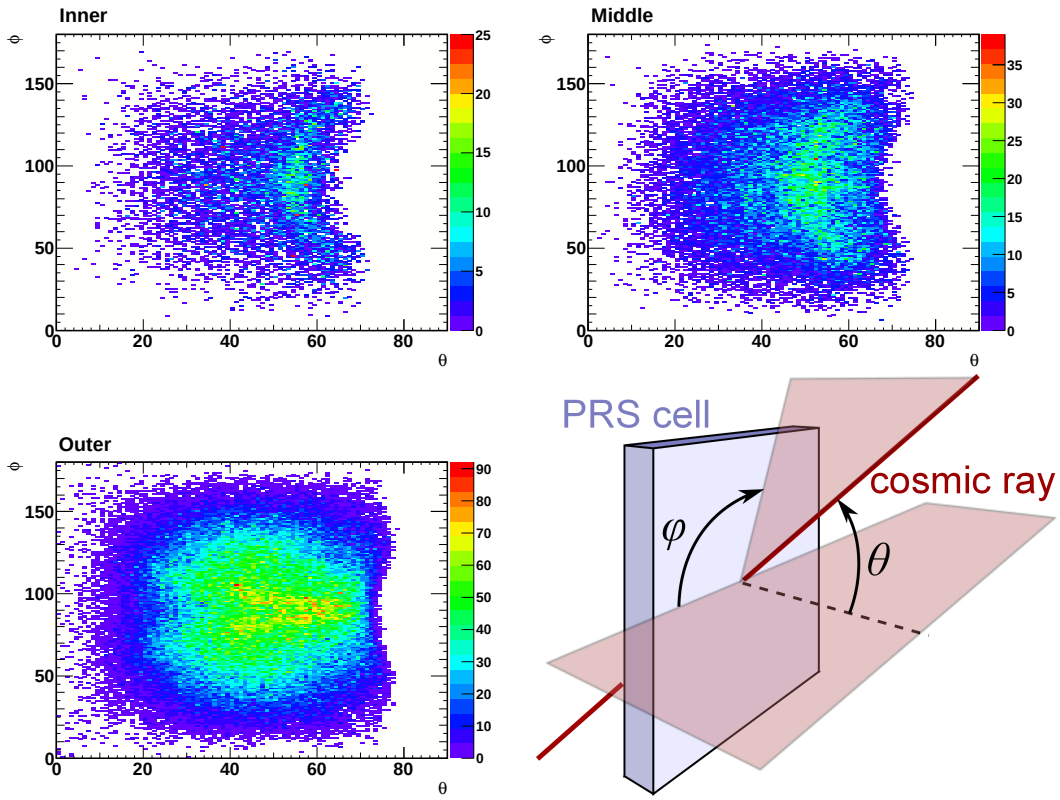

Figure 4.12: *Dependency of number of tracks reconstructed with calorimeter information only, registered in a sample of cosmic rays in 2009, with track angles θ and ϕ. It can be interpreted as a not normalised probability of an observation of a track with a given set of parameters. Plots are given for three regions of the preshower detector. For particles coming from back of the cell ($\theta' > 90\,\mathrm{deg}$), the inversion is applied: $\theta = \pi - \theta'$.*

figure 4.12. The distributions of the probability of observing a cosmic event as a function of these coordinates is given in the same figure.

4.4.2 Event selection

The first part of the analysis was an off-line selection of the collected events. The following steps of the selection were taken (after each step a cumulative efficiency of all steps up to the current step, respect to the entry statistics is given):

1. **Track reconstructibility**
   Only the events with a cosmic ray track reconstructed were kept. Cumulative efficiency is $(91.82 \pm 0.06)\%$.

2. **Track quality cut**
   A minimum ionising particle track geometry was determined from energy deposits in HCAL and ECAL. As a result of the fit, among other parameters, uncertainties of the fit at the PRS plane were calculated, named respectively σ_x and σ_y for horizontal and vertical uncertainties. A distribution of the $\sqrt{\sigma_x}$ and $\sqrt{\sigma_y}$ is presented in the figure 4.13. To keep only properly extrapolated tracks, the following cut is applied:

   $$\sqrt{\sigma_x} < 100 \text{ mm} \quad \wedge \quad \sqrt{\sigma_y} < 150 \text{ mm}. \tag{4.7}$$

   The cumulative efficiency after this step is $(69.65 \pm 0.09)\%$.

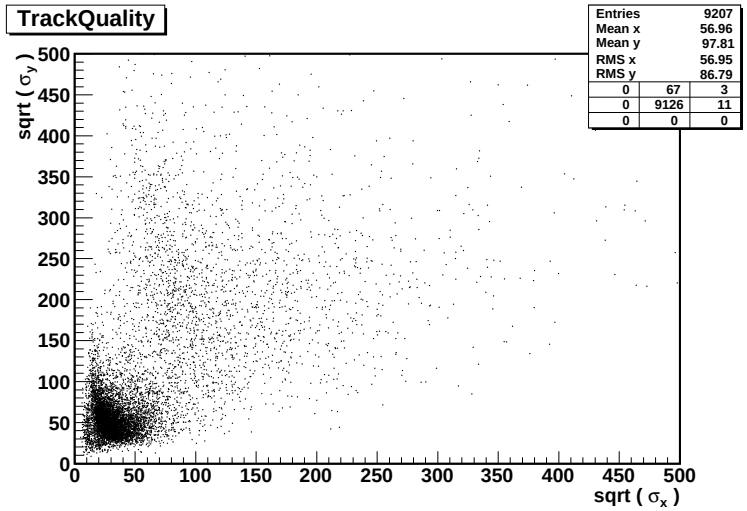

Figure 4.13: *Scatter plot of the square roots of the uncertainties σ_x and σ_y in millimetres of a track entry position to a cell of the PRS detector for a statistics of 9207 tracks.*

3. **PRS multiplicity cut**
   A number of cells of the PRS with an electronic response is larger than 10 ADC counts in an event was calculated for each event, called the multiplicity $n(PRS >$

10 *ADC*). For the reference, the value of 100 ADC counts was a target for a minimum ionising particle response for the calibrated detector in cosmic particles data taking mode. A cut which keeps only the events with $n(PRS > 10\ ADC) < 50$ was introduced. The idea of this cut was to reject huge showers of secondary cosmic rays in which a proper track reconstruction was impossible and additionally to remove the electronic resets of the PRS which effect in a simultaneous signal generation in all cells in one 25 ns time gap. The PRS multiplicity is presented in the figure 4.14. The cumulative efficiency is $(69.33 \pm 0.09)\%$.

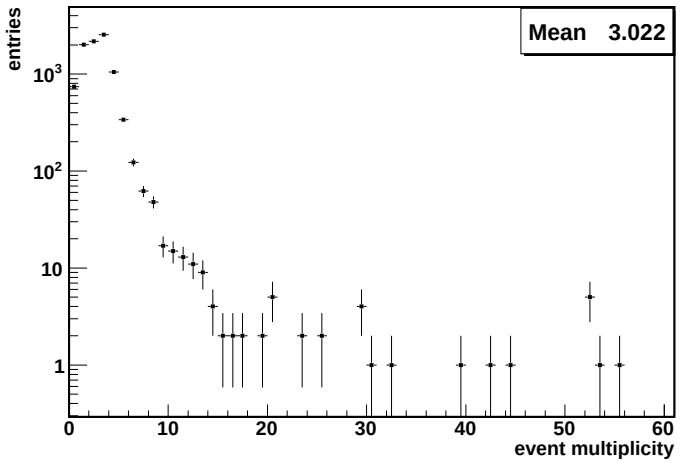

Figure 4.14: *Multiplicity of preshower cells with signal larger than 10 ADC counts in a sample of 9207 cosmic events.*

4. **ADC count response threshold**
   A minimum response of 20 ADC counts for a cell in a 25 ns gap in which a cosmic event was registered was required to keep the cell for the further analysis. The cumulative efficiency is $(57.57 \pm 0.10)\%$.

5. **Time correction possible**
   Only the cells for which a time correction was possible were stored. The time correction is a procedure in which a proper time of arrival is calculated from the asymmetry of the charge stored in the consecutive time gaps. When the time of arrival is obtained, a correction derived for the model of the charge distribution as a function of the time of arrival is applied to the measured charge in that cell. The result is the total energy deposit in the cell from the passage of the cosmic ray particle. The cumulative efficiency is $(50.08 \pm 0.10)\%$.

Finally the statistics from autumn 2009 cosmic runs available for the next part of the analysis was 2.073.989 of cosmic entries. The entry is defined as a cell which has passed the cuts and lies inside the region of $\chi^2 < 9$, where the χ^2 is defined as:

$$\chi^2(Topo|Track) = \frac{(x_t - xc)^2}{\sigma_{x,t}^2 + \Delta x_c^2/4} + \frac{(y_t - yc)^2}{\sigma_{y,t}^2 + \Delta y_c^2/4}. \tag{4.8}$$

x_t and y_t are points of entrance of a particle to the cell, extrapolated from the track fit. $\sigma_{x,t}$ and $\sigma_{y,t}$ are uncertainties extrapolated to the entrance of the particle to the cell. x_c and y_c are locations of centres of cells. Δx_c and Δy_c are cell sizes. The distribution of χ^2 is presented in the figure 4.15. The collected statistics corresponds to number of entries as large as 800 for the outer part and not lower than 90 for the inner part. The plot which shows the distribution of the number of entries per channel is shown in the figure 4.16.

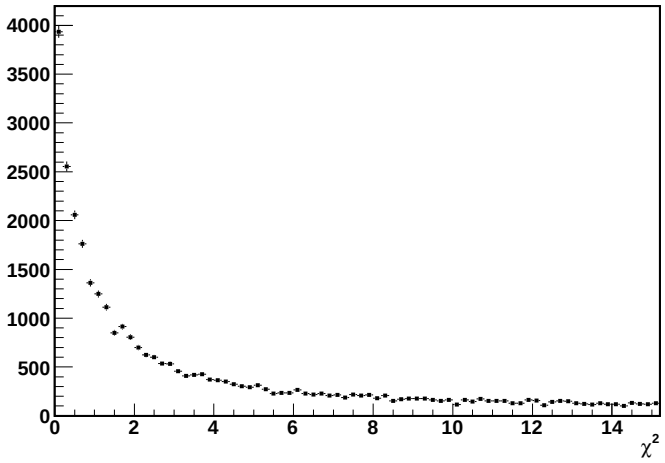

Figure 4.15: χ^2 *defined as in the equation 4.8 distribution for a sample from 2009 cosmic events.*

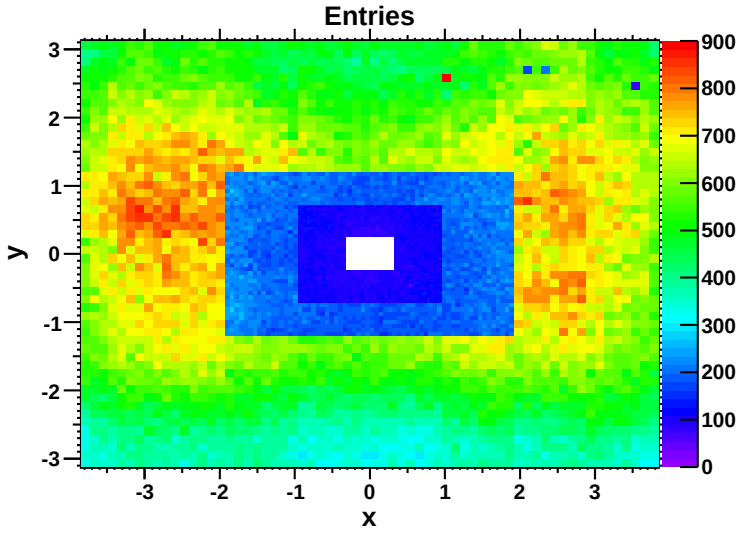

Figure 4.16: *Number of entries per cell used for 2009 calibration with cosmic rays.*

4.4.3 Track length correction used

For calibration purposes one would use only particles which pass a calorimeter cell perpendicularly to the calorimeter plane. Unfortunately, cosmic particles cross the detector with different angles, thus their paths inside cells are different. An explanatory picture of a cosmic ray track passing a cell of the outer part of the PRS detector is presented in the figure 4.17. An assumption was made that a result of a fit of a track to signals from ECAL and HCAL is not enough precise to testify that the calculated entrance point of the track into a cell is correct. As a result of that, it was decided to use an averaged formula of track length correction for given angular parameters of each track.

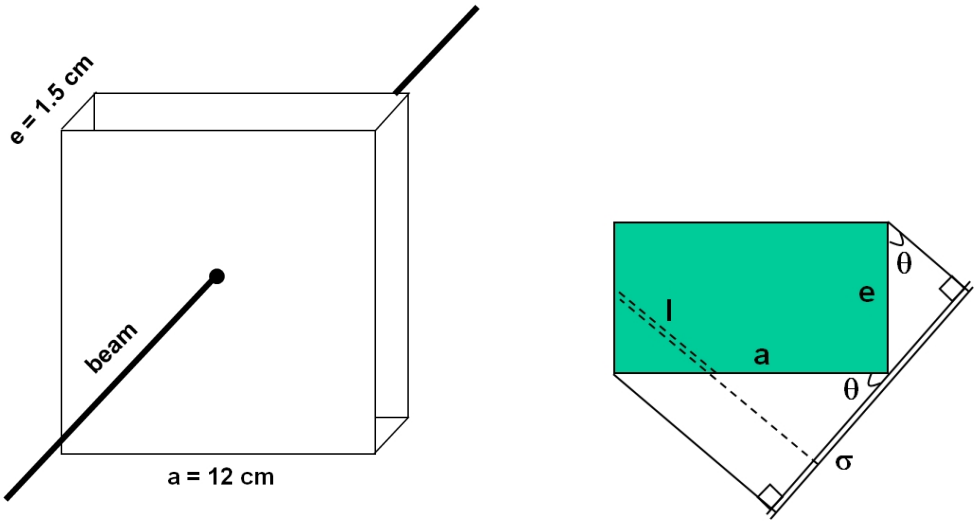

Figure 4.17: *PRS cell geometry isometric view (left) and top view (right).*

The formula which was used was derived from an equation of the cross section σ of a cell for a track with given angles θ and ϕ:

$$\sigma = a(a\cos(\theta) + e\sin(\theta)(\sin(\phi) + \cos(\phi))), \tag{4.9}$$

where a and e are the cell front plane length and the cell depth respectively. Additionally the volume V of the cell is defined as:

$$V = a^2 e, \quad V = \sigma < l >,$$

where $< l >$ is an average track length for the parameters θ and ϕ. Combining the equations, the result is:

$$< l >= \frac{ae}{a\cos(\theta) + e\sin(\theta)(\sin(\phi) + \cos(\phi))}. \tag{4.10}$$

A plot of the correction with a comparison between the model and a simulation is presented in figure 4.18. For the cosmic ray calibration the applied correction is expressed as:

$$\overline{ADC} = ADC_{measured}\frac{e}{< l >} \tag{4.11}$$

$ADC_{measured}$ is the total charge collected from the cell corrected for the time of arrival, $\overline{ADC}$ is the charge corrected for the track length inside the cell and it is the value of the charge stored in histograms for the purpose of further analysis.

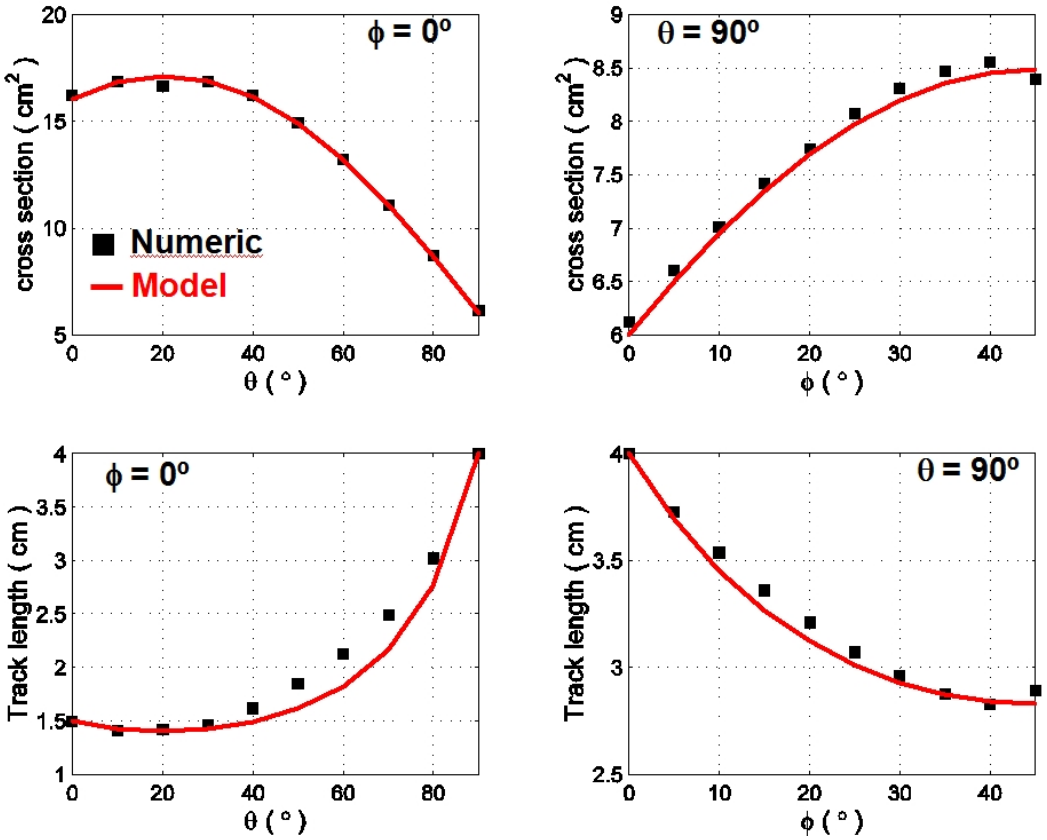

Figure 4.18: *Comparison of simulated and model based cosmic particles track length corrections for cells from the inner part of the PRS detector for two boundary cases:* $\phi = 90\,\mathrm{deg}$ *and* $\theta = 0\,\mathrm{deg}$. *The section of crossed zone (cross section) is presented on the top and the average track length itself in the bottom line. Let us notice that we are only interested in getting a qualitative correction. The dependency of simulated data from the model results in negligible uncertainty in the calibration.*

4.4.4 Track length correction systematic error

The track length correction was based on $1/ < l >$ averaged correction. However, it should be rather $< 1/l >$. This averaging needs some envelope efficiency function which has to be applied at the borders, where $l \to 0$. The correct model of averaging of $< 1/l >$ was never proposed.

The effect of the averaging $1/ < l >$ is shown in the figure 4.19. One can find there distributions of the corrected ADC counts of cosmic rays minimum ionising particles for two ranges of the θ zenith angle: $\theta < 60°$ and $\theta \geq 60°$ for three regions of the preshower detector. Visible differences between distributions for two regions are observed. The difference of the mean value of the distribution between $\theta < 60°$ and

$\theta \geq 60°$ is the largest in the outer region and is equal to 4 ADC counts, it means 4% of the requested MIP deposit value. It shows that used correction for track lengths led to an error in the estimation of the most probable value of the energy deposit in the preshower by a minimum ionising particle passing the detector perpendicularly to its plane.

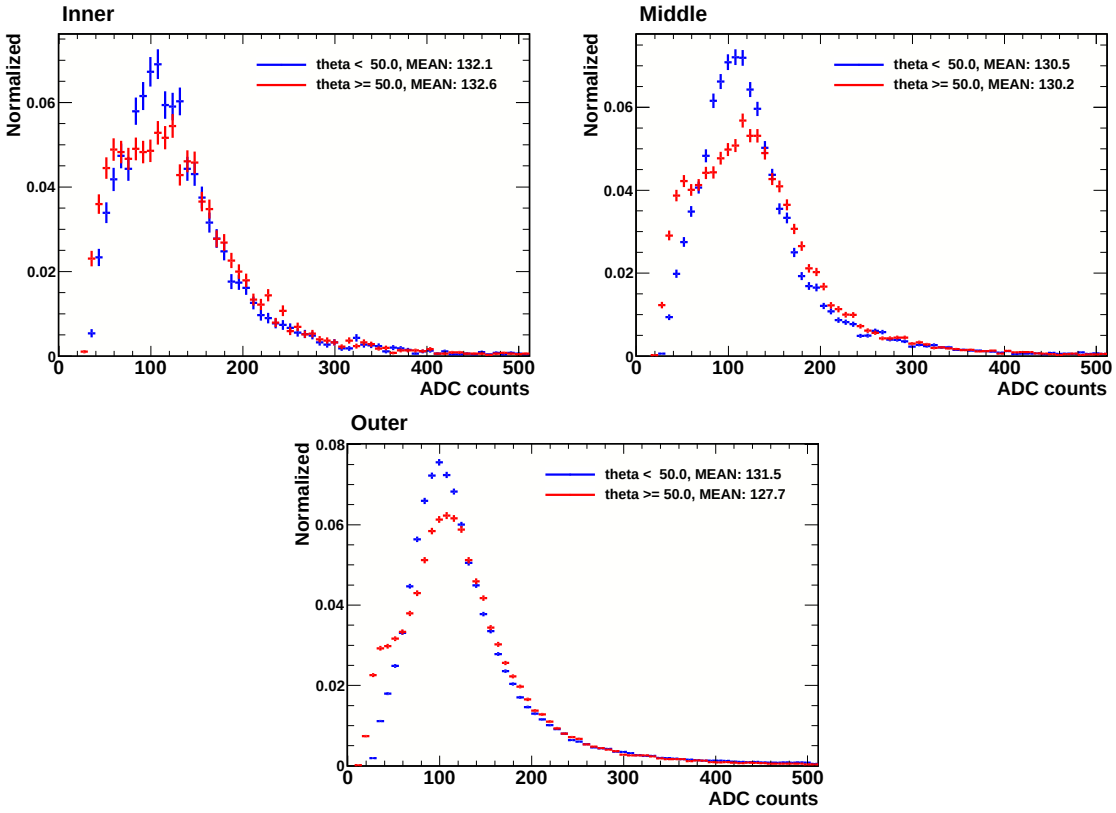

Figure 4.19: *Distributions of the energy deposit of minimum ionising particles obtained with cosmic rays data sample for different regions of the preshower detector. Two histograms for each region are plotted, depending on the zenithal angle of arrival of the cosmic particle θ. Blue points correspond to $\theta < 50°$. Red points for $\theta \geq 50°$.*

4.4.5 Results

One fit for each detector channel was performed. The global results of the most probable value of energy deposit for MIP are presented in the figure 4.20. The basic understanding of the results is that they represent within the precision based on 2009 cosmic events statistics how well was the pre-calibration done in 2008. As one can observe, the spectrum of MPV varies between regions, but it is similar for both sides of the detector. For the inner region MPV covers very wide range of values (RMS 17 ADC counts for the C side and 19 ADC counts for the A side). For the middle the spread is a bit lower (RMS 16 ADC counts for the C side and 16 ADC counts for the A side). The outer part presents a structure different from the other: most of the fit values are centred around (90 $\pm$ 10) ADC counts, while there is also a second

Region	Mean σ_{MPV} (ADC count)	RMS of σ_{MPV} (ADC count)
C side		
Outer	2.60	0.97
Middle	5.7	1.8
Inner	9.8	3.9
A side		
Outer	2.83	0.98
Middle	6.0	1.7
Inner	11.3	3.9

Table 4.2: *Uncertainty of the MPV fit result obtained during the calibration with cosmic rays.*

Gaussian like part for high MPV values ($120 - 130$ ADC counts). This is the result of different high voltage settings set in the precalibration, as it can be seen in the figure 4.20.c), where board structure exhibits.

As the statistics differs from one region to another, it can be predicted that the precision of the fit varies with similar pattern. The distributions of the uncertainty of the MPV value σ_{MPV} of the fit are given in the figure 4.21. The extraction of the mean and RMS values of these distributions is available in the table 4.2. From these values, one can conclude that average precision of the extraction of the MPV values (due to statistics) for the outer region is $\sim 3\%$, for the middle $\sim 6\%$ and for the inner $\sim 11\%$.

4.4.6 Numeric gains

Numeric gains assigned with 2009 cosmic events statistics are shown in the figure 4.22. A global distribution of numeric gains by side is shown in the sub-figure a) and b), while the values for each cell are shown in 2D plot in the sub-figure c). The inner region numeric gains assigned in 2009 cosmic calibration procedure are often at the limit, it means that they are equal 1 or 2. It is the result of low statistics for the inner, and thus large uncertainties of the fit results and large spread of MPV values.

A comparison between numeric gains from the precalibration and the cosmic rays calibration from 2009 is given in the figure 4.23.

4.5 Inter-calibration with collisions

4.5.1 Calibration used in 2010

4.5.1.1 MIP selection

This calibration was performed with the first collision data registered in 2009. Two approaches to selecting minimum ionising particles were examined:

- Requiring a hit in the SPD in fron of the PRS cell. One can use it with raw data written on the tape.

(a)

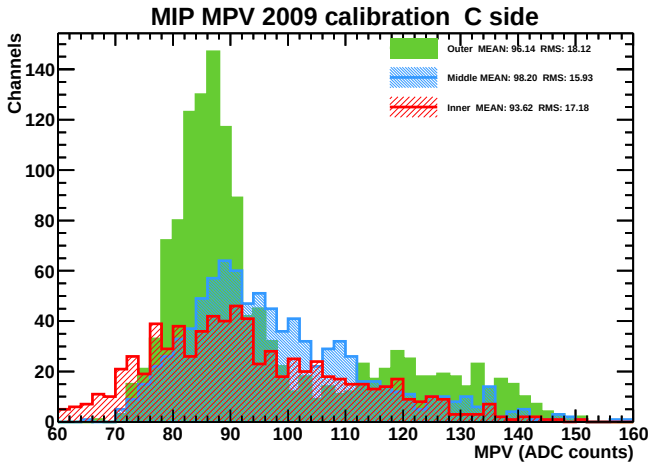

(b)

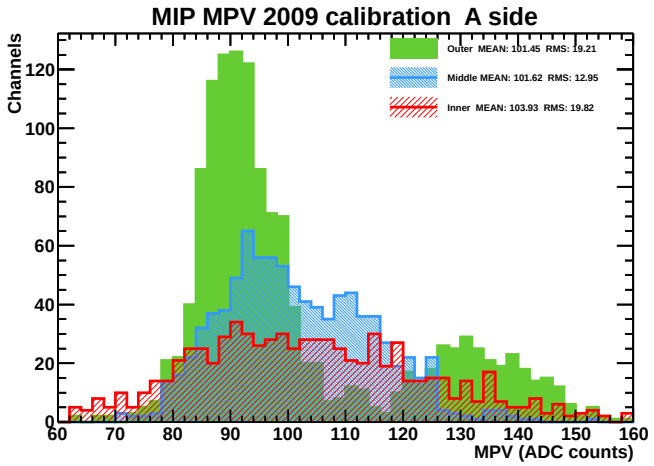

(c)

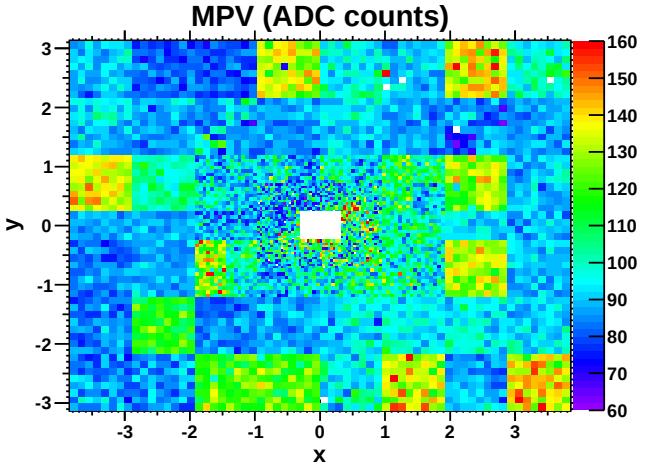

Figure 4.20: *Distributions of the most probable values of the energy deposit in terms of ADC counts electronic output for minimum ionising particles obtained from the fit of the model (distribution: Landau convoluted with Gaussian) based on 2009 cosmic rays statistics. (a) C side, (b) A side, (c) 2D view of the whole PRS detector.*

(a)

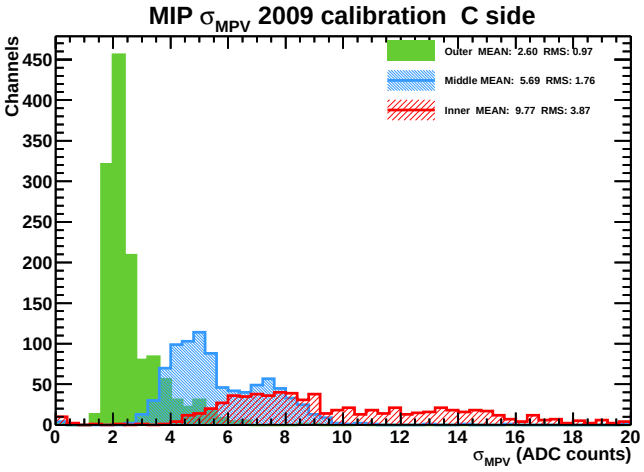

(b)

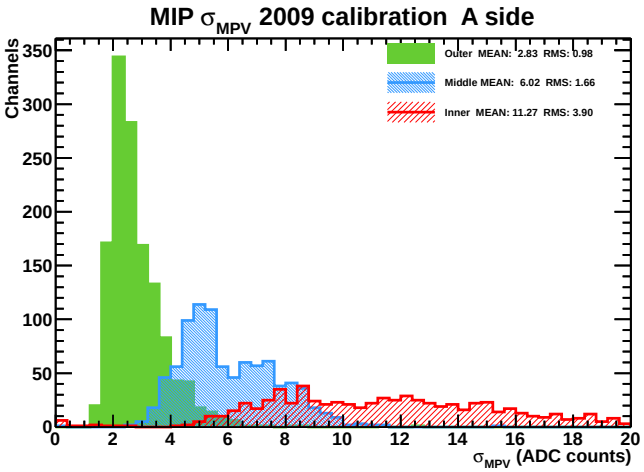

Figure 4.21: *Distribution of the uncertainty in ADC counts of the extracted MPV value for each PRS channel from the fit of the model to 2009 cosmic rays data.*

(a)

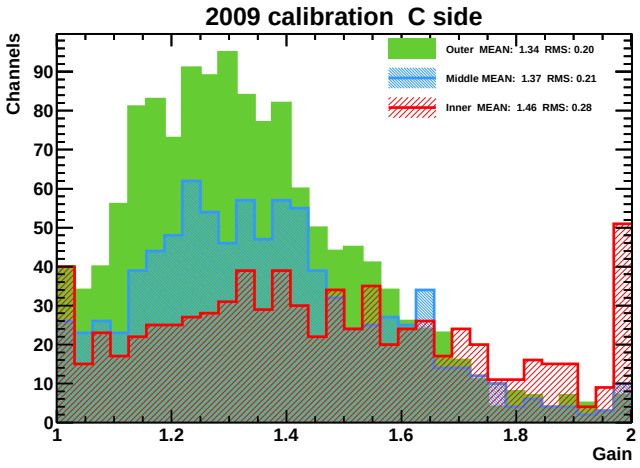

(b)

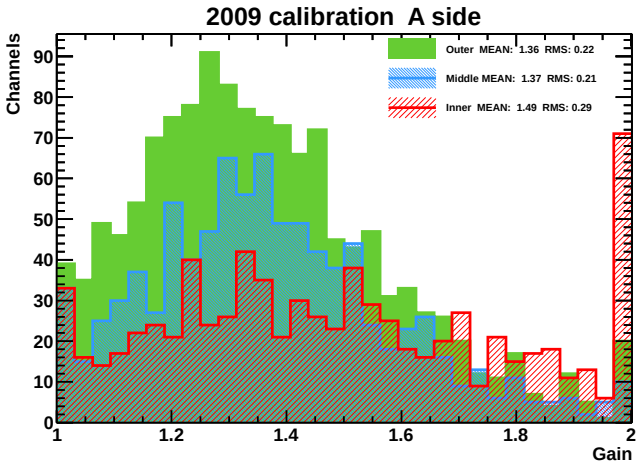

(c)

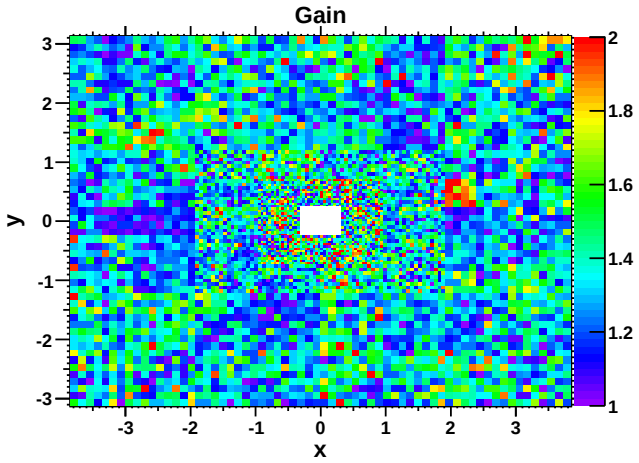

Figure 4.22: *Numeric gains assigned during 2009 calibration with cosmic rays by sides: C (a) and A (b), and in 2D view for each cell (c).*

(a)

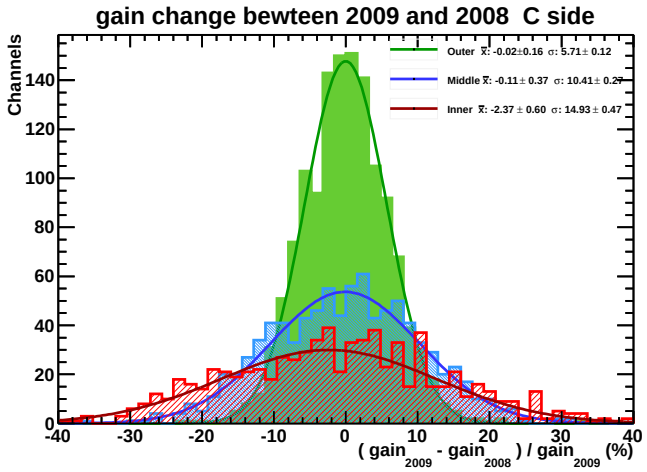

(b)

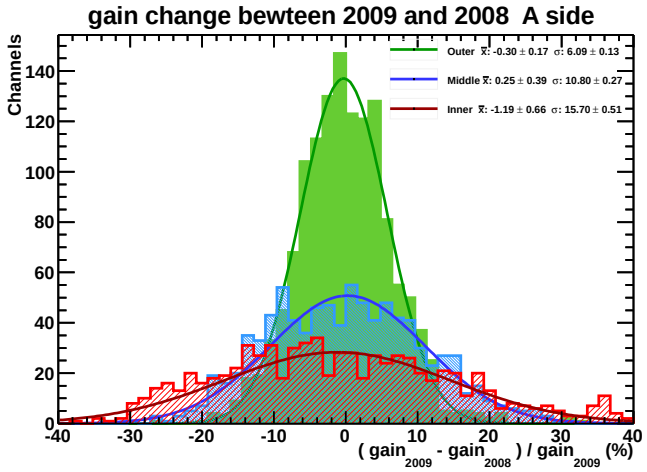

(c)

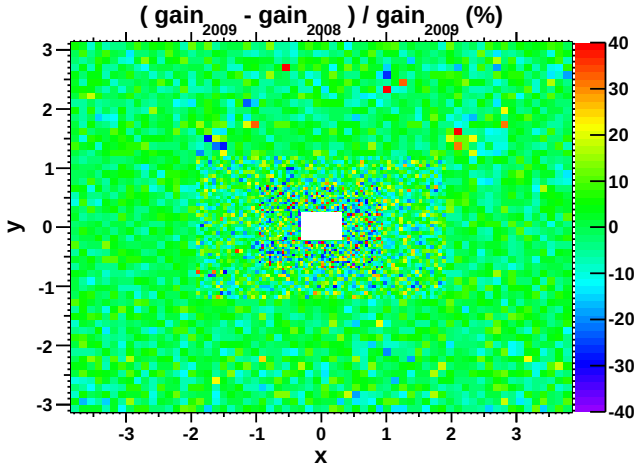

Figure 4.23: *Comparison between numeric gains assigned in processes of calibration done in 2008 and 2009.*

- Requiring a single track pointing at the PRS cell. It requires reconstructed data for track selection.

The first method can be used to scrutinise the data, when the fully reconstructed events are not available. However, this selection accepts also significant amount of mild electromagnetic background, while the selection with tracks do not suffer from this background. The charge histogram comparison of the two selection for an example channel is given in the figure 4.24. For the calibration described in this section, the selection with a single tracks pointing at the preshower cell was used. The average statistics of selected tracks per board is presented in the figure 4.16.

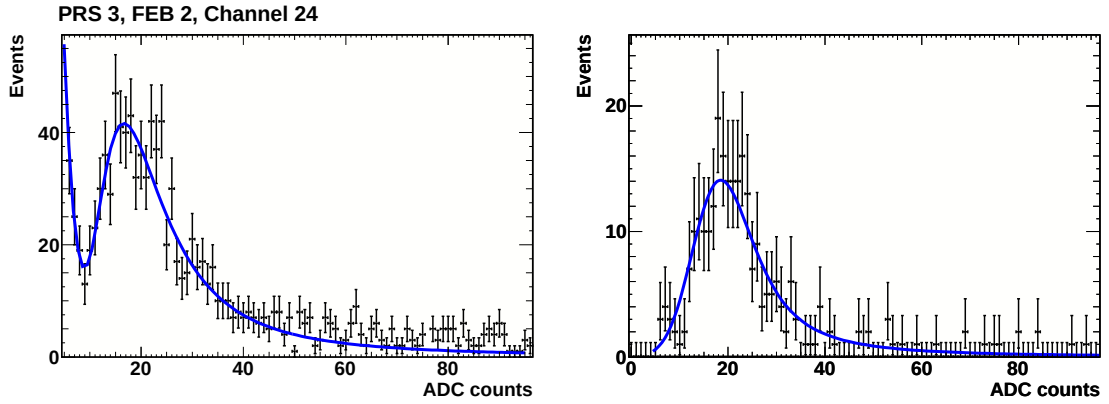

(a) SPD in front of PRS (b) A track pointing to a PRS cell

Figure 4.24: *Two distributions of energy deposit in a PRS cell: (a) requiring that for each signal in the PRS cell there is a cell of SPD detector which is fired, (b) requiring that for each signal in the PRS cell there is a single track pointing at that cell. The fits are performed: (a) exponential (electromagnetic background) plus Landau, (b) Gaussian convoluted with Landau.*

4.5.1.2 Description and results

This calibration was performed without splitting for different bunch crossing parities due to low statistics available. Signal in one 25 ns time interval (T0) was used. No track length inside cell correction was applied. The results of the fit of the MIP deposit model in terms of MIP MPV, by sides, are given in the figure 4.26. The average values are summarised in the table 4.3.

The average response varies between the regions. These differences have two reasons:

- The systematic errors in the track length correction used in the calibration with cosmic rays (section 4.4.4).

- No track length correction applied in the described calibration. From the simulation (figure 4.27) it is expected, that the difference between the inner and the outer in the response for MIP is $\sim 10\%$ without this correction.

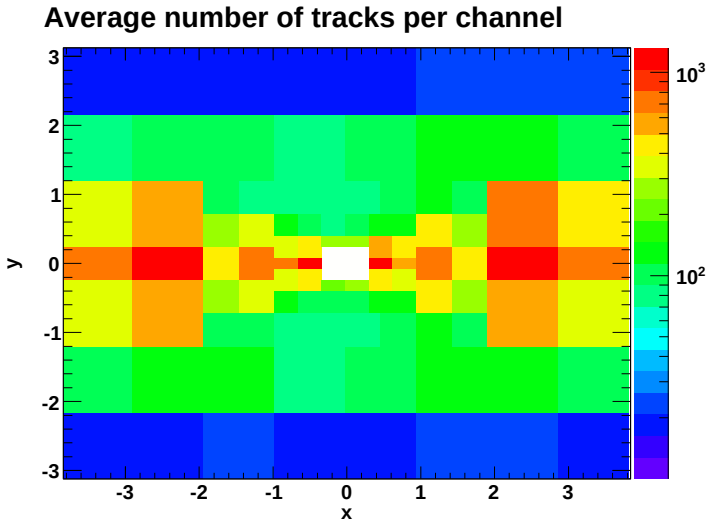

Figure 4.25: *Average number of tracks per preshower cell for each front-end board of the detector available from the first collision data collected in 2009.*

	C side		A side	
	μ_0 (ADC counts)	σ_μ (ADC counts)	μ_0 (ADC counts)	σ_μ (ADC counts)
Outer	24.03 ± 0.07	2.35 ± 0.06	23.22 ± 0.08	2.84 ± 0.07
Middle	21.82 ± 0.07	1.93 ± 0.05	20.21 ± 0.10	2.70 ± 0.09
Inner	20.21 ± 0.11	2.70 ± 0.09	18.22 ± 0.12	2.69 ± 0.09

Table 4.3: *Parameters of the distributions of the MPV MIP deposits in the preshower cell by minimum ionising particles obtained with requirement for a track pointing at the preshower cell.*

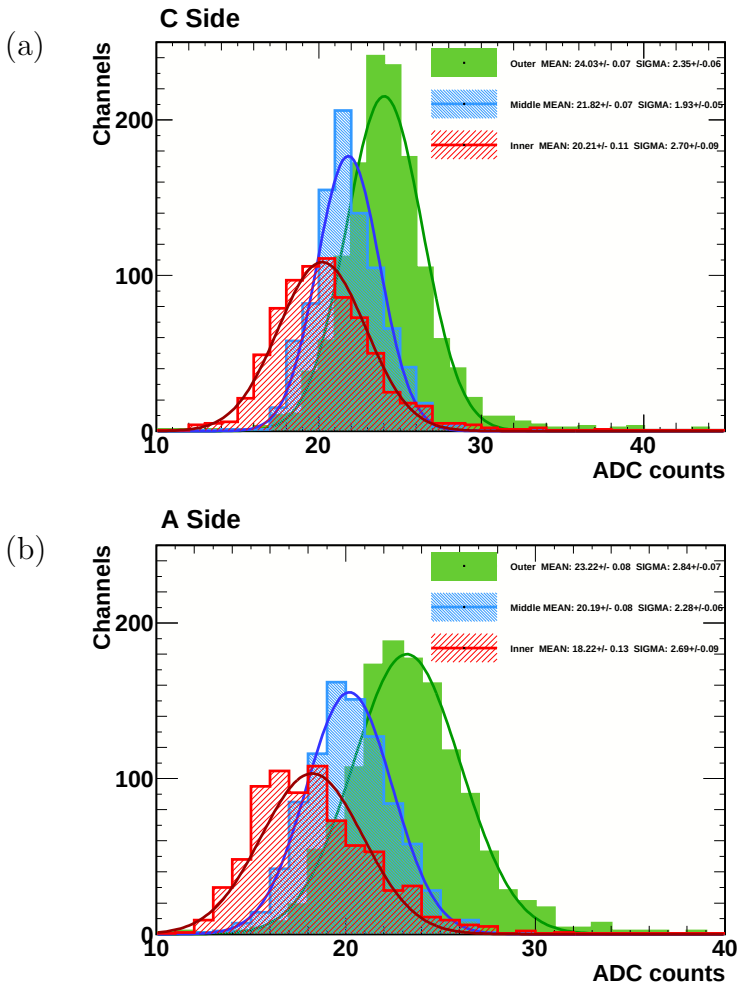

Figure 4.26: *Distributions of the most probable value of the energy deposit of minimum ionising particle in a cell of preshower detector obtained from the fit of the convolution of the Landau and the normal distribution. A single track pointing at the preshower cell is required.*

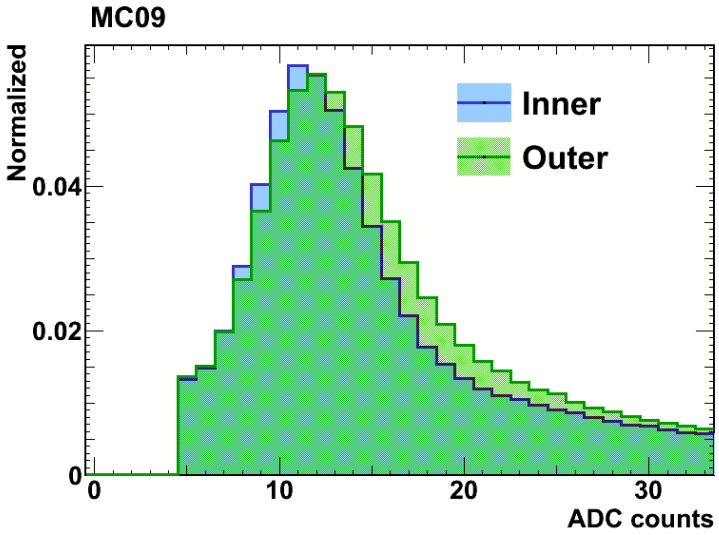

Figure 4.27: *Distribution of the energy deposit inside a calorimeter cell for two regions: blue – inner, green – outer. The data sample used for plotting is the Monte Carlo minimum bias sample MC09. MIP MPV value used in the generation was 10 ADC counts. A signal in the SPD cell in front of the preshower cell is required. The most probable value of the deposit of minimum ionising particles is larger for the outer than for the inner. It is a result of longer track lengths of particles inside outer cells than inside inner cells.*

4.5.1.3 Numeric gains

New numeric gains were assigned for all boards except the most top and most bottom boards in the outer region, where the average statistics (below 50 events per cell) did not allow to be more precise than with the calibration with cosmic rays. The new numeric gain values are presented in the figure 4.28. Already from the distribution of the numeric gain values it is visible, that this calibration performance is better than the previous calibration with cosmic rays. When one compares the distributions with the plots from the calibration with cosmic rays (figure 4.22), one can observe, that in the new calibration the spread of assigned values of the numeric gains is much lower in the inner region than it was previously. It is also less common to have assigned the border value of 1 or 2. It means, that the precision inside the inner region with this calibration is better.

4.5.2 Software corrections used in reconstruction of 2010 data

A check of the calibration used in 2010 was performed in April 2010. The statistics used was the first 9 million of minimum bias events registered in 2010. This corresponds to 28 millions of tracks. The objective of this check was to produce a set of corrective coefficients put in the database, which would be used in the reconstruction of events during reprocessing. The software allowed for a single corrective factor per cell, so bunch crossing parities were not split.

The calibration was done with tracks. Track length corrections were applied. For

(a)

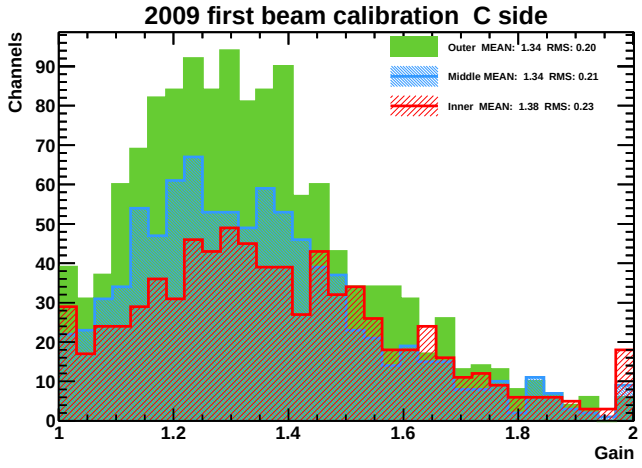

(b)

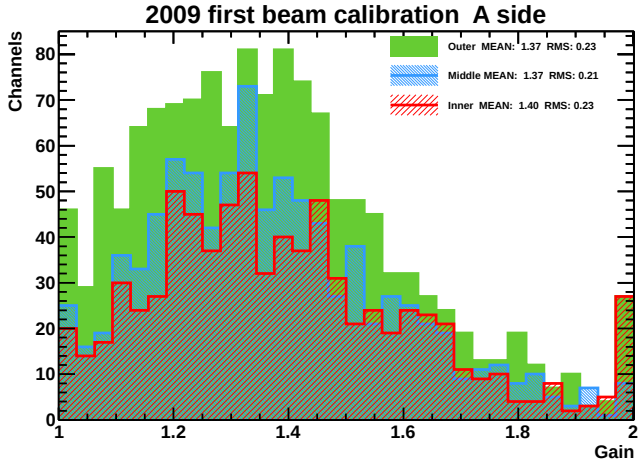

(c)

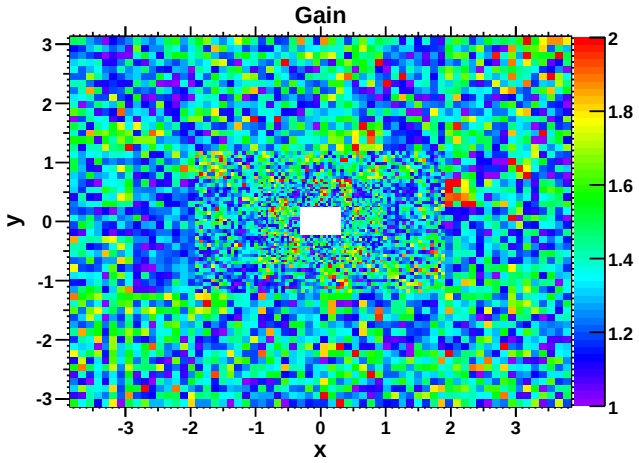

Figure 4.28: *Numeric gains assigned during calibration with first collisions of proton beams in 2009 sides: C (a) and A (b), and in 2D view for each cell (c). The numeric gains for the top most and the bottom mostrows of front-end boards of the outer region are taken from the calibration with cosmic rays.*

(a)

(b)

(c)

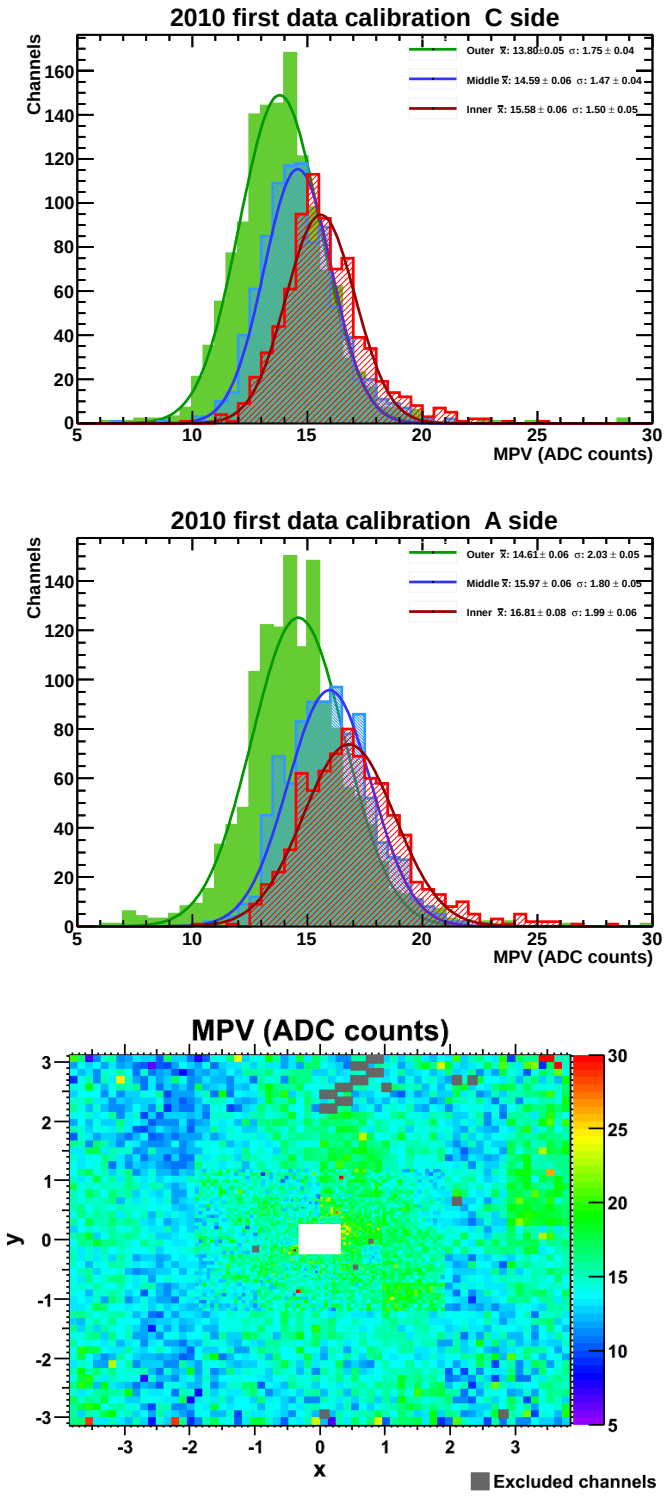

Figure 4.29: *Most probable values of energy deposit of minimum ionising particle extracted from fits by regions with the first 28 millions of 2010 data.*

Region	MPV (ADC count)	σ_{MPV} (ADC count)	σ_{MPV}/MPV
C side			
Outer	13.80 ± 0.05	1.75 ± 0.04	12.7%
Middle	14.59 ± 0.06	1.47 ± 0.04	10.1%
Inner	15.58 ± 0.06	1.50 ± 0.05	9.7%
A side			
Outer	14.61 ± 0.06	2.03 ± 0.05	13.9%
Middle	15.97 ± 0.06	1.80 ± 0.05	11.3%
Inner	16.81 ± 0.08	1.99 ± 0.06	11.8%

Table 4.4: *Characteristic parameters of the distributions of MPV of MIP energy deposit by channel obtained with the first calibration with 2010 data.*

each channel a distribution of a convolution of a Gaussian and a Landau was fit. The results of the fit in terms of the most probable value of Landau are presented in the figure 4.29. To each distribution presented in the figure a fit of a Gaussian distribution is made. The results of these fits are given as the table 4.4.

The systematical shift between regions is the result of the high voltage change between the years 2009 and 2010. The results allow to conclude that the calibration of the detector used in 2010 (inside the electronics) was between $9.7\% - 13.9\%$, depending on region.

4.5.3 Calibration used in 2011

4.5.3.1 Description and results

The calibration used in 2011 was performed during winter 2010/2011. The best knowledge of the detector was used with proper corrections applied. The statistics used was more than 170 millions of minimum bias events from *Reco5Stripping9* data tag. Even if at that time there were more recent versions of reconstruction available, due to minimum bias pre-scaling the available statistics was lower. Histograms were filled with degained ADC count values, corrected for track length, and split for even and odd bunch crossing number. Fits were performed with a sum of exponential and a convolution of Gaussian and Landau. Finally, the residual pedestals values were subtracted. The results – degained and corrected for the pedestals values – are presented in the figure 4.30.

4.5.3.2 Numeric gains

The next step, exactly as in the previous calibrations, was the assignment of numeric gains, but independently for even and odd bunch crossing. The procedure looks exactly the same but effectively there is two times more channels to assign gains, because each channel is counted twice: with even MPV and odd MPV. The figure 4.31 shows the distribution of the numeric gains by region and bunch crossing id parity.

The plots containing numeric gains are given in the figure 4.32. They are the final proof that splitting by bunch crossing number was a indispensable for the calibration.

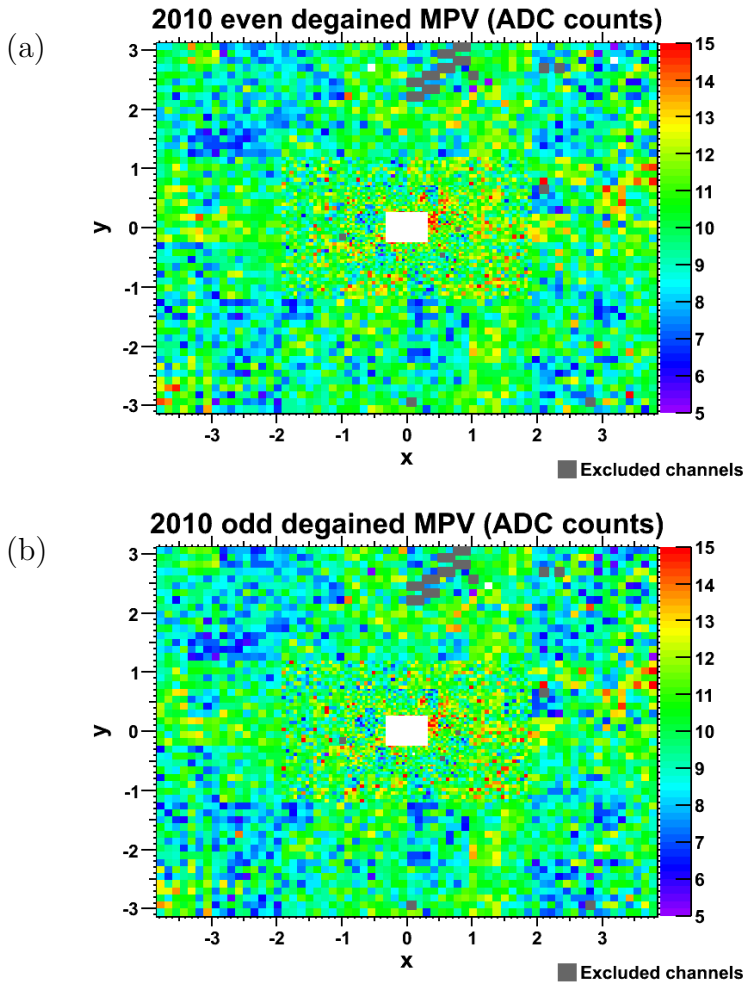

Figure 4.30: *Degained most probable value of minimum ionising particle deposit for preshower channels (in ADC counts) split by even (a) and odd (b) bunch crossing parity.*

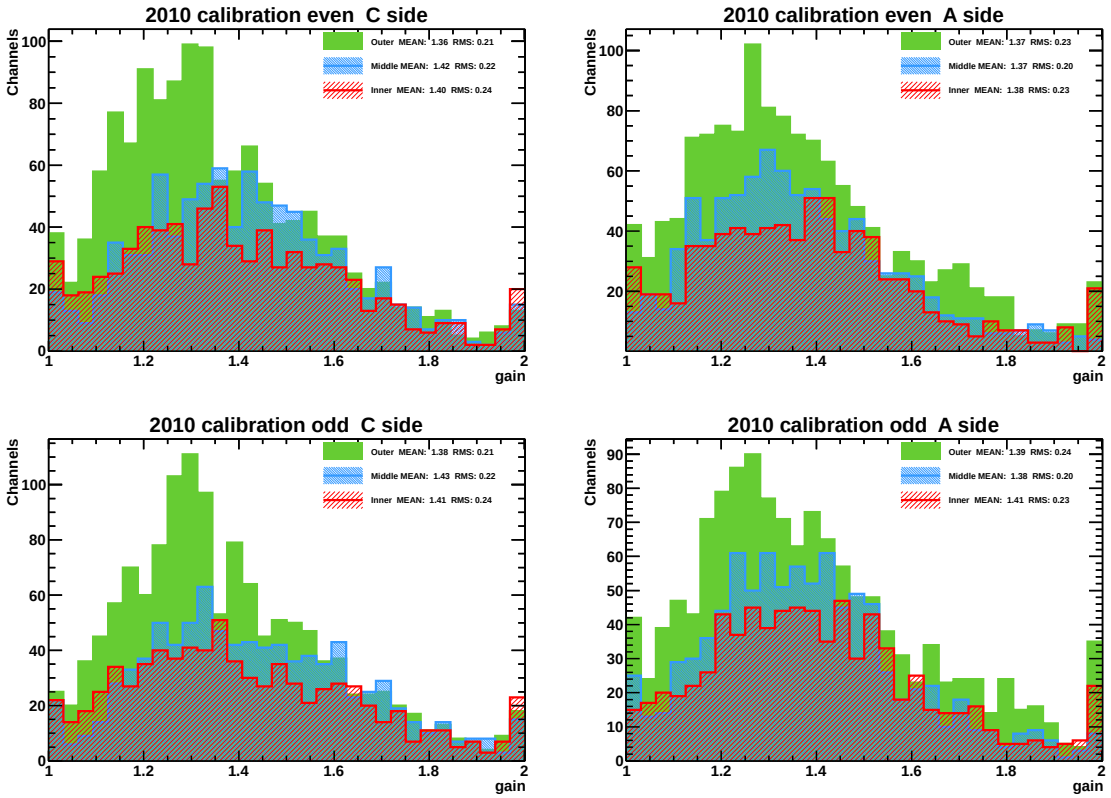

Figure 4.31: *Numeric gains by region assigned during 2010 calibration. The top row shows the results for even bunch crossing number, the bottom row is for odd numbers.*

The figure shows correlations between even and odd numeric gains assigned during 2010 calibration split for six regions of the detector. The results indicate large correlations between the numeric gains – which is expected. However there is a fraction of points which lay in a non negligible distance from the diagonal. Additionally they show that some regions like the outer C and the inner A are almost perfectly correlated (more than 95%), while the middle C is only at 73% correlation. Because all known corrections which can make such large difference were taken into account during 2010 calibration, it is very surprising that kind of conspiracy for certain regions. It suggests that the problem lies in the hardware. There are many possibilities and because of the limited access to the detector it is very difficult to examine them. One can be linked to the electronics front-end boards, another may be the cabling. The study of the source of these effects is not finished yet.

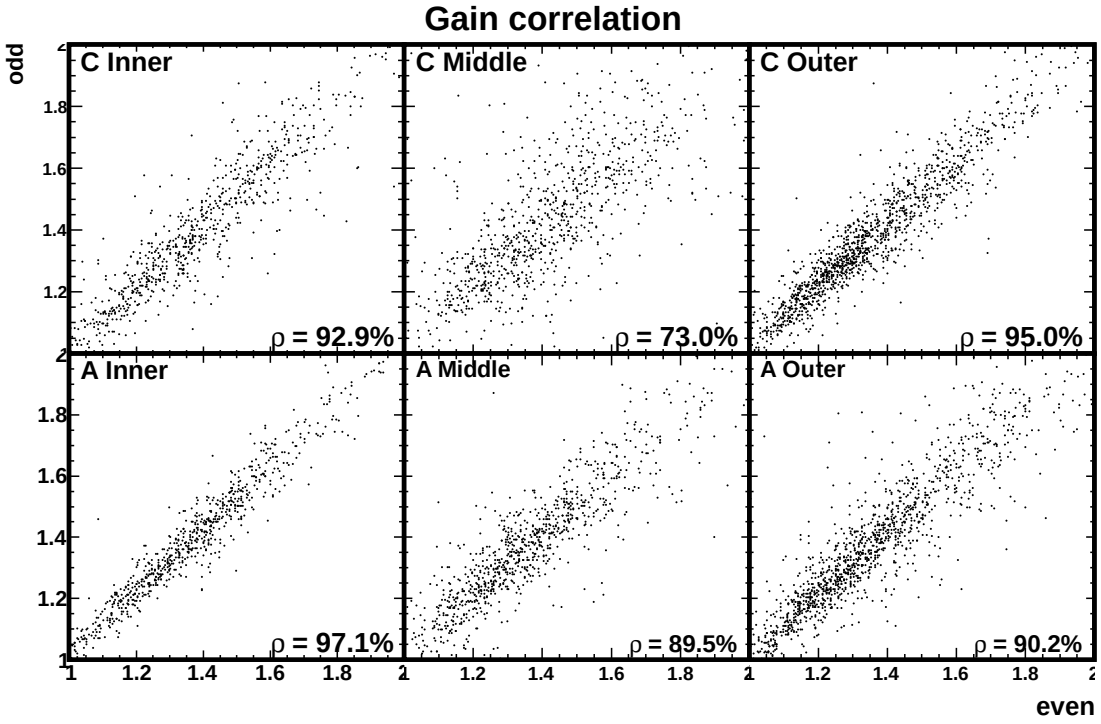

Figure 4.32: *Correlations between even and odd numeric gains assigned during 2010 calibration. Numeric gains of range [1,2] are given for both axes.*

4.6 High voltage settings

The high voltage changes are performed accordingly to the high voltage scaling law described in Appendix A.

4.6.1 Cosmic rays settings

The photomultiplier high voltage settings used for cosmic rays data taking period were chosen to give approximately MPV of 100 ADC counts per MIP. The values for each board (photomultiplier) are presented in the figure 4.33.(a).

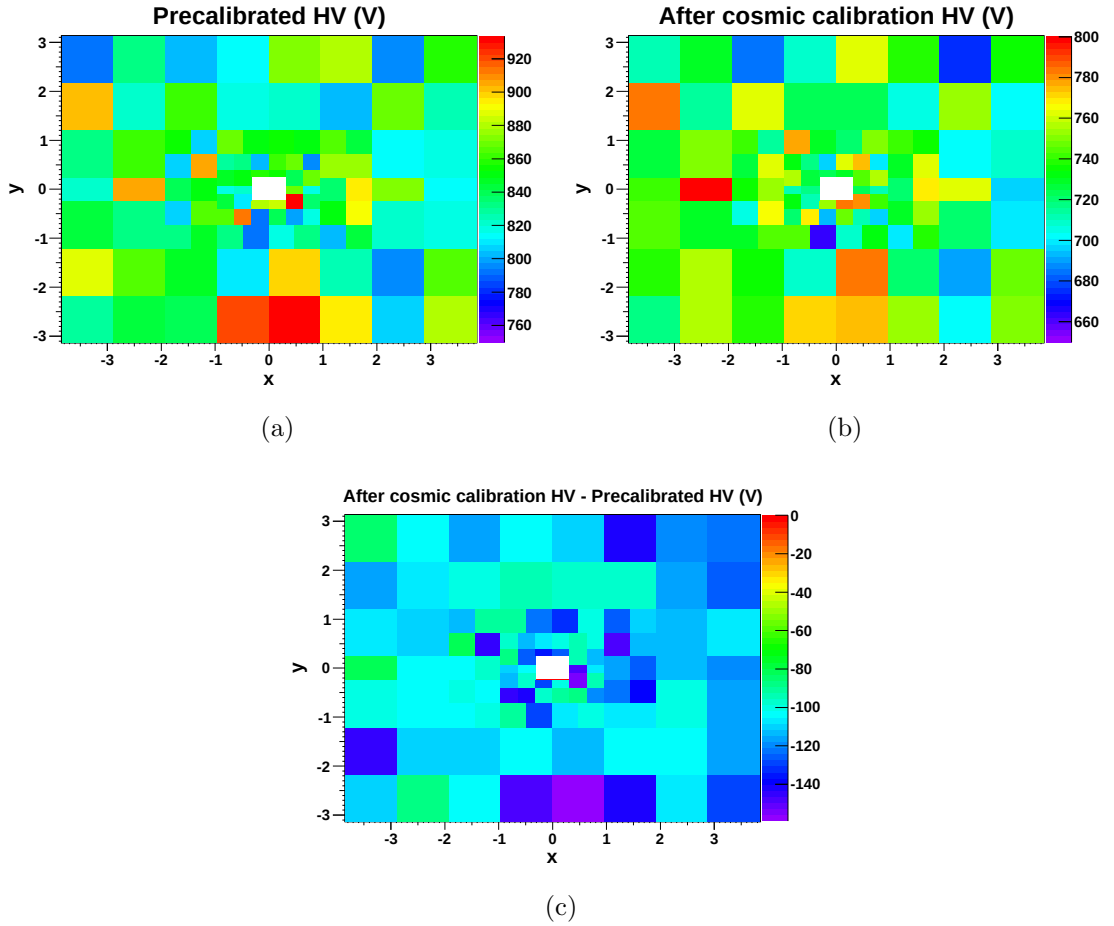

(a) (b)

(c)

Figure 4.33: *High voltage settings before the calibration with cosmic rays (a) – pre-calibration, and after the calibration with cosmic rays (b) – the detector prepared for the first collisions in 2009 with the MPV of* 20 ADC counts *for MIP. The difference between two is shown in the bottom plot (c).*

4.6.2 Settings used in 2009 for collisions

The objective of the calibration with cosmic rays was to set as uniform as possible detector for the first proton beams collision. The target value of the MPV for the calibration used in 2010 was 20 ADC counts in a time gap of 25 ns (T0). To achieve this, the high voltage settings were changed and the settings before and after the change are presented in the figure 4.33. Typically the change was from -140 V to -90 V.

The new high voltage settings for the boards with the shortcut in the LED power supply system (Appendix A) were chosen assuming the average β parameter of the high voltage law. It resulted in the ratio of MPV values per MIP after and before the high voltage change of ~ 0.3. For that value, accordingly to the plot in the figure A.6, the uncertainty of the new calibration due to the shortcut was 4.5%.

4.6.3 Settings used in 2010

High voltage settings prepared for 2010 were initially planed to be a correction to the settings used for the first collisions in 2009. They were based on the average MIP MPV value for each region. The high voltage values, and their change respect to the previous one are presented in the figure 4.34. The correction was overestimated, and thus the MIP MPV values in 2010 were lower than expected 20 ADC count.

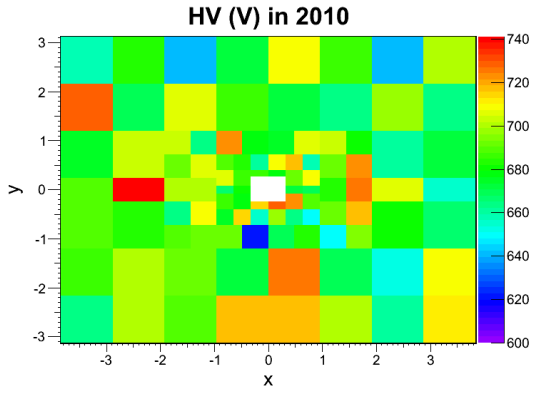

(a)

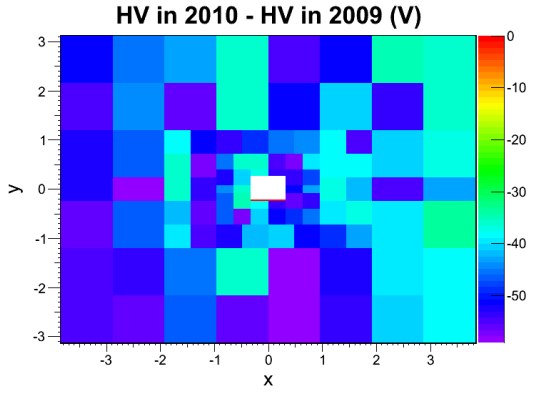

(b)

Figure 4.34: *High voltage settings used in 2010 (a), and the difference between the settings used in 2010 and 2009 for collisions (b).*

4.6.4 Settings used in 2011

The target for the year 2011 was 10 ADC counts which is the nominal designed ADC counts value for the MIP MPV. The figure 4.35 presents the new high voltage settings, extended by the plots of the high voltage change respect to the values used in 2010.

4.7 Energy flow calibration

4.7.1 Method description

Another method of calibration[87, 88] was designed for PRS, ECAL and HCAL. Conversely to the MIP calibration, it can be used with low statistics. The principle of it uses the fact that locally a total energy flow through a small region (and connected with that sum of energies of particles that were registered in the region) should change so slow that in a first approximation it is constant. For a given cell, a sum of the total energies from 9 cells in a cluster of 3 by 3 cells centred at that cell is computed. A calibration factor C^i_{EF} for the cell i is defined as:

$$C^i_{EF} = \frac{\frac{1}{9}\sum_{j \in neighbors} E_j}{E_i} \tag{4.12}$$

However this approach gives a systematic bias at the borders between geometrical regions. To overcome it, an extension to the method was invented. It needs an assumption that the detector is symmetrical, which means that the fluxes for cells: (x, y), $(-x, y)$, $(x, -y)$, and $(-x, -y)$ have to be the same. What can disturb the symmetries and limits the precision of the method are:

- Differences in upstream material in front of the calorimeter.
- Calorimeter plane tilt respect to the beam pipe axis.
- Asymmetries in the magnetic field.

Keeping in mind the limitations, we can look in details to the improved method. A cell located in column m and row n ($cell^{m,n}$) in a reasonable period should gather the same energy as all symmetrical sisters of this cell, so $cell^{-m,n}$, $cell^{m,-n}$ and $cell^{-m,-n}$. m and n are counted from the centre of the detector. A calibration factor for the cell $cell^{m,n}$ is then:

$$C^{m,n}_{EF} = \frac{\frac{1}{4}\left(E_{m,n} + E_{-m,n} + E_{m,-n} + E_{-m,-n}\right)}{E_{m,n}} \tag{4.13}$$

The obtained set of C_{EF} applied to the calibration should make the detector uniform.

4.7.2 Results for calibration used in 2010

Using a method which is a combination of the approaches described above, a check of the preshower calibration was performed. The first took place before the first calibration with minimum ionising particles – effectively showing the performance of initial calibration used in 2010(figure 4.36.a). The second test was performed on the

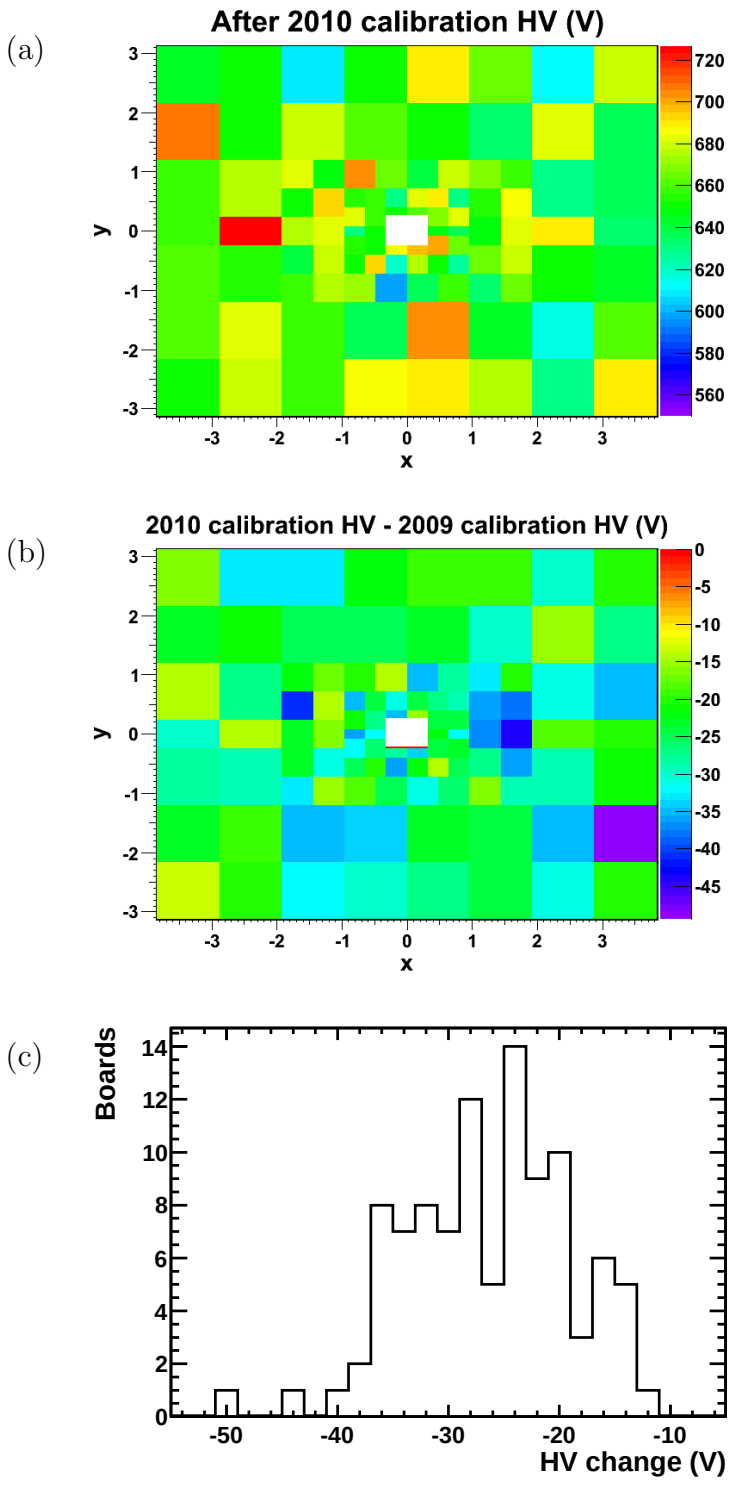

Figure 4.35: *a) High voltage settings used in 2011 (after 2010 calibration). b) and c) Change of the high voltage settings respect to the settings used in 2010 calibration (after 2009 calibration).*

sample with 2010 software calibration applied (figure 4.36.b). The results in terms of mean calibration factor and root mean square are given in the table 4.5. The interpretation is that the energy flow says that 2009 calibration precision was 9.5%, while 2010 software calibration is 6.9%. However it is important to remember that the intrinsic precision of the energy flow method is 4%.

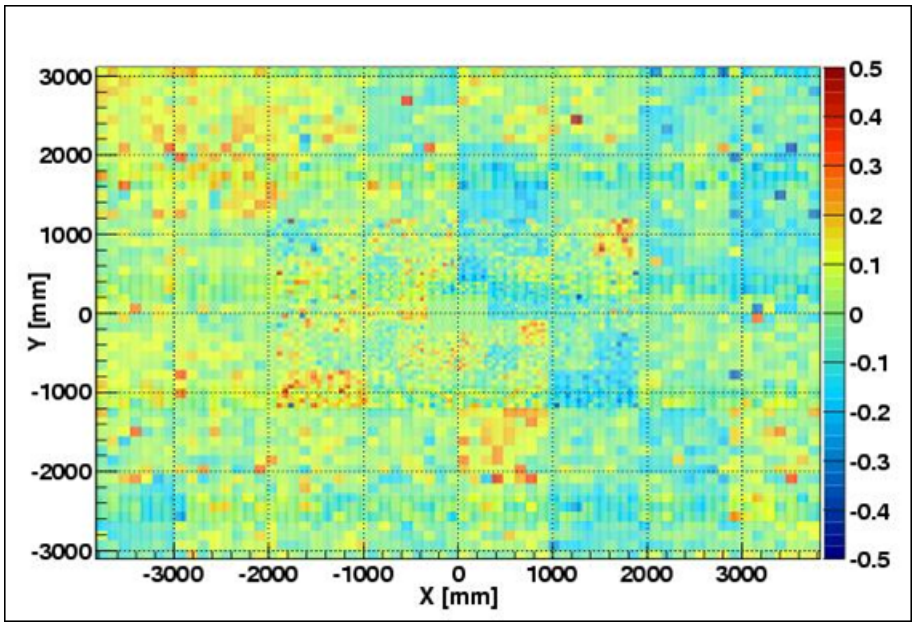

(a) Before calibration with MIP

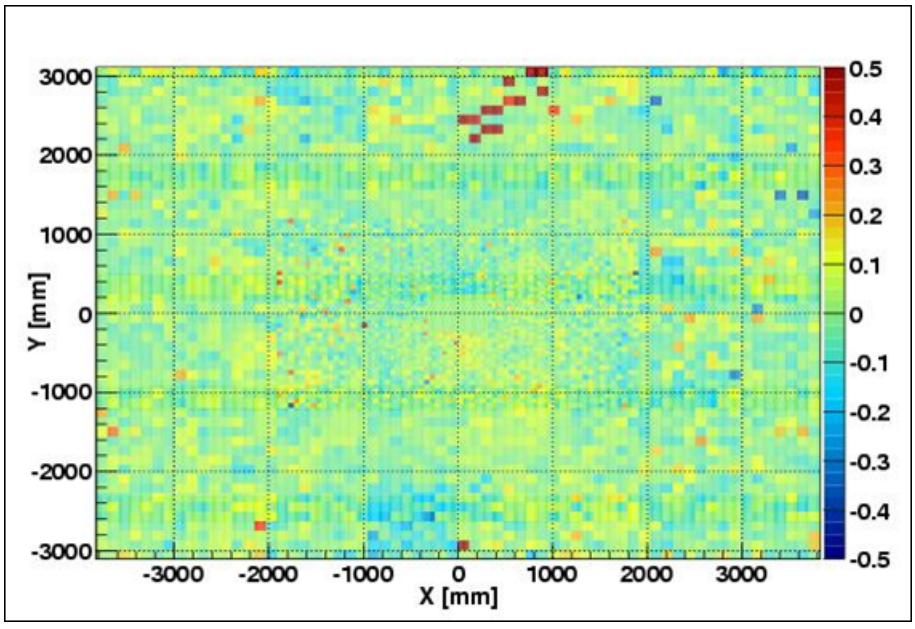

(b) After calibration with MIP

Figure 4.36: *Energy flow cell calibration factors obtained a) before the calibration of the preshower with minimum ionising particles, b) after the calibration with minimum ionising particles. Dark cells in PRS 5 are caused by problematic front-end board which made the calibration of those channels impossible.*

Region	initial 2010 calibration		2010 calibration in the database	
	mean	RMS	mean	RMS
Inner	1.5%	9.9%	0.9%	6.6%
Middle	1.5%	10.6%	0.8%	7.4%
Outer	1.0%	8.5%	0.6%	6.7%
Global	1.3%	9.5%	0.7%	6.9%

Table 4.5: *Energy flow calibration results with 2010 data before and after application of the calibration with minimum ionising particles. The effectiveness of the calibration can be related to the RMS results.*

Region	C side	A side
Inner	64%	77%
Middle	59%	70%
Outer	58%	54%

Table 4.6: *Linear correlation coefficients between the calibration with energy flow and the calibration with minimum ionising particles.*

It is worth to check correlations between the energy flow calibration and the minimum ionising particles calibration. For the comparison 2010 first data were used. The comparison was made for energy flow calibration coefficients and MIP calibration coefficients. A MIP calibration coefficient is defined as a ratio of a difference between measured most probable values of MIP and an average MIP value to a root mean square of MIP most probable values distribution:

$$c^i_{MPV} = \frac{MPV_i - \overline{MPV_{region}}}{\sigma_{MPVregion}}. \tag{4.14}$$

The results are presented in the figure 4.37 and an extraction of the linear correlation coefficients is made in the table 4.6. The correlation between the variables is quite satisfactory, between 54% and 77%. The lowest correlation is for the outer where the spread of energy flow coefficients is larger than MIP MPV calibration coefficients. It is not surprising because we are reaching the intrinsic precision of the method. This allows to conclude that since the MIP calibration is more precise than the energy flow, and the energy flow stated that the software 2010 calibration is not worse globally than 7%, that the real calibration is at least as good as this 7%.

4.7.3 Results for calibration used in 2011

A test of calibration used in 2011 was performed on a sample of almost 2 million of raw events registered on 21.03.2011[89]. Since the energy flow operates on an averages it is not sensitive to even and odd differences. For example, it is not sensitive to an eventual wrong assignment of even and odd numeric gains.

The results of the test are shown in the figure 4.38. One can notice an improvement respect to the previous year, from 6.9% in 2010 to 4.6% in 2011. It is fair to interpret it as a proof that the calibration of the preshower in 2011 was better than 5%.

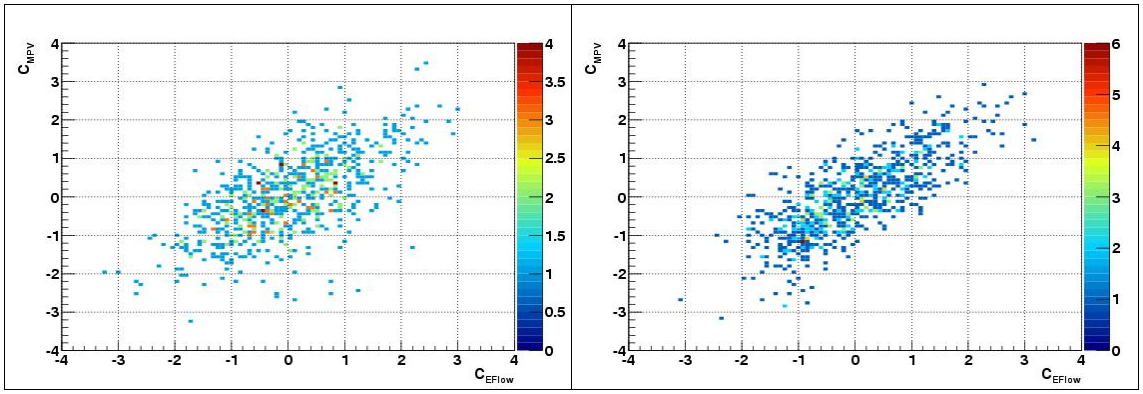

(a) Inner C (b) Inner A

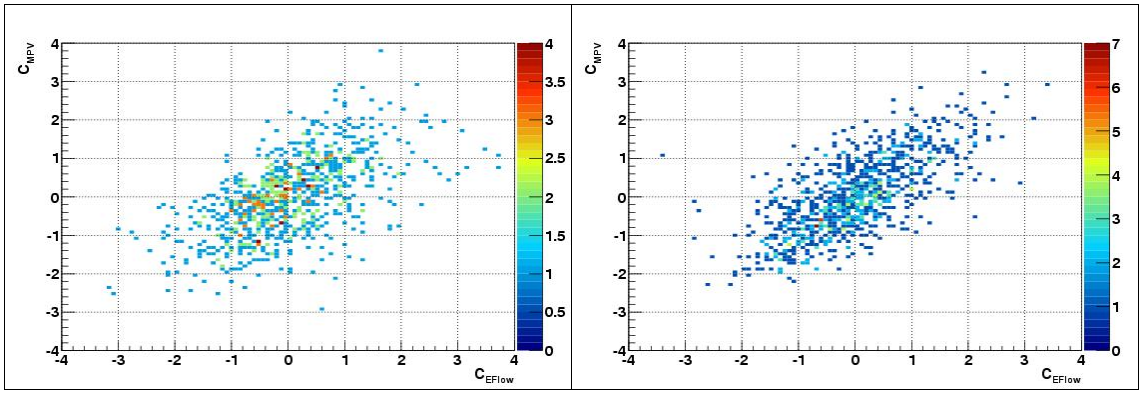

(c) Middle C (d) Middle A

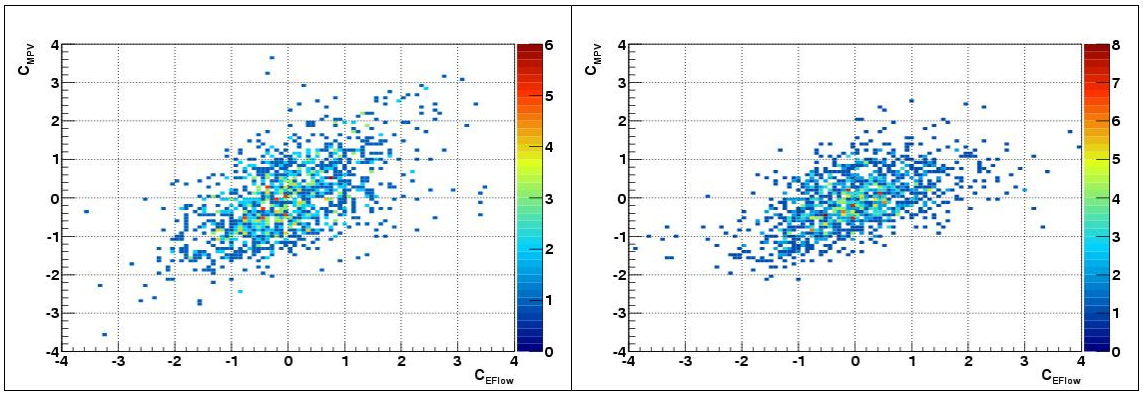

(e) Outer C (f) Outer A

Figure 4.37: *Correlations between energy flow coefficients (horizontal axis) and calibration with minimum ionising particles most probable value coefficients (vertical axis) for six regions of the preshower.*

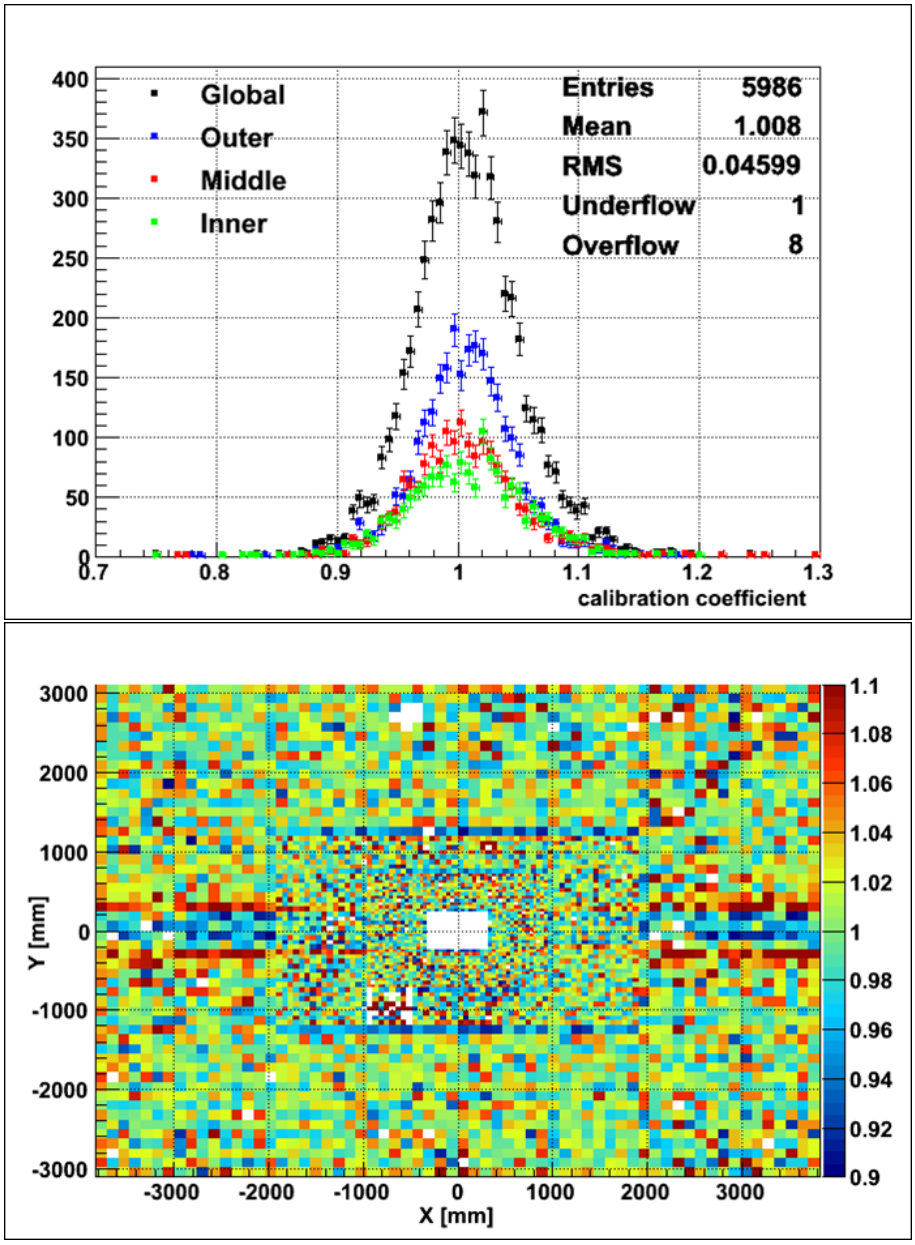

Figure 4.38: *Run 87771 energy flow results.*

4.8 Problematic channels

The detector contains 6016 channels. Almost all of them were working correctly in 2010, but not surprisingly, there were some which failed or behaved strangely. These are the major types of problems spotted in 2010:

- Channels not working – dead channels (figure 4.39.a).
  Two channels[2] like that were found in PRS 7 FEB 7. Almost no statistics was registered for those channels.

- No minimum ionising particle signal shape (figure 4.39.b).
  No Landau-like shape while the number of entries in a histogram is close to the numbers of entries of neighbours. 19 channels spotted. 16 of them in PRS 6 FEB 4 – the problem was due to broken half of a half-board in the front-end electronics. The board was changed during shutdown activities in the beginning of 2011. The rest 3 channels[3] behaviour is not explained.

- Uncorrected pedestals[4] (figure 4.39.c).
  There are two cases in this group. The first group consists of channels for which numbers of entries in the first non-empty bins of energy deposit histograms are not negligible, but the pedestal shape can be fit by an exponential function. Those channels have pedestals not enough separated from the signal range or the pedestal correction applied was to low. The second group are channels for which pedestal values are out of range of available electronics corrections, thus they are irreducible. It appears as a double peek in histograms. The narrower peek, Gaussian shaped is the pedestal shape, the next peek (at larger ADC count values) is the MIP shape.

- Untypical shapes (figure 4.39.d).
  During manual scan of histograms a set of channels[5] was found with shapes more or less different from a Landau-like shape. Usually the distributions had one main peek with some secondary peeks, or the structure was characterised with large fluctuations between neighbour bins. The source of this problems is not known.

Totally, 99.6% of channels were working properly in 2010.

4.9 Monte Carlo studies

4.9.1 Kinematic distributions

It is required that each operation performed during calibration procedure is well understood and completely under control. It means that the behaviour of the detector

[2]Channels: 5569, 5571.

[3]Channels: 3253, 5144, 5433.

[4]Channels with the largest pedestal peeks: 1931, 3627, 3885.

[5]Channels: 1364, 1437, 1510, 1575, 1631, 1668, 1728, 1761, 1819, 1887, 2004, 2095, 2097, 2865, 3796, 3845, 3953, 4204, 4344, 4416, 4418, 4515, 5195, 5199, 5204, 5316, 5340, 5467, 5479, 5493, 5518, 5577, 5594, 5615.

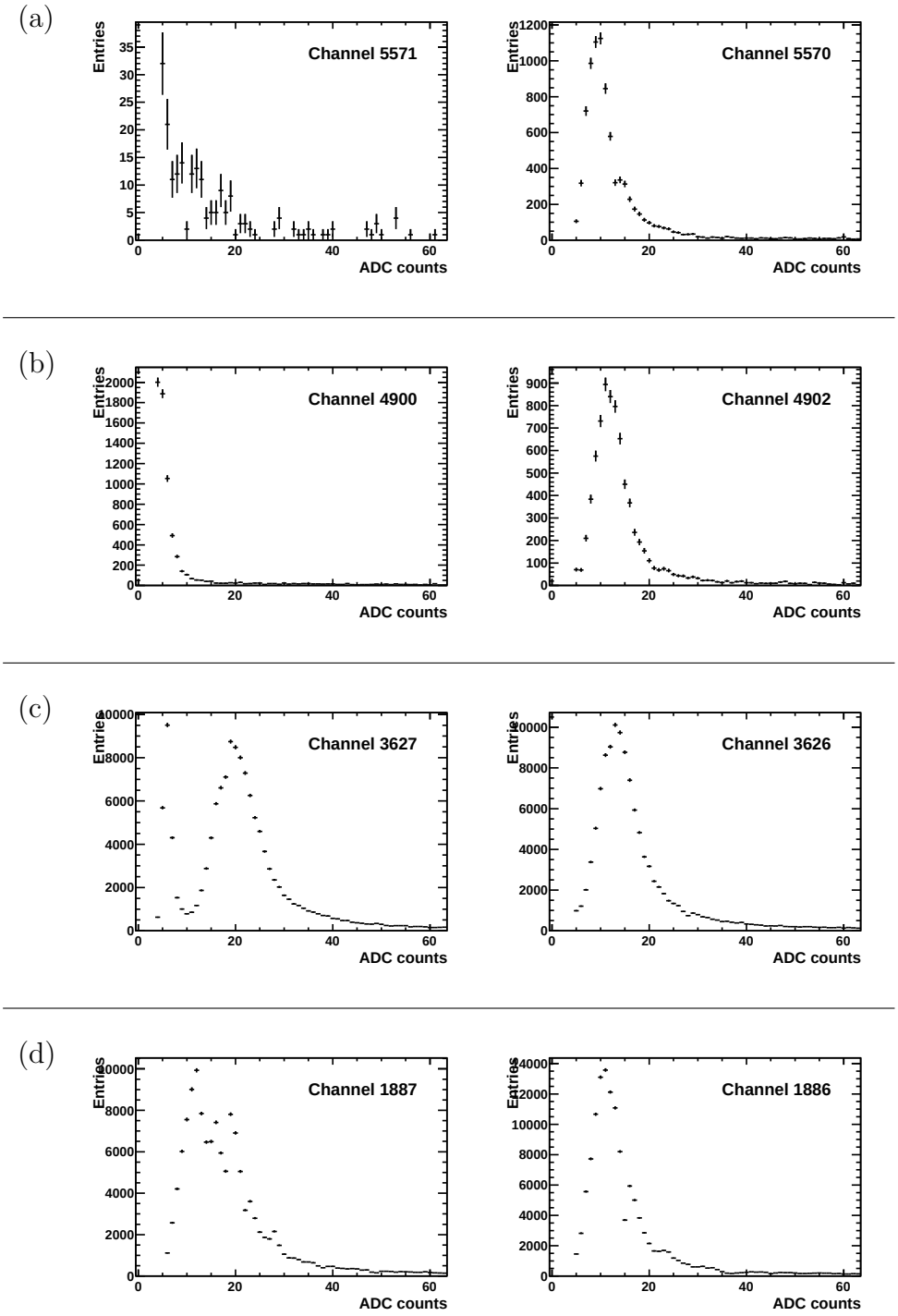

Figure 4.39: *Problematic channel types representatives. In the left column a problematic channel is given, while the right column contains a neighbour of the problematic channel to show as a reference a proper channel shape in the region. Four types of channels were categorised: a) not working, b) no MIP shape, c) uncorrectable pedestals, d) untypical shape.*

is known and every sample of data used for calibration is properly selected and has the properties which are predicted. It needs mastering together the detector and the environment. To be certain that the environment in reality is the same as we think that it is, it is necessary to compare the data with the best theoretical prediction. The best theoretical prediction in case of the LHCb experiment is Monte Carlo, and precisely for the data taken in 2010, a Monte Carlo sample with a common name MC10. The sample used in this analysis is a *minimum bias* sample, which means that there are minimal requirement to save an event. The same cuts are applied to the data. The Monte Carlo is simulated under conditions which are believed to be the best description of the detector with parameters of 2010 data taking period. Precisely, this simulation is parametrised by energy per particle in each beam equal to 3.5 TeV and number of interactions per bunch crossing equal to 2.5. However, there are still possible differences between the reality and the simulation. The largest one is the difference of the multiplicity of particles produced in interactions. The real data shows that this multiplicity is larger than predicted with the simulation. It is observed both in terms of reconstructed tracks and calorimeter occupancy and reflects our poor knowledge of inclusive particle production at these unprecedented energies as well as the background environment of the machine.

The comparison starts from kinematic distributions. The comparison concerns all reconstructed charged protoparticles. The regions are considered separately: inner, middle and outer.

The distributions of momentum are presented in the figure 4.40. The distributions of transverse momentum are shown in the figure 4.41. The first observation is that the distributions are similar in shape. The average momentum decreases from the inner to the outer. It can be explained by the fact that particles are bent in the magnetic field. Particles of the largest momentum are bent less than low momentum particles. It means that particles of the largest momentum are moved more away from the beam pipe. Transverse momentum behaves similarly, because it is correlated with momentum. Lower momentum leaves lower available values of transverse momentum.

When one looks more precisely on the distribution one can discover the fact that the 2010 data distributions are different from the MC10. Spectra are harder in Monte Carlo. It is due to the production, fragmentation and hadronisation processes which were not tuned at these energies. For the calibration process the significance of the differences are not important. First, because the calibration of the preshower doesn't depend on Monte Carlo predictions. Second, the calibration with 2010 statistics is not enough precise to deal with differences due to different momentum spectra.

The distributions presented in the figures 4.40-4.41 are split by regions. One can expect that this division is not enough detailed to show the real structure of momenta distributions in different regions of the detector. It is expected that they change rapidly when moving across the detector because of the magnetic field. The outcome is that different momenta regions "prefer" different detector regions. For six different momenta ranges, a 2D map of number of tracks passing through a cell in a given sample is prepared, one map for each momenta range. Similarly for transverse momenta distributions. The results are presented in the Appendix B, in the figures B.1 and B.2 for MC10 and in the figures B.3 and B.4 for the 2010 data. The conclusion from those plots is that the patterns are similar for the real data and the Monte Carlo.

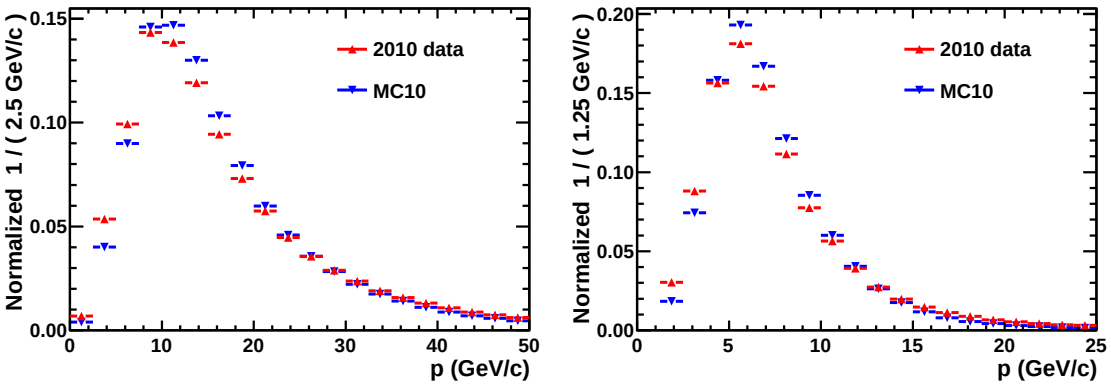

(a) Inner

(b) Middle

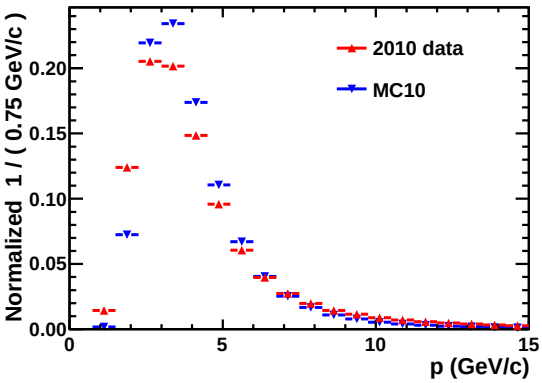

(c) Outer

Figure 4.40: *Distributions of momentum of reconstructed charged protoparticles with 2010 data (red) and Monte Carlo MC10 (blue).*

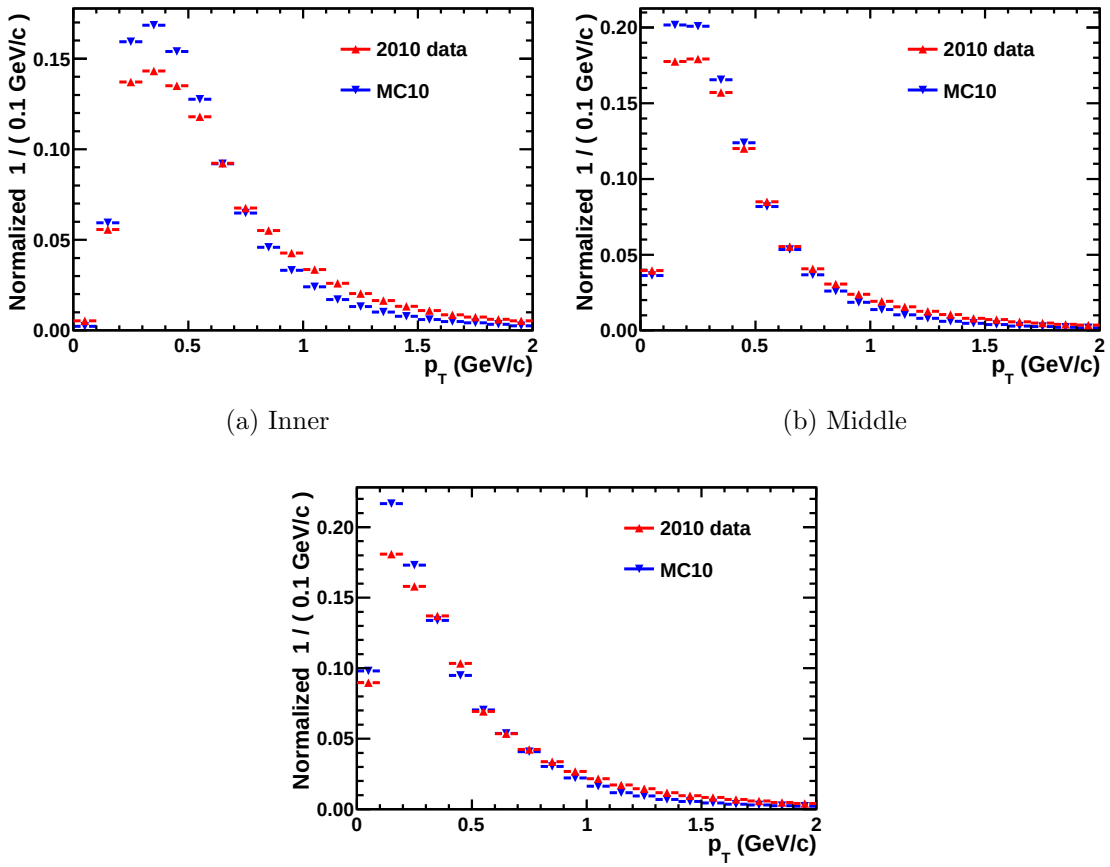

(a) Inner

(b) Middle

(c) Outer

Figure 4.41: *Distributions of transverse momentum of reconstructed charged protoparticles with 2010 data (red) and Monte Carlo MC10 (blue).*

4.9.2 Rounding in track length correction

The procedure of calibration was tested on MC10 minimum bias sample. The same procedure as the one applied to the 2010 collision data was used. It means for each channel a histogram of integrated charge in ADC count was produced. Track by track, length corrections was applied. Then a fit of a sum of exponential and a convolution of Gaussian and Landau was performed. The results – the most probable value of the Landau – interpreted as the most probable value of energy deposit of minimum ionising particles are presented in the figure 4.42. There are different mean values for different regions – it is expected for 2010 simulation and such behaviour was programmed to reflect the real detector status where differences in most probable value of MIP deposits between regions were observed in 2010.

It is expected that the distribution of the MPV values should be normal. The simulation fixes the MPV value, thus the only difference between two channels observations come from uncertainties connected with the method of the MPV extraction. However the distribution of the outer region doesn't look like a normal distribution with a kind of double structure. It is an indication of a systematic error of the method. On the two dimensional plot of MPV as a function of cell location, one can notice a dark blue ring shape centred in the centre of the detector. The ring is stretched slightly along y axis. The MPV values in the ring are lower than for the other areas of the outer part of PRS. The shape like that can be linked with the momentum distributions of particles which are similar (figure 4.40). On the other hand there is no physical reason that such range of momentum which is the most probable in the ring gives almost 10% difference in MPV. There has to be something correlated to the momentum but it can't be the momentum itself. A suspected property is an angle at which particles pass preshower cells.

The zenith angle of crossing a cell (already presented in the figure 4.48 is related to the cell location. Similarly as the momentum is correlated with the location – and thus such similarity between the two. It points to the track length correction formula which can introduce the systematic effects. In fact again everything concentrates on rounding. In a perfect world we would like to apply the correction of length of track directly on a precise analog signal, before analog-digital conversion is applied with it rounding. Unfortunately we can only apply the correction to an integer which is the result of the conversion. When we want to apply any correction to that (like the track length correction) we have to be very careful. When we have a correction which reduces the MPV value only by a fraction of ADC count, then it can't be simply calculated as a rounded difference of the uncorrected value and the correction. A correction should result in putting two fractional inputs into two bins of corrected ADC count histograms with proper weights calculated for each bin. Consider an example in which the electronics response for a track was equal to 18 ADC count, while the correction from the track length not equal to the depth of the cell is equal to 0.6 ADC count. We can't just say that the corrected value is equal to 17 ADC count, which is the rounded result of the difference 17.4 ADC count. We have to put something into the bin of 17 ADC count and something in the bin of 18 ADC count. It tempts to say that "something" has to be a weight of 0.6 in the bin 17 and a weight of 0.4 in the bin 18. This simplest approach is wrong because it assumes that an internal distribution of each bin is flat. While it is not true – for example if we take a bin which is just

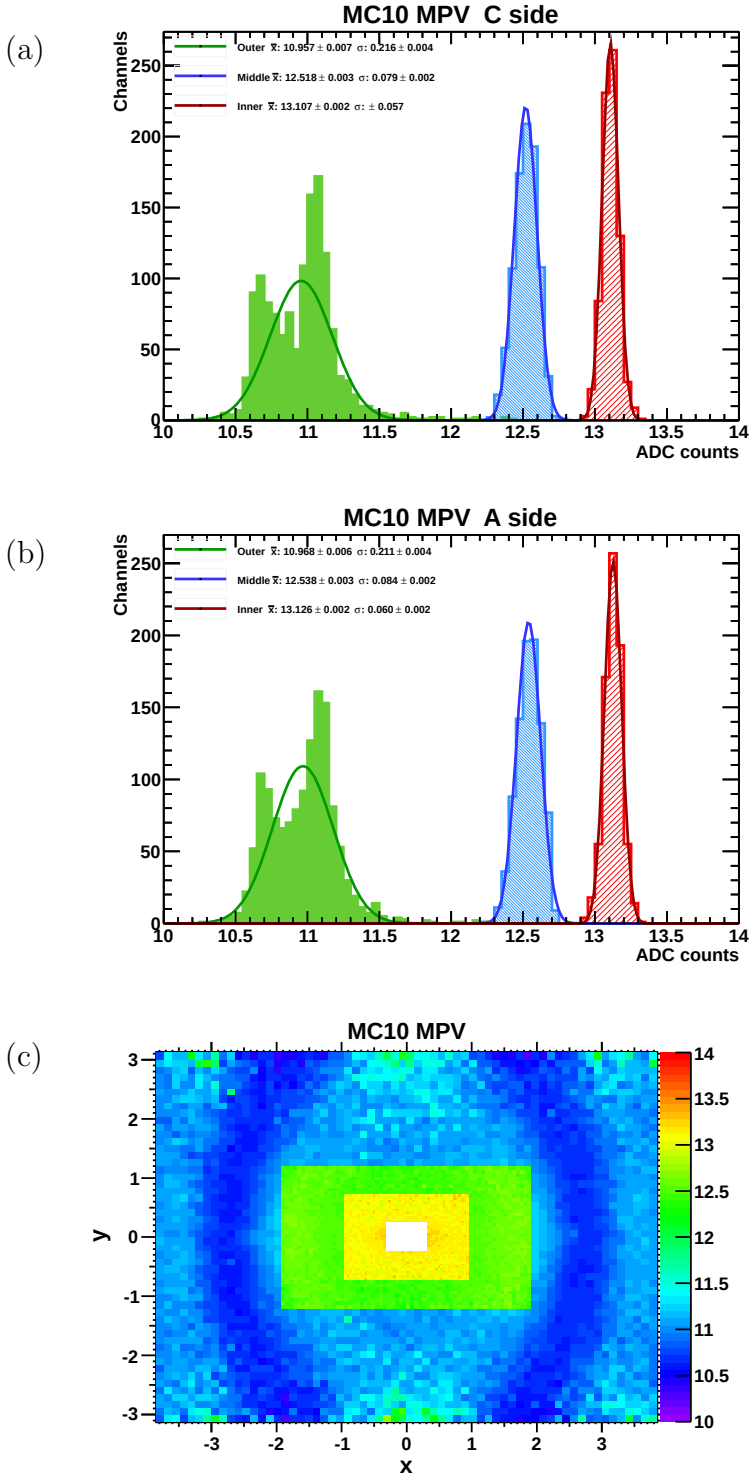

Figure 4.42: *Fit values of MIP MPV obtained from MC10 minimum bias sample with track by track length correction applied.*

after the MPV MIP value it is much more probable that an entry in that bin was closer to the MPV value (so closer to the lower edge of the bin). No matter of the probability everything which is from the left bin edge to the right bin edge is rounded to the value in the centre.

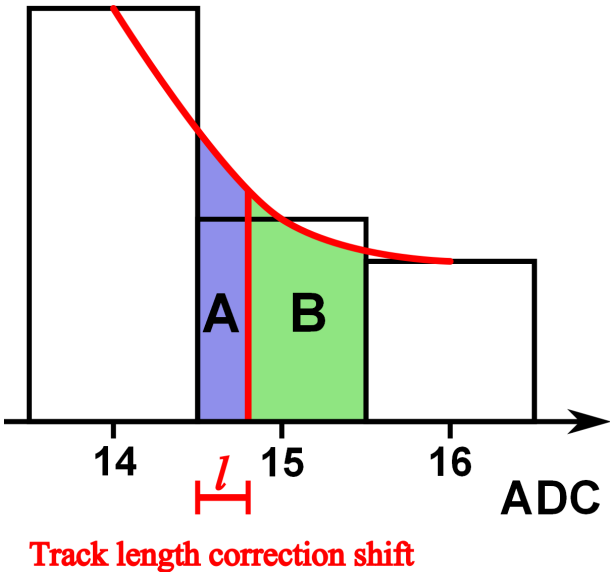

Figure 4.43: *Schematic representation of weighting track length correction accordingly to the correction magnitude. Details of the method are discussed in the text.*

Even if the information about real distributions of the ADC count inside a bin are not accessible, we are still able to guess approximate shapes of the distributions. The principle of the method lies in a fact that the distributions should be continues. For a given bin Z an internal distribution is calculated with a help from neighbour bins. A second order polynomial is calculated from a group of three bins Z, $Z-1$ and $Z+1$. Then it is assumed that internal distribution of Z is realised accordingly to that polynomial. The illustration of the method is presented in the figure 4.43. We can look at the example situation referred in the picture. When a track length correction of l has to be applied to bin of 15 ADC counts, then it is considered that the area proportional to the area A on the picture has to be shifted to bin 14, and the rest – the area proportional to the B has to remain in 15. In other words, corrected track entry will consist of two inputs:

- into bin 14 of the weight equal to $A/(A+B)$,
- into bin 15 of the weight equal to $B/(A+B)$.

That way a proper normalisation is assured.

With the new correction applied to the Monte Carlo, the calibration seems to work much better (figure 4.44). The distributions of MPV values of MIP are much sharper than before and the ring of low values is not present anymore. The two dimensional plot shows a perfect uniformity.

This new, weighted track length correction has not been used yet in the calibration. It will be used in the future calibration. In the results presented in this document,

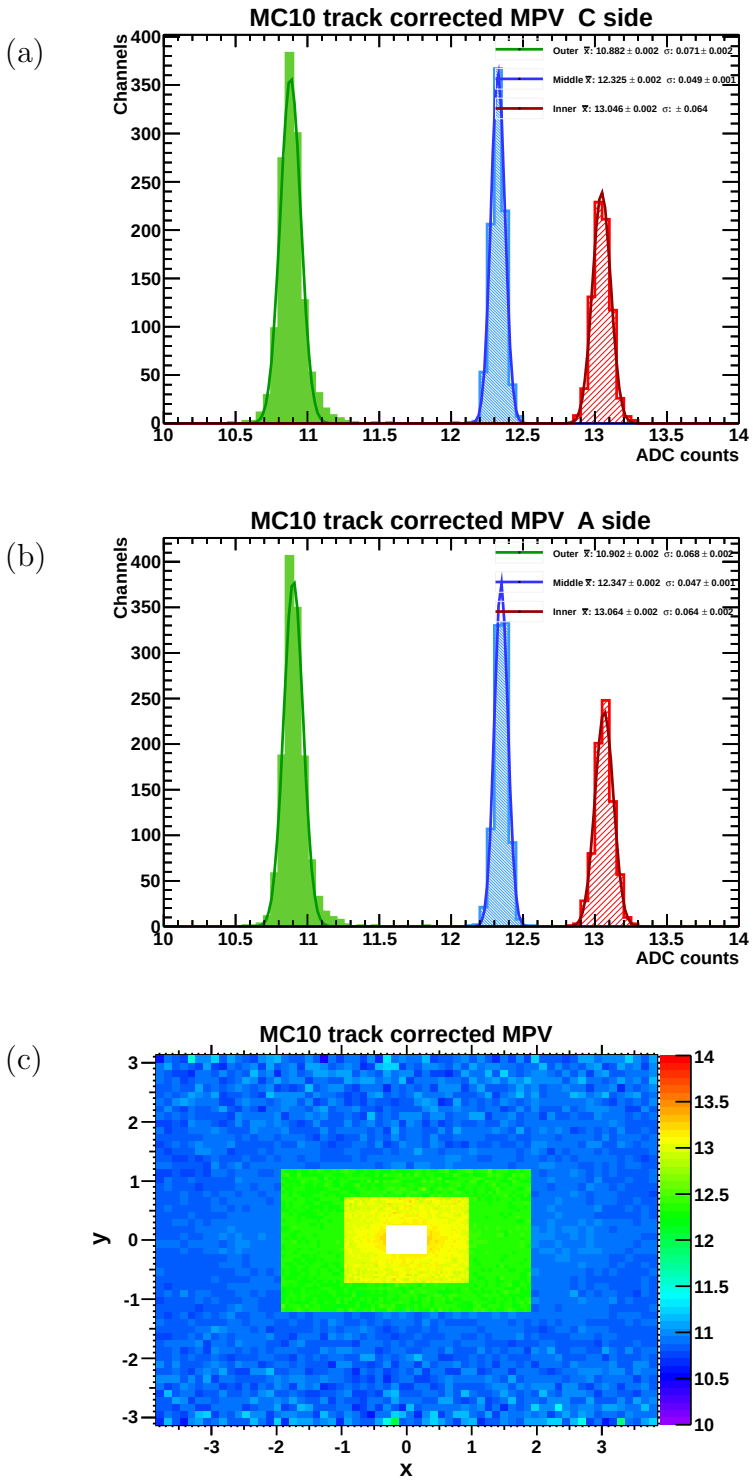

Figure 4.44: *Fit values of MIP MPV obtained from MC10 minimum bias sample with improved, weighted track length correction handling as foreseen for 2011 calibration.*

only track by track length correction, described in the beginning of this section, is applied.

4.10 Alignment

4.10.1 Introduction to alignment

The alignment of the preshower is made respect to the tracking system. The detectors are opened typically once per year during winter break, and after each movement the detector has to be realigned. The alignment should be checked each time when the tracking system itself calibration changes, however typical corrections to the tracking system are so small that the impact on the alignment between the tracking system and PRS is much below the precision of the method of position calibration.

The initial position of the PRS detector was set accordingly to its designed position. A survey of the detector is performed each time, when the detector is displaced. It is performed in order to check the proper replacement. However, survey measurements are not precise enough for the physics purposes and hence data driven alignment with respect to the tracking system is required. This document presents results of two realignment measurements performed in the middle of 2010, and in the beginning of 2011. Additionally, a comparison with Monte Carlo results is given.

The importance of a correct alignment is essential for the inner region, while the outer is the least affected region by misalignment. A hypothetical misalignment of an order of 10 mm along one axis means an inefficiency of 25% for the inner, 17% for the middle and only 8% for the outer.

4.10.2 Realignment method description

It is possible to measure the position where a particle enters the PRS accordingly to an extrapolation from tracking system data only. On the other hand, from information available from the preshower we can not determine which part of a cell was hit by the particle. Even if the information about the alignment is not available track by track it can be retrieved statistically. One can build a map of each cell – divide each one for small squares – and when there is a track point at a given square note whether it resulted in a signal in the cell or not. One cell may be not enough so one can extend the map for the neighbours of the cell. With enough statistics of tracks one can have an efficiency/inefficiency map of the cell. That map contains an information about displacement of the cell respect to the tracking system.

Practically, in 2010 we are limited by the statistics available – it was typically not enough to build such inefficiency map for each cell with a satisfactory precision. Another limit comes from the fact, that the correction to the alignment which can be applied has some constraints. It is linked to the software limitations. User can define for each side a vector of translation and a vector of rotation which have to be applied to align the detector. Eventually if there is a need, an additional correction can be applied to the y position of each supermodule. The result is that we can sum up the statistics from all cell of the same size at least by boards. If we consider only translations in x and y, then we can sum the boards by region in each supermodule.

The final simplification is a projection of the two dimensional maps on the axises x and y for each supermodule/board. To reduce impact of the misalignment along x axis when aligning along y axis, a part of region 10 mm wide from the border parallel to x axis is removed. Similarly when aligning along y, a region parallel to y axis is removed. The schematic picture showing the removed regions is presented in the figure 4.45.

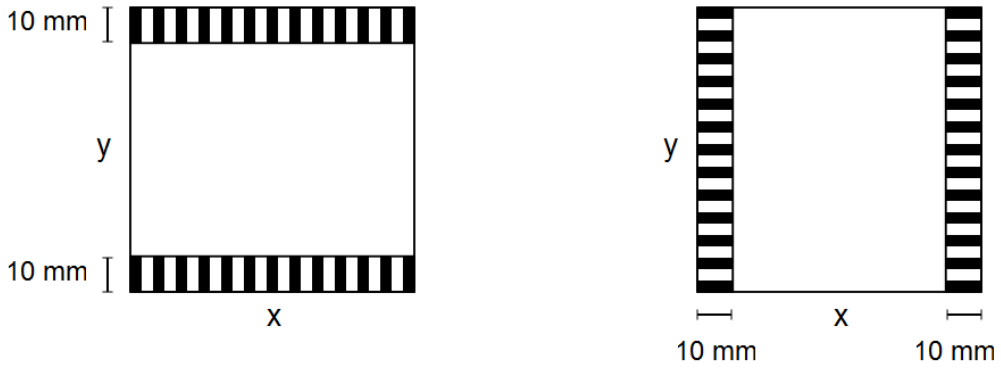

(a) (b)

Figure 4.45: *Areas of cells which are excluded in the detector alignment. The removed regions are marked with stripes. (a) alignment along* x *axis. (b) alignment along* y *axis.*

The plots of inefficiency prepared as described here for the simulation and the real data from 2010 and 2011 are given in the next sections. There are plots for alignment along both x and y axes. The regions shown in the plots are PRS 3 andd PRS 4, so the inner part of the detector – the part which is the most sensitive to misalignment.

4.10.2.1 Track selection

There was no special requirement on the track used for the alignment. No special selection based on types of particles was used (the statistics was not limited to MIPs as in the calibration, but electrons were also used). The only requirement was that the tracks which are used for the alignment of C side have the same charge, while all A side tracks have the opposite charge than the C side. However, there are regions for low x absolute values for which both positive and negative tracks are present, but their paths to the preshower are different, especially their zenith angle at which they enter PRS front plane. Very different zenith angles could produce unpredictable effects at borders and this is the reason why it is required to separate different charges. The charge that is used, is the one for which the statistics for a given side is larger. The difference in the statistics of positive and negative tracks for a given sample between the sides is caused by the magnetic field polarity. For "down" polarity, negative charge tracks are usually bent to the C side and positive charge are bent to the A side. For "up" polarity, negatives go to the A side and positives go to the C side. The way

how the separation between negative and positive charges is realised in the data is presented in the figure 4.46. The plots presented in the figure 4.49 are prepared with magnetic field down polarisation. It means that presented in the figure results for PRS 3 are obtained with negative charge tracks only, and results for PRS 4 are obtained with positive charge tracks only.

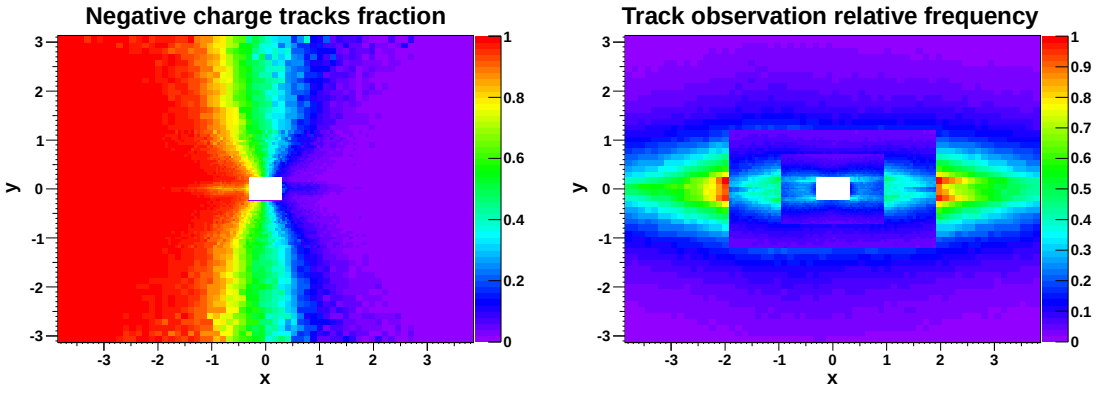

(a) (b)

Figure 4.46: *(a) Fraction of negative charge tracks pointing at a cell respect to the total number of tracks as a function of cell location. MC10 data. (b) Relative observation frequency of a track as a function of cell location (positive and negative charge tracks are not distinguished). The highest statistics cell has value equal to* 1*. MC10 data.*

4.10.2.2 Misalignment value extraction

Once a histogram of inefficiency for a given region is prepared it should look like a well shape with low inefficiency for tracks pointing inside cells. At the borders, it should rise to the level of 100% inefficiency. The width of the region of intermediate inefficiency – slope – is caused by:

- Track fit and extrapolation error.
  A measured uncertainty of track extrapolation at the PRS plane is presented in the figure 4.47. The presented data are taken from 2011 runs. The uncertainty on y, which reaches up to 6 mm is typically larger than the uncertainty on x, reaching 4 mm. The uncertainties rises as the distance from the beam pipe measured along x axis.

- Crossing angle different from 90 °
  Charged particles have some p_T when crossing the PRS detector, mostly due to bending inside the magnetic field. The more far away from the detector centre is the particle, the larger is the crossing angle. The plot of the distribution of the zenith angle for each part of the detector is presented in the figure 4.48(a). The existence of non-perpendicular tracks means that it is possible that a track is not fully contained inside one preshower cell but crosses two cells. It may

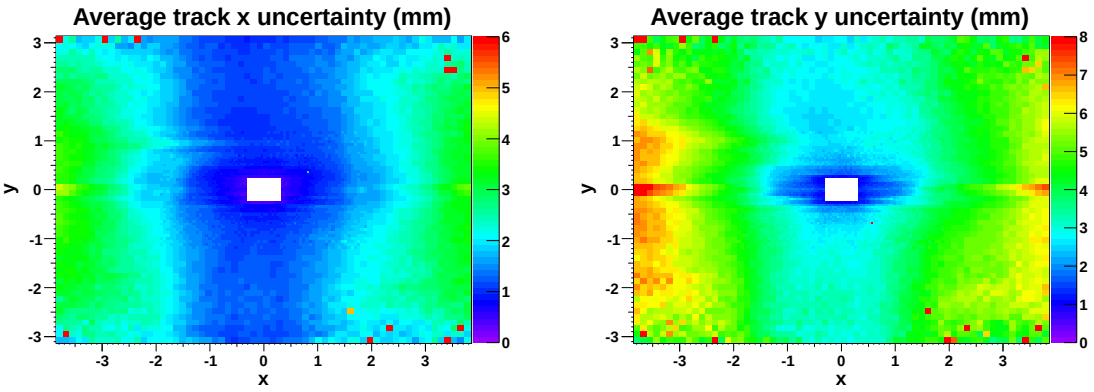

Figure 4.47: *Average uncertainty of track position at the PRS plane in mm. Left –* x *uncertainty, right –* y *uncertainty. Plots prepared with 2011 data sample.*

enter through a cell closer to the detector centre and escape through the cell of our interest or it can enter through it and escape through a neighbour located further away from the beam pipe. In the first case it lowers inefficiency in the region of few millimeter from the border in direction to the detector centre. In the second case it rises the inefficiency in the last few millimeter of the cell on the opposite side. It happens because even if a particle enters through the selected cell, it travels inside it for only a part of the whole distance of travel inside PRS, and thus the probability of registering a signal in that cell is reduced. The plots b) in the figure 4.48 shows the displacement between entrance point and exit point of tracks in function of the location. The difference rises from the inner to the outer. It is as low as 1 mm for the inner and reaches more than 6 mm for the most left and the most right parts of the outer.

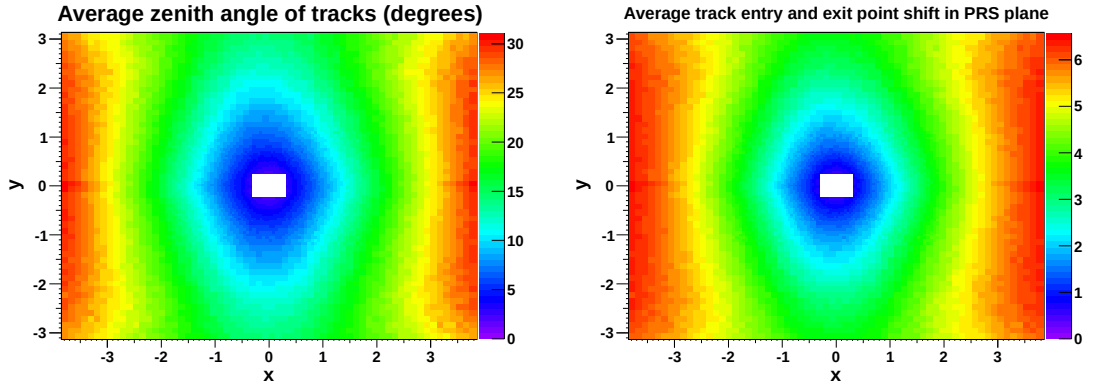

(a) (b)

Figure 4.48: *a) 2011 data average zenith angle of tracks for each cell in degrees. b) Average displacement between entrance to PRS point and exit from PRS point for tracks with 2011 statistics.*

- Materials between scintillators
  Not the whole cell volume is filled with scintillating plastic. The cells are covered with Tyvek paper. Also, at the borders of the modules, there is a mechanic structure. Additionally, light collection efficiency at the borders of scintillator can be reduced. Summing up all the things it means that cells are less efficient when a particle crosses them at their borders.

To measure the shift of each cell, board or supermodule, an assumption is made that left and right slopes of inefficiency curve are equally distant from centre of virtual cell. Then for a given plot of inefficiency an algorithm is performed (as in the figure 4.49:

1. For each side slope perform a linear fit to the inefficiency histogram around a bin with the value of inefficiency closest to 50%.

2. Search for the inefficiency value for which the distance between points lying on both slope fits for that inefficiency value is equal to the scintillating cell length. Draw a line segment between the two points.

3. The distance between the middle of that line segment and the centre of the cell is the searched displacement of the region. It means that the opposite value is the shift that has to be applied during realignment of the detector.

4.10.2.3 Re-alignment strategy

It was mentioned that a correct alignment is more important for the inner than for the outer. Because the number of parameters available for manipulation to perform the re-alignment is limited, the first objective is to re-align the inner as best as possible, paying less attention to the other regions.

The procedure starts with preparation of inefficiency histograms for the inner region. Misalignment calculation as described above is then performed for each of the histograms. The shifts obtained from these calculations are temporarily considered as the shifts that have to be applied to realign. The next step is a comparison between the shifts for the whole inner and shifts calculated independently for each board of the whole PRS detector. If the agreement is good, then the realignment is done. If the values are different than it has to be considered using more detailed realignment, like re-rotating the detector or move each supermodule independently. As we will see later, the additional manipulation was never needed, and a single translation for each side gave satisfactory results.

4.10.2.4 Monte Carlo alignment

The method was tested with MC09 and checked with MC10. The results were consistent, so here we refer to MC10 only.

Inefficiency histograms obtained with MC10 are presented in the left column of the figure 4.49. The first observation is that the histograms for the shift along x axis are not symmetrical with very steep slope on the side closer to the detector centre and much smoother change on the other side. The reason of that effect has not been

found. It is expected that this difference is an outcome of not perpendicularity of tracks which cross cells. On the other hand histograms for y axis are symmetrical.

The shift extraction method results are[6]:

- PRS 3, x shift is 0.3 mm, y shift is 0.0 mm,
- PRS 4, x shift is -0.3 mm, y shift is 0.0 mm.

More detailed results of the shift calculations, given for all boards independently, are presented in the first row of the figure 4.50. Shifts along x axis are lower than 1.0 mm for the inner, and lower than 1.5 mm for the rest. Shifts along y axis are typically lower than 0.5 mm. By construction the Monte Carlo is fully aligned, so the numbers quoted here can be understood as an estimation of a systematical uncertainty of the method. It means that we can't align the detector better than 1.5 mm along x and better than 0.5 mm along y with this procedure. We can say that the detector is satisfactory aligned when the misalignment is not larger than 1 mm for the inner and the simulation check described here shows that the proposed method allows reaching that level. This Monte Carlo driven systematic uncertainty is reflected in the fact, that all results given here are presented with precision of 0.1 mm.

4.10.2.5 2010 alignment

The 2010 data re-alignment was done in the middle of the year 2010. It has to be mentioned here, that the method used for the re-alignment relies heavily on a proper alignment of the tracking system. The tracking system for this re-alignment was not yet perfectly calibrated which will be visible on the distributions. The sample of minimum bias events registered up to the end of June 2010 were used. The data reconstruction tag was *Reco5*, and the stripping tag was *Stripping9*. Inefficiency histograms for the inner region are presented in the middle column of the figure 4.49. The shapes on the plots are somehow different from the simulation plots. The slopes are more symmetrical and less steep. The plateaus at the far left and far right of the histograms are not visible. Even for a distance from the cell centre equal to the cell size the inefficiencies don't stabilise, but rise almost constantly. The maximum values of inefficiency for presented scales are around 0.8 which is much lower than 1.0 for the Monte Carlo. On the other side – a plateau in the middle of a cell is also located at greater value of inefficiency than for the simulation. One can also spot a small step in three histograms. All described effects are caused by the same reason – miscalibrated tracking system in the beginning of LHCb activity in 2010. The fact that the trackers were not calibrated well enough suggests that one should not expect a perfect alignment for all regions of the detector with these data.

Starting from the inefficiency plots for the inner the following shift results were obtained:

- PRS 3, x shift is -7.1 mm, y shift is -9.6 mm,
- PRS 4, x shift is -2.6 mm, y shift is -9.9 mm.

[6]Statistical uncertainties are not given, because of the complicity of the extraction method and fact, that the systematics is much more dominant than the statistics.

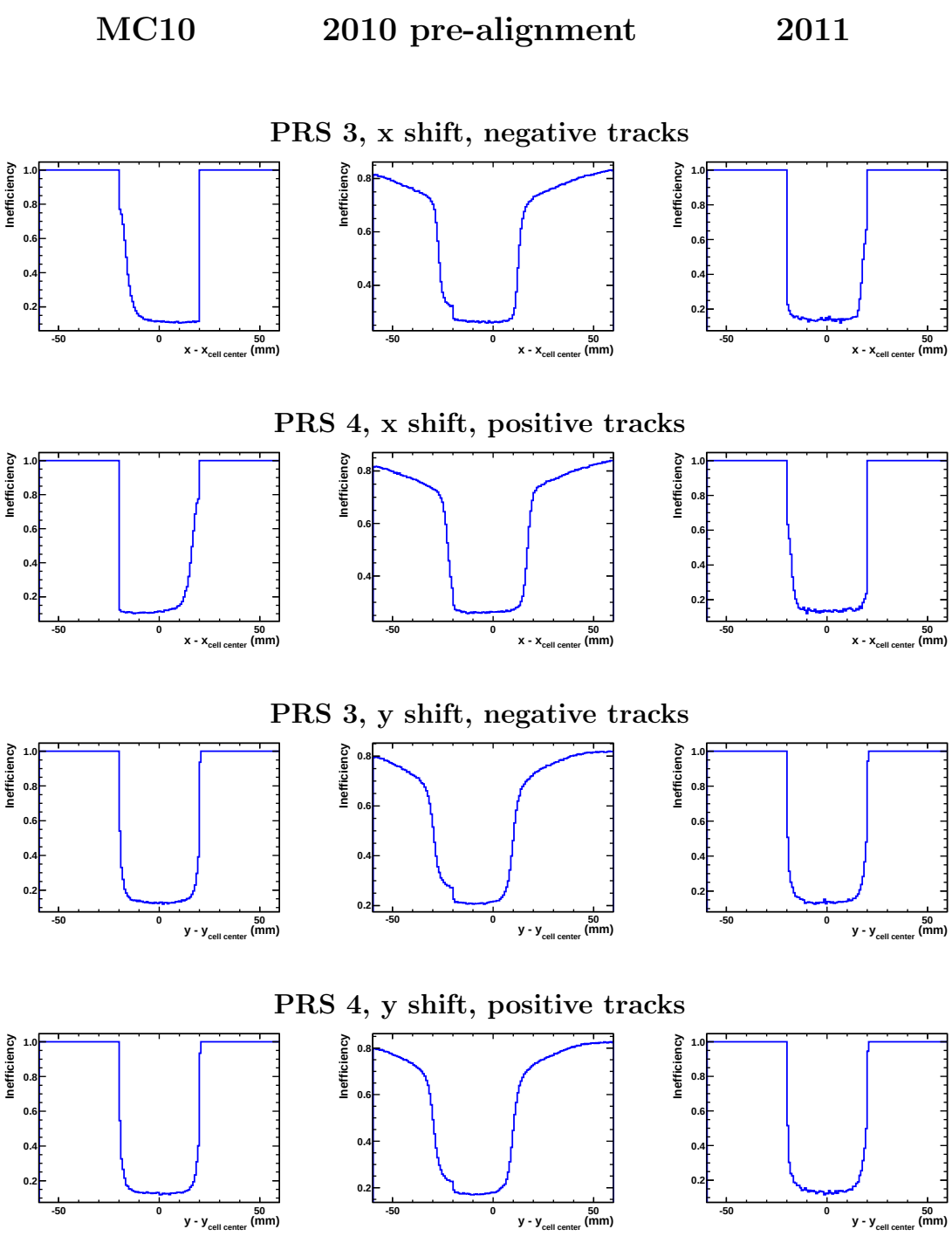

Figure 4.49: *Histograms of the inefficiency of the preshower cells for charged tracks histograms as a function of the position of the entrance point to a cell respect to the cell centre. Inefficiency is defined as a number of events in which no signal in the cell was registered for a track which entered the cell through a certain region, divided by the number of events. The columns from the left: simulation MC10, 2010 data, 2011 data. The rows from the top: PRS 3* x *postion, PRS 4* x *postion, PRS 3* y *postion, PRS 4* y *postion. PRS 3 is the inner region C side, PRS 4 is the inner region A sided.*

The realignment was performed using these numbers. After, a procedure of creation of inefficiency plots for each board of the detector was performed, followed by finding the shifts algorithm. The results are shown in the figure 4.50.

The first conclusion from the 2010 realignment campaign was that the detector before realignment was quite significantly misaligned. It was shifted about 1 cm in y and almost 1 cm in x for the C side. This could result in almost 40% efficiency decrease for the inner part C side for finding a signal in the preshower in a cell crossed by a track of a charged particle.

Secondly it is visible in the plots in the figure 4.50 that applying a simple translation driven by the inner region only doesn't cure the misalignment for the whole detector. There are still the most left and the most right regions were the remaining misalignment in x is up to 6 mm. For the remaining misalignment in y the worst region is the top corner of the C side, where the value of it reaches 10 mm. Although these values themselves show that there is something not completely mastered in the relative alignment between the tracking system and the preshower, the problem is not really significant. A misalignment of such level can be problematic for the inner, but for the outer the impact is much lower.

Knowing that the tracking system was not perfectly calibrated at the time of the measurement it was decided not to apply any further corrections and wait for better precision of the system.

4.10.2.6 2011 alignment

The 2011 alignment check was performed with the data collected in 2011 from the beginning of the year to the middle of April. The sample used was a minimum bias sample tagged as *Reco8Stripping13b*. During a break in LHC operations in winter 2010/2011 the halves of the preshower were opened, and then closed again before the machine restart. It means that the position of each side had possibly changed since the previous alignment, particularly in x.

First a check of the inner region alignment was performed. The results in the form of inefficiency histograms are available in the right column of the figure 4.49. The shape of the histograms is this time much more similar to the Monte Carlo prediction than the 2010 signal, supporting the idea that the tracking system is far better aligned, at least that the extrapolation of tracks is better mastered. The top and the bottom values are almost the same for 2011 data and the simulation. Similarly the steepness of slopes is comparable. However for the alignment along x axis, the shapes are like mirrored respect to the $x = 0$. This fact has not been explained yet. Nevertheless, the difference is not significant enough to disturb realignment precision.

The values of the shift measured with the first 2011 data are:

- PRS 3, x shift -0.1 mm, y shift -0.1 mm,
- PRS 4, x shift 0.1 mm, y shift -0.1 mm.

The results show a perfect alignment of the detector respect to the tracking system. It may suggest that the 2010 realignment was performed well together with a fortunate parking the halves of the detector at almost the same place as they were in 2010. Encouraged by these results, it is interesting to investigate more detailed structure of

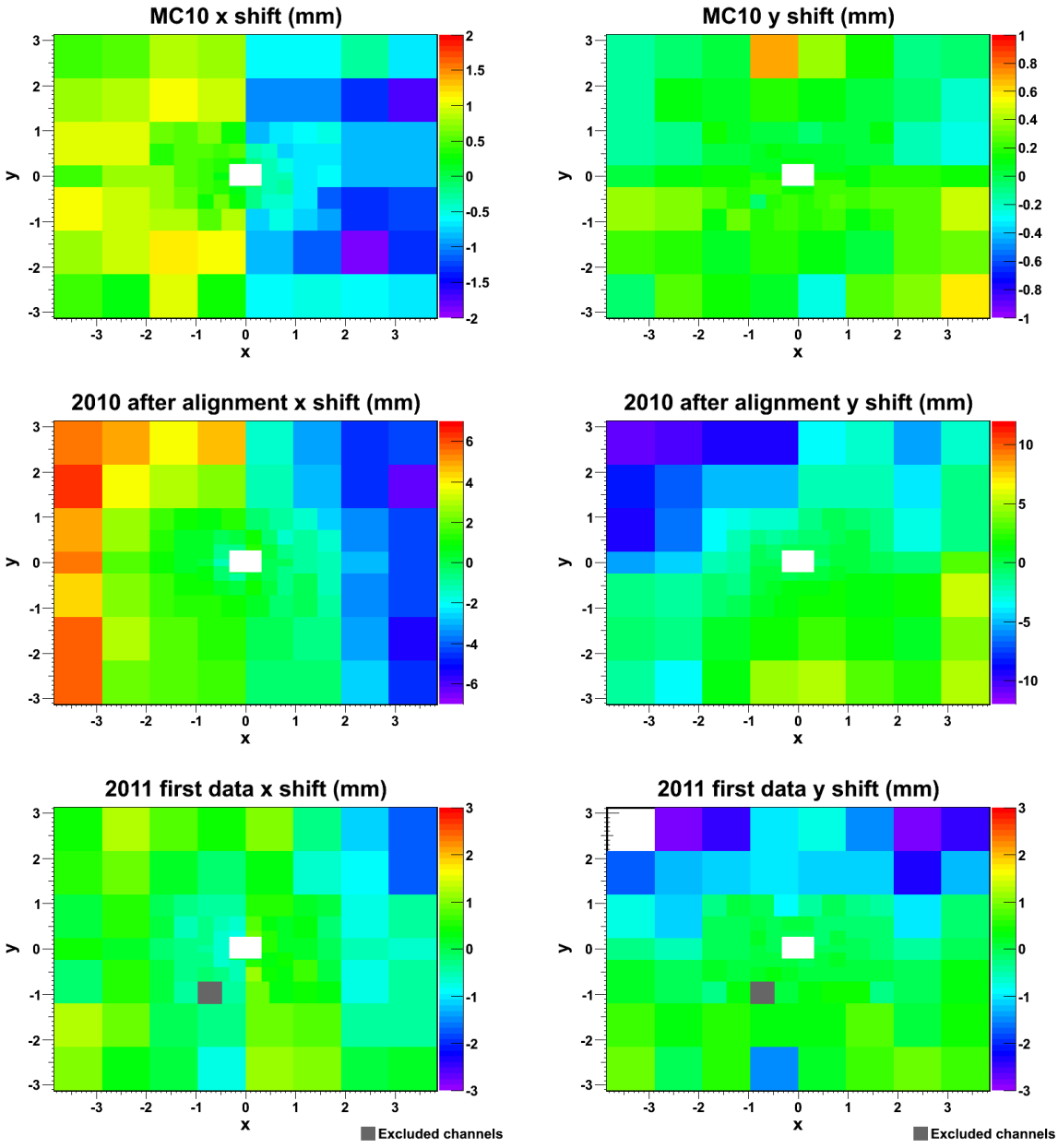

Figure 4.50: *Misalignment of the board of PRS respect to the tracking system of LHCb for different measurements. The left column – misalignment in* x *axis. The right column – misalignment in* y *axis. The rows from the top: simulation MC10, 2010 data after realignment, 2011 data.*

the misalignment measured in 2011. The results for the boards are presented in the most bottom line of the figure 4.50. Starting from the x axis – there is no board of misalignment larger than 2 mm and almost all boards lie within 1 mm from 0. The y misalignment is a bit larger, but still below 3 mm everywhere except of one board in the outer C side. Negative values of shift for the top of the detector may suggest a little tilt of which could be applied to remove the misalignment at all. Nevertheless the 2011 results were better than expected and showing that the detector is aligned, thus no realignment action was needed.

4.11 Summary

The 2010 data-driven corrective factors for odd and even bunch crossing number on top of the HV settings provided a satisfactory calibration of the PRS data. No further offline correction was needed for the purpose of the PRS calibration, both supported by regular Energy Flow or MIP survey of the detector.

The critical point of the MIP calibration is certainly the survey of the pedestal variations. It is anecdotic, as far as the electromagnetic trigger efficiency or the electromagnetic energy measurement corrections are concerned. However, a typical variation of 1 ADC count results in a 10% systematic shift of the MIP and must be controlled. Automated tools are in place at the pit to follow-up pedestal variations and correct whether it is required.

A comprehensive set of tools has been developed in the framework of this thesis for the Preshower calibration and alignment. It will be used in the forthcoming years to survey at the detector accuracy.

Chapter 5

Exploratory work: $B^0_{(\mathrm{S})} \to hh\pi^0$ observation with 2010 data

This part describes an exploratory work on charmless three-body decays of neutral B mesons with one π^0 in the final state. The main points of interest of this work are decays which lead to the final state of $K\pi\pi^0$, however analyses which aims at observation of other modes are similar. Thus the results for decays into $\pi\pi\pi^0$ and $KK\pi^0$ (for which the same method of determining the branching fraction can be used) are also briefly described.

The description begins from Monte Carlo simulations. It follows trigger, stripping and selection efficiency studies, and aims for an observation with 2010 LHCb data. The objective of the work presented here was to scrutiny the real data, and to prepare grounds for the future analysis.

5.1 Monte Carlo

The initial goal of the analysis is the measurement of the γ angle of the unitarity triangle with $B_s^0 \to K\pi\pi^0$. That resulted in a choice of preparing the analysis in a way to obtain the best performance for this decay mode. However the result should be quite easily applicable to any other $hh\pi^0$ decay mode. The mentioned decay of B_s^0 had never been observed before so the branching ratio was unavailable. It means also that there was no branching ratio of the decay through intermediate resonances. On the other hand we needed a well prepared, simulated Monte Carlo sample to use it for preparation and tests of the analysis. So we decided to design a resonant structure of the decay with branching ratios of the decays through different resonances guessed from the example of $B^0 \to K\pi\pi^0$ [16] and $D^0 \to K\pi\pi^0$. The presence of the resonances is required because they shift the kinematic properties of the daughter particles. The list of the resonances included with the corresponding branching fractions is given in the table 5.1.

The simulation of decaying B_s^0 is done with EVTGEN [90], which incorporates PYTHIA engine (6.24.2). EVTGEN is a part of the simulation software used by the LHCb Gauss environment. The intermediate resonance particle types are correctly simulated, and the decays are processed accordingly to the type of the particle. The models used for the simulation are: phase space (PHSP), scalar particle into scalar and vector (SVS), scalar into scalar and tensor (STS), vector into two scalar particles (VSS), and tensor into two scalar particles (TSS). Two examples of the angular distribution of the particles produced in decays of a vector resonance K^* and a scalar K_0^* is presented in the figure 5.1. In each event a one of b quarks from a pair of $b\bar{b}$ produced has to hadronise into B_s^0, and that particle decays in one way from the list of allowed decays. The decays are forced to finish with one and the same final state which is $K\pi\pi^0$. Only the events in which all the particles (B_s^0, and $K\pi\pi^0$) are produced inside the detector acceptance (typically 250 mrad) are used in the next step of the simulation. This step is the propagation of all the particles in the detector with Geant software.

To ensure a proper generation of the Monte Carlo samples, the steering card of EVTGEN with the setting described above was tested. The test was performed with the generation steps only, without any propagation of the particles through the detector. The results as a Dalitz histograms (figure 5.2) were obtained. Additionally to the typical Dalitz plot, a *square Dalitz* plot was prepared. This approach is characterised by a better separation of the resonances in the most interesting regions of interference for B meson decays than the usual one. The plot is obtained by a non-linear transformation of variables:

$$m' = \frac{1}{\pi} \arccos\left(2\frac{m_{\pi\pi} - m_{\pi\pi}^{\min}}{m_{\pi\pi}^{\max} - m_{\pi\pi}^{\min}}\right) \tag{5.1}$$

$$\theta' = \frac{1}{\pi}\theta, \tag{5.2}$$

where in case of $B_s^0 \to K^-\pi^+\pi^0$: $m_{\pi\pi} = \sqrt{s_{\pi^+\pi^0}}$ is the invariant mass of the two pions, $m_{\pi\pi}^{\max} = m_{B_s^0} - m_{K^-}$ is the maximum available mass to the two pion system, $m_{\pi\pi}^{\min} = m_{\pi^+} + m_{\pi^0}$ is the minimum available mass of two pions, θ is the angle between π^+ and K^- in $\pi^+\pi^0$ rest frame. It is necessary to mention that the plots do not

Intermediate state	Relative branching fraction	EVTGEN model used
$K^{*-}(892)\pi^+$	0.060	SVS, VSS
$K_0^{*-}(1430)\pi^+$	0.134	PHSP, PHSP
$K^{*-}(1410)\pi^+$	0.010	SVS, VSS
$K_2^{*-}(1430)\pi^+$	0.007	STS, TSS
$K^{*-}(1680)\pi^+$	0.011	SVS, VSS
$K^{*0}(892)\pi^+$	0.119	SVS, VSS
$K_0^{*0}(1430)\pi^0$	0.267	PHSP, PHSP
$K^{*0}(1410)\pi^0$	0.020	SVS, VSS
$K_2^{*0}(1430)\pi^0$	0.014	STS, TSS
$K^{*0}(1680)\pi^0$	0.023	SVS, VSS
$K^-\rho^+(770)$	0.179	SVS, VSS
$K^-\rho^+(1450)$	0.028	SVS, VSS
$K^-\rho^+(1700)$	0.034	SVS, VSS
Non-resonant	0.094	PHSP

Table 5.1: *Relative branching ratio of the decay of B_s^0 to final state $K^-\pi^+\pi^0$ through selected intermediate resonance states. These parameters have been used in produced steering cards of the EVTGEN generator. This is an educated guess from $B^0 \to K\pi\pi^0$ [16] and $D^0 \to K\pi\pi^0$.*

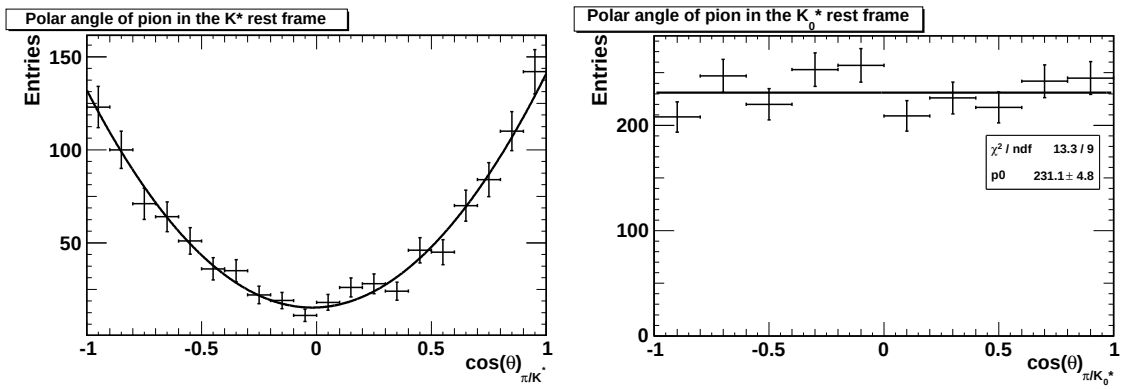

(a) (b)

Figure 5.1: *Polar angle θ of a pion produced in the decay of: a) K^*, b) K_0^*. The angle is measured in the rest frame of the resonance particle from the direction of flight of the resonance particle. The histograms are made from the simulated decays. In case of vector resonance K^* a fit of parabola is performed, as the distribution for vector should be described by $1 - \cos^2\theta$. In case of scalar resonance K_0^* a flat distribution is fit (also a proper model for scalar decay).*

include any resolution from the detector ability to reconstruct the particles, hence we have an asymptotic detector.

The square Dalitz plot allows to observe the resonant structure and the interference regions. However the identification of the resonances is less natural. The figure 5.3 contains the plots of all resonances included in the simulation of the decay $B_s^0 \to K\pi\pi^0$.

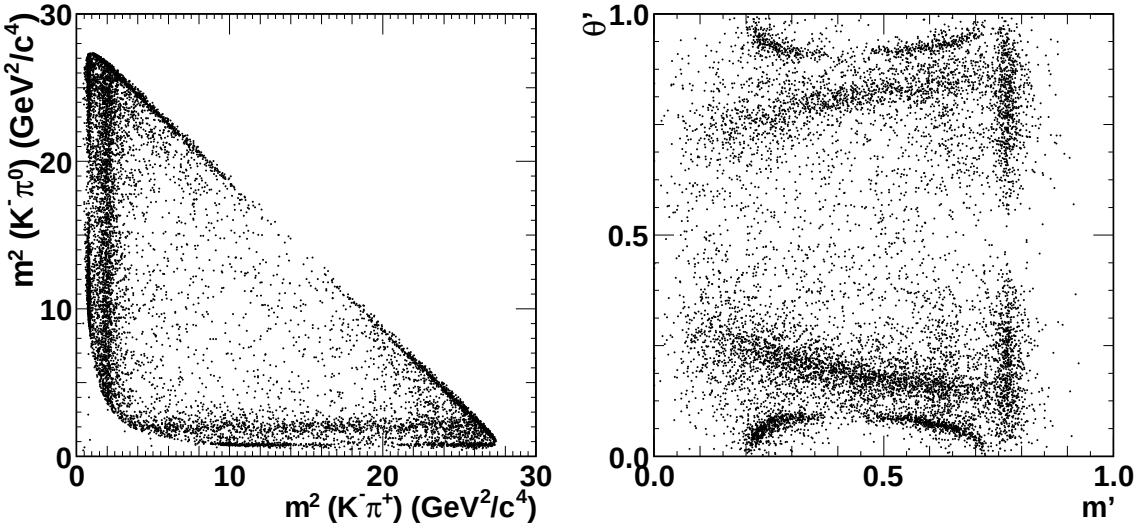

Figure 5.2: *Dalitz plots of the decay of* $B_s^0 \to K^-\pi^+\pi^0$. *The plot on the right side is a* square Dalitz plot. *The definition of the variables is given in the text (equations 5.1 and 5.2. The plots are produced from the MC generated particles without reconstruction process.*

The first set of the simulated data with the decay described here was produced at the time when the expected energy of the LHC was 5 TeV per beam and the visible number of interaction per bunch crossing equal to 0.6. The settings of the EVTGEN were tuned to reflect these conditions. The second set of the Monte Carlo was produced[1] with the energy of 3.5 TeV per beam and the number of visible interaction per bunch crossing equal to 2.3.

5.2 Neutral pion reconstruction

The separation between two photons coming from the decay of π^0 depends on the momentum of π^0 (figure 5.4). For large momentum the distance is comparable to calorimeter cell size. This means, that both photons may share the same calorimeter cluster.

At the construction level, π^0 particles in the LHCb experiment are divided into two species [91]: merged and resolved. Merged π^0 are the one for which two photons share

[1]The whole process of production was my responsibility.

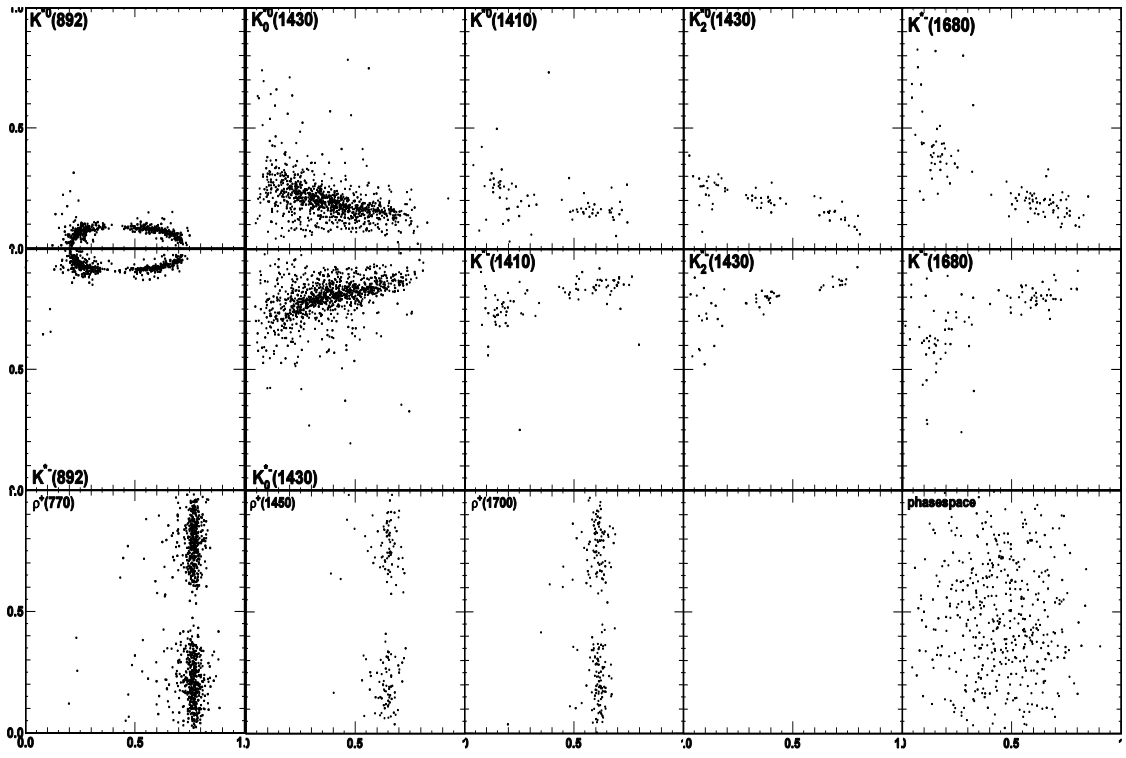

Figure 5.3: *Dalitz square plots for different intermediate resonances of the simulated decay of* $B^0_s \to K^-\pi^+\pi^0$.

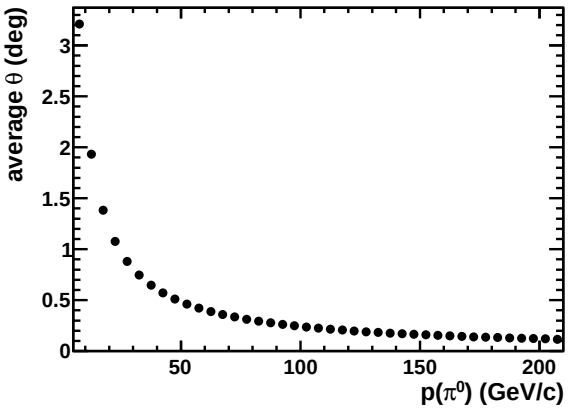

Figure 5.4: *Average angle* $\langle\theta\rangle$ *between to photons from the decay of* π^0 *as a function of* π^0 *momentum. Plot obtained from simulation. Only angular calculations are made and no reconstruction is applied. If a* π^0 *decays inside VELO, then the angle of* 0.2° *means that the separation between two photons at the calorimeter is approximately 4 cm.*

the same calorimeter cluster. The other specie of π^0 is characterised by larger separation of the two photons, which allows reconstructing both of them independently, and then combining them together to build the π^0. Directly from this short description one can conclude that resolved π^0 are reconstructed more precisely and the resolution of the mass of reconstructed particles is better than for merged π^0. The type of a reconstructed π^0 coming from a charmless decay of B^0 is also linked to the transverse momentum (figure 5.5). High momentum π^0 affects photon directions in the lab rest frame by boost, effectively reducing their spread. It means that high momentum π^0 are more probable to be merged than resolved. It is reflected also in the algorithms which reconstruct merged π^0 – there is a cut on the transverse momentum of merged π^0 is $p_T(\pi^0) > 2$ GeV/c.

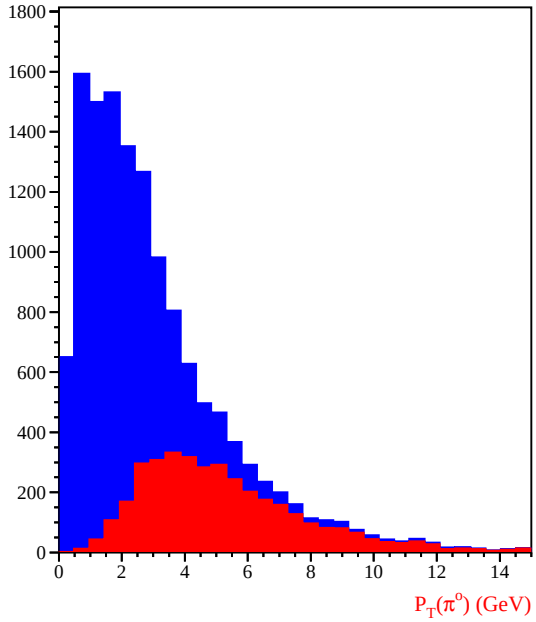

Figure 5.5: *Monte Carlo transverse momentum distributions for reconstructed merged (red) and resolved (blue) π^0 particles from $B^0 \to \pi^+\pi^-\pi^0$ [91]. Sample generated with $\sqrt{s} = 14$ TeV.*

5.3 Trigger

Let us first bring the basic conditions of trigger used in 2010 interesting from the point of view of this analysis. For more details, the interested reader can look into TCK (Trigger Configuration Key) settings list [92]. The table 5.2 presents cuts used for various L0 trigger configuration. One variable requires a comment: SPD maximum multiplicity cut was designed to reject events with the largest particle multiplicities, which require significantly more CPU time in the further trigger stages. Which The analysis requires that at least one of the three HLT2 lines `B2HHPi0_Merged`, `B2HHPi0_Resolved`, `Topo0STF2Body` decision is positive. The first two were designed

in the Clermont-Ferrand group [73]. `B2HHPi0_Merged` is a dedicated line for merged π^0, while `B2HHPi0_Resolved` is for resolved π^0. The last one is a global line for decays with two reconstructed tracks. The cuts used in these lines are presented in the table 5.3 and in the table 5.4.

TCK	L0Photon min photon E_T (MeV)	L0Hadron min hadron E_T (MeV)	L0Electron min electron E_T (MeV)	SPD max multiplicity
0029	4400	3600	3000	900
002a	3200	3600	3000	900
002c	3200	3600	3000	450
0030	4400	2600	3000	900
0031	4400	3600	3000	450

Table 5.2: *Cuts for different L0 decisions and SPD multiplicity cut for 5 TCK settings used in 2010.*

Cut	Description
true	HLT1 photon line decision
< 350	number of tracks in VELO
> 4000 MeV/c^2	B minimum mass
< 6000 MeV/c^2	B maximum mass
> 2000 MeV/c	minimum B transverse momentum π^0
> 0.0001	B vertex fit probability
< 25	B primary vertex impact parameter significance
> 0.99987	B pointing angle
> 64	B flight distance significance
> 500 MeV/c	charged hadrons minimum transverse momentum
> 5000 MeV/c	charged hadrons minimum momentum
< 5	charged track fit χ^2 per degree of freedom
> 9	charged track primary vertex impact parameter significance
> 1200 MeV/c	π^0 minimum transverse momentum

Table 5.3: *Cuts used in HLT2 lines `B2HHPi0_Merged, B2HHPi0_Resolved`.*

5.4 Stripping

After the data registered by the LHCb detector are written to the data storage, they are reconstructed event by event. This process is done basically once, and all physicists use the same reconstruction. However, the amount of data after the reconstruction (which means after the HLT2 trigger) is quite huge. Among interesting events there is also a lot of unimportant background. To reduce it and to help reducing computing power needed for each analysis, a procedure of stripping was designed. During this

Cut	Description
< 350	number of tracks in VELO
> 4000 MeV/c^2	B minimum window
< 7000 MeV/c^2	B maximum window
> 2000 MeV/c	minimum B transverse momentum π^0
< 25	B primary vertex impact parameter significance
> 0	B pointing angle
> 64	B flight distance significance
> 500 MeV/c	charged hadrons minimum transverse momentum
> 5000 MeV/c	charged hadrons minimum momentum
< 5	charged track fit χ^2 per degree of freedom
> 16	charged track primary vertex impact parameter significance
> 1500 MeV/c	largest transverse momentum
> 4000 MeV/c	sum of transverse momentum
> 100	sum of charged track impact parameters significance
< 3	lowest track fit χ^2 per degree of freedom
true	all particles from the same primary vertex
< 0.12	distance of the closest approach between tracks

Table 5.4: *Cuts used in HLT2* `TopoOSTF2Body` *line.*

procedure all events are looped and sorted accordingly to the requirements. The stripping consists of different sets of cuts, called streams. The interesting from the point of view of this analysis is the stream called *Bhadron*, which comes from the fact that it contains the stripping selections of the decays of B mesons into hadrons. The stream contains a set of *lines*. The line is a piece of code which aims at a reconstruction of a given decay mode. First it builds the mother particle (in case of *Bhadron* these are for example B mesons) from daughter particles, the candidate mother particle is saved in the data file and can be used later. Additionally if at least one valid candidate is built, the event is stored in the stream.

The stripping code used for this analysis was designed by the Clermont-Ferrand group [73]. The line is designed to select any decay of the neutral B meson (B^0 or B_s^0) into three particles: two hadrons (each one can be π or K) and one π^0.

To reduce false candidate construction ratio a set of cuts was designed in the stripping. The cuts are collected in the table 5.5. The table reflects the *Stripping12* configuration, and this version of stripping was used for the analysis of 2010 data presented here. In the stripping all charged particles are assumed to be pions. No cut is applied on particle likelihood so this assumption doesn't reject kaons. It only influences the mass of the combination of the three particles: $\pi\pi\pi^0$. However the allowed mass window for the combination is wide (4200 MeV/c^2 to 6400 MeV/c^2) and doesn't reduce the acceptance of real and well reconstructed candidates, because the most probable shift of the combination mass due to assignment of pion mass to a kaon is about 60 MeV/c^2. The stripping is then suitable for the pre-selection of $B^0 \to \pi\pi\pi^0$, $B^0 \to K\pi\pi^0$, $B^0 \to KK\pi^0$, $B_s^0 \to \pi\pi\pi^0$, $B_s^0 \to K\pi\pi^0$, and $B_s^0 \to KK\pi^0$.

A test of the stripping cuts was performed on a simulated MC10 Monte Carlo

Cut	Description
> 4200 MeV/c^2	B minimum mass
< 6400 MeV/c^2	B maximum mass
> 3000 MeV/c	minimum B transverse momentum merged π^0
> 2500 MeV/c	minimum B transverse momentum resolved π^0
> 0.001	B vertex fit probability
< 9	B primary vertex impact parameter significance
> 0.99995	B pointing angle
> 64	B flight distance significance
> 500 MeV/c	charged hadrons minimum transverse momentum
> 5000 MeV/c	charged hadrons minimum momentum
> 0.000001	charged track probability
> 25	charged track primary vertex impact parameter significance
> 2500 MeV/c	merged π^0 minimum transverse momentum
> 1500 MeV/c	resolved π^0 minimum transverse momentum
> 0.2	resolved π^0 photons gamma confidence level

Table 5.5: *Cuts used in the stripping of the real data for the selection of* $\mathrm{B_{(s)}}^0 \to hh\pi^0$.

sample of $B^0_s \to K\pi\pi^0$ with the resonant structure as described above. Additionally for the reference a sample of MC10 Monte Carlo sample of inclusive $b\bar{b}$ production was used as a background sample[2]. The results as comparison plots of different stripping variables can be found in the Appendix C, in the figures C.1 and C.2 for the merged π^0, and in the figures C.3 and C.4 for the resolved π^0. Additionally the accepted ranges of the variable values are marked. The results confirm the correctness of the stripping design.

5.5 Efficiency study

5.5.1 Limitations

Before presenting the results we would like to know precisely what we should expect. Thus, we can estimate all efficiencies from the Monte Carlo. Then we can compare the real data results with the expectations. Of course this not always follow that direction – sometimes the curiosity comes before the best understanding of the situation. In fact that was the case of $\mathrm{B_{(s)}}^0 \to K\pi\pi^0$ observation in the LHCb. The first observation made with 2010 data were far different from the prediction derived from the Monte Carlo samples available at that time. That disagreement triggered searches for

[2]To reduce computing power cost the samples were prepared with some pre-cuts. The mass window was set to 500 MeV/c^2 around the B^0_s mass. The additional cuts were: vertex fit probability $B\_VtxProb > 0.001$, track fit probability $\pi\_TrackProb > 0.000001$, B pointing angle $B\_DIRA > 0.99$, B primary vertex impact parameter $B\_IPChi2 < 100$. The cuts on $B\_VtxProb$ and $\pi\_TrackProb$ were the same as in the stripping, however they are very mild and they remove only the candidates for which the probability linked to the reconstruction of the tracks and the B vertex is very low.

understanding the difference and mastering the data as much as possible. It lead us to a preparation and a generation of a new Monte Carlo sample tuned to reproduce better the situation as in 2010. Though this chapter is written more in the logical order (from the first step of the simulation, already presented, to the observation) than in the historical order.

As it was already mentioned the primary goal was the measurement concerning $B_s^0 \to K\pi\pi^0$. That is why the Monte Carlo sample prepared had been chosen to simulate that decay. On the other hand that decay had been never observed before, so for a comparison between the simulation and the data the decay mode of $B^0 \to K\pi\pi^0$ was used. We assume that the efficiencies are equal for B_s^0 and B^0 decays.

5.5.2 Expected yields formula

The expected number of events of $B^0 \to K\pi\pi^0$ in a sample of data can be expressed as:

$$\mathrm{N} = \mathscr{L} \cdot \sigma_{b\bar{b}} \cdot 2 \cdot f_\mathrm{d} \cdot BR(B^0 \to K\pi\pi^0) \cdot \epsilon_{tot}. \tag{5.3}$$

We start describing the variables in the equation from $\mathscr{L}$, which is the integrated luminosity. For the 2010 data available in the *Stripping12* it is about 32 pb^{-1}. Then $\sigma_{b\bar{b}}$ which is the cross section for the production of $b\bar{b}$ quark pair in two proton interaction at the energy of the LHC. This value has been measured already by the LHCb [93] at $(284 \pm 20 \pm 49)$ μb. The factor 2 states for two b quarks produced in each pair. f_d is the hadronisation fraction for a $\bar{b}$ quark into $\bar{b}d$ meson, or alternatively a b quark into $b\bar{d}$. Accordingly to [56] it can be estimated[3] as 0.3 at the level of 30% precision. $BR(B^0 \to K\pi\pi^0)$ is the branching ratio of the decay $B^0 \to K\pi\pi^0$ measured [2] to be equal to $(3.59^{+0.28}_{-0.24}) \cdot 10^{-5}$. The final term – ϵ_{tot} – is a factor which combines all the efficiencies which conduct from a B^0 meson into the observation and the selection of the decay from the decay products. It can be estimated on the simulated data. In that case it can be represented as a product of:

$$\epsilon_{tot} = \epsilon_{gen} \cdot \epsilon_{trig} \cdot \epsilon_{GEC} \cdot \epsilon_{strip} \cdot \epsilon_{sel}, \tag{5.4}$$

where ϵ_{gen} is the efficiency of the generator level initial angular cuts, ϵ_{trig} is the trigger efficiency, ϵ_{GEC} is the efficiency of the *global event cut* which is a special part of the trigger (and will be discussed later), ϵ_{strip} is the stripping efficiency, and ϵ_{sel} is the selection efficiency. We will focus on these efficiencies in the next section. The ϵ_{tot} formula factorises. It is important as the order in which the cuts (and the efficiencies) are applied is different on the real data and the Monte Carlo. For the real data it goes: *generation* $\to$ *trigger* $\to$ *stripping* $\to$ *selection*. For the Monte Carlo it is: *generation* $\to$ *stripping* $\to$ *trigger* $\to$ *selection*

In the calculations presented in the next sections, the Monte Carlo mismatching is neglected.

[3] If we assume the hadronisation fraction from LEP measurements, we obtain $f_d \sim 0.4$. It must be said that different value of f_{Λ_b} was obtained in the LHCb, effectively modifying f_d to be 0.3 ± 0.1.

5.5.3 Monte Carlo efficiencies

In this section the extraction method of the efficiencies is described first, while the numbers are given in the end of this part. We start the description from one the first steps of the Monte Carlo sample generation. It was already mentioned that particles have to be produced in an approximate geometrical acceptance of the LHCb detector. That cut does not depend on the type of π^0 as it is applied before the type can be distinguished. This cut is named *generator level* cut (ϵ_{gen}).

The next efficiency evaluated on the simulated sample of data is the stripping efficiency. The numerator of this efficiency is the number of events that pass the stripping. The denominator is the number of events that pass the generator level cut. In fact this efficiency is more than just a stripping efficiency. It is the first step which contains the hidden Monte Carlo matching efficiency. It is also the first step where the discrimination between merged and resolved π^0 is made. The numbers here include the probability of registering a π^0 as merged or resolved[4]. Additionally the stripping efficiency with this construction (with the denominator of the number of events passing the generator level cut) includes the reconstruct ability of the event.

The trigger efficiency is calculated on the stripped events from the MC. Similarly to the previous step, the numerator is the number of events that receive *pass* decision from the trigger, and the denominator is the number of events that pass the stripping. The trigger efficiency comes from the emulation of the trigger functionality offline. During 2010 data taking period various trigger configuration have been used. The summary of the efficiencies for different trigger conditions is given in the tables 5.6 and 5.7. An average number, weighted with the luminosity, is also calculated and will be used for further calculations.

L0 TCK	$\mu_1 = 0.6$, 10 TeV (%)	$\mu_2 = 2.3$, 7 TeV (%)	Integrated $\mathcal{L}$ (pb^{-1})
0029	45.7 ± 0.7	42.1 ± 1.3	3.0
0031	45.7 ± 0.7	42.1 ± 1.3	0.1
0030	50.7 ± 0.7	46.6 ± 1.3	2.3
002a	53.1 ± 0.7	49.8 ± 1.3	14.4
002c	53.1 ± 0.7	49.8 ± 1.3	11.5
Average	52.2 ± 0.5	48.8 ± 0.8	sum = 31.3

Table 5.6: *Trigger efficiencies [73] for merged π^0 split by L0 TCK. The average weighted by integrated luminosity is also given. The global event cut is not applied.*

The very special efficiency ϵ_{GEC}, which value for the real data events is not reproduced in the Monte Carlo. The global event cut is the cut on the multiplicity of hits in the SPD (also reflected in the number of tracks in VELO). The trigger system of the LHCb (table 5.2) uses this variable. For the Monte Carlo it has a minor impact, however for the real data it is estimated to be $\epsilon_{GEC} = (60 \pm 20)\%$. The source of

[4]It means that if our stripping was 100% efficient, then for a hypothetical ratio of merged to resolved of 2:1, the stripping efficiency would be 67% for merged π^0 and 33% for resolved π^0.

L0 TCK	$\mu_1 = 0.6$, 10 TeV (%)	$\mu_2 = 2.3$, 7 TeV (%)	Integrated $\mathcal{L}$ (pb^{-1})
0029	32.2 ± 0.7	28.9 ± 1.2	3.0
0031	32.2 ± 0.7	28.9 ± 1.2	0.1
0030	43.0 ± 0.7	40.1 ± 1.3	2.3
002a	35.0 ± 0.7	30.7 ± 1.2	14.4
002c	35.0 ± 0.7	30.7 ± 1.2	11.5
Average	35.3 ± 0.5	31.2 ± 0.8	sum = 31.3

Table 5.7: *Trigger efficiencies [73] for resolved π^0 split by L0 TCK. The average weighted by integrated luminosity is also given. The global event cut is not applied.*

this disagreement has not been understood yet and lies in the poor knowledge of the inclusive particle production in *pp* collisions. Thus the efficiency of the GEC has been scaled empirically [73] to fit the real data observation. This also the reason why it was separated from the ϵ_{trig}.

The selection determination efficiency will be described later. The efficiencies of all steps, except the selection, split for two simulation conditions($\mu_1 = 0.6$, energy in the mass-centre 10 TeV, and $\mu_2 = 2.3$, 7 TeV) can be found in the table 5.8. Additionally a comparison between the two samples is shown in the table 5.9.

	$\mu_1 = 0.6$, 10 TeV		$\mu_2 = 2.3$, 7 TeV	
	Merged (%)	Resolved (%)	Merged (%)	Resolved (%)
Generator level	16.98 ± 0.05		16.25 ± 0.05	
Stripping	1.83 ± 0.03	1.64 ± 0.03	1.54 ± 0.04	1.44 ± 0.04
Trigger (2010) Without GEC	52.2 ± 0.5	35.3 ± 0.5	48.8 ± 0.8	31.2 ± 0.8
Total	0.162 ± 0.003	0.098 ± 0.002	0.128 ± 0.003	0.076 ± 0.003

Table 5.8: *Efficiencies of various steps (generation, trigger and stripping) of the decay of $B_s^0 \to K\pi\pi^0$ for two MC samples.*

The comparison between the two Monte Carlo generations shows that the total efficiency for high$-\mu$ ($\mu_2 = 2.3$, 7 TeV) is only about 80% of the efficiency for $\mu_1 = 0.6$, 10 TeV. The result is similar for both merged and resolved π^0. With this information we can't yet determine what is the impact of the different number of interaction per bunch crossing and the different available energy. We will discuss it in the next two sections. Nevertheless it is well visible that the conditions used for the optimisation for the most of the elements used for the analysis of 2010 data (trigger and stripping) give higher efficiencies. And we know that these conditions are also more unrealistic.

	Ratio μ_2/μ_1	
	Merged (%)	Resolved (%)
Generator level	95.7 ± 0.4	
Stripping	84 ± 3	88 ± 3
Trigger (2010) Without GEC	93.5 ± 1.8	88 ± 3
Total	79 ± 2	76 ± 4

Table 5.9: *Ratio of various steps (generation, trigger and stripping) efficiencies efficiencies between two Monte Carlo samples: the* high μ *sample (μ_1 = 0.6, 10 TeV) and the* low μ *sample (μ_2 = 2.3, 7 TeV)*

5.5.4 Reconstruction ability

Even with the simulation we observed that there is a difference between two simulation conditions. It is worth to check if the efficiency of reconstruction of particles coming from our decay in both cases. We prepared two test samples of B^0_s candidates constructed from combinations of $K\pi\pi^0$ combinations without any cut except of the mass window cut (B^0_s mass $\pm$1000 MeV/c^2). Then we scanned the samples event by event. For each event we looped over the set of candidates, and for each candidate we check if it contains any particle which matches Monte Carlo daughter of B^0_s. If the answer is positive, we know that the daughter is reconstructed. If we are not able to find any candidate with a given daughter matched, then we assume that the particle is not reconstructed. The efficiencies of the reconstruction prepared with that procedure are given in the table 5.10. These values are not absolute reconstruction efficiencies, but include the acceptance and matching efficiencies.

Sample	Merged π^0 (%)	Resolved π^0 (%)	$\pi^\pm$ (%)	$K^\pm$ (%)
μ_1 = 0.6, 10 TeV	12.4 ± 1.0	21.8 ± 1.2	64.9 ± 1.6	68.0 ± 1.5
μ_2 = 2.3, 7 TeV	10.9 ± 1.0	25.4 ± 1.4	68.7 ± 1.5	67.9 ± 1.5

Table 5.10: *Efficiencies of the reconstruction of the daughter particles produced in the decay of $B^0_s \to K\pi\pi^0$ for two Monte Carlo samples.*

The comparison of the efficiencies estimated on the two samples (*low* μ: $\mu_1 = 0.6$, 10 TeV; and *high* μ: $\mu_2 = 2.3$, 7 TeV) shows no significant difference between them. The efficiencies for the charged particles are compatible. They are bit less than 70%, what can be a bit surprising, but for the explanation we can find immediately in the previous paragraph. The efficiencies for π^0 exhibit small leakage of merged π^0 into resolved π^0 for *high* μ respect the *low* μ. It is expected as the available energy in the interaction is also lower (7 TeV versus 10 TeV in the mass centre frame), which should impact momentum values from the B^0_s up to π^0. Only π^0 of the highest energy are reconstructed as merged, and thus the ratio of merged π^0 is lower in the sample at 7 TeV. It is compensated by larger fraction of resolved π^0. We can conclude that there is no significant impact of the change in the parameters of the energy and the

visible number of interaction on the efficiencies of the reconstruction of B_s^0 daughters. Hence, the difference between stripping and trigger efficiencies for two samples can not come from reconstruction.

5.5.5 Difference in kinematic and topology

The plots of the variables used in the stripping for both MC samples $\mu_1 = 0.6$, 10 TeV and $\mu_2 = 2.3$, 7 TeV are located in the Appendix C, in the figures C.5-C.8. There are small differences between distributions of the two samples. The global difference between efficiencies of stripping and trigger for both samples is a combination of multiple small differences. The effect seems to be shared between the kinematic variables (which exhibit different energies available) and the topological variables (which can be linked to the multiplicity effects).

5.5.6 Yields before selection

Reinvestigating the equations 5.3 and 5.4, it is possible to estimate the expected numbers of $B^0 \to K\pi\pi^0$ before the application of the selection. The inputs and the estimated yield for 2010 data are given in the table 5.11. The result is 160 ± 30 events with merged π^0, and 90 ± 20 events with resolved.

Variable	Merged	Resolved
$\mathscr{L}$	$32\ \text{pb}^{-1}$	
$\sigma_{b\bar{b}}$	$(284 \pm 20 \pm 49)\ \mu\text{b}$	
f_d	0.3 ± 0.1	
$BR(B^0 \to K\pi\pi^0)$	$(3.59^{+0.28}_{-0.24}) \cdot 10^{-5}$	
$\epsilon_{gen}\epsilon_{trig}\epsilon_{strip}$	0.128 ± 0.003	0.076 ± 0.003
ϵ_{GEC}	0.6 ± 0.2	
Yields	160 ± 30	90 ± 20

Table 5.11: *Yield formula inputs and the output for $B^0 \to K\pi\pi^0$ for 2010 data.*

5.6 Signal selection

5.6.1 Selection design

The selection of $B^0_{(s)} \to K\pi\pi^0$ decays was designed within the very convenient TMVA environment [94]. A conservative approach was chosen, and it was decided that the selection would be made with a Fisher discriminant. The discriminant was trained against the signal sample already described: the Monte Carlo sample of $B_s^0 \to K\pi\pi^0$ with $\mu_2 = 2.3$ and the energy in the centre of mass equal to 7 TeV. The background sample choice was more complicated. No proper model of the background was simulated. The only possibility of getting a reasonable background sample was to use the real data. The typical strategy of training against the combinations outside the

signal mass range was chosen. That approach ensures that no correctly reconstructed signal events are included in the background set. However it does not assure that all signal-like events are excluded from the sample.

The resolution of the $B^0_{(s)}$ reconstruction was predicted to be about 100 MeV/c^2. Thus it was decided that it would be safe to remove the candidates with the mass between B^0 mass minus 300 MeV/c^2, and $B^0_{(s)}$ mass plus 300 MeV/c^2. It means that the background sample was defined as $K\pi\pi^0$ combinations from the real data registered in 2010, which had passed the stripping cuts of the mass in one of two allowed ranges: [4200 MeV/c^2, 4980 MeV/c^2] and [5670 MeV/c^2, 6400 MeV/c^2].

The typical loose cut on particle likelihood was used: the charged pion log likelihood of being a kaon had to be lower than 0, and the kaon log likelihood of being a kaon had to be larger than 0. Additionally it was required that the event in which a candidate was registered had been triggered by at least one of the HLT2 lines: `B2HHPi0_Merged, B2HHPi0_Resolved, Topo0STF2Body`.

The selection was prepared independently for merged and resolved π^0. A list of variables used to build the discriminant is given in the table 5.12. Both samples: the signal and the background, were split equally into two subsamples: the training sample, and the testing sample. After the optimisation with the training sample, an efficiency test was performed on the test sample. From the results of the efficiency tests, the working points for the selections were chosen. The decision was made on the basis of the best signal over square root of the sum of signal plus background ($S/\sqrt{S+B}$). The number of signal was the estimated yield presented in the previous section. The number of background was the number of events in the real data after the stripping the range of $\pm$300 MeV/c^2 from the B^0 mass.

5.6.2 Signal and background modelling

In the next sections, we perform fits of a model which is constructed as a sum of a Gaussian for the signal and an exponential for the background. The background structure is predicted to be complicated, so a simple exponential may be not sufficient to model it properly. Thus, the result of the fits have to be considered with caution.

5.6.3 Merged π^0 results

The distributions of the discriminant response for the optimisation with merged π^0 for both the signal and the background are presented in the figure 5.6. Additionally a plot of the signal efficiency versus background rejection is given. From the optimisation the best signal significance cut was calculated to be at $Fisher > 0.03$. The corresponding signal efficiency for that cut was 66%, and the background rejection of 90%. The significance itself was estimated to be $S/\sqrt{S+B} = 1.5$. The efficiency on the signal results in an expectation of 106 ± 19 events of $B^0 \to K\pi\pi^0$ with merged π^0 with 2010 statistics.

The plot of the mass of the combination of $K\pi\pi^0$ is presented in the figure 5.7. The signal shape is not well established. Even if the number of signal events estimated from the fit (140 ± 40) is consistent with the expectation, the uncertainty is large. Similarly the other parameters of the fit.

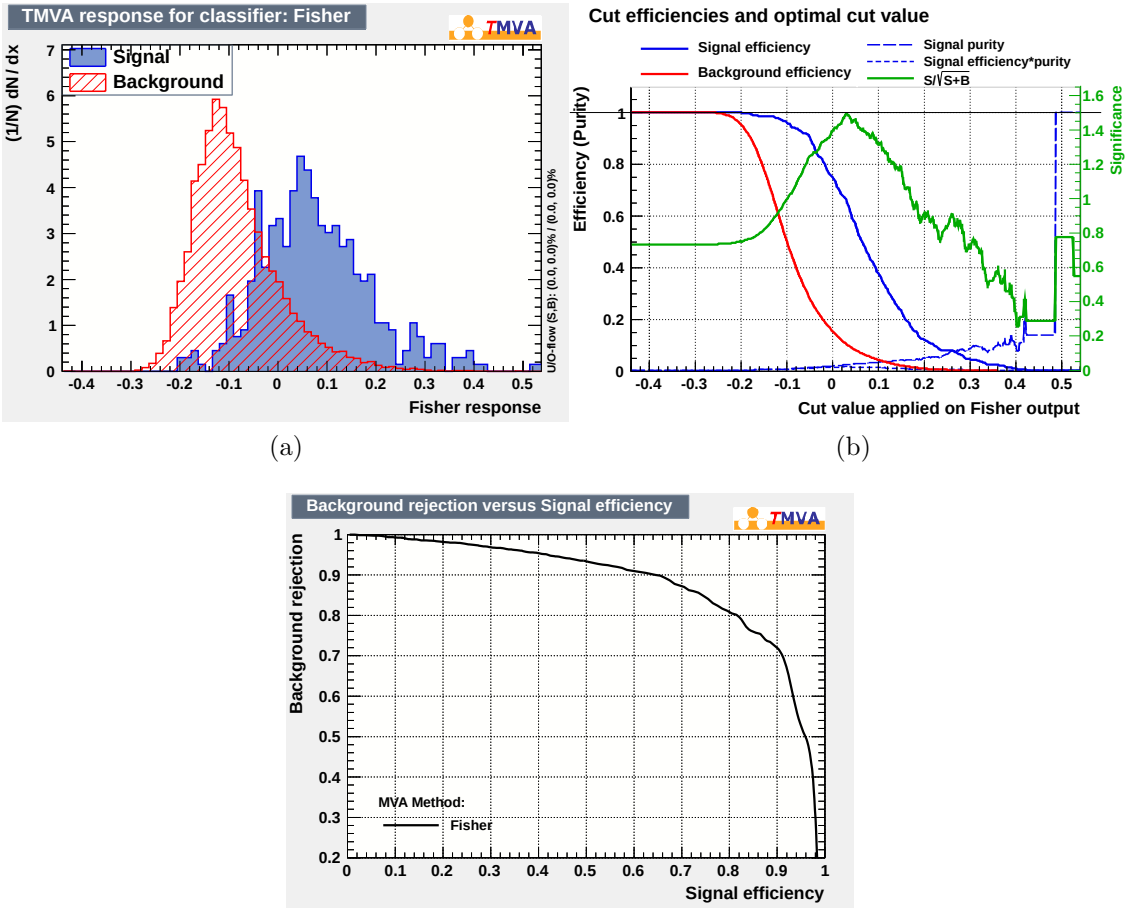

(a) (b)

(c)

Figure 5.6: *Fisher discriminant response (a), the efficiencies and the signal significance (b), and the signal efficiency against the background rejection (c) for the selection with merged* π^0.

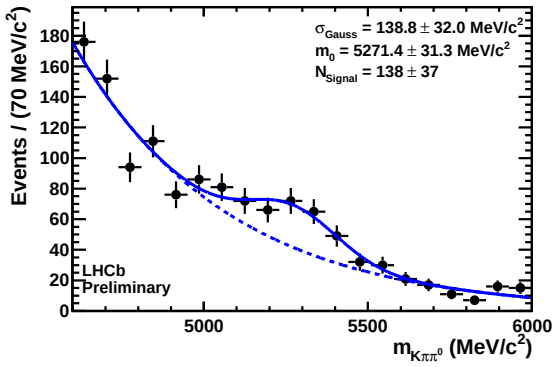

Figure 5.7: *Histogram of the mass of* $K\pi\pi^0$ *after the selection with Fisher discriminant with cut at* $Fisher > 0.03$. *The fit of a sum of a Gaussian and an exponential background is drawn.*

Variable	Description
$B0\_PT$	B transverse momentum
$B0\_IPCHI2\_OWNPV$	B primary vertex impact parameter significance
$B0\_DIRA\_OWNPV$	B pointing angle
$B0\_ENDVERTEX\_CHI2$	B end vertex fit χ^2
$B0\_FDCHI2\_OWNPV$	B flight distance significance
$Kminus\_PT$	kaon transverse momentum
$piplus\_PT$	pion transverse momentum
$pi0\_PT$	neutral pion transverse momentum
$Kminus\_IPCHI2\_OWNPV$	kaon primary vertex impact parameter significance
$piplus\_IPCHI2\_OWNPV$	pion primary vertex impact parameter significance
$gamma0\_PT$	transverse momentum of the lower transverse momentum photon (resolved only)
$gamma0\_P$	momentum of the lower transverse momentum photon (resolved only)
$gamma\_PT$	transverse momentum of the higher transverse momentum photon (resolved only)

Table 5.12: *List of variables used to build the Fisher discriminant.*

It is worth looking more deeply into the internal structure of the background. A contour plot of the B mass versus the mass of the combination of $K\pi$ (figure 5.8) exhibits two regions. The first is at the mass of B^0 and the mass of K^{*0} from $K\pi$. The second is located at masses lower than the proper B^0 mass, and at the mass of D^0. It is a background coming from the decays of B into D^0. We can easily remove this background with a cut on the mass of the combination of $K\pi$. We should clear the D^0 by removing: $|m_{K\pi} - m_{D^0}| > 200$ MeV/c^2. The result after the purification is presented in the figure 5.9. Now the signal shape is better visible – the significance has raised. However still the shape of the modelled, exponential background is not perfect. The number of signal events from the fit is 139 ± 31, so close to the expectation.

We can try to examine more deeply the second, interesting region from the contour plot – K^{*0}. To do that we require that the mass of the combination of $K\pi$ is within the range: $|m_{K\pi} - m_{K^{*0}}| < 150$ MeV/c^2. Using this cut we plot again the mass of $K\pi\pi^0$ (figure 5.10). The signal Gaussian shape is visible very well (75 ± 13 events). This number is much larger than estimated predicted yield for the decay $B^0 \to K^{*0}\pi^0$ (assuming table 5.11, selection efficiencies, $BR(B^0 \to K^{*0}\pi^0) = (3.6 \pm 0.8) \cdot 10^{-6}$ [2], the estimated yield is 7 ± 3). This allows to consider that there can be a specific physical background which contributes to the peak. It can be the decay of $B^0 \to K^{*0}\gamma$, which branching ratio $BR(B^0 \to K^{*0}\gamma) = (4.33 \pm 0.15) \cdot 10^{-5}$ [2] is comparable to charmless $B^0 \to K\pi\pi^0$. The decay can fill the region when the photon is misidentified as π^0. Thus a dedicated method of discrimination between π^0 and γ is needed – it will be described in the next chapter.

Coming back to the fit, the central value of the mass fit is shifted towards larger

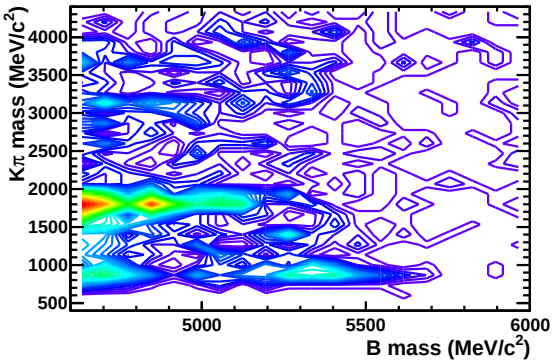

Figure 5.8: *Contour plot of the mass of* $\mathrm{B_{(s)}}^0$ *candidates versus the mass of the combination of* $K\pi$*. The candidates have to pass the merged* π^0 *selection of* $Fisher > 0.03$*.*

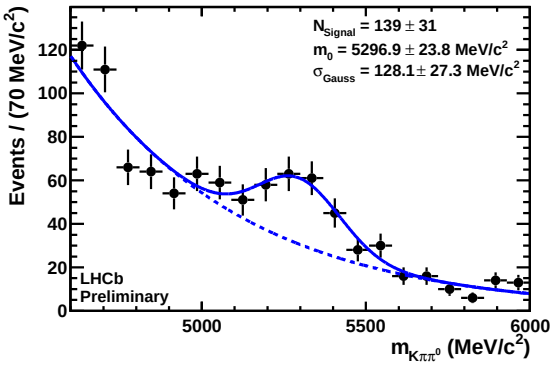

(a)

Figure 5.9: *Histogram of the mass of* $K\pi\pi^0$ *with merged* π^0 *and* D^0 *background removed. The selection is made with Fisher discriminant with cut at* $Fisher > 0.03$*.*

values than the B^0 mass, but the result is still consistent with B^0 PDG mass. The shift may come from the imperfect background shape which seems not to model properly the low mass region, which is polluted by different background types than just a pure combinatorial.

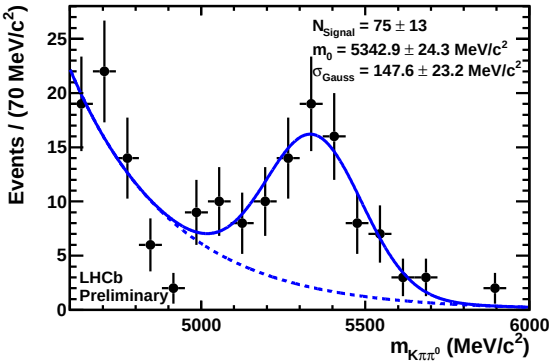

(a)

Figure 5.10: *Histogram of the mass of $K\pi\pi^0$ with merged π^0 requiring that $K\pi$ form the resonance of $K(892)^{0*}$.*

5.6.4 Resolved π^0 selection

The selection for resolved π^0 was optimised similarly to the merged one. The Fisher discriminant response and the signal efficiency against the background selection is shown in the figure 5.11. The best significance estimated is equal to 0.8. The corresponding cut for the discriminant value is $Fisher > 0.03$. The signal efficiency for this cut is equal to 64%, and the background rejection is equal to 92%. Applying it to the 2010 data one can expect 58 ± 12 events of signal of $B^0 \to K\pi\pi^0$.

Applying the selection to the data registered in 2010 we obtain the histogram in the figure 5.12. No signal peak is observed. We can try to cut harder on the discriminant response: at the value of 0.13. The signal efficiency estimated on the Monte Carlo with this cut is 19%, which means that we should observe about 25 events in the data from 2010. The results with this cut are presented in the figure 5.13. A small bump (15 ± 7 events) is present. On the other hand this value is still consistent with no observation of signal at all. The background shape seems again to be not mastered enough.

5.7 $KK\pi^0$ mode

An exercise of applying the selection with merged π^0 to the sample of $KK\pi^0$. For each kaon a cut on the log likelihood of being a kaon is applied: $pidK_K > 5$. The result is presented in the figure 5.14.a). Again a fit of a sum of a Gaussian and an exponential is performed. Clearly we can state that we observe a peak (55 ± 15 events from the fit of the signal). However when we compare the signal mass range with the mass of the

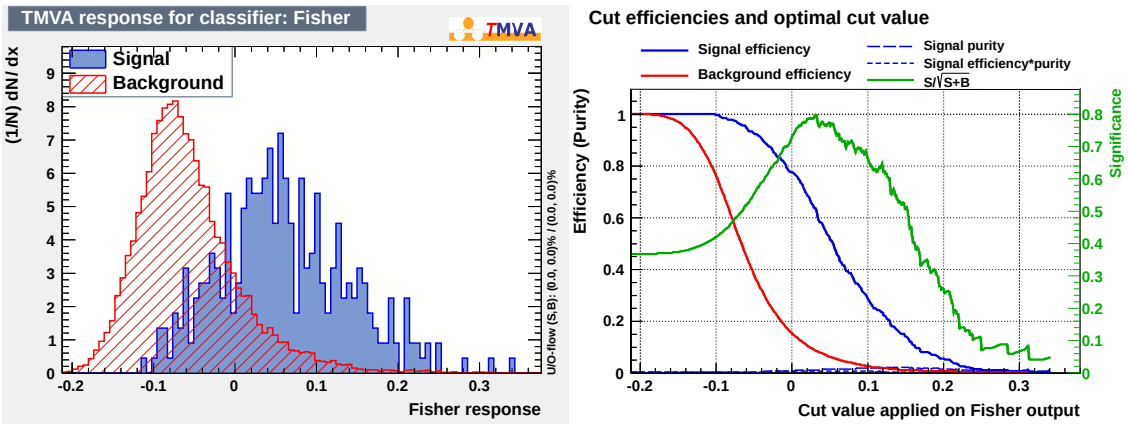

(a) (b)

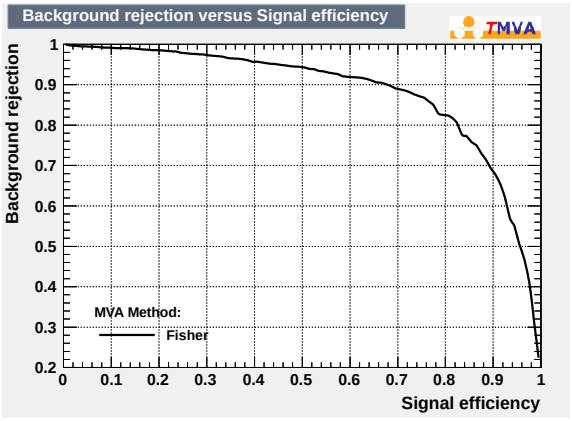

(c)

Figure 5.11: *Fisher discriminant response (a), the efficiencies and the signal significance (b), and the signal efficiency against the background rejection (c) for the selection with resolved* π^0.

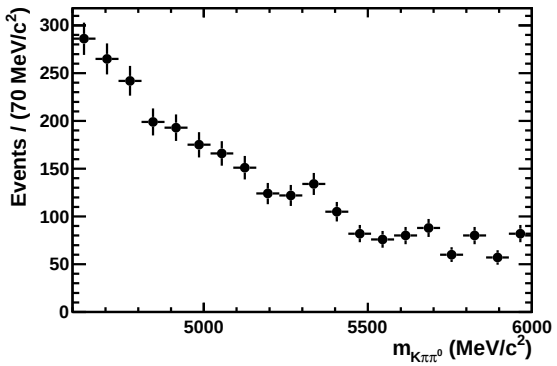

Figure 5.12: *Histogram of the mass of* $K\pi\pi^0$ *with resolved* π^0*, after the selection with Fisher discriminant with cut at* $Fisher > 0.03$*, which is the best* $S/\sqrt{S+B}$ *cut..*

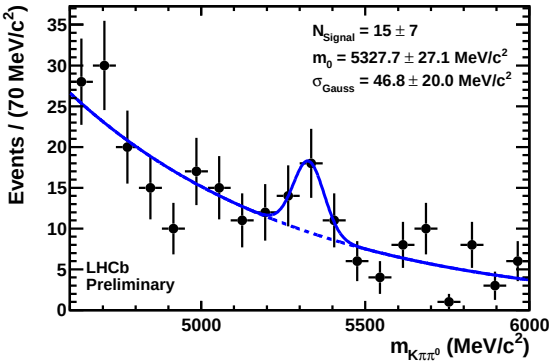

Figure 5.13: *Histogram of the mass of $K\pi\pi^0$ with resolved π^0, after the selection with Fisher discriminant with cut at Fisher > 0.13*

combination of two kaons (figure 5.14.b), then we see that two kaons most likely come from a resonance which has to be Φ. Again, a contribution of $B^0_s \to \Phi\gamma$ radiative decays must be expected. However, under the mass of B^0_s not only Φ is present, and this means that we can observe hints of charmless decays of $B^0_s \to KK\pi^0$. Further and more detailed analysis is needed, especially to purify the sample from γ background.

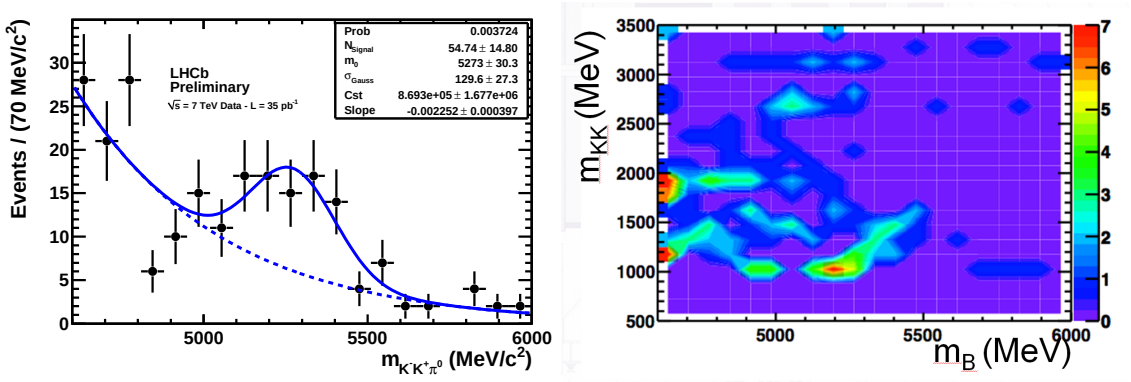

(a) (b)

Figure 5.14: *a) The histogram of the mass of $KK\pi^0$ built with merged π^0, after the selection with Fisher discriminant with cut at Fisher > 0.02. b) The contour plot made with the same selection presenting the mass of the B candidate versus the mass of the system of KK. The Φ resonance is observed.*

5.8 $\pi\pi\pi^0$ mode

A similar analysis to the presented here for $K\pi\pi^0$ was performed by [73] for $B^0 \to \pi\pi\pi^0$. The same stripping was used, but the Monte Carlo signal sample was different – the sample of $B^0 \to \pi\pi\pi^0$ decays. When using the Fisher discriminant one can expect to find 39 events of merged π^0 and 15 events of resolved π^0 signal. The significances

are accordingly 3.0 and 1.4. It is already visible that the expectation from 2010 data are very modest.

The results of the application of the selection to the real data are given in the figure 5.15 (merged π^0) and in the figure 5.16 (resolved π^0). For each histogram a fit of a sum of a Gaussian and an exponential is made.

The result of the fit in terms of the number of signal events for merged π^0 is 40 ± 20 with the Fisher discriminant. The fit and the histogram shows only a small hints of the signal.

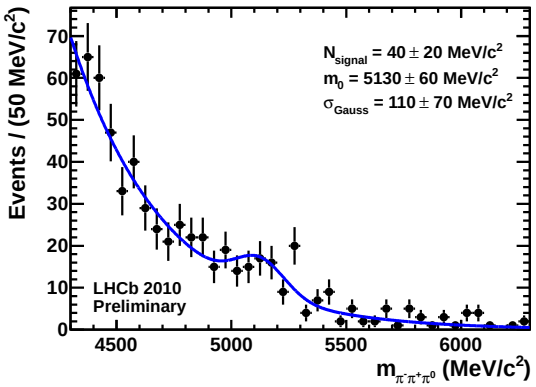

Figure 5.15: *Mass of $\pi\pi\pi^0$ built with merged π^0 with a dedicated selection made with a Fisher discriminant. The selection is optimised for the best $S/\sqrt{S+B}$. Plots from [73].*

The result of the fit for resolved π^0 is 15 ± 8 signal events. Even if there is a small bump as a result of the fit, the number is consistent with 0. With this statistics it is impossible to claim that an observation is made.

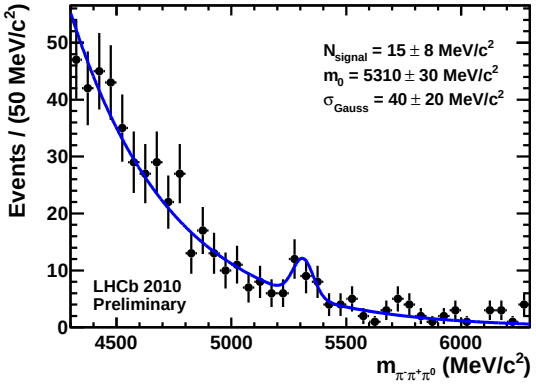

Figure 5.16: *Mass of $\pi\pi\pi^0$ built with resolved π^0 with a dedicated selection made with a Fisher discriminant [73].*

The expectation from the efficiencies of the discriminants on the signal combined with the statistics of the year 2010 gives very low numbers. Adding a non-reducible

background, the significance of the signal is reduced so much that it is impossible to state firmly that the signal is observed.

5.9 Summary

The first, exploratory work on charmless neutral B mesons decays into finals states of $hh\pi^0$ took place in the very same moment of the recalibration of the calorimeters (suffering from an ageing under the operation of the LHC). The modest statistics does not allow to conduct the necessary splitting of the data in regions of the detection and along the converted/unconverted nature of the clusters. Still, charmless $hh\pi^0$ signals have been observed and the contamination of radiative decays have been spotted. The current design of the π^0/γ separation is not satisfactory to quantify the effect and this point is the subject of the next chapter.

Chapter 6

π^0/γ separation

In the previous part the first results of $B \to K\pi\pi^0$ and $B \to KK\pi^0$ obtained with 2010 statistics were presented. However the signal may be largely contaminated by a specific kind of background – the combinations with photons which mimic π^0. In this chapter we will give a solution, which allows selection of purified sample of π^0. On the other hand, this selection is capable of removing π^0, and it will be used in the analysis of $B^0 \to K^*\gamma$ and $B_s^0 \to \phi\gamma$. The results for π^0 will be mainly presented in this chapter. Nevertheless the results for γ selection will be presented in the end.

We aim at producing efficiency versus purity performance of the tool directly from the data. This is the purpose of a dedicated calibration stream of the LHCb stripping, which reconstruct prompt $D^0 \to K\pi\pi^0$.

The work described here implies colleagues from the Barcelona Group (M. Calvo and R. Vasquez). The target is to produce the tool and the calibration tables by the end of the year 2011. This chapter discusses the state of art of the development.

6.1 $B \to X\gamma$ physics

Radiative penguin decays are a good and sensitive laboratory for tests of Standard Model. The radiative penguin of B are induced by flavour changing neutral currents and are sensitive to new couplings from beyond the SM physics. On the other hand radiative B decays give access to the ratio of $|V_{td}/V_{ts}|$ other than from $\Delta m_d/\Delta m_s$ [95].

CP violation in radiative B decays may be measured in two ways. The first mechanism is a direct CP violation (CPV) which results in a difference of the decay rates of $B \to X\gamma$ and $\overline{B} \to \overline{X}\gamma$. The prediction for SM are that direct CP violation is lower than 1% for $B \to s\gamma$ and lower than 16% for $B \to d\gamma$ [96]. However some SM extensions give a space for direct CP asymmetries up to $10\% - 40\%$ from contributions of new particles [97]. Unfortunately the experimentally accessible cases are more difficult from the theoretical point of view. The other possibility is a mixing induced CP violation which occurs when a neutral B meson and the charge conjugate of it have transitions to the same final state $X^0\gamma$. A review of these measurements can be found in [98].

The LHCb experiment can bring new measurements in these areas. The first is the measurement of the branching ratio of $B_s^0 \to \phi\gamma$. But the core of the radiative programs is the proton polarisation. Which cannot be measured directly with $b \to s\gamma$ transitions but is addressible in time dependent measurements of $B_s^0 \to \phi\gamma$.

These are the perspectives for the experiment, while the situation as it is in the beginning of the year 2011 just allows to establish observations of the important modes for the future analyses. The results with the 2010 integrated luminosity of about 37 pb^{-1} can be found in [99]. Two plots are also presented here: the $B^0 \to K^*\gamma$ signal in the figure 6.1, and the $B_s^0 \to \phi\gamma$ signal in the figure 6.2. The statistics 30 times larger will be available at the end of the year 2011.

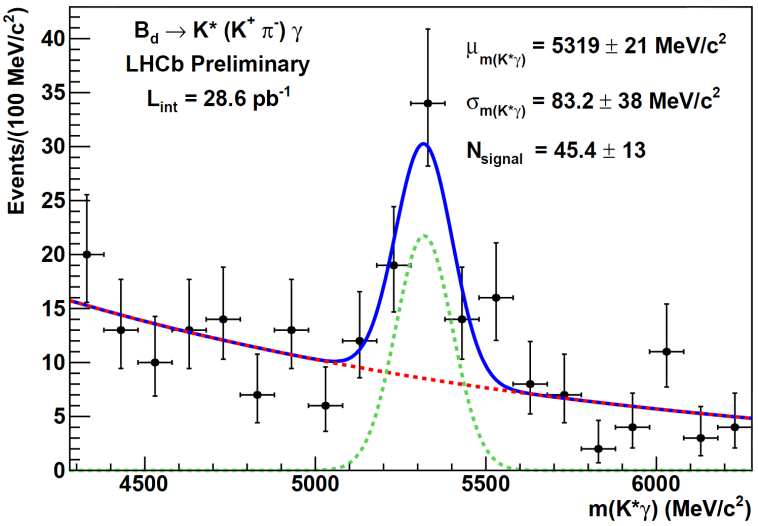

Figure 6.1: *The $B^0 \to K^*\gamma$ signal from the entire 2010 data set, corresponding to about* 37 pb^{-1} *of integrated luminosity [99].*

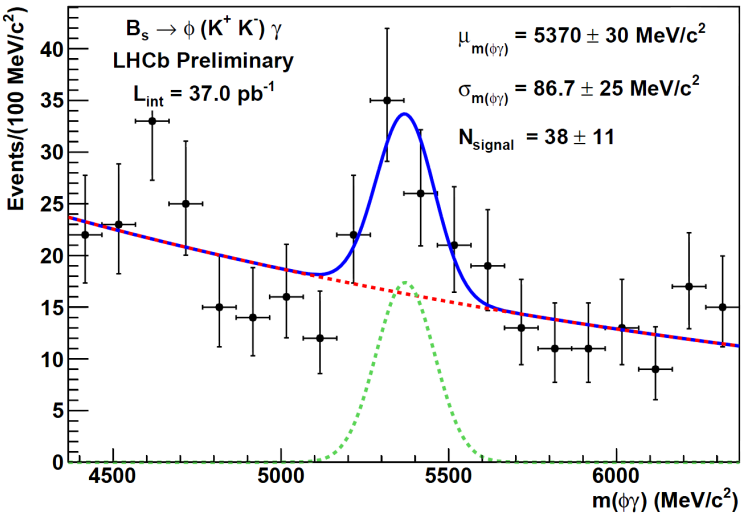

Figure 6.2: *The $B_s^0 \to \phi\gamma$ signal from the entire 2010 data set, corresponding to about* 37 pb^{-1} *of integrated luminosity [99].*

6.2 K$\pi\pi^0$ and K$^*\gamma$ case

In the previous chapter the plots of K$\pi\pi^0$ combinations were presented, searching for decay of $B^0_{d/s} \to K\pi\pi^0$. We have discussed the likely contamination of the radiative decay $B^0 \to K^*\gamma(K^* \to K\pi)$. Kinematic and topological variables for these two decays are similar. Background events from $B^0 \to K^*\gamma$ will pass the selection (with a global efficiency similar to $B^0 \to K\pi\pi^0$). An example can be found in the figure 6.3 which is a reconstructed mass histogram from K$\pi\pi^0$ combinations with merged π^0 with MC10 simulation of $B^0 \to K^*\gamma$.

Hence, without accessing to calorimetric data, it is impossible to distinguish event by event π^0 from γ. However it is possible to observe statistically how often photons sneak through the selection. In the figure 6.4 three histograms of merged π^0 mass are presented. The plots are made for two signal samples: $B^0_s \to K\pi\pi^0$, $B^0 \to K^*\gamma$, and for 2010 data. The histograms are filled with particles that build B^0 from $K\pi\pi^0$ which pass the selection described in the previous chapter. One can observe an evident difference in reconstructed π^0 mass from π^0 and γ samples, where γ are much more probable to have lower masses. Additionally the comparison proves that 2010 data candidates are not only consisted of γ.

There are two clear objectives of the analysis. The first is to build a discriminant π^0 versus γ from calorimeter information. the second is to assign quantitative data-driven performances of this discriminative tool.

Finally it is essential to mention that the problem of misidentified photons is not present for candidates with resolved π^0.

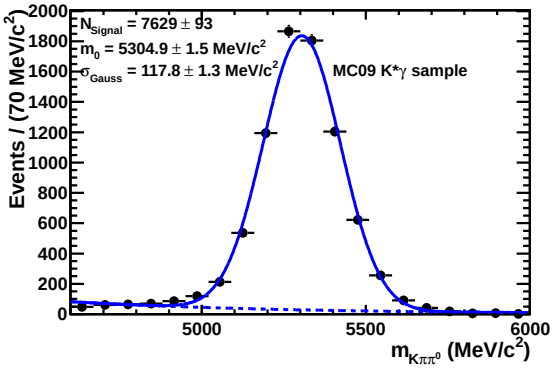

Figure 6.3: *Distribution of mass of combination of $K\pi\pi^0$ with merged π^0 obtained from MC09 $B^0 \to K^*\gamma$ sample with $\mathrm{B}^0_\mathrm{s} \to hh\pi^0$ stripping and $K\pi\pi^0$ selection applied.*

6.3 Discriminant construction

Merged π^0 are defined as an unique cluster inside the calorimeter. We will scrutinise in the following the characteristics of such a cluster and how it is different from a single γ cluster. Among the natural variables one might think about energy asymmetry and skewness of the cluster as the basis of the discriminant.

The first discriminant was based on the ECAL variables only. We came with the idea that the PRS can help with the discrimination. The motivation was rather clear: usually development of cascade starts before ECAL. Adding the preshower information may improve the efficiency, as this allows to measure shower transverse distribution at two stations. The next sections will concentrate on presentation of variables used to build the discriminants, computations of efficiencies of detectors alone and combined, and investigation usefulness of the detectors for π^0/γ separation. Let us start with the ECAL.

6.3.1 ECAL variables

An ECAL cluster [100] is a set of nine cells (three by three) built around a local maximum of the energy deposit. Let us define a local numbering of the cells inside the cluster as in this table[1]:

7	8	9
4	5	6
1	2	3

By construction, the cell with the largest deposit is the central cell (5), denoted also as *seed*. It is required that the transverse energy of the largest deposit is greater than 50 MeV. For all cells in the cluster we define ϵ_i as the energy deposit of the cell i. The global position of the cell is denoted by x_i and y_i.

An original concept of the method presented in 2003[101] contained 4 variables:

[1]This representation is valid for most of the cells. However, it has to be modified for cells located near the boundaries. The modified cluster definition does not change the definitions of the variables used to built the discriminant.

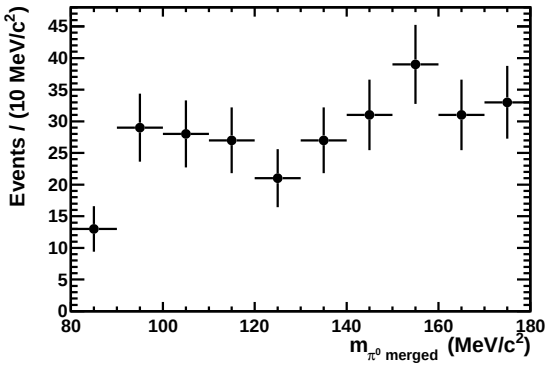

(a) Homemade MC09 K$\pi\pi^0$

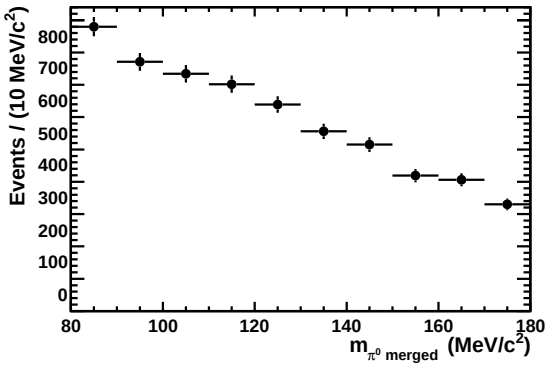

(b) MC09 K$^*\gamma$

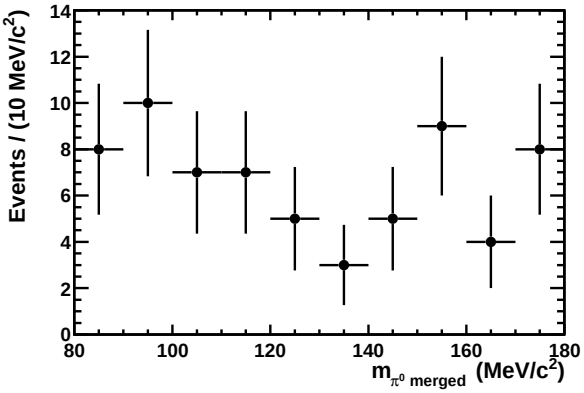

(c) 2010 data

Figure 6.4: *Distributions of mass of merged π^0 from combinations of $K\pi\pi^0$ which pass $\mathrm{B}^0_\mathrm{s} \to hh\pi^0$ stripping and $K\pi\pi^0$ selection from samples: a) dedicated MC09 of $\mathrm{B}^0_\mathrm{s} \to hh\pi^0$, b) MC09 $B^0 \to K^*\gamma$, c) 2010 data.*

- $r2$
  which can be interpreted as a second order momenta of internal spread inside a cluster. It is defined as:

$$r2 =< r^2 >= S_{xx} + S_{yy} = \frac{\Sigma_i \epsilon_i ((x_i - x_c)^2 + (y_i - y_c)^2)}{\Sigma_i \epsilon_i}, \tag{6.1}$$

  where

$$x_c = \frac{\Sigma_i \epsilon_i x_i}{\Sigma_i \epsilon i}$$
$$y_c = \frac{\Sigma_i \epsilon_i y_i}{\Sigma_i \epsilon i}.$$

- $r2r4$
  which is defined as:

$$r2r4 = 1 - (< r^2 >^2 / < r^4 >) = \frac{\Sigma_i \epsilon_i ((x_i - x_c)^4 + (y_i - y_c)^4)}{\Sigma_i \epsilon_i}. \tag{6.2}$$

  The variable contains information about the importance of tails in energy deposits in a cluster. It describes how spiky is the cluster.

- Asymmetry $asym$ defined as:

$$asym = \frac{S_{xy}}{\sqrt{S_{xx} S_{yy}}} = \frac{\Sigma_i \epsilon_i (x_i - x_c)(y_i - y_c)}{\sqrt{(\Sigma_i \epsilon_i (x_i - x_c))\,(\Sigma_i \epsilon_i (y_i - y_c))}}, \tag{6.3}$$

  which measures orientation of a cluster of an ellipsoidal shape.

- κ – kappa value describing how squeezed is a cluster and is defined as:

$$\kappa = \sqrt{1 - 4\frac{S_{xx} S_{yy} - S_{xy}^2}{(S_{xx} + S_{yy})^2}} = \sqrt{1 - 4\frac{\det S}{\mathrm{Tr}^2 S}}, \tag{6.4}$$

  where again:

$$\begin{aligned} S_{xx} &= \frac{\Sigma_i \epsilon_i (x_i - x_c)^2}{\Sigma_i \epsilon_i}, \\ S_{yy} &= \frac{\Sigma_i \epsilon_i (y_i - y_c)^2}{\Sigma_i \epsilon_i}, \\ S_{xy} &= \frac{\Sigma_i \epsilon_i (x_i - x_c)(y_i - y_c)}{\Sigma_i \epsilon_i}. \end{aligned}$$

These variables measure different characteristics of cascade signal shape in the cluster. They are strongly correlated and it is necessary to use a multivariate analysis technique to benefit numerically from their discriminative power. Additionally to these variables, three energy depend were added[102]:

- E_{seed} – the largest energy deposit in a cluster divided by the total energy in the cluster.

- E_{2nd} – the sum of the largest energy deposit and the second largest energy deposit divided by the total energy in the cluster.

- $E_{cluster}$ – the energy of a cluster.

Again internal correlations between these variables and correlations between them and geometrical variables are predicted.

In the presented set, all variables except of $E_{cluster}$ are independent of absolute energy. $E_{cluster}$ must be considered with caution. It is not a discriminative variable itself, but a control variable. the final tool is currently developed without this variable, but the results gathered in this chapter contain it in order to make a fair comparison with the previous tool.

6.3.2 PRS variables

The nature of the discrimination between merged π^0 and γ is obviously identical in the preshower and one is tempted to build the same variables as for the ECAL. Some comments are given here in order to introduce the differences. The first limitation respect to ECAL is the frequency of saturation of at least one channel. The PRS dynamics is 10-bits, limited at the energies of deposit $\sim$ 300 MeV. Often when a cascade starts to develop before scintillator, a flux of particles is so intensive that it results in a signal larger than the limit of analog-digital converters. On the other hand, sometimes a photon (or eventually but less probable a pair of photons) doesn't leave any energy above TELL1 threshold in PRS. Both cases can result in distributions that are not smooth in some regions, but rather like steps or boolean information (there is no signal/there is something, there is an overflow/the signal is measurable). Finally a set of variable was chosen. Even if some are less powerful than the other (like asymmetry and kappa) they are kept to give some help in cases where other variables fail, because their correlation with the others is very modest. Here is the full list of the variables:

- $sumE = \Sigma_i \epsilon_i$
  A simple sum of energies in all cells of the cluster. Differently from ECAL cluster energy, this variable does not depend much on the particle energy.

- $r_{Ectr} = \frac{\epsilon_5}{sumE}$
  A fraction of the total energy in the PRS cluster deposited in the central cell of the cluster. If no energy in the preshower is deposited then the value of 1 is set. A small value of r_{Ectr} indicates a cluster with a small spread, hence signs off statistically a merged π^0.

- $E_{corner} = max(\epsilon_4 + \epsilon_1 + \epsilon_2, \epsilon_2 + \epsilon_3 + \epsilon_6, \epsilon_6 + \epsilon_9 + \epsilon_8, \epsilon_8 + \epsilon_7 + \epsilon_4)$
  A maximum energy deposited in one of the corners of the cluster. Again, it is a measure of the skewness of the PRS cluster. A low E_{corner} values statistically signs a photon.

- r_{1st}
  A ratio of the largest energy deposit to the total energy in the PRS cluster

$sumE$. When the sum is equal to 0, the value assigned to this variable is equal to 1. Values close to 1 are expected for γ.

- r_{2nd}
  A ratio of the second largest energy deposit to the total energy in the PRS cluster. When $sumE = 0$ the variable is defined to be equal to 0.
- $ar2$
  Defined as $r2$ for ECAL.
- $ar2r4$
  Defined as $r2r4$ for ECAL.
- $asym$
  Defined as $asym$ for ECAL.
- κ
  Defined as κ for ECAL.
- $multi_0, multi_{15}, multi_{30}, multi_{45}$
  A set of four multiplicities, for each a different threshold is set. The threshold is a minimum energy in MeV that has to be found in a cell to count it as a cell that contains the signal. For example $multi_{30}$ is the total number of cells in the cluster for which the deposits are larger than 30 MeV. The multiplicities have to be strongly correlated, however they work a bit differently for different regions. The set of four was chosen with a hint from the first pre-optimisation that the best separation between signal and background is obtained for $multi_{30}$ and $multi_{40}$.

The variables derived from the ECAL variables are calculated with a small modification respect to the ECAL variables. Whenever x or y is used, it is defined as:

$$x_i = \begin{cases} -1 & \text{when} \quad i \in \{1,4,7\} \\ 0 & \text{when} \quad i \in \{2,5,8\} \\ 1 & \text{when} \quad i \in \{3,6,9\}, \end{cases}$$

$$y_i = \begin{cases} -1 & \text{when} \quad i \in \{1,2,3\} \\ 0 & \text{when} \quad i \in \{4,5,6\} \\ 1 & \text{when} \quad i \in \{7,8,9\}. \end{cases}$$

This definition is independent of cell size and thus independent of region. However the same electromagnetic cascade will give different values for different regions with that definition.

6.4 Discriminant optimisation

6.4.1 Basics

6.4.1.1 Discriminant type

It was decided that for optimisation and application TMVA framework[94] should be used. A boosted decision tree (BDT) type discriminant was chosen. The first

check showed that it is similarly powerful in terms of discriminative power as neural networks, while it needs significantly less time for the optimisation process. Let us note that a MLP was used with the previous optimisation with the ECAL variables only. The final choice for the discriminant will be a neural network.

6.4.1.2 Signal sample

The signal sample used for the optimisation was the Monte Carlo sample described in the previous chapter. It was a dedicated set of 200 thousand events of MC09 simulated data $B_s^0 \to K\pi\pi^0$ with beam energy equal to 3.5 TeV and realistic number of visible interactions per bunch crossing set to 2.3. Only the candidates of $K\pi\pi^0$ which passed the merged π^0 selection described in the previous chapter were chosen.

6.4.1.3 Background sample

A background sample was Monte Carlo MC09 official production of $B^0 \to K^*\gamma$ with the statistics of a bit more than 1081 thousand of events. Exactly the same procedure of creation and selection of candidates was applied as for signal. It means that for each event, candidates of $K\pi\pi^0$ with merged π^0 which pass the selection were selected.

6.4.1.4 Kinematic distributions

π^0 and γ discrimination depends on kinematic regime. It was already mentioned in the section 5.2 that π^0 photon separation depends on the momentum. The distributions of momentum and transverse momentum of π^0 candidates built from the Monte Carlo samples of $B_s^0 \to K\pi\pi^0$ and $B^0 \to K^*\gamma$ are presented in the figure 6.5.

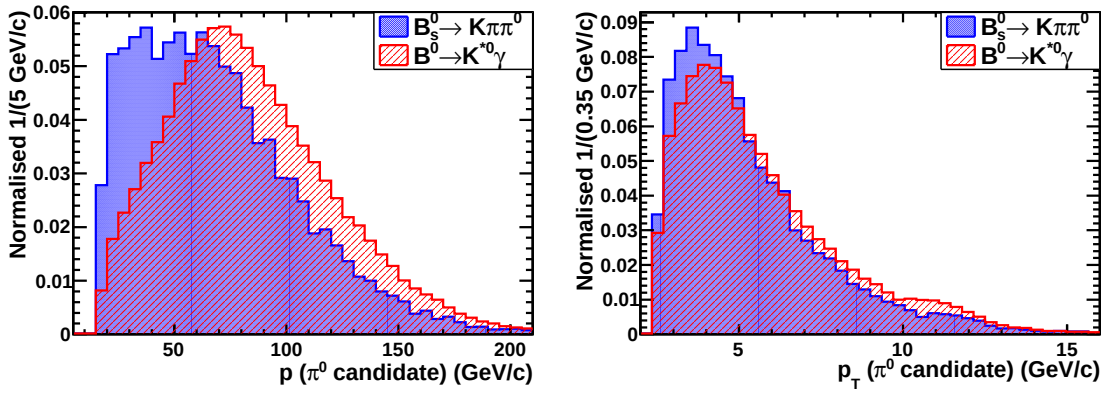

(a) (b)

Figure 6.5: *Momentum (a) and transverse momentum (b) distributions for π^0 candidates constructed from Monte Carlo samples of $B_s^0 \to K\pi\pi^0$ (blue) and $B^0 \to K^*\gamma$ (red).*

6.4.1.5 Optimisation

The discriminant was trained independently for each region of the calorimeter: inner, middle and outer. It was first trained with ECAL variables only to check the reported [102] results with the signal and the background proper for this case. Next it was trained with PRS variables only to check how efficient the preshower can be alone. Finally the optimisation with all variables included was done.

The optimisation was done in two steps: training and testing. The statistics used for the optimisation was 5546 events for the signal and 34059 events for the background. The samples were split equally and randomly between training and testing. None of training was found to be overtrained.

It is interesting to look at distributions of the variables used for the optimisation. Because of the number of plots (20 variables times 3 regions equal to 60) they can be found in the Appendix C. Additional plots from the optimisations, like linear correlations are also presented there.

6.4.2 Optimisation with ECAL variables only

The results in terms of histograms of discriminant response for the signal and the background for optimisation with ECAL variables only are presented in the figure 6.6. Additionally efficiency and rejection fraction curves are available. The characteristic values are grouped in the table 6.1. Some of the variables are highly correlated, like $ar2r4$ and E_{seed} for which the correlation is from 52% to 78% depending on the region, for both the signal and the background. Typical performances are: signal efficiency of 80%, and efficiency on background of 70%. Interestingly, the best efficiency if found in the middle region, while the inner is the second in terms of efficiency on the signal. It can be understood as the middle receives a significantly smaller flux of particles than inner while the granularity is still quite good.

Region	B=0.01	B=0.10	B=0.30
Inner	0.234	0.609	0.810
Middle	0.263	0.648	0.838
Outer	0.229	0.540	0.787

Table 6.1: *π^0 signal selection efficiency with the boosted decision tree discriminant optimised with the ECAL variables. Columns for corresponding values of efficiencies on background γ sample B equal to 0.01, 0.10 and 0.30.*

6.4.3 Optimisation with PRS variables only

The second step of this analysis was to consider the preshower variables alone. The results are given in the figure 6.7 with an extraction of three working points in the table 6.2. The distributions are more spiky than in the ECAL only discriminant which is a result of spikes in variables distributions for events where there is no signal in PRS or there is only one cell of PRS above TELL1 threshold. The efficiencies are

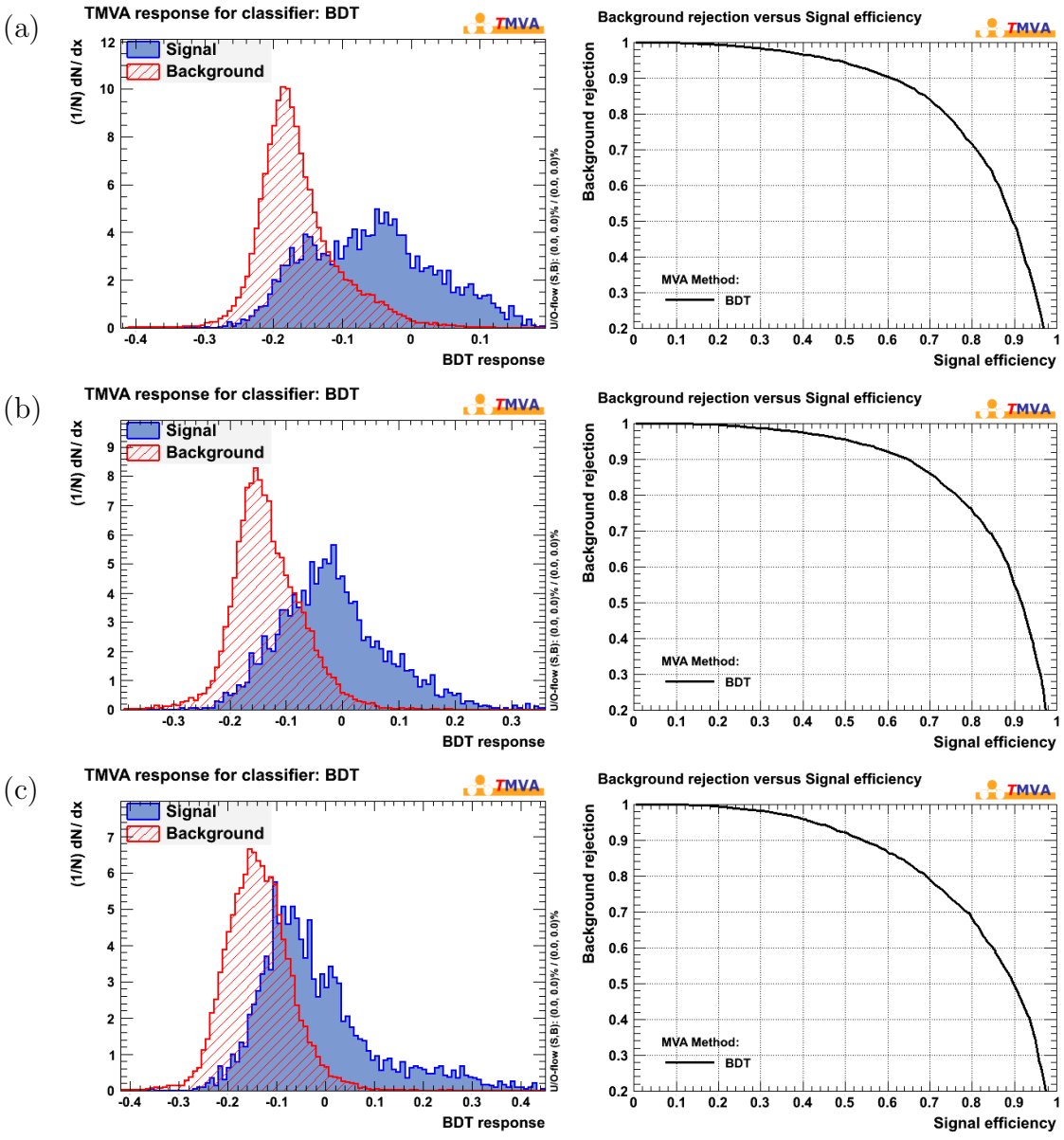

Figure 6.6: *π^0/γ discriminant training control plots. Optimisation with the ECAL variables only. In the left column the discriminant response for signal (π^0) and background (γ). In the right column: γ rejection against π^0 selection efficiency. Three regions are optimised independently: a) inner, b) middle, c) outer.*

slightly lower than for ECAL. The preshower alone can reject 70% of photons, while the efficiency on π^0 is 70%.

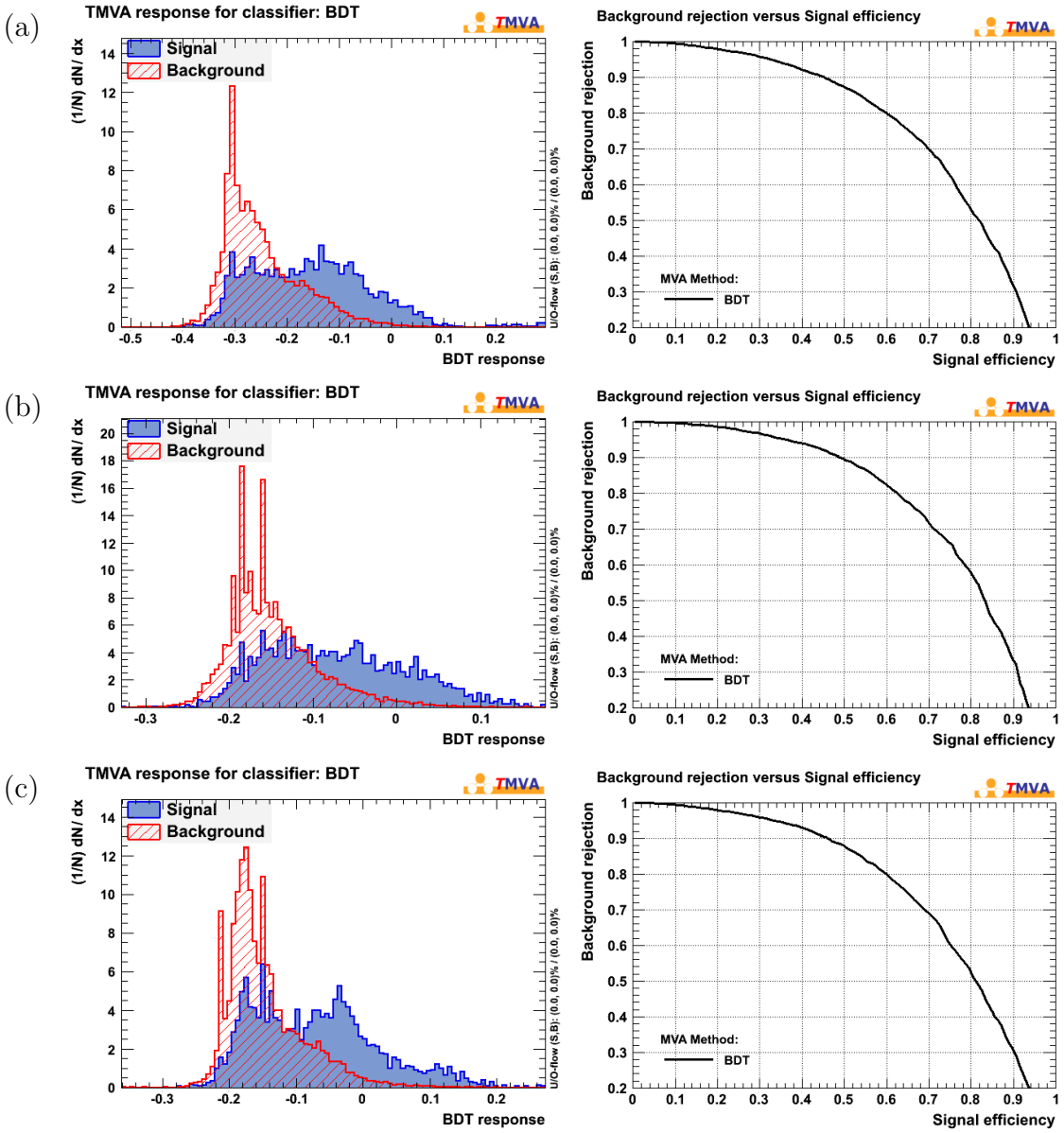

Figure 6.7: *π^0/γ discriminant training control plots. Optimisation with the PRS variables only. In the left column the discriminant response for signal (π^0) and background (γ). In the right column: γ rejection against π^0 selection efficiency. Three regions are optimised independently: a) inner, b) middle, c) outer.*

In case of this discriminant the geometrical, variables: $ar2$, $ar2r4$, *kappa* and *asym* are less powerful than deposits ratios and multiplicities. Though their correlations with any other variables are very low, with an exception of correlations between $ar2$ with r_{E2nd} and $ar2$ with r_{E1st}, which reaches about 50% to 60%. Because of these low correlations they are useful even if their discriminative power is not very impressive.

Region	B=0.01	B=0.10	B=0.30
Inner	0.130	0.451	0.699
Middle	0.166	0.489	0.712
Outer	0.127	0.460	0.691

Table 6.2: *π^0 signal selection efficiency with the discriminant optimised with the PRS variables. Columns for corresponding values of efficiencies on background γ sample B equal to 0.01, 0.10 and 0.30.*

6.4.4 ECAL and PRS optimisation comparison

A comparison of the two discriminants was done (figure 6.8). The whole statistics of both π^0 and γ samples was used to produce the plots. The responses of the discriminants built on PRS variables only and ECAL variables only were measured simultaneously. The comparison shows that correlation between the two is visible for both π^0 and photons. However measured linear correlation between ECAL and PRS is within 30% for γ in the outer and 43% for π^0 in the inner. The region on 2D plots which is occupied by photons is quite well concentrated. It is also the region where non-negligible part of the signal π^0 lays. Moreover the most significant number of π^0 events is located close to the region of the highest correlation between ECAL and PRS.

These plots support the statement that the addition of PRS to ECAL discriminant shall improve the performance of the separation. This should be the most significant for the outer, where the correlations are the lowest, and the least significant for the inner with the largest correlations. The best improvement is obtained for large π^0 efficiencies and low γ rejection fractions.

6.4.5 Performance of optimisation with ECAL and PRS variables combined together

The same procedure of optimisation as before but for all variables was performed and the results are in the figure 6.9. The histograms of the discriminant responses are again smoother thanks to ECAL contribution. Output logs from TMVA suggest that both types of variables (ECAL and PRS) are quite equally used in creation of decision trees. The table 6.3 presents the signal efficiency versus background rejection for this optimisation. The improvement relative to the optimisation with the ECAL variables only is given in the table 6.4.

The most significant improvement is observed for low background retention factor. Relatively to the optimisation with the ECAL variables only, for background retention of 1%, it is 6% in the inner, 15% in the middle and 25% in the outer. As we will see later, analyses with π^0 require tight π^0 selection. Hence, the addition of the preshower is not negligible, especially for the outer region.

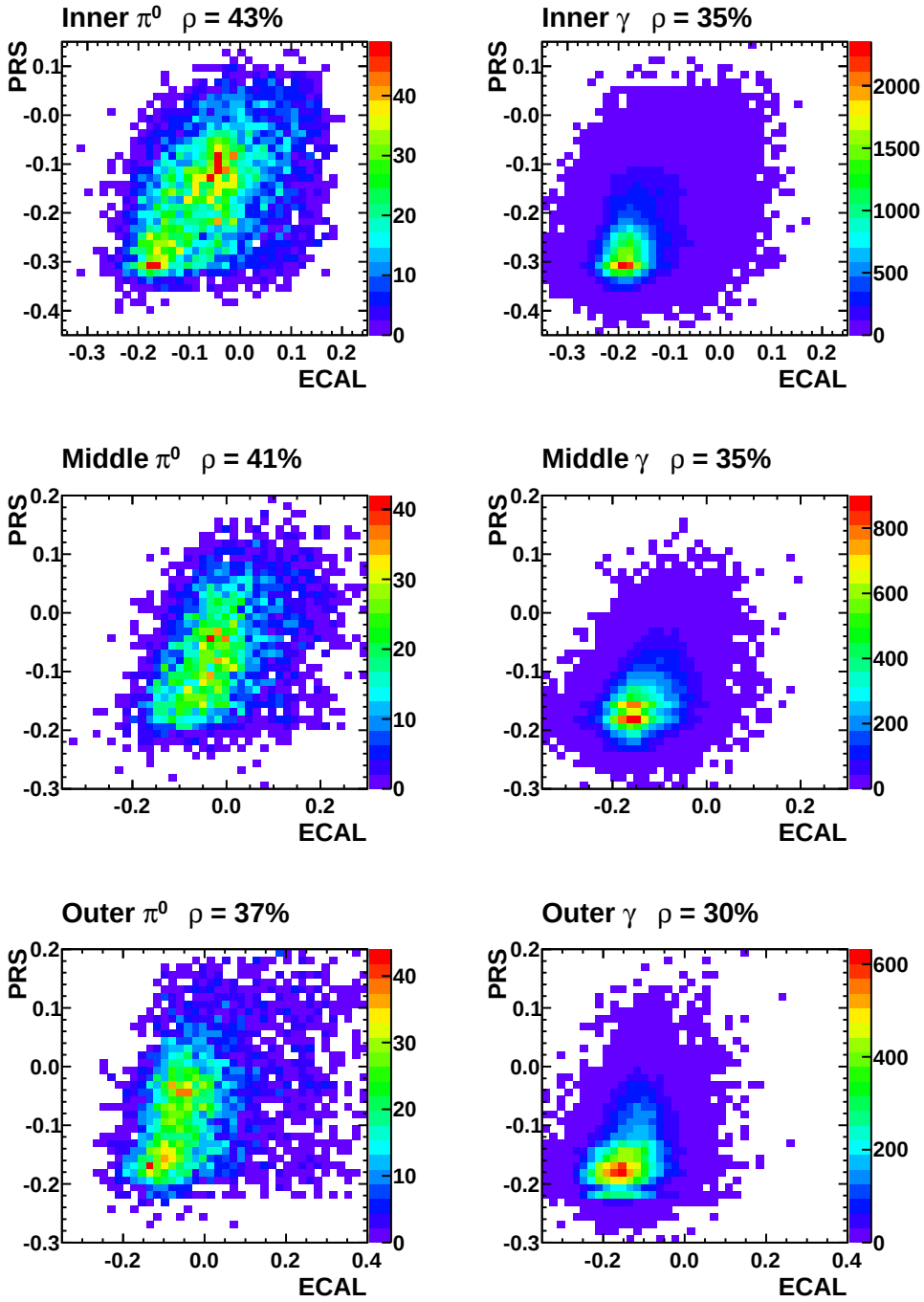

Figure 6.8: *Comparison between response of discriminant trained with the ECAL variables only and response of discriminant trained with the PRS variables only for inner, middle and outer. The left column shows the comparison prepared with π^0 sample from dedicated MC09 $B_s^0 \to K\pi\pi^0$, while the right column shows the same comparison for the sample of γ from MC09 $B^0 \to K^*\gamma$. Colours represent absolute number of events. The signal correspond to 200 thousand of generated events and the background correspond to 1081 thousand of generated events.*

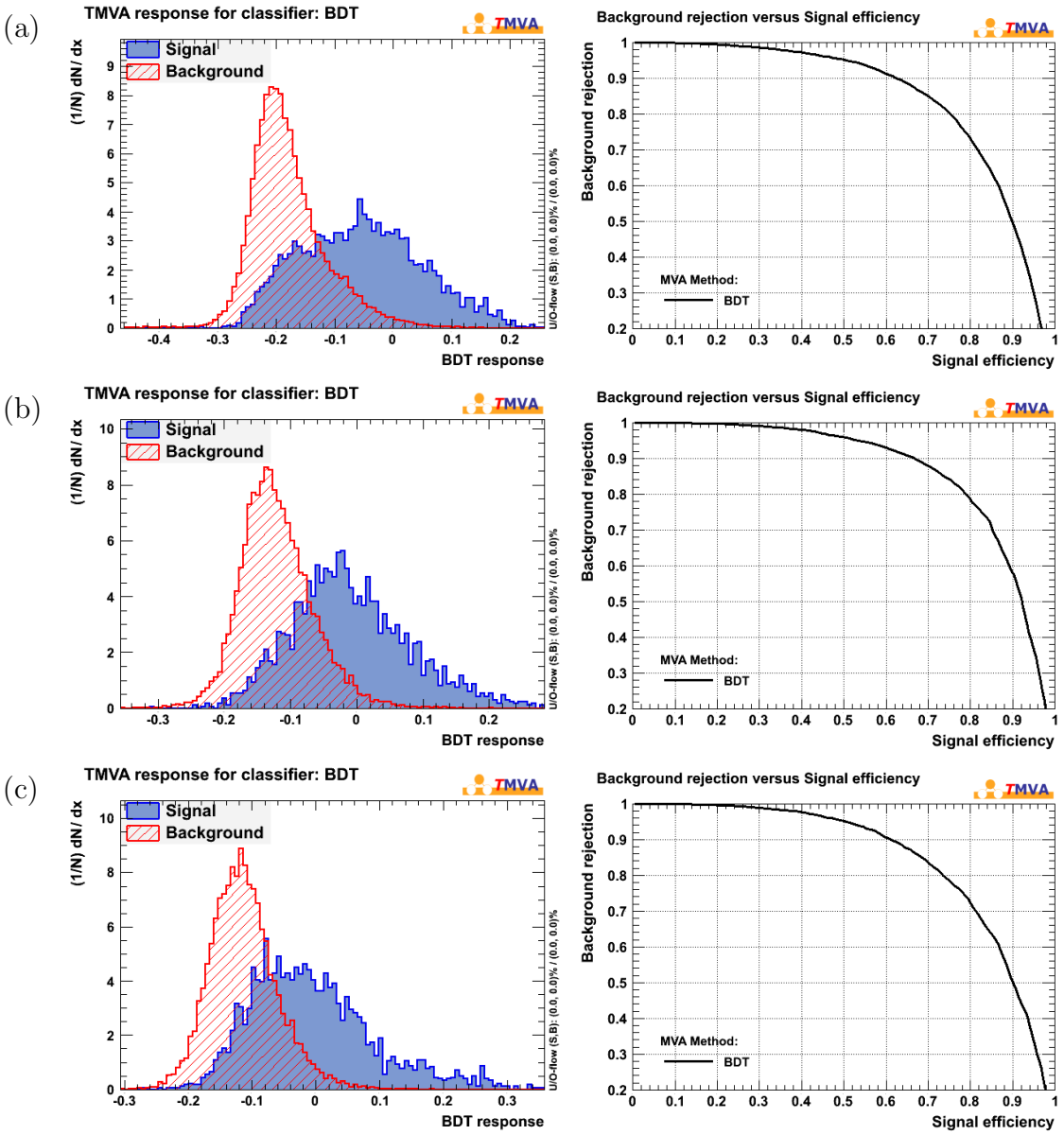

Figure 6.9: *π^0/γ discriminant training control plots. Optimisation with both ECAL and PRS variables used together. In the left column the discriminant response for signal (π^0) and background (γ). In the right column: γ rejection against π^0 selection efficiency. Three regions are optimised independently: a) inner, b) middle, c) outer.*

Region	B=0.01	B=0.10	B=0.30
Inner	0.247	0.623	0.816
Middle	0.302	0.666	0.853
Outer	0.286	0.610	0.812

Table 6.3: *π^0 signal selection efficiency with the discriminant optimised with the ECAL and PRS variables used together. Columns for corresponding values of efficiencies on background γ sample B equal to 0.01, 0.10 and 0.30.*

Region	B=0.01	B=0.10	B=0.30
Inner	+6%	+2%	+1%
Middle	+15%	+3%	+2%
Outer	+25%	+13%	+3%

Table 6.4: *Relative improvement in the efficiency between the discriminant based on the ECAL and PRS variables together, and the discriminant based on the ECAL variables only.*

6.5 Real data check with D^0 sample

As it was mentioned in the introduction, there is a possibility to check the discriminant before applying to the sample of $K\pi\pi^0$ coming from B hadrons. With the method described here it is possible to test if the discriminant works correctly on the real data. The sample that is available for that check is a channel of $D^0 \to K\pi\pi^0$. It allows to test both signal selection with merged π^0 and background rejection with photons from resolved π^0. This stream will benefit in 2011 of a very large statistics. Results reported in this chapter are based on the 2010 data. The correct performance measurement of the π^0/γ discrimination is ongoing with the 2011 data.

6.5.1 Stripping

The decay of $D^0 \to K\pi\pi^0$ is available for the analysis in the real data from a stream called *charm control*. A selection which is used for stripping the data was designed by R. Lefevre from Clermont-Ferrand group. The purpose of the stream is to provide a set of data of a mode which is well described. It can be used for calibration purposes, basically related to π^0 measurements. The selection of *charm control* stream is a set of cuts. These cuts are described in the table 6.5.

Cut	Description
$>$ 1300 MeV	D^0 minimum mass
$<$ 2400 MeV	D^0 maximum mass
$>$ 0.001	D^0 vertex fit probability
$<$ 9	D^0 impact parameter
$>$ 0.9999	D^0 direction angle
$>$ 64	D^0 flight distance significance
$>$ 300 MeV	charged tracks transverse momentum
$>$ 600 MeV	charged tracks transverse momentum for resolved π^0
$>$ 0.000001	charged track fit probability
$>$ 16	charged track impact parameter respect to primary vertex
$>$ 2000 MeV	merged π^0 transverse momentum
$>$ 1000 MeV	resolved π^0 transverse momentum
$>$ 0.2	resolved pi^0 photons confidence level

Table 6.5: Charm control $D^0 \to K\pi\pi^0$ *stripping selection cuts. If not explicitly noted the same cut is applied for merged and resolved* π^0.

6.5.2 Selection

The stripping cuts are already quite hard. Trying to compare distributions of various variables for Monte Carlo D^0 sample and stripped data outside D^0 mass range – where we expect to have background mostly, one can find that they are very similar. Thus very efficient purifying of the sample is impossible. With that knowledge, extended by the fact that the design of D^0 selection is not the primary objective of the discriminant analysis, it was decided to use simple square cuts rather than a sophisticated discriminant. The set of cuts used for the selection is explained in the table 6.6.

Cut	Description
> 0.99995	D^0 direction angle
> 150	D^0 flight distance significance
< 9	D^0 vertex fit χ^2
< 9	D^0 impact parameter significance
> 40	sum of impact parameter significances, to remove charged particles from primary vertices
< 5	track fit χ^2 per degree of freedom
< 5	track fit χ^2 per degree of freedom
> 3500 MeV	D^0 transverse momentum
> 30000 MeV	D^0 momentum
> 500 MeV	K transverse momentum
> 500 MeV	π transverse momentum
> 2500 MeV	π^0 transverse momentum
> 5	K log likelihood to be a kaon
< 0	π log likelihood to be a kaon

Table 6.6: *Selection of signal of $D^0 \to K\pi\pi^0$. Applied for both merged and resolved π^0.*

6.5.3 Merged π^0 from $D^0 \to K\pi\pi^0$

The plots of mass of D^0 candidates built from $K\pi\pi^0$ with merged π^0 candidates before and after selection is presented in the figure 6.10. For the purpose of discriminant check the mass range of 1785 MeV/c^2 $< m_{K\pi\pi^0} <$ 1945 MeV/c^2 is used, which is approximately the region of $\pm 2\sigma$ from D^0 mass, where σ is taken from the fit performed on the sample after the selection. The signal over square root of signal plus background, it means $S/\sqrt{S+B}$, in that region before the selection is approximately 72, and after the selection almost 81, with purity of 28% and 64% respectively. A Gaussian shape of π^0 mass spectrum is emphasised by the selection (figure 6.11).

6.5.4 Resolved π^0 from $D^0 \to K\pi\pi^0$

The sample of resolved π^0 is initially purer and with a better mass resolution than the merged π^0 sample. Even without selection the mass distribution of D^0 candidates (figure 6.6) reveals that the signal is well defined with a shape of double Gaussian.

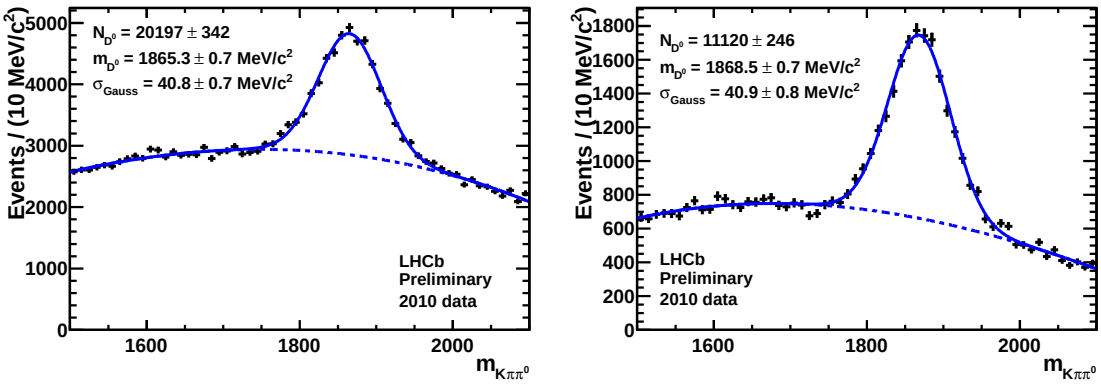

(a) (b)

Figure 6.10: *Mass of $K\pi\pi^0$ combinations with merged π^0 after $D^0 \to K\pi\pi^0$ stripping (a) and after the stripping and the selection (b) with 2010 data. The fits are made with a sum of a normal distribution for the signal and a third order polynomial for background parametrisation.*

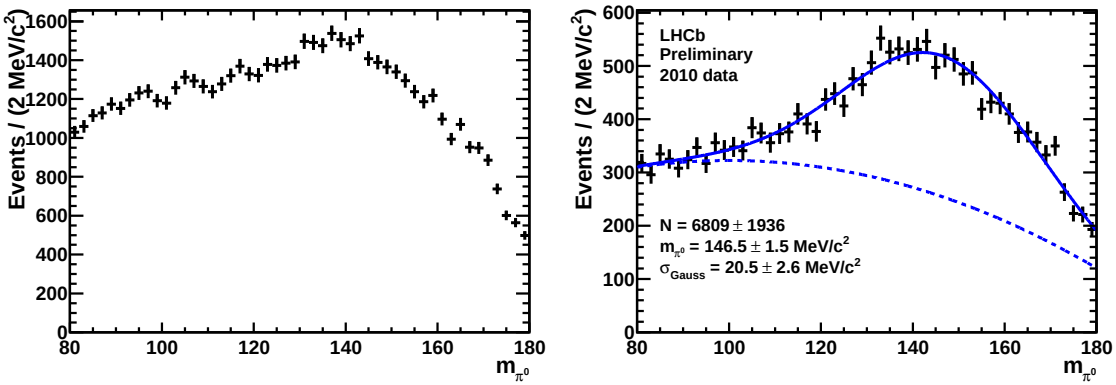

(a) (b)

Figure 6.11: *Mass of merged π^0 for combinations of $K\pi\pi^0$ from 2010 data with mass* 1785 MeV/c^2 $< m_{K\pi\pi^0} <$ 1945 MeV/c^2 *which pass the stripping (a) and the selection (b). The fit is made with a sum of a normal distribution and a second order polynomial.*

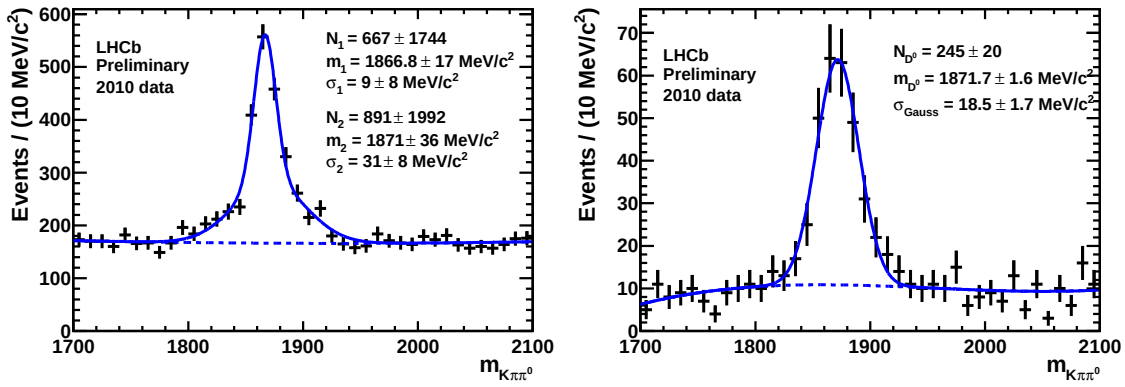

(a) (b)

Figure 6.12: *Mass of $K\pi\pi^0$ combinations with resolved π^0 after $D^0 \to K\pi\pi^0$ stripping (a) and after the stripping and the selection (b) with 2010 data. The fits are made with: a) a sum of two normal distributions for the double structure of the signal and a third order polynomial for background parametrisation, b) a sum of a normal distribution and a third order polynomial.*

After the selection the statistics is not sufficient to observe that double structure, however the purity of the sample increases a lot. For the test of the discriminant only the candidates which masses comply with 1805 MeV/c^2 $< m_{K\pi\pi^0} <$ 1925 MeV/c^2 requirement are selected – it corresponds to a bit more than $\pm 2\sigma$ from D^0 mass, where σ is taken from the fit performed on the sample after the selection. The $S/\sqrt{S+B}$ for that range of $\pm 2\sigma$ is around 25 before the selection, and around 17 after the selection. The significance drops, however the purity increases: from 43% to 65%.

Each resolved π^0 is constructed from two photons and both of the photons from selected π^0 within the accepted D^0 mass range are used for the test of the discriminant. It means that the available statistics of γ is twice the statistics of D^0.

6.5.5 Discriminant response

For testing the π^0/γ discriminant samples of π^0 and γ from 2010 data as described before were used. The test was performed for all regions independently. The results in terms of discriminant response histograms are given in the figure 6.13. First by looking at ranges of accessible values of the response we can notice that they are comparable to the Monte Carlo for π^0. Even the shape of the distributions in this case is similar. On the other hand, the γ results are quite far from expectations expected with the simulation. Discriminant responses are lower of about 0.1 for the data than for the Monte Carlo. The effect of the shift is the largest for the inner and the lowest for the outer. It makes the separation between the signal of π^0 and the γ background better than in the simulation. However, the statistics for photons from resolved π^0 is relatively low (at least respect to the statistics of merged π^0).

The histograms from the figure 6.13 allow to compute rejection fraction of γ as a function of efficiency of π^0 selection. The results are presented in the figure 6.14.

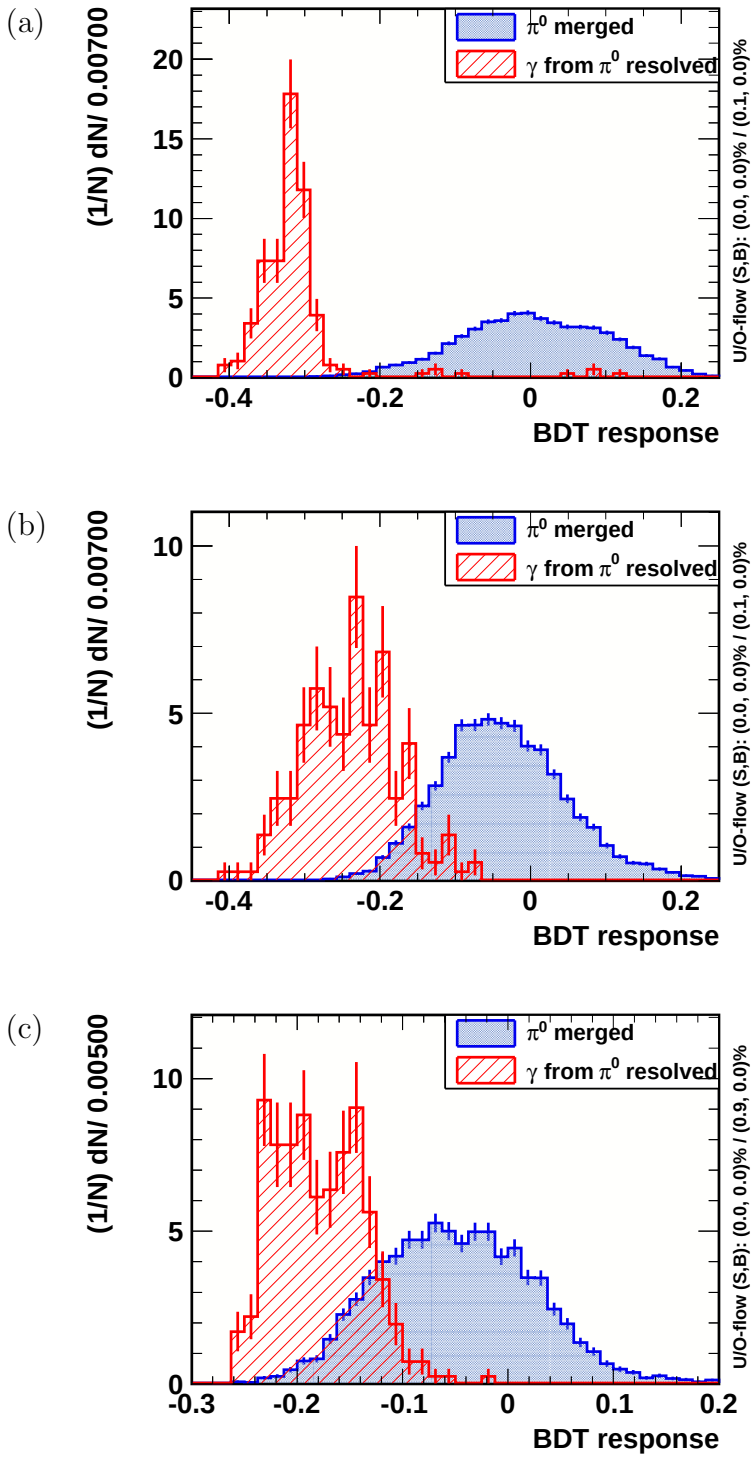

Figure 6.13: *Boosted decision tree discriminant response on 2010 data sample of* $D^0 \to K\pi\pi^0$ *for inner (a), middle (b) and outer (c).*

Roughness of the curves is caused by low statistics. The plot for the inner, as already noticed, displays an outstanding distinction between the two species for this set of data.

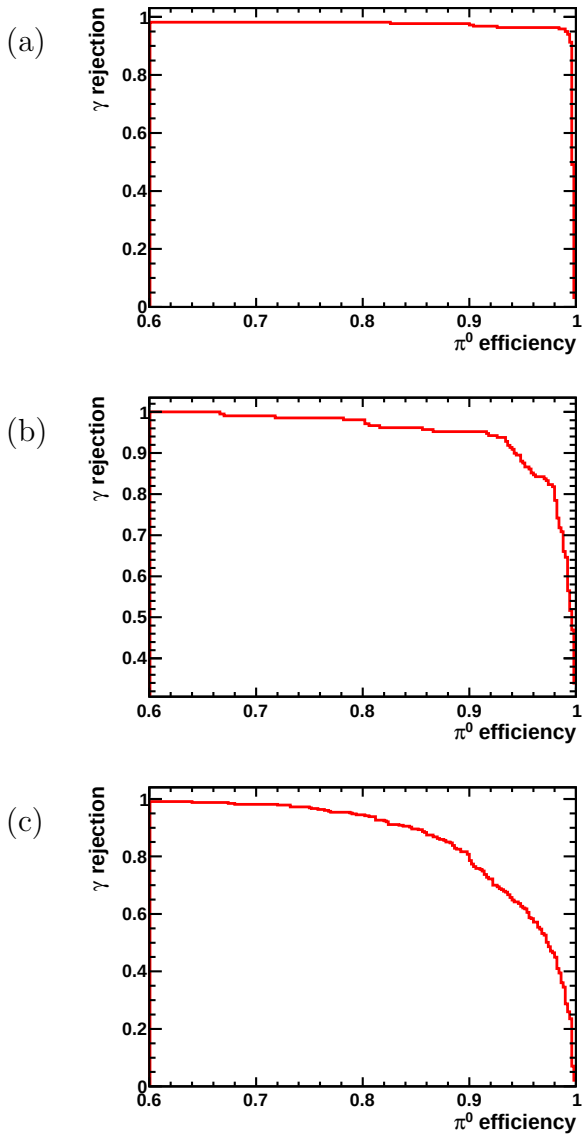

Figure 6.14: *Rejection factor of γ versus efficiency for π^0 with the discriminant tested on the sample of $D^0 \to K\pi\pi^0$. Three regions are presented: a) inner, b) middle, c) outer.*

We have to keep in mind, that photons from $B^0 \to K^*\gamma$ and from resolved π^0 coming from the decay of $D^0 \to K\pi\pi^0$ are in very different kinematic regime (figures 6.5 and 6.15). Hence, the difference as observed in this section is predictable.

To build the efficiency maps for kinematic properties corresponding to merged π^0 and photons from B decays, more statistics is needed. This will bring the 2011 data. The analysis is ongoing and benefits from the exploratory work presented in this chapter. However even with larger statistics high momentum region may be not

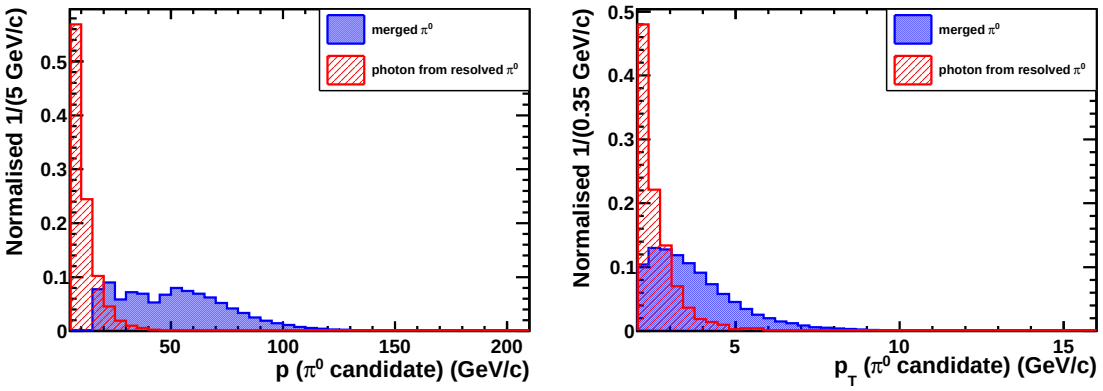

(a) (b)

Figure 6.15: *Momentum (a) and transverse momentum (b) distributions for merged π^0 candidates (blue) and γ from resolved π^0 constructed from $D^0 \to K\pi\pi^0$ data sample.*

accessible for photons from resolved π^0. For large momentum photons, it is possible to consider looking into the sample of $D^{*0} \to D^0\gamma$.

6.6 K$\pi\pi^0$ and K$\pi\gamma$

The aim of the discriminant was to help remove γ background from $hh\pi^0$ analyses. Still nothing prevents from its application to analyses where physicists are interested in photons. Both use case are possible, but this part will concentrate in the first application. It was already discussed in the previous chapter that in 2010 data it was hard to find charmless $hh\pi^0$ signal from B mesons decays. A trick that helped to emphasise the peek in the mass distribution was based on $K^* \to K\pi$ selection. However we questioned the authenticity of $B^0 \to K\pi\pi^0$ decay. The fact that only that trick made us able to see the signal clearly suggested that a significant contribution of $K^*\gamma$ decays is likely. Now we have a tool which allows us to test that signal and state firmly what is π^0 and what is γ.

6.7 $K\pi\pi^0$ with π^0/γ separation

6.7.1 Statistics

In this part, two samples of $K\pi\pi^0$ will be described. One is the sample from 2010 data taking marked as *Reco8Stripping12b* with the latest calorimeter correction and knowledge as of beginning of July 2011. The integrated luminosity corresponding to that sample is: (31.93 ± 0.06) pb^{-1}. The second sample was taken in 2011, known as *Reco9Stripping13*, also with the latest calorimeter corrections as of beginning of July 2011. The luminosity for that sample is: (142.7 ± 0.2) pb^{-1}. Each time first a comparison between the two data samples is made. If they agree, they are summed to increase the statistics. Let us notice that 2011 data were not benefitting from the

calibration of the ECAL.

6.7.2 Application of the discriminant

First, we will look at mass plots of reconstructed B mesons with the latest data (figure 6.16). They are prepared with $hh\pi^0$ stripping line with merged π^0. The selection applied is the same as described in the previous chapter. The Fisher discriminant response cut is set at 0.03, so each candidate response has to be larger than that value. It is the point for which the best $S/\sqrt{S+B}$ is predicted for 2010 data. Additionally $K\pi$ combinations with mass within 200 MeV from D^0 mass are removed. For each distribution a fit is performed of a Gaussian for signal plus an exponential for background. As mentioned in the previous chapter, this is definitely an inadequate fit model, but a convenient benchmark for the sake of the characterisation of the discriminant impact.

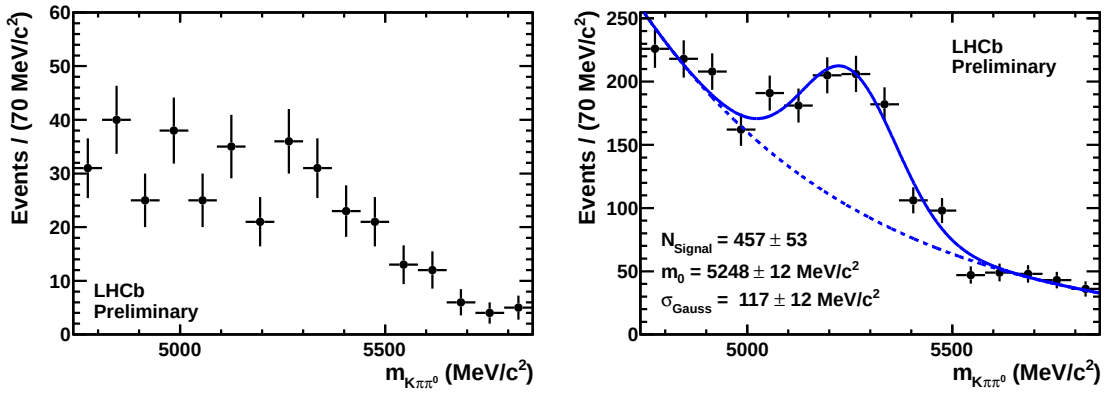

(a) 2010 (b) 2011

Figure 6.16: *Mass of reconstructed B candidates from $K\pi\pi^0$ with 2010 data (a), and 2011 data (b). The fit: sum of normal distribution and exponential.*

Let us focus on 2011 data, as the 2010 statistics does not allow to observe a signal shape. The width is decreased to (117 ± 12) MeV/c^2, however the central value of the normal distribution is a bit to low (5248 ± 12) MeV/c^2. The uncertainties on the numbers of observed signal events (140 ± 60 and 460 ± 50) are large and it is connected to the fact that Gaussian and exponential for background are not the best model to fit the data.

We can apply the π^0/γ discriminant. The working point is chosen for the best significance of the signal on a sample equally populated by π^0 and γ. The result is presented in the figure 6.17. 70% of candidates resist the discriminant application, while the Monte Carlo driven efficiency for this working point expectation is 80%. It is consistent with the hypothesis of 25% of photons in the initial sample.

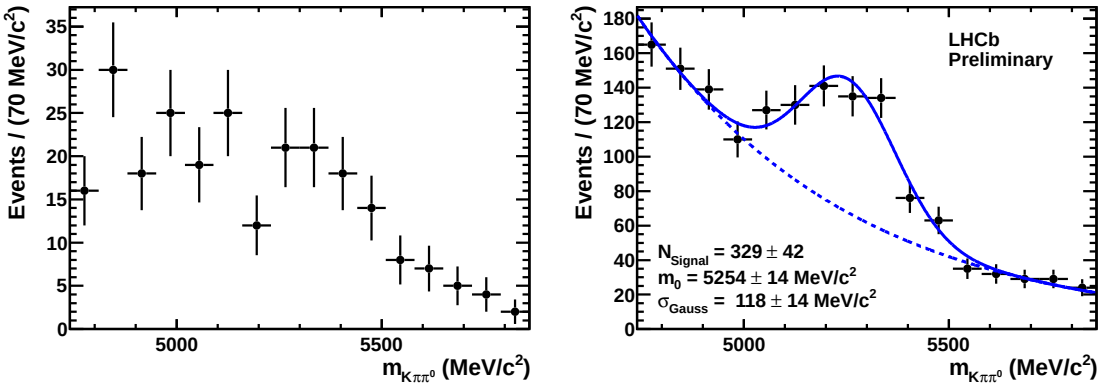

(a) 2010 (b) 2011

Figure 6.17: *Mass of reconstructed B candidates from $K\pi\pi^0$ after application of π^0/γ discriminant (cut of > -0.15 for the inner, > -0.05 for the middle, > -0.10 for the outer) with 2010 data (a), and 2011 data (b).*

6.7.3 Selecting K*(892)

The previous analysis of 2010 showed that requiring that a combination of K and π gives $K^*(892)$ purifies B^0 mass distribution intensively, no matter if π^0 is real or not. $K^*(892)$ is common for both $B^0 \to K\pi\pi^0$ and $B^0 \to K\pi\gamma$, thus it is a good laboratory to check the π^0/γ discriminant. The mass of Kπ from $K\pi\pi^0$ combinations is plotted in the figure 6.18 with the selection of B^0 applied. For the analysis of $K^*(892)$ structure the mass range between 812 MeV/c^2 and 972 MeV/c^2 is used.

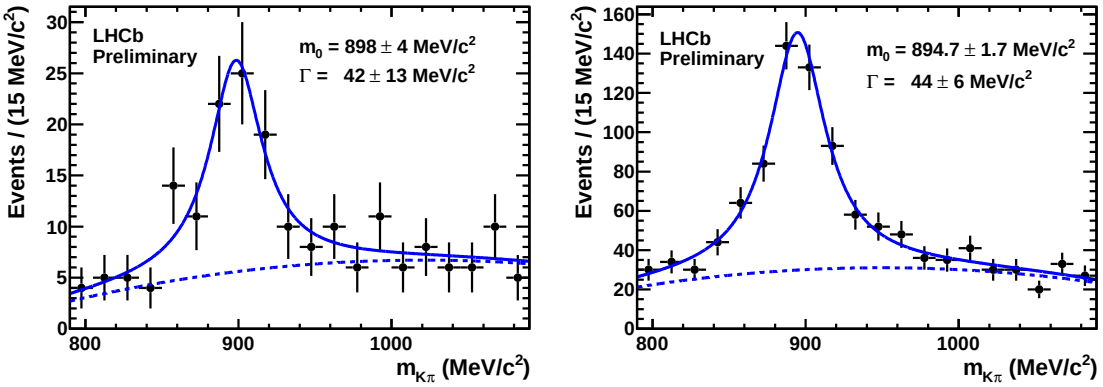

(a) 2010 (b) 2011

Figure 6.18: *Mass of $K\pi$ after B^0 selection for 2010 (a) and 2011 (b) data. The fit of a sum of a Breit-Wigner distribution and a second order polynomial is performed in both cases. The dashed lines represent background modelled with the polynomial.*

For the selected region of $K^*(892)$ mass, plots of discriminant response are prepared for both 2010 and 2011 statistics (figure 6.19). The plots are consistent between

2010 and 2011. They show a distribution of the BDT which is inconsistent with a photon contribution only.

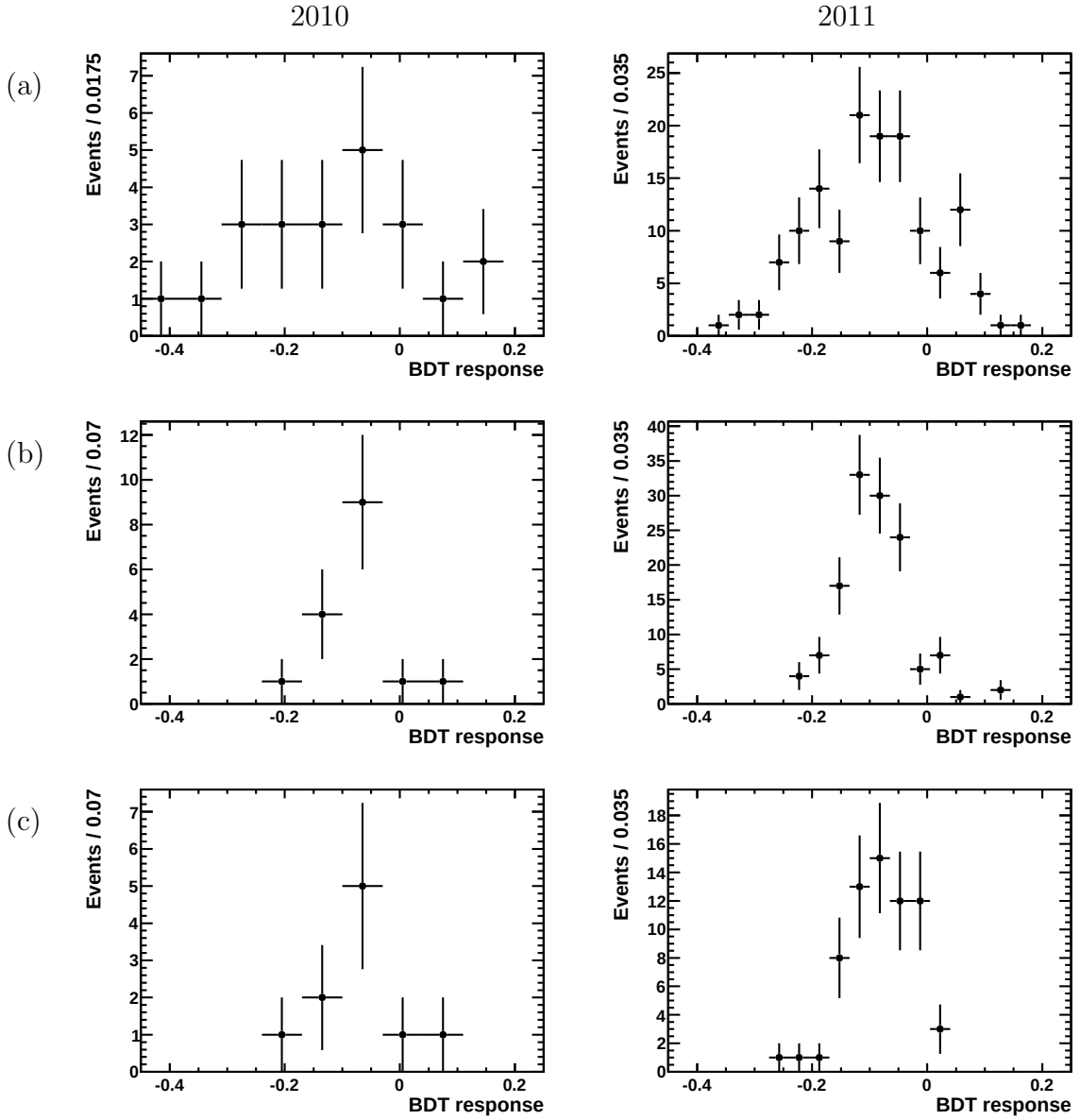

Figure 6.19: *π^0/γ discriminant response for events with $K^*(892)$ intermediate resonance by region: a) inner, b) middle, c) outer. The left column is for 2010 data, and the right column for 2011 data. B^0 selection is applied.*

Since the distributions for 2010 and 2011 are consistent within statistical errors, we can use the two samples together for plotting mass of π^0, which accordingly to the figure 6.4 is also capable of disclosing the original character (π^0 or γ) of π^0 candidates. The figure 6.20 shows a comparison of distributions of π^0 candidates mass for two cuts on discriminant response: the first preferring π^0 and the second preferring γ. The first is defined as the best point for selection of π^0 when the initial numbers of π^0 and γ are equal – it means that the response is larger than -0.15 for the inner, -0.09 for

the middle, and -0.10 for the outer. Monte Carlo driven efficiencies are about 80% for π^0 and about 20% for γ. The second is the same but with the opposite sign – the response has to be lower than -0.15 for the inner, -0.09 for the middle, and -0.10 for the outer to select γ. The performances for that cut are around 20% for π^0 and 80% for γ. Additionally the sum of all regions is given in the figure 6.21.

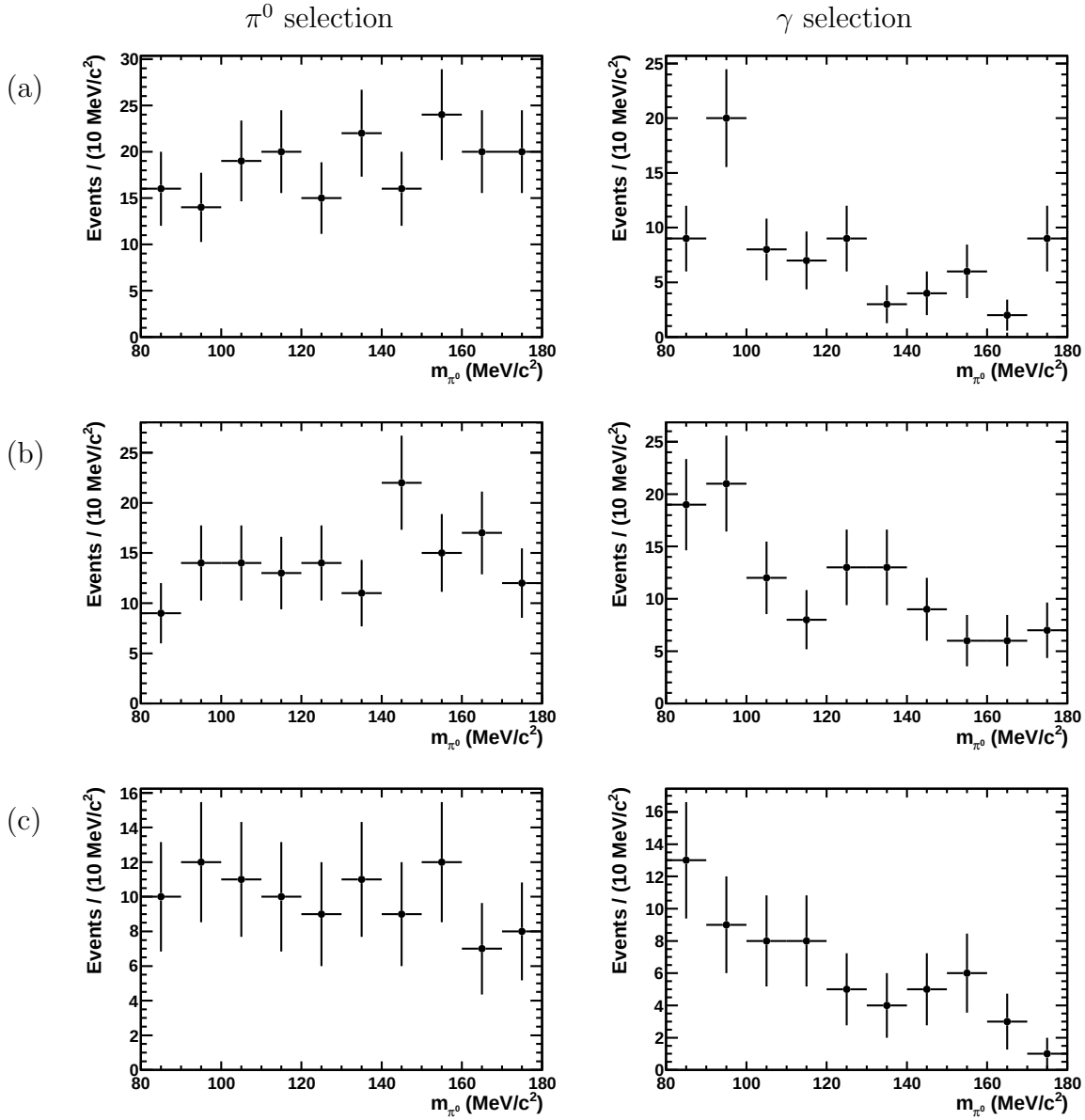

Figure 6.20: π^0 *candidates mass for two discriminant selections: preferring* π^0 *(left column) and preferring* γ *(right column). The cuts are described in the text. Three regions are presented: a) inner, b) middle, c) outer.*

It the π^0 preferred case it is impossible to find a Gaussian shape for signal. But it is the same for the simulation (figure 6.4). The γ case is more convincing that the selector works properly. The distributions are comparable to the γ plot in the figure 6.4, where low masses are more probable.

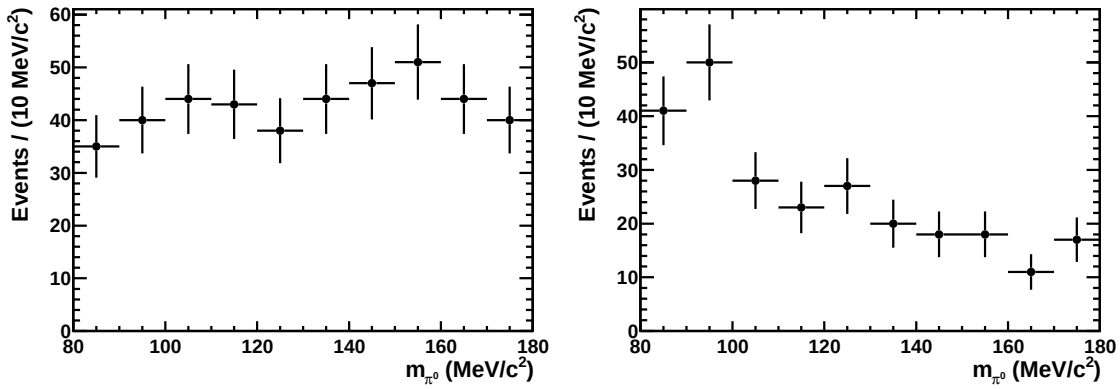

(a) π^0 selection (b) γ selection

Figure 6.21: *π^0 candidates mass for two discriminant selections: preferring π^0 (a) and preferring γ (b). All regions together.*

6.7.4 Tightening the selection

The next steps was trying to fully separate radiative decays from π^0. The definition of tightened π^0 selection was designed such that for each region the efficiency for background γ is the same and equal to 1.5%. It means that the discriminant responses has be larger than: 0.00 for the inner, 0.01 for the middle, 0.01 for the outer. Corresponding efficiencies on signal π^0 are respectively: 30%, 37% and 37%.

The tightened criteria for γ are defined such that the efficiency for π^0 is the same and equal to 10% for all regions. The response of the boosted decision tree has to be lower than -0.19 for the inner, -0.12 for the middle and -0.12 for the outer. The efficiencies for γ are then 50%, 58% and 48%.

All efficiencies are calculated from the Monte Carlo optimisation of the discriminant. The selections with described cuts and efficiencies ensure that the outcome is very pure.

The tightened selections were used to prepare new plots of π^0 mass. This time to increase the statistics all events that pass the selection of $B^0 \to K\pi\pi^0$ are used. The results are presented in the figure 6.22. Now the difference between π^0 criteria and γ is distinct. The histogram for π^0 cuts is fit with a sum of two normal distributions and is consistent with the π^0 hypothesis. On the other hand γ criteria give the outcome which is very similar to the one predicted by the Monte Carlo. The number of events decreases linearly with the mass, as in the figure 6.4.b).

Looking now at $K\pi\pi^0$ combinations, the mass distributions are given in the figure 6.23). The result for 2010 sample is not enough to perform a fit. The 2011 data behave much better and allow us to make a fit of a sum of a Gaussian for signal and an exponential background. The resolution is much improved with respect to the figure 6.17. The histogram of the sum of 2010 and 2011 data is given in the figure 6.24.a). The number of events obtained from the fit is equal to 102 ± 14. The central value of the normal distribution is (5310 ± 15) MeV/c^2 and the width (87 ± 12) MeV/c^2.

Let us conclude the achievements presented in this part of the chapter. First,

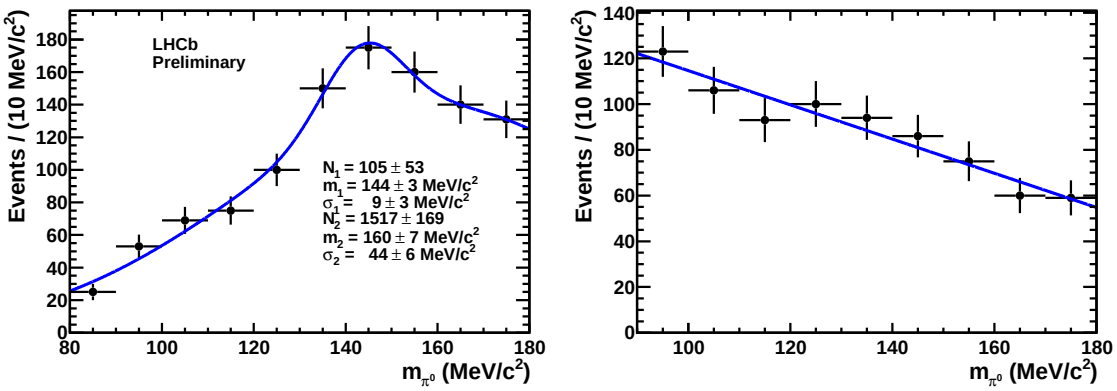

(a) π^0 tight selection (b) γ tight selection

Figure 6.22: *π^0 candidates mass for two tight selections: a) π^0, fit by a sum of two Gaussian functions, b) γ, fit by a first order polynomial.*

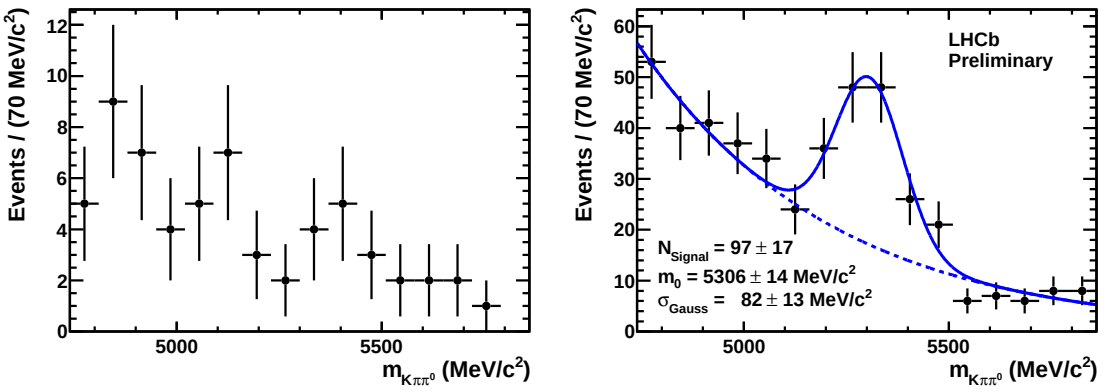

(a) 2010 (b) 2011

Figure 6.23: *Mass of reconstructed B candidates from $K\pi\pi^0$ after application of tight π^0 discriminant cuts (> 0.00 for the inner, > 0.12 for the middle, > -0.12 for the outer) with 2010 data (a), and 2011 data (b). Fit of a Gaussian plus an exponential performed for 2011 statistics.*

tightening the selection yields almost pure sample of $K\pi\pi^0$. We have used a very simple model built from a Gaussian and an exponential. The internal structure of the signal understanding will come with a larger statistics.

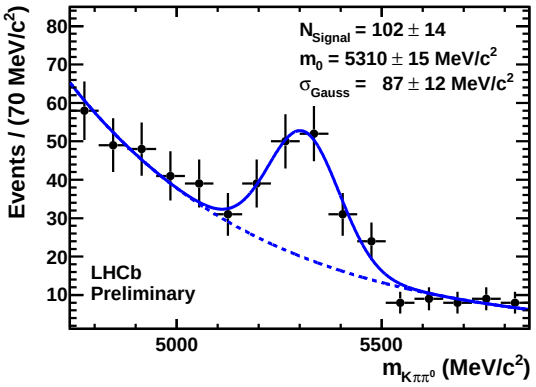

(a)

Figure 6.24: *Mass of reconstructed B candidates from $K\pi\pi^0$ after application of tight π^0 discriminant cuts. 2010 and 2011 statistics used together.*

6.7.5 Tight $K^*\gamma$

It is interesting to see also if the inverted selection (the tight γ selection) finds any signal in the B^0 mass range. The discriminant tight cut, as described above, is applied to the data (2010 and 2011) of $K\pi\pi^0$ to find candidates which are constructed with photons misidentified as π^0. The result is presented in the figure 6.25. The number of signal like events is equal to 75 ± 19, centred at (5266 ± 14) MeV/c^2 with resolution of (66 ± 22) MeV/c^2. Assuming the efficiencies which are taken from the simulation, the result allows to say that the initial sample in the peaking region of B^0 mass was similarly populated by candidates with real π^0 and candidates with γ.

6.7.6 Dalitz plot of $K\pi\pi^0$

In order to build the Dalitz plot, one applies the $B^0 \to K\pi\pi^0$ selection. The D resonance are not removed, and they should exhibit in the plane. Then tight π^0 selection with π^0/γ boosted decision tree is applied. The final move is a cut on $K\pi\pi^0$ combination mass, which is driven by the fit results from the figure 6.24.a). It is 3σ from fitted B^0 mass: 5072 MeV/c^2 $<$ m$_{K\pi\pi^0}$ $<$ 5540 MeV/c^2. The figure 6.26.(a) shows the Dalitz plot results. It is supplemented by three plots of masses of combinations of daughters (figure 6.26.b-d). The Dalitz space occupied by the events is limited on the bottom right side of the plot – for high square masses of $K\pi$. It is natural as it comes from the kinematics that stays behind π^0 construction. That part of the space is populated by resolved π^0. There are two main resonances visible for $K\pi$ combinations: $K^*(892)^0$ and D^0. There is also an excess at the mass slightly below 1500 MeV/c^2 which is consistent with $K_0^*(1430)$ hypothesis. The last possibility for this combination is J/ψ with misidentified π as K. It is more difficult to state

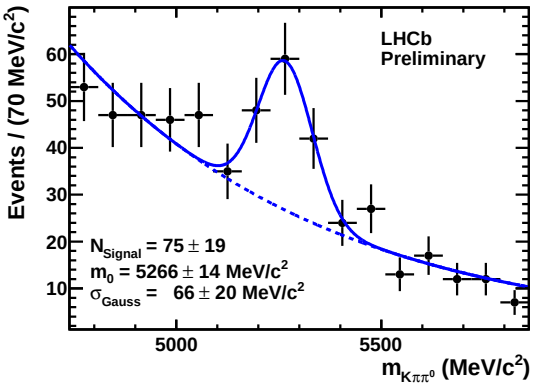

(a)

Figure 6.25: *Mass of reconstructed B candidates from $K\pi\pi^0$ after application of tight selection of γ misidentified as π^0. The signal is not the real $K\pi\pi^0$, but it is the real $K\pi\gamma$ with γ which mimics π^0.*

explicitly which resonances are present in $h\pi^0$ combinations, because of the merged π^0 resolution. Still, the $K_0^{*\pm}(1430)$ and the diagonal $\rho^\pm \to \pi^\pm\pi^0$ bands are present. $K^{*\pm}(892)$ is very unlikely to be found in $K^\pm\pi^0$ combinations, where the π^0 is merged, because of the dynamics of the decay.

6.8 KKπ^0 with π^0/γ separation

With 2010 data a signal of KKπ^0 was spotted. At that point, it was already considered that it can be contaminated by $(\phi \to KK)\gamma$. Here, again the 2010 and the 2011 data are summed. The very same exercise as described for $K\pi\pi^0$ was performed with $KK\pi^0$ final states. Both kaons are required to have $Kpid_K > 5$, and the tight selections (directed towards γ and π^0 respectively) are applied. The π^0 mass distributions obtained this way are displayed in the figure 6.27. The $KK\pi^0$ mass distribution along these two selections (figure 6.28) show that the spectrum is dominated by $B_s^0 \to \phi\gamma$ candidates. More data will be needed to figure out a $KK\pi^0$ contribution.

6.9 Summary

In the end of this chapter, let us conclude the achievements and present some perspectives for the future.

We have started from a construction of π^0/γ discriminator, which has to serve $hh\pi^0$ and radiative decays analyses. The new tool has been optimised in a realistic kinematic regime with respect to the existing tool. In addition, it was extended with preshower information to enhance the performance. It was possible to convincingly apply the tool to $hh\pi^0$ final states and draw some preliminary conclusions on radiative decays contamination.

The next step is to release this combined PRS/ECAL tool (the work is ongoing with the Barcelona group). Then to measure its performance on the data thanks to

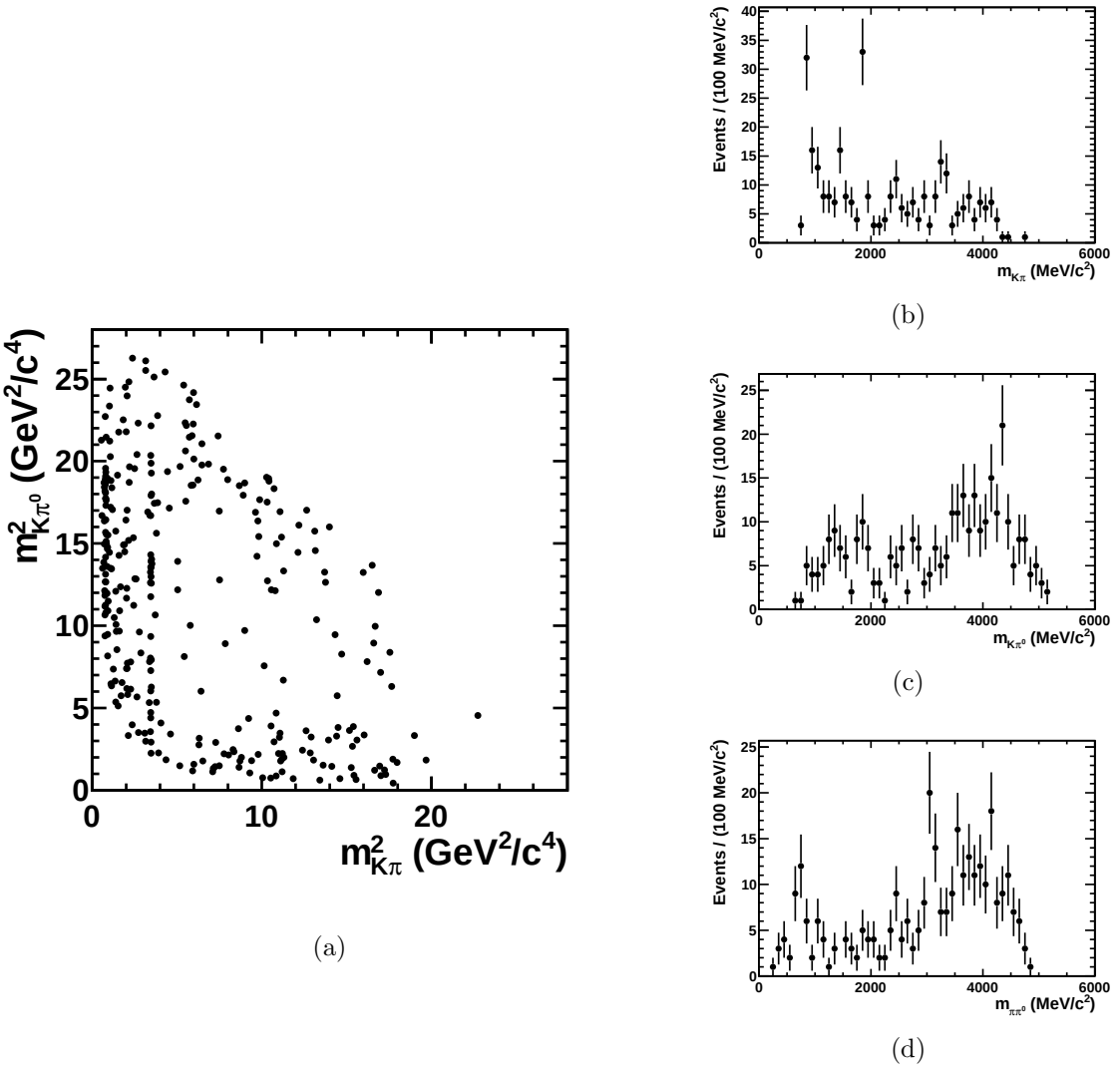

(a) (b) (c) (d)

Figure 6.26: *Resonant structure of $K\pi\pi^0$ combinations selected with tight π^0 cuts and with mass region of combination of $K\pi\pi^0$: 5072 MeV/c^2 < m$_{K\pi\pi^0}$ < 5540 MeV/c^2. The Dalitz plot (a) is accompanied by three histograms, one for each combination of two daughters: $K\pi$ (b), $K\pi^0$ (c), $\pi\pi^0$ (d).*

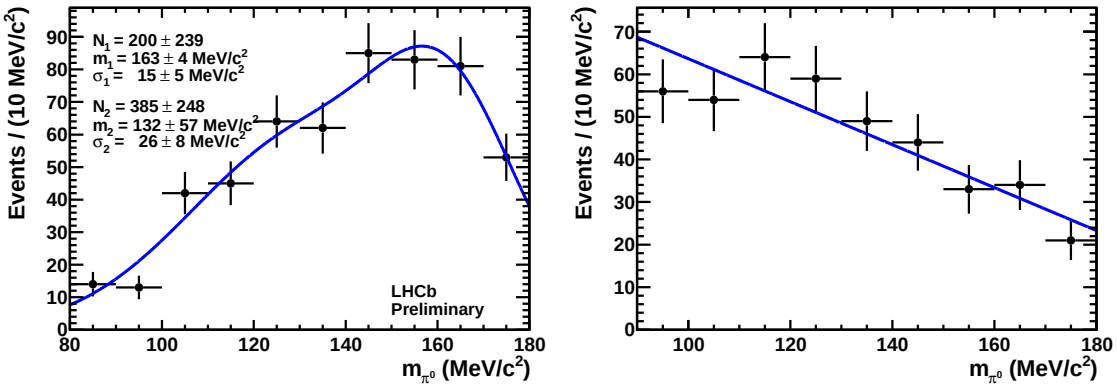

(a) π^0 selection (b) γ selection

Figure 6.27: *Mass of merged π^0 candidates with: a) tight selection of π^0 (b), and tight selection of γ.*

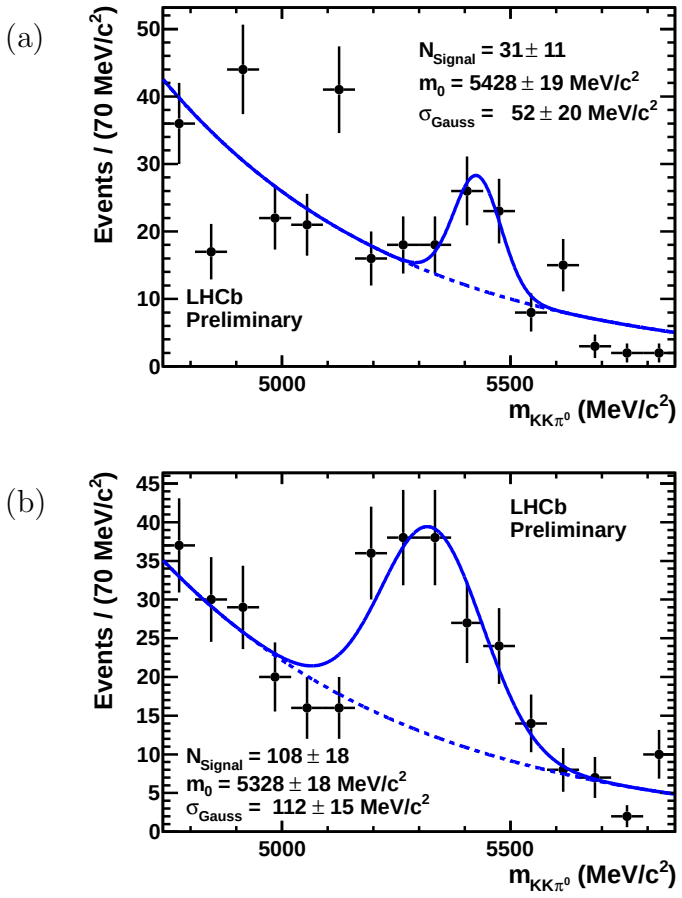

Figure 6.28: *Mass of the combination of $KK\pi^0$ candidates with merged π^0. The tight selection with π^0/γ discriminant are applied: the selection of π^0 (a), and the selection of γ (b).*

$D^0 \to K\pi\pi^0$ events with the 2011 statistics. The analysis of the latest reprocessed data will in addition benefit from the calibration of the electromagnetic calorimeter, which results in a typical resolution of 90 MeV, very much improved with respect to the 150 MeV typically achieved in this exploratory work.

Chapter 7

Charmless 3-body decays with a K^0_S in the final state

Studies of the three-body charmless decays of neutral B mesons with a K^0_S in the final states has several physics objectives. When considering $B^0 \to K^0_S\pi\pi$ and $B^0 \to K^0_S KK$, one can access the weak phase of the B^0 mixing in $b \to s\bar{s}s$ and $b \to s\bar{d}d$ transitions. The weak phase of B^0_s mixing can be accessed through the corresponding decay processes. The main physics objective lies in a comparison with those CKM angles (β and β_s) measurements obtained with charmonia final states. For these latter decays, the common prejudice is that their decay is free from additional weak phase. Hence, one might probe with charmless decays the presence of new CP violating phases in the decay (ΔF=1). The second usage comes with γ angles extraction from $B^0_s \to K\pi\pi^0$, described in the previous chapters, where one needs $B^0_s \to K^0_S\pi\pi$ to extract the strong phase. Finally, the first physics that can be reached is the measurement of the branching fractions of unobserved modes. The branching fraction measurements will be the core of this chapter.

From the exploratory work done with 2010 data, we found that the first reachable mode is the decay of $B^0_s \to K^0_S K\pi$. We will focus mainly on it in this chapter. However, with 2011 statistics, one can think about an observation of $B^0_s \to K^0_S\pi\pi$, so a few sections will be dedicated to this mode.

The procedure of measurement requires several steps to be taken. The trigger and the stripping have to be mastered. Data structure has to be understood and various mode contributions have to be identified. A selection has to be designed and efficiencies have to be evaluated. Finally, yields have to be extracted. The analysis of the three-body decays described here is conducted together with the Warwick group [103]. As of the middle of October 2011 it is still ongoing and the final numbers are not accessible. However, I would like to describe my contributions to these measurements. Additionally, I will present the concept of the analysis in areas, where the work is currently ongoing.

7.1 Introduction

A value of the B weak mixing phase $\sin 2\beta$ was measured first by BABAR and Belle in 2001 by studying CP violation in decays governed by $b \to c\bar{c}s$ transitions (e.g. $B^0 \to J/\psi K^0_S$) [105, 106]. The current average from B factories (figure 7.1) is equal to 0.678 ± 0.020 [16]. The first result obtained with the LHCb has been also published [107] with 35 pb^{-1} recorded in 2010. The value is equal to $0.53^{+0.28}_{-0.29} \pm 0.05$, which is consistent with the B factories measurement and tells the long way to reach B factories sensitivities in time-dependent analyses. The statistical and systematical uncertainties will be reduced with the increase of the statistics analysed.

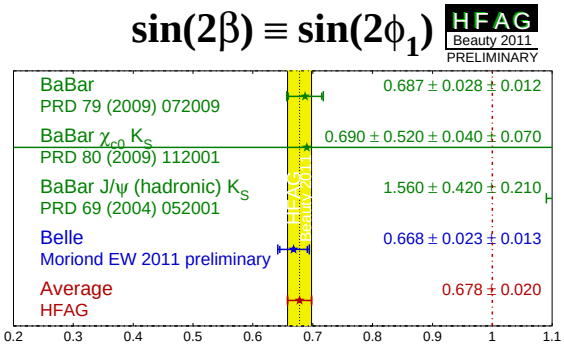

Figure 7.1: *Averages of* $\sin 2\beta$ *from the B factories [16].*

The very same weak mixing phase to a good approximation can be reached in charmless 3-body B decays, where in absence of $b \to c$ amplitudes, $b \to s$ penguin contributions are enhanced. By a comparison of the charmonia modes and the charmless modes, one can search for physics contribution beyond the SM. A hypothetical difference between the two would indicate that there are new amplitudes contributing to $b \to q\bar{q}s$ penguin decays.

To measure the CP asymmetries in the B^0 decays, hence the $\sin 2\beta^{\text{eff}}$ parameter, one wants to use final states which are CP eigenstates. In the 3-body decays considered in this chapter, $K^0\pi\pi$ and K^0KK, the final state is a non-CP eigenstate. However, one can require that the decay passes an intermediate CP defined step as $f_0(980)K^0_S$, $\rho^0(770)K^0_S$, or ϕK^0_S. This approach allows to consider the problem as a quasi 2-body decay. The quasi 2-body approach is limited by the presence of other structures in phase space which might interfere with the "signal" resonances. This drawback can be overcome in the full study of the accessible phase space through a Dalitz analysis.

Let me mention that the physics reach discussed above supposes that these decays are driven by penguin diagrams.

K^0hh final states can be accessed through $b \to u$ transitions though. They are doubly CKM suppressed but their amplitude might be enhanced by hadronic factors. A further virtue of the Dalitz analysis approach is that it yields enough information to extract relative phases and amplitudes. B factories have conducted such work and the figure 7.1 summarises their outcome.

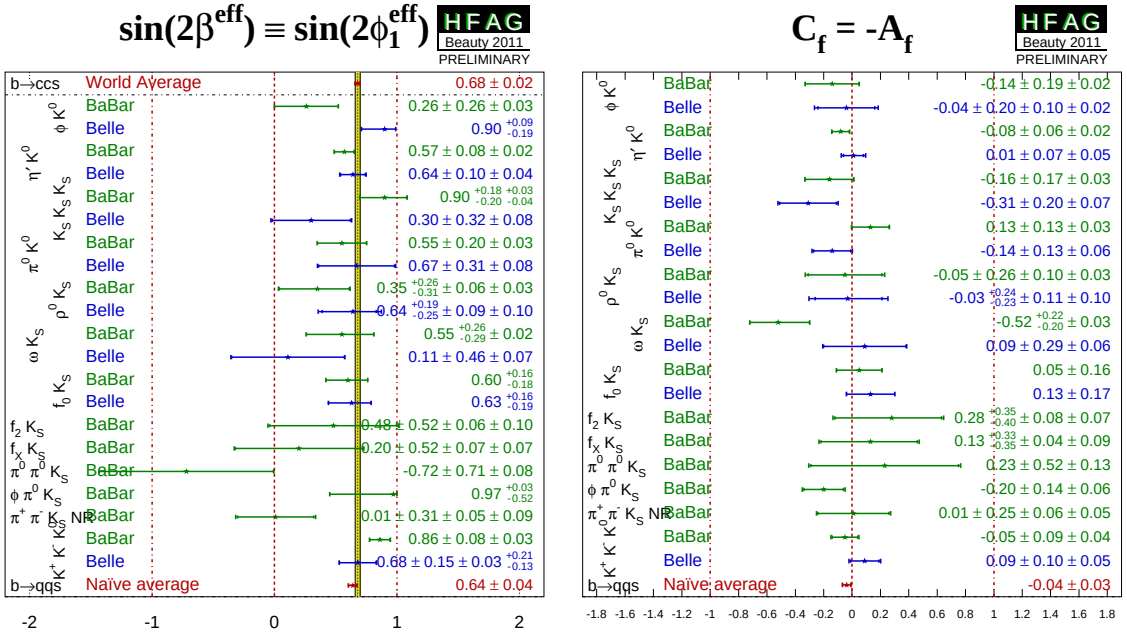

Figure 7.2: *Comparison of* $\sin 2\beta^{\text{eff}}$ *(left) and* A_{CP} *(right) from different charmless* $b \to q\bar{q}s$ *modes [16].*

The measurements of this kind in the LHCb, the full Dalitz analyses of $K_S^0\pi\pi$ and K_S^0KK modes, are not yet possible because of the insufficient statistics available so far. Hence, in this chapter we will concentrate on branching fraction measurements, which require lower integrated luminosities and are the very first step in the installation of the (time-dependent) Dalitz analysis.

7.2 K_S^0 reconstruction

In the LHCb, one can find two types of K_S^0, which differ from each other in types of π tracks used for the reconstruction (figure 7.3). K_S^0 built from two long tracks are simply denoted by *KSLL*, while K_S^0 built from two downstream tracks are *KSDD*. Decays with the two types of K_S^0 are considered independently.

7.3 Exploratory work with 2010 data

The first stage of the analysis was an exploratory work similar to the one presented in the Chapters 5 and 6. This time, the laboratory was the charmless decay mode $B^0 \to K_S^0\pi\pi$. The PDG [2] branching fraction for $B^0 \to K^0\pi\pi$ is $(4.96 \pm 0.20) \cdot 10^{-5}$. The process is the same as previously, so we will present the results only.

For efficiencies estimation a dedicated sample of Monte Carlo MC09 of $B_s^0 \to K_S^0K\pi$ with beam energies and average number of visible interactions equal: 10 TeV

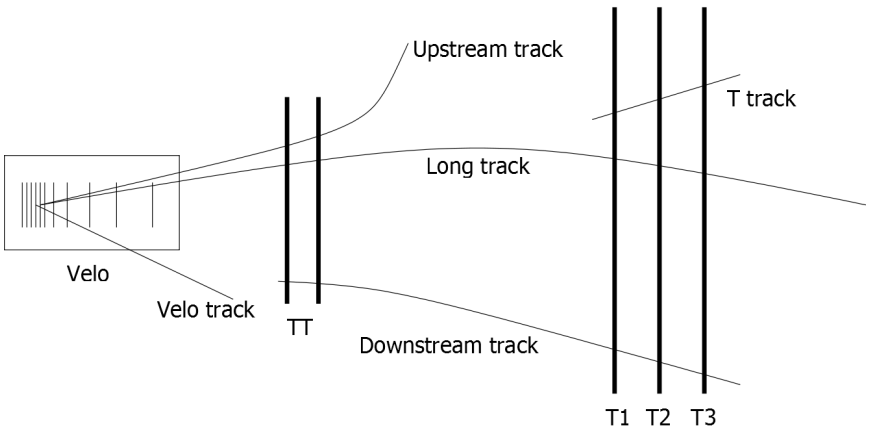

Figure 7.3: *LHCb track types.*

and $\mu = 0.6$ accordingly. During the process of stripping, $K^0_S hh$ candidates are constructed, where each h can be a π or a K. The hadrons have to be opposite sign. The cuts used in stripping *Stripping12b* are presented in the table 7.1. The trigger efficiencies are given in the table 7.2. The trigger does not include any exclusive HLT2 line for $K^0_S hh$ decays. The events are passing mostly through 2-, 3- or 4-body topological lines. Various step efficiencies, except of the selection efficiency, are given in the table 7.3. Using these efficiencies to fill the equation 5.3, one obtains, for 2010 integrated luminosity of $\mathcal{L} = 35$ pb^{-1}, the estimated expected number of events after stripping ~ 140 for DD K^0_S, and ~ 90 for LL K^0_S.

The selection was again based on a Fisher discriminant prepared with the TMVA [94] with a set of square cuts applied to kinematic variables in order to keep control onto the Dalitz plane, while the Fisher was trained with topological variables. As the signal, the Monte Carlo sample described in this section was used. As the background, the mass sidebands of the B^0 signal mass region from the real data were used. The region is defined as $|m_{K^0_S\pi\pi} - m_{B^0}| > 60\ MeV/c^2|$, where 60 MeV/c^2 corresponds to approximately three times the expected resolution. The summary of the cuts and the variables is given in the table 7.4. The working point for Fisher discriminant was chosen on a basis of the best $S/\sqrt{S+B}$, where S is the expected signal number taken from the Monte Carlo, and B is the number of background events taken from the data. Assuming Monte Carlo efficiencies, after selection approximately ~ 50 events with K^0_SDD were expected, and ~ 20 events with K^0_SLL.

After application of the selection, two types of background were identified. The most significant group was the decay of $B^0 \to K^0_S J/\psi$, where J/ψ decayed into two μ misidentified as π. The other type of background were decays of D, so the decays with charm. Both backgrounds were removed with mass cuts[1]. The result are presented in the figure 7.4. As in the previous chapters, one has to consider the fit model with caution as it is displayed for approximate estimation only, and it does not represent the background structure properly.

The main conclusions from the exploratory work were:

[1]They removed regions were: $m_{J/\psi} \pm 54$ MeV/c^2 (3 times the resolution each side) and $m_D \pm 40$ MeV/c^2 (2 times the resolution each side).

Cut	Description
> 5079 MeV	B combination minimum mass
< 5559 MeV	B combination maximum mass
> 0.999	B direction angle
> 1.0 mm	B flight distance
< 12	B vertex χ^2
> 0.05 mm	impact parameter (IP) of the largest PT daughter
> 0.0	sum of hh IP's
< 5	track χ^2 per degree of freedom for all tracks (including K^0_S)
< 0.3 mm	distance of closes approach of hh
< 30 MeV	K^0_S mas window
> 800 MeV	B daughter medium PT particle cut, LL
> 4000 MeV	B daughters PT sum, LL
> 30	B flight distance significance, LL
< 0.08 mm	B impact parameter respect to the primary vertex, LL
> 50	K^0_S flight distance significance respect to the best primary vertex, LL
< 12	K^0_S vertex fit χ^2, LL
> 800 MeV	B daughter medium PT particle cut, DD
> 4300 MeV	B daughters PT sum, DD
> 30	B flight distance significance, DD
< 0.08 mm	B impact parameter respect to the primary vertex, DD
> 50	K^0_S flight distance significance respect to the best primary vertex, DD
< 12	K^0_S vertex fit χ^2, DD
> 6000 MeV	K^0_S momentum, DD

Table 7.1: *Stripping12b KSHH line cuts.*

TCK	Integrated luminosity nb^{-1}	SPD cut	K^0_S LL	K^0_S DD
0x001e0030	2117	900	$(33.0 \pm 0.6)\%$	$(22.9 \pm 0.6)\%$
0x001f0029	3078	900	$(21.4 \pm 0.6)\%$	$(15.8 \pm 0.6)\%$
0x002a002a	4179	900	$(21.3 \pm 0.6)\%$	$(17.3 \pm 0.6)\%$
0x002b002a	1839	900	$(21.3 \pm 0.6)\%$	$(17.3 \pm 0.6)\%$
0x0025002c	1946	450	$(21.4 \pm 0.5)\%$	$(15.5 \pm 0.5)\%$
0x002e002c	8911	450	$(21.3 \pm 0.6)\%$	$(17.3 \pm 0.6)\%$
0x002e002a	8669	900	$(21.3 \pm 0.6)\%$	$(17.3 \pm 0.6)\%$

Table 7.2: *Trigger efficiencies for $K^0_S hh$ events. 2010 TCK configurations. Global event cut efficiency is not included.*

	K^0_S DD	K^0_S LL
Generator level	$(20.68 \pm 0.06)\%$	
Stripping	$(3.09 \pm 0.04)\%$	$(1.63 \pm 0.03)\%$
Trigger 2010 without GEC	17%	21%
Total with GEC	0.065%	0.042%

Table 7.3: *Efficiencies of various steps (generation, trigger and stripping) of the decay of* $B^0_s \to K^0_S\pi\pi$.

Square cuts	
Variable	Description
$B\_PT > 3500$ MeV	B transverse momentum
$pi\_PT > 800$ MeV	π transverse momentum
$KS_PT > 1600$ MeV	K^0_S transverse momentump
Fisher variables	
Variable	Description
B_FDCHI2	B flight distance significance
B_IPCHI2	B impact parameter significance
B_DIRA	B pointing angle
$B\_ENDVERTEX\_CHI2$	B end vertex fit χ^2
KS_IPCHI2	K^0_S impact parameter significance
pi_IPCHI2	π impact parameter significance

Table 7.4: *Exploratory selection settings for 2010 data.*

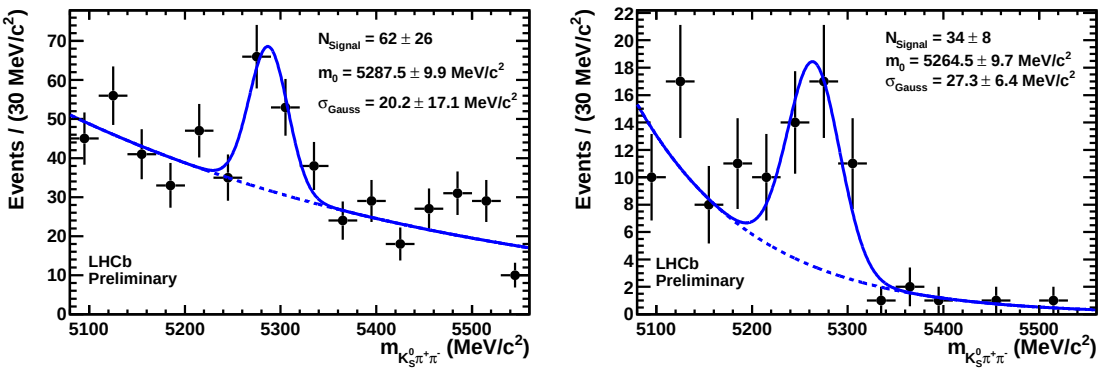

(a) K^0_S DD (b) K^0_S LL

Figure 7.4: *Exploratory selection results for* $K^0_S\pi\pi$ *combinations with 2010 data.*

- The expected yields are slightly lower than the results obtained from the data. However, one has to keep in mind that the fit model was imperfect and so the uncertainty involved significant.
- Two types of background were identified: the decays with charm mesons and J/ψ.
- The mass window cut in stripping was narrow. That implied narrow mass sidebands for signal optimisation and will cause problems for background model fit.

7.4 Data samples

The analysis is performed with the data recorded in 2010 ($\mathcal{L} = 35$ pb^{-1}), described in the previous section, and with a subsample of the data recorded in 2011 corresponding to about $\mathcal{L} = 230$ pb^{-1}. The sample from 2011 was recorded under unique trigger configuration between the end of June and beginning of September. It has passed the *Stripping15* (table 7.5). The data from the first part of the year 2011 were not used, because the stripping used (*Stripping13b*) contained an error which prevented reconstructing candidates inside the correct mass range. However, these data will be available after the next reprocessing.

Monte Carlo samples used in the analysis described in the rest of this chapter were generated under unique MC10 conditions of beam energies equal to 3.5 TeV and a pile-up factor of $\nu = 3$, corresponding to a number of visible interactions per bunch-crossing of $\mu \approx 2.4$. These conditions have to be as close as possible to the typical conditions for the 2010 real data.

For the signal modelling a set of Monte Carlo data was prepared, which contains six different decay modes:

- $B^0 \to K_S^0\pi\pi$,
- $B^0 \to K_S^0 K\pi$,
- $B^0 \to K_S^0 KK$,
- $B_s^0 \to K_S^0\pi\pi$,
- $B_s^0 \to K_S^0 K\pi$,
- $B_s^0 \to K_S^0 KK$.

These decays have been generated in phase space, for both magnet polarities. The statistics available for each mode is equal to 2 millions of events.

7.5 Background

One can expect that in conditions of the LHC the analysis of K_S^0 may have to deal with background modes which have measured branching fractions, and with modes

Cut	Description
> 5079 MeV	B combination minimum mass
< 5559 MeV	B combination maximum mass
> 0.9999	B direction angle
> 1.0 mm	B flight distance
< 12	B vertex χ^2
> 0.05 mm	impact parameter (IP) of the largest PT daughter
> 15.0	sum of hh impact parameter significances
< 4	track χ^2 per degree of freedom for all tracks (including K^0_S)
< 3.0	distance of closes approach significance of hh DD
< 5.0	distance of closes approach significance of hh LL
< 30 MeV	K^0_S DD mas window
< 20 MeV	K^0_S LL mas window
> 800 MeV	B daughter medium PT particle cut
> 4500 MeV	sum of PT of B daughters , LL
> 50	B flight distance significance
< 8	B impact parameter significance
> 80	K^0_S flight distance significance respect to the best primary vertex, LL
< 12	K^0_S vertex fit χ^2, LL
> 4800 MeV	B daughters PT sum, DD
> 50	K^0_S flight distance significance respect to the primary vertex, DD
< 12	K^0_S vertex fit χ^2, DD
> 6000 MeV	K^0_S momentum, DD

Table 7.5: *Stripping15 KSHH line cuts.*

which have been never observed before. While the first type can be well modelled with a Monte Carlo, the second can be modelled only to a certain extent. Hence, the analysis requires that the data are scrutinised for existence of different background decay modes, both fully reconstructed and partially reconstructed.

In this part I will refer to the signal selection, however the selection construction itself will be introduced in the next part. This order is supported by the fact, that the background structure influenced a lot the selection optimisation method.

7.5.1 Modes identified from the data

7.5.1.1 $K_S^0\mu\mu$

Topologically, the decay $B^0 \to K_S^0(J/\psi \to \mu\mu)$ has similar properties as the signal. The mass difference between π and μ is small, so this kind of background will occupy the same mass range as the signal. The misidentification affect also $K\pi$ and KK modes, where the background is displaced from the B^0 mass. Misidentification in $K\pi$ results in larger masses, significantly contributing to masses around the B_s^0 mass. The branching fraction of $B^0 \to J/\psi K_S^0$ makes it a significant background. Additionally, the decay into $B^0 \to \psi(2S)K_S^0$ has been observed. The histogram of mass of $\pi\pi$ combinations from 2011 data with the selection applied is given in the figure 7.5.

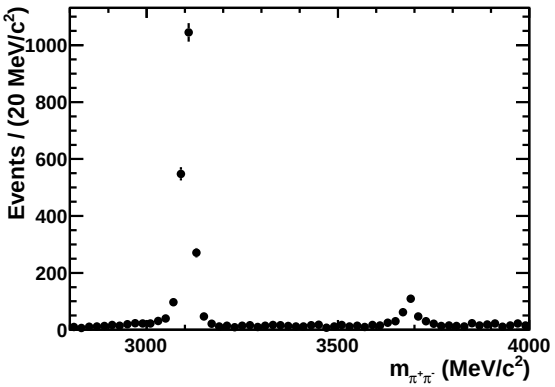

Figure 7.5: *Mass of $\pi\pi$ for $K_S^0\pi\pi$ masses consistent with B^0 hypothesis. The selection applied to the statistics from 2011.*

This type of background is removed by requiring that hadron tracks do not fit muon stations signal.

7.5.1.2 Baryonic decays

The difference in masses between B_s^0 and Λ_b is approximately 250 MeV/c^2. This value allows to reflections of Λ_b decays to appear inside our mass window, when a proton is misidentified as π or K (figure 7.6). We have managed to identify two decay modes in our sample. These are: $\Lambda_b \to (\Lambda_c \to pK_S^0)\pi$ (figure 7.7) and $\Lambda_b \to D_s p$. The latter one branching fraction has not been measured yet.

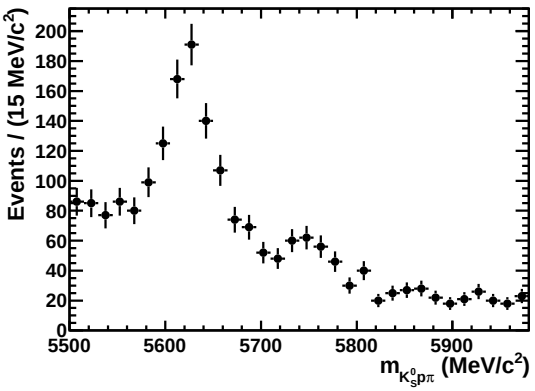

Figure 7.6: *Mass of $K^0_S\pi p$ combinations with DD K^0_S candidates. The selection applied to the statistics from 2011. Proton log likelihood respect to the pion likelihood has to be $PIDp > 5$.*

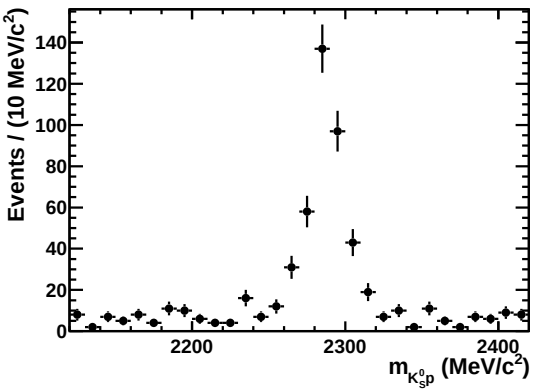

Figure 7.7: *2011 data mass of $K^0_S p$ combinations with DD K^0_S candidates for $K^0_S\pi p$ combinations consistent with Λ_b mass. Proton PID has to be $PIDp > 5$.*

The background model for partially reconstructed backgrounds described along these lines is notoriously insufficient and only serves the purpose of the commissioning of the Branching Fractions ratios measurements. It will improve when the MC background currently under production will allow to assess a shape for each of the partially reconstructed cases: non-reconstruction of a γ, a π^0 or a $\pi^\pm$. Despite theses words of caution, some yet unobserved modes are lying in a mass region where the background from partially reconstructed is a low contribution, and hence legitimate statistical statements on the yields.

Still, we can obtain now an approximate shape of the reflection of this background to $K^0_S\pi\pi$ from the data. For this reason, we select $K^0_S\pi p$ combinations with mass $|m_{K^0_S\pi p} - m_{\Lambda_b}| < 60$ MeV/c^2 (Λ_b selection), $|m_{K^0_S p} - m_{\Lambda_c}| < 40$ MeV/c^2 (Λ_c selection), and we reconstruct the combination mass under $K^0_S\pi\pi$ hypothesis. The result is presented in the figure 7.8.

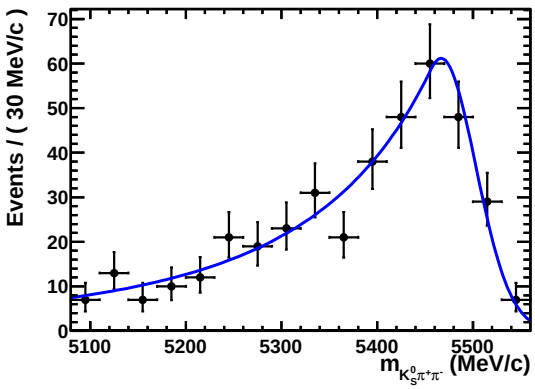

Figure 7.8: *2011 data mass of $K^0_S\pi\pi$ combinations with DD K^0_S candidates with Λ_b and Λ_c selections applied. Crystal Ball PDF [104] is fitted.*

7.5.1.3 $B^0_s \to (D \to hh)h$

Another type of fully reconstructed modes is when a B meson decays into two-body Dh combination, and D can be D^0, $D^\pm$, or D_s decaying into $K^0_S\pi$, $K^0_S K$, or $K\pi$. The selection efficiency on these modes is reduced because of the lifetime of D mesons, which impacts B vertexing probability. Mass vetoes under each D hypothesis are applied at the moment of estimating the yields. The situation will be different when analysing the Dalitz plane.

7.5.2 MC background studies

7.5.2.1 Signal cross-feed

By assigning the mass of π to a K in $B^0_s \to K^0_S K\pi$, or the mass of K to π in $B^0 \to K^0_S\pi\pi$, one can obtain signal mass shape which is shifted towards B^0 or B^0_s accordingly. The figures 7.9 and 7.10 present the signal reflection obtained on the

Monte Carlo samples. The shapes can be modelled by Crystal Ball probability density function [104].

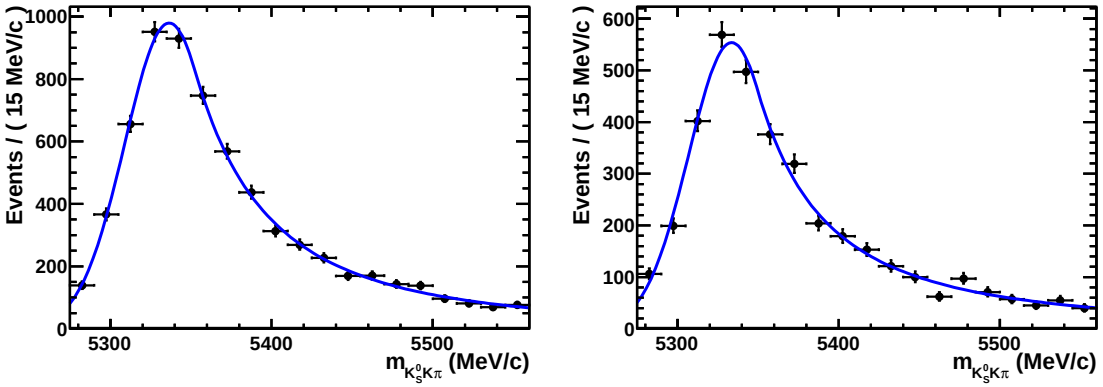

(a) K^0_S DD (b) K^0_S LL

Figure 7.9: *Histogram of $K^0_S K\pi$ combination mass obtained from the MC sample of $B^0 \to K^0_S \pi\pi$ by assigning the mass of K to one of the pions. Signal selection is applied. The fits with Crystal Ball PDF are superimposed.*

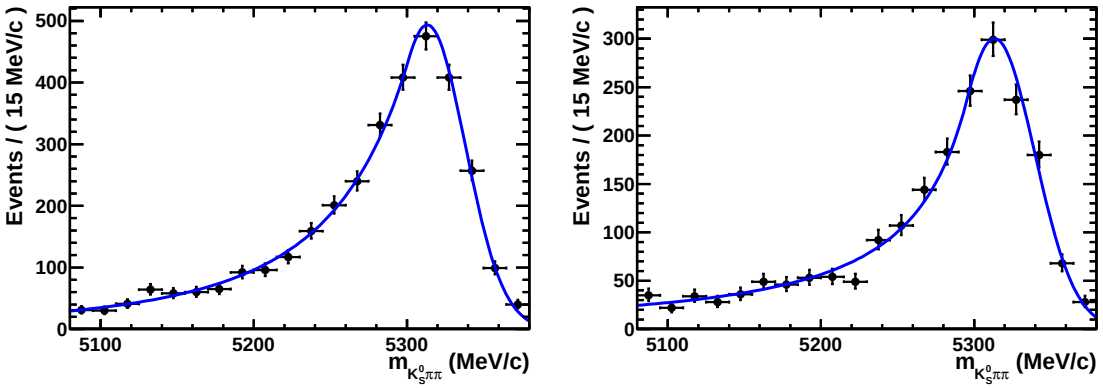

(a) K^0_S DD (b) K^0_S LL

Figure 7.10: *Histogram of $K^0_S \pi\pi$ combination mass obtained from the MC sample of $B^0_s \to K^0_S K\pi$ by assigning the mass of π to the kaon. Signal selection is applied. The Crystal Ball PDFs are fitted.*

This kind of background can be greatly reduced with PID cuts, however a fraction of it will always remain and needs to be modelled.

7.5.2.2 $B^0 \to \eta' K^0_S$

This decay of $\mathcal{BR}(B^0 \to \eta' K^0) = (6.6 \pm 0.4) \cdot 10^{-5}$ [2] starts the list of partially reconstructed background. It means, the decays into four particles in the final state,

where one particle is missing. In this case a photon is missing, as η' decays in the following way $\eta' \to \eta(\rho^0 \to \pi\pi)\gamma$. The photon energy spectrum is mild, and it results in the fact that $K_S^0\pi\pi$ combination mass can be very close (tenths of MeV/c^2) to the B^0 mass. A histogram of the mass of $K_S^0\pi\pi$ is given in the figure 7.11. The distribution can be fitted by a convolution of an Argus PDF [104] and a Gaussian. The width of the Gaussian is fixed to the MC resolution of the $B^0 \to K_S^0\pi\pi$ signal, equal to 16.4 MeV/c^2. The characteristic parameter of the Argus PDF, the mass threshold obtained from the fit is equal to $m_{T\eta'} = (5261.6 \pm 1.8)$ MeV/c^2.

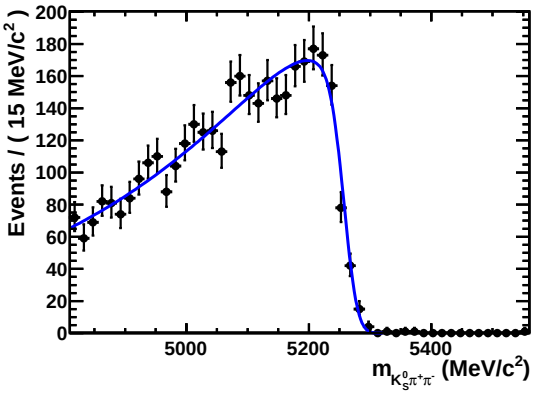

Figure 7.11: *Histogram of $K_S^0\pi\pi$ combination mass with DD K_S^0 obtained from the MC sample of $B^0 \to \eta' K_S^0$. The figure obtained with 2 millions of $\eta' K_S^0$ events. Signal selection is applied. Fit model: convolution of Argus and Gaussian.*

7.5.2.3 $B \to (D \to K_S^0\pi\pi)\pi$

In this type of decay of the energy taken by the missing particle is larger than in case of $\eta' K_S^0$. A mass histogram obtained from the Monte Carlo sample of $B^0 \to (D^- \to K_S^0\pi^-\pi^0)\pi^+$ ($\mathcal{BR}(B^0 \to D^-\pi^+) = (2.68 \pm 0.13) \cdot 10^{-3}$, $\mathcal{BR}(D^- \to K_S^0\pi\pi^0) = (6.99 \pm 0.27) \cdot 10^{-2}$ [2]) is presented in the figure 7.12. Again, a convolution of an Argus and a Gaussian is fitted. The width of the Gaussian is also fixed to be 16.4 MeV/c^2. The Argus mass threshold from the fit is: $m_{TD^0} = (5175 \pm 10)$ MeV/c^2. The maximum of the distribution is located outside the mass window used in *Stripping*12*b* and *Stripping*15, which will make this mode hard to be fitted from the data. Thankfully, the mass window for the next version of stripping is enlarged ($m_{B^0} \pm 500$ MeV/c^2) and will allow to perform the fit.

7.5.2.4 Modes to be analysed

The modes described in the last two points have been the only convenient modes produced in the MC10 conditions before. However there are other background modes that are considered. Proper EVTGEN decay files have been prepared and the samples are about to be generated and analysed. All considered background decay modes (including existing samples) are listed in the table 7.6.

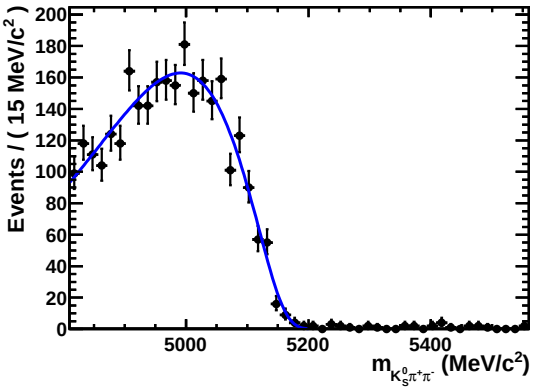

Figure 7.12: *Histogram of $K^0_S\pi\pi$ combination mass with DD K^0_S obtained from the MC sample of $B^0 \to (D^- \to K^0_S\pi^-\pi^0)\pi^+$. The figure obtained with 2 millions of events. Signal selection is applied. Fit model: convolution of Argus and Gaussian.*

Fully reconstructed	Partially reconstructed
$\Lambda_b \to \Lambda_c\pi$, $\Lambda_c \to pK^0_S$,	$B^0 \to \eta' K^0_S$
$\Lambda_b \to D_s\pi$, $D_s \to K^0_S\pi$	$\Lambda_b \to D^*_s p$, $D^*_s \to D_s\gamma$,π^0
	$B \to (D \to K^0_S\pi\pi)\pi$
	$B^0 \to K^0_S\pi\pi\gamma$
	$B \to K^*\rho$
	$B \to K^*K^*, K^*\phi$

Table 7.6: *MC10 background modes considered in the analysis.*

7.5.3 Combinatorial background

The combinatorial background shape has to be extracted from the data. Two models are considered: an exponential background, which becomes in the limit a flat background. We plan to add a dedicated stripping line for $K_S^0 h^+ h^+$, $K_S^0 h^- h^-$ combinations which should allow to obtain a pure combinatorial shape.

7.6 Selection design

7.6.1 Concepts

Let us begin with the concepts of the selection construction:

- The selection aims at rejecting the combinatorial background. It will be inefficient on the partially or fully reconstructed background (hence the physical background), as the properties of the background are very similar to the signal. The physical background will be included in the fit.

- The selection should rely on topological variables mostly. The kinematic variables are strongly related to the resonant structure of the decays. We do not want to bias the Dalitz plane, so we have to avoid kinematic cuts on daughters.

- The selection has to be optimised for DD and LL K_S^0 independently.

- A multivariate analysis, boosted decision tree (BDT) discriminant, is used to deal with possible, non-linear correlations.

7.6.2 Data sets

As a signal sample, we use all six MC10 modes of $K_S^0 hh$. Their properties except of B_s^0/B^0 masses are almost the same, so we can use them together. We consider all MC matched $K_S^0 hh$ candidates which have passed $Stripping12b$ cuts.

As a background sample, we take a subsample of $K_S^0 \pi\pi$ real data from the year 2010. First, we have to remove B mesons mass range. We want to optimise on combinatorial background only. The low masses part of the mass window, as already proved in the previous section, is contaminated by partially reconstructed B background. Hence, we decide to keep only the high masses part of the mass window. We ask for $m_{K_S^0\pi\pi} > 5400$ MeV/c^2. Additionally, we want to remove the baryonic contribution. We do that with mass cuts on the combinations of $K_S^0 \pi p$ and $K_S^0 p$. We further remove D mesons mass ranges in two-body combinations. For LL sample we ask for B/K_S^0 vertex separation larger than 50 mm. The Vertex separation is defined as a distance between the B decay vertex, and the vertex of $K_S^0 \to \pi^+\pi^-$. This cut aims at removing significant contribution of background combinations constructed with false K_S^0. The last cut used is $p_T(B) > 1000$ MeV/c – which has to remove the low transverse momentum combinations constructed with tracks from primary vertices.

The statistics used for training of the discriminant is given in the table 7.7. Low number of events in the background sample of LL K_S^0 is caused by the pre-cuts on vertex separation and B transverse momentum.

K_S^0 DD		K_S^0 LL	
Signal	Background	Signal	Background
38389	15786	17588	2874

Table 7.7: *Number of events in the samples used for training of the BDT discriminant.*

7.6.3 Variables

A set of variables used in the optimisation is given in the table 7.8. The histograms of the variable values and the linear correlation plots can be found in the Appendix D, in the figures E.1- E.4.

There are variables which exhibit non-linear correlations. The impact parameter significances of the two charged hadrons is a perfect example. This and another illustrations are presented in the figure 7.13. The superimposed trending histograms can be used to express the non-linear character of the correlation. These plots justify the decision of using the multivariate BDT technique, which is able to treat non-linear correlations correctly [94].

The importance of the variables in the decision process can be found in the table 7.9. Let us note some observations:

- Among the variables, the impact parameter significances of the charged hadrons are the most discriminative ones. Low values of this parameter is a distinctive characteristic of particles coming from primary vertex.

- The similar impact parameter of K_S^0 is also powerful, but only for LL K_S^0. For DD the signal shape is more background like. Taking in account that DD momentum resolution is less precise than LL, the loss of discriminative power in this case is expected. For the same reason, the flight distance significance of DD K_S^0 is not used in the optimisation.

- The next significant variable in terms of discriminant power is the transverse B momentum. The combinatorial background spectrum is much softer than the signal spectrum.

- The signal has to originate in a primary vertex, two variables are designed in that respect: B_DIRA_OWNPV – which measures the quality of pointing, and B_IPCHI2_OWNPV – which is the impact parameter significance of the reconstructed B. They are correlated for signal and receives a very significant weight in the decision tree.

- Finally, the flight distance significance of B candidate. It is highly correlated with impact parameter significances of the daughters for the signal, and it brings

some additional information for the background. This is the other way of expressing that the B candidate is inconsistent with the primary vertex hypothesis.

- For some of the topological variables, their range covers a few orders of magnitude, so the logarithm of the value is used in the optimisation and in the plots.

Variable	Description
B_PT	B transverse momentum
B_IPCHI2_OWNPV	B primary vertex impact parameter significance
B_DIRA_OWNPV	B pointing angle
$B\_ENDVERTEX\_CHI2$	B vertex fit χ^2
B_FDCHI2_OWNPV	B flight distance significance
h_IPCHI2_OWNPV	hadron primary vertex impact parameter significance
$KS\_ENDVERTEX\_CHI2$	K^0_S vertex fit χ^2
$KSLL\_FDCHI2\_OWNPV$	K^0_S flight distance significance, LL only
KS_IPCHI2_OWNPV	K^0_S hadron primary vertex impact parameter significance

Table 7.8: *List of variables used to build $K^0_S hh$ BDT discriminant.*

Variable	Importance DD	Importance LL
B_PT	0.165	0.168
B_IPCHI2_OWNPV	0.110	0.111
B_DIRA_OWNPV	0.037	0.086
$B\_ENDVERTEX\_CHI2$	0.068	0.059
B_FDCHI2_OWNPV	0.139	0.074
h_IPCHI2_OWNPV	0.192	0.129
$KS\_ENDVERTEX\_CHI2$	0.035	0.059
$KSLL\_FDCHI2\_OWNPV$	not used	0.064
KS_IPCHI2_OWNPV	0.069	0.126

Table 7.9: *BDT variable importance [94] ranking, normalised to 1.*

7.6.4 Working point selection

The discriminant response histograms are displayed in the figure 7.14. A choice of the BDT response cut was based on the largest signal significance $S/\sqrt{(S+B)}$. Two working points have been chosen, based on the purpose:

1. $B^0 \to K^0_S\pi\pi$ selection. The initial number of signal events was based on the expected number of signal events before the stripping obtained in the exploratory

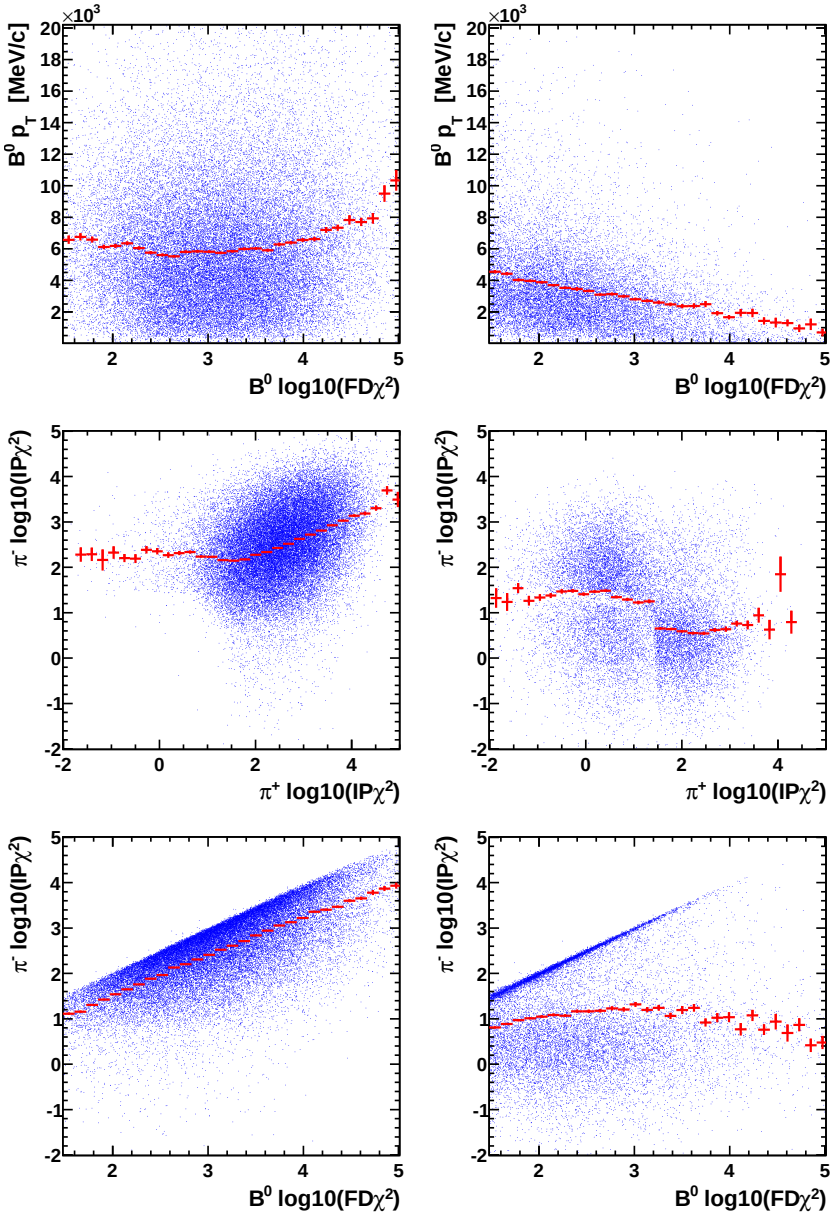

Figure 7.13: *Correlations between selected BDT parameters for signal (left) and background (right) for K^0_S DD samples. The red histograms show trending of the averages.*

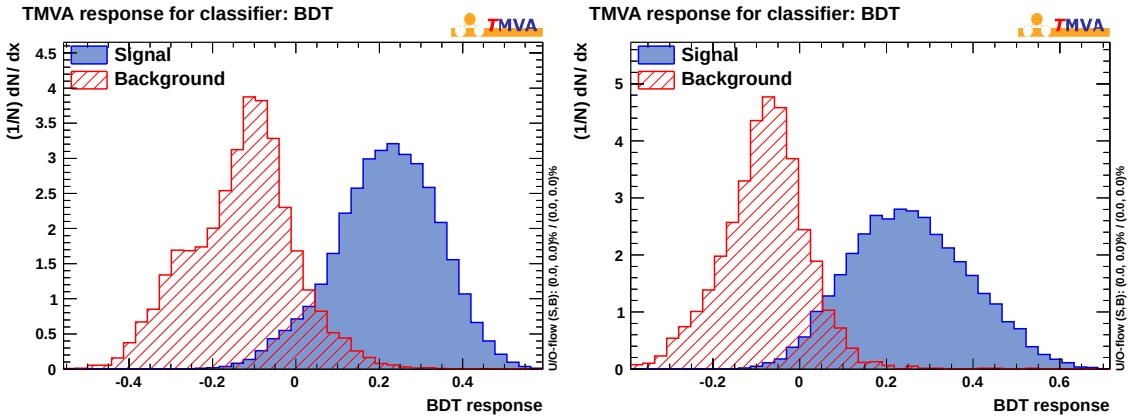

(a) K^0_S DD (b) K^0_S LL

Figure 7.14: *BDT discriminant response for signal and background.*

work described in the beginning of this chapter. As the combinatorial background initial statistics estimation, number of events from 2010 data for mass range 5240 MeV/c^2 $< m_{K^0_S\pi\pi} <$ 5320 MeV/c^2 after all D, Λ_b, Λ_c and Ξ_b background removal was used.

2. $B^0_s \to K^0_S K\pi$ selection. The initial number of signal events was the fourth part of the statistics used in the first point. It is a rough estimation based on the ratio f_s/f_d. The background initial statistics was defined as number of events in the $K^0_S K\pi$ sample inside mass region defined as 5326 MeV/c^2 $< m_{K^0_S\pi\pi} <$ 5406 MeV/c^2, where all D, Λ_b, Λ_c and Ξ_b were removed.

The efficiencies on the signal and the background are given in the table 7.10.

Optimisation	K^0_S DD		
	BDT Cut	ϵ Signal	ϵ Background
$B^0 \to K^0_S\pi\pi$	0.20	0.56	0.004
$B^0_s \to K^0_S K\pi$	0.23	0.46	0.002

Optimisation	K^0_S LL		
	BDT Cut	ϵ Signal	ϵ Background
$B^0 \to K^0_S\pi\pi$	0.13	0.82	0.012
$B^0_s \to K^0_S K\pi$	0.21	0.63	0.003

Table 7.10: *BDT discriminant efficiencies.*

7.7 PID cuts

We have already mentioned that the cross-feed between $K^0_S\pi\pi$ and $K^0_S K\pi$ signals occurs. It is suppressed by PID cuts to a certain extent. We define:

- a kaon as a particle with $PIDK > 5$,
- a pion as a particle with $PIDK < 0$.

This arbitrary choice was based on Monte Carlo PID efficiencies presented in the figures 7.15 and 7.16.

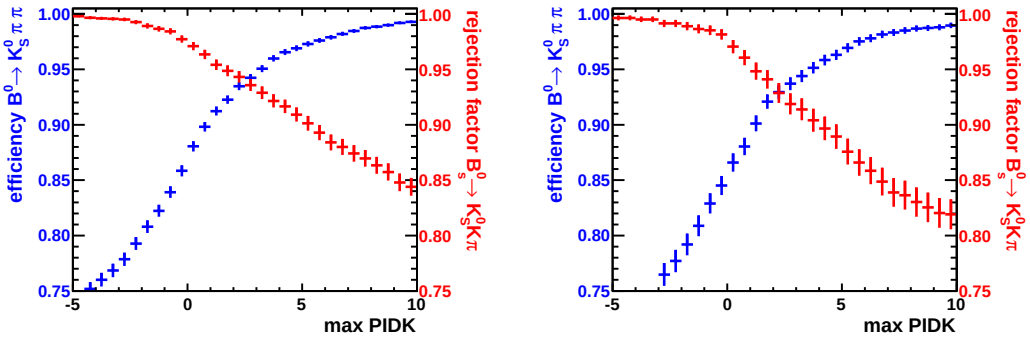

(a) K^0_S DD (b) K^0_S LL

Figure 7.15: *Efficiencies over MC10 sample of the PID cut $PIDK < maxPIDK$ applied to the both charged hadrons. Blue histogram: efficiency on $B^0 \to K^0_S\pi\pi$. Red histogram: rejection fraction on $B^0_s \to K^0_S K\pi$.*

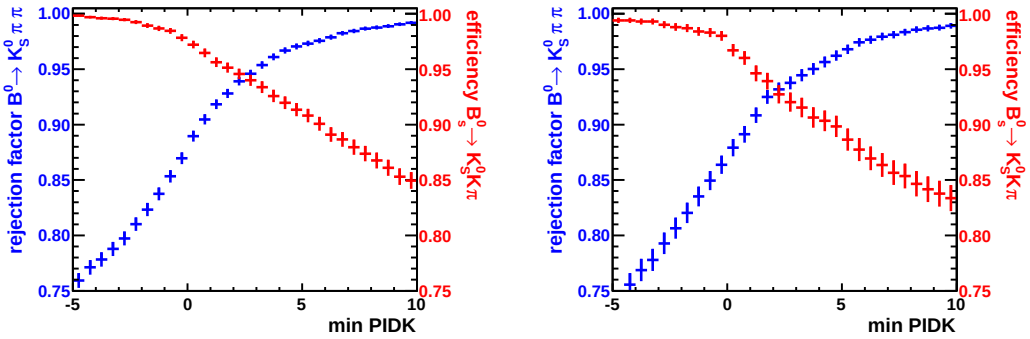

(a) K^0_S DD (b) K^0_S LL

Figure 7.16: *Efficiencies over MC10 sample of the PID cut $PIDK > minPIDK$. Blue histogram: efficiency on $B^0_s \to K^0_S K\pi$, cut applied to the kaon. Red histogram: rejection fraction on $B^0 \to K^0_S\pi\pi$, cut applied to one randomly chosen hadron..*

Monte Carlo particle identification efficiencies are not reproduced on real data. Hence, we can not use them for anything else than the definition above. For the measurement, one has to use PID efficiency tables based on particle p, p_T and track multiplicity in the event. The evaluation of these efficiencies for our data and a proper weighting of events accordingly to them is currently ongoing [103].

7.8 Fit model

We construct the model, which we will use to fit the data with the components:

- B^0 and B_s^0 signal shapes. Two Gaussian distributions of the same width. The central values are left free and their initial values are set to the PDG values.
- Combinatorial background shape described by an exponential e^{Cx}. We limit the parameter with $C \leq 0$. It means that the shape can become a flat function for $C = 0$.
- $B^0 \to \eta' K_S^0$ partially reconstructed background. All parameters are taken from the fit to the Monte Carlo sample.
- $B \to (D \to K_S^0 \pi\pi)\pi$ partially reconstructed background. Again, the parameters are taken from the Monte Carlo.

Each component contribution is left free for the fit to adjust it. The fit is performed on the unbinned data set.

Additionally, we remove from the data all possible two-body combinations with mass cuts: $D^0 \to K\pi$, $D^0 \to \pi\pi$, $D^+ \to K_S^0\pi^+$, $D_s \to K_S^0\pi$, $D_s \to K_S^0 K$, $\Lambda_c \to K_S^0 p$, $\Lambda_b \to K_S^0 \pi p$, $\Xi_b \to K_S^0 \pi p$.

We will use this model only for scrutiny the data. The final model, which will be used for branching fraction measurements, will be extended by knowledge gained from the ongoing studies of the rest of Monte Carlo samples.

7.9 $K_S^0\pi\pi$ channel

7.9.1 2010 data fit

First, we can look into 2010 data. We apply the selection with a cut dedicated to $B^0 \to K_S^0\pi\pi$, as we would like to observe this mode first. The histogram with the fit, and the fit results are presented in the figure 7.17. In both cases the combinatorial background parameter C is expected to be 0, which means a flat distribution. Obtained yields for DD K_S^0 are: 75 ± 17 for B^0, and 0 ± 9 for B_s^0. For LL K_S^0 they are: 29 ± 8 for B^0, and 15 ± 6 for B_s^0. They are in good agreement for $B^0 \to K_S^0\pi\pi$ with the expected yields estimated on the MC. They mean also a hint of B_s^0 observed.

7.9.2 2011 data fit

The integrated luminosity from 2011, used in the analysis presented in this part, is $\mathcal{L} = 230$ pb^{-1} from *Stripping*15.

The same procedure as in the previous paragraph is repeated for the 2011 data of $K_S^0\pi\pi$ (figure 7.18. The selection cut is again the one optimised for $B^0 \to K_S^0\pi\pi$. The fits converged with different slope of the combinatorial background, which is flat in case of LL K_S^0, and which is characterised by $C = -0.0033 \pm 0.0005$ for DD K_S^0. On the other hand, in case of DD, the expected number of partially reconstructed D events is equal to zero. Such differences between DD and LL are not well-founded physically, meaning that with this statistics, it is impossible to justify the simple model used in the fit. We can imagine, that the combinatorial background is driven by the parts of histograms above the mass of B_s^0, which is limited by the mass window definition inside the stripping.

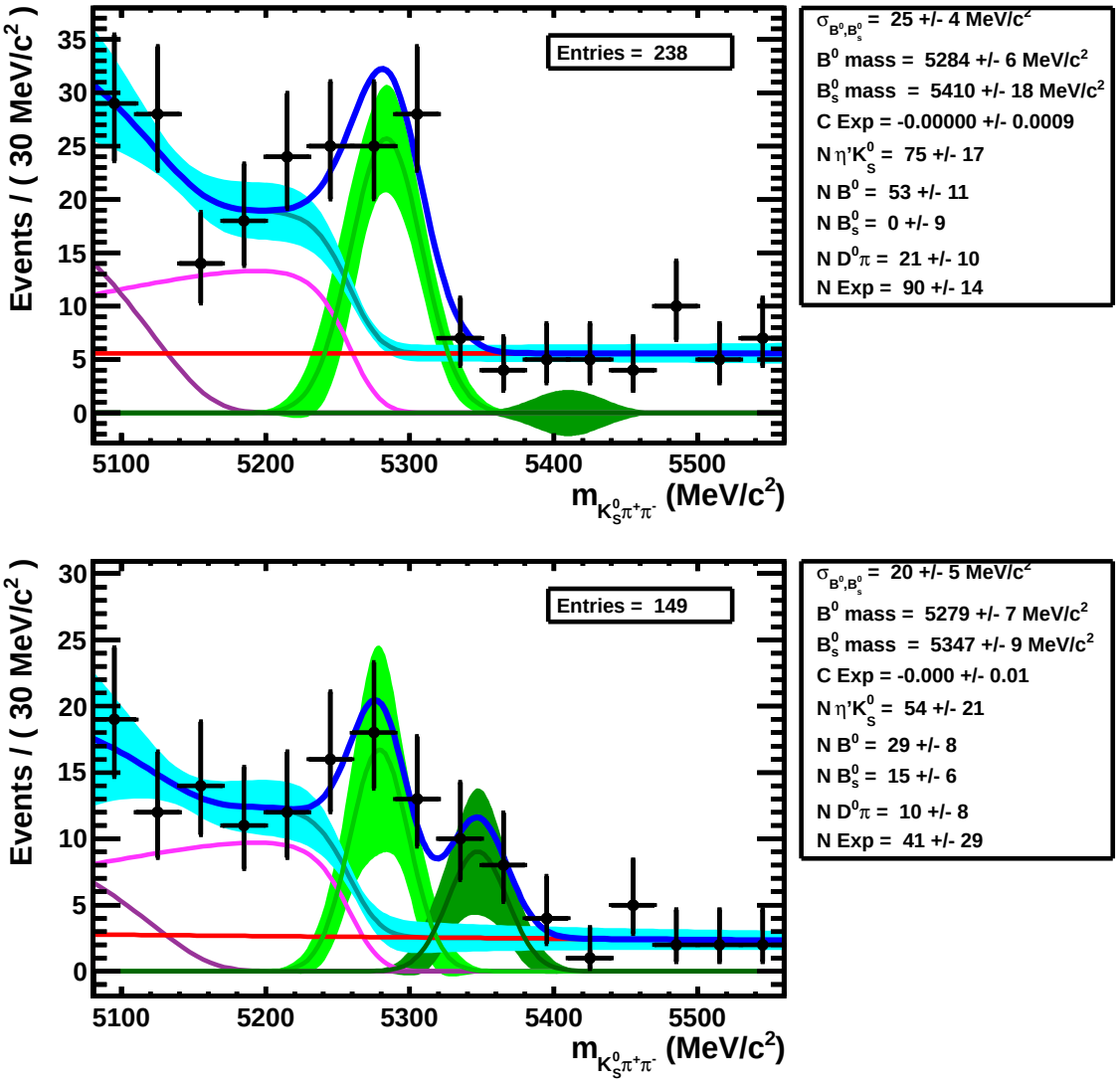

Figure 7.17: *Histograms of $K^0_S\pi\pi$ combination mass, obtained with the selection optimised for $B^0 \to K^0_S\pi\pi$, applied to the 2010 data. Top: DD K^0_S candidates; bottom: LL K^0_S candidates. Blue line – the fit model. Light green – B^0 signal shape (line) and $\pm1\sigma$ band. Dark green – B^0_s signal shape (line) and $\pm1\sigma$ band. Red line – combinatorial background. Magenta line – $\eta' K^0_S$ background. Violet line – $D\pi$ partially reconstructed background. Cyan – all background types combined (line) with $\pm1\sigma$ band.*

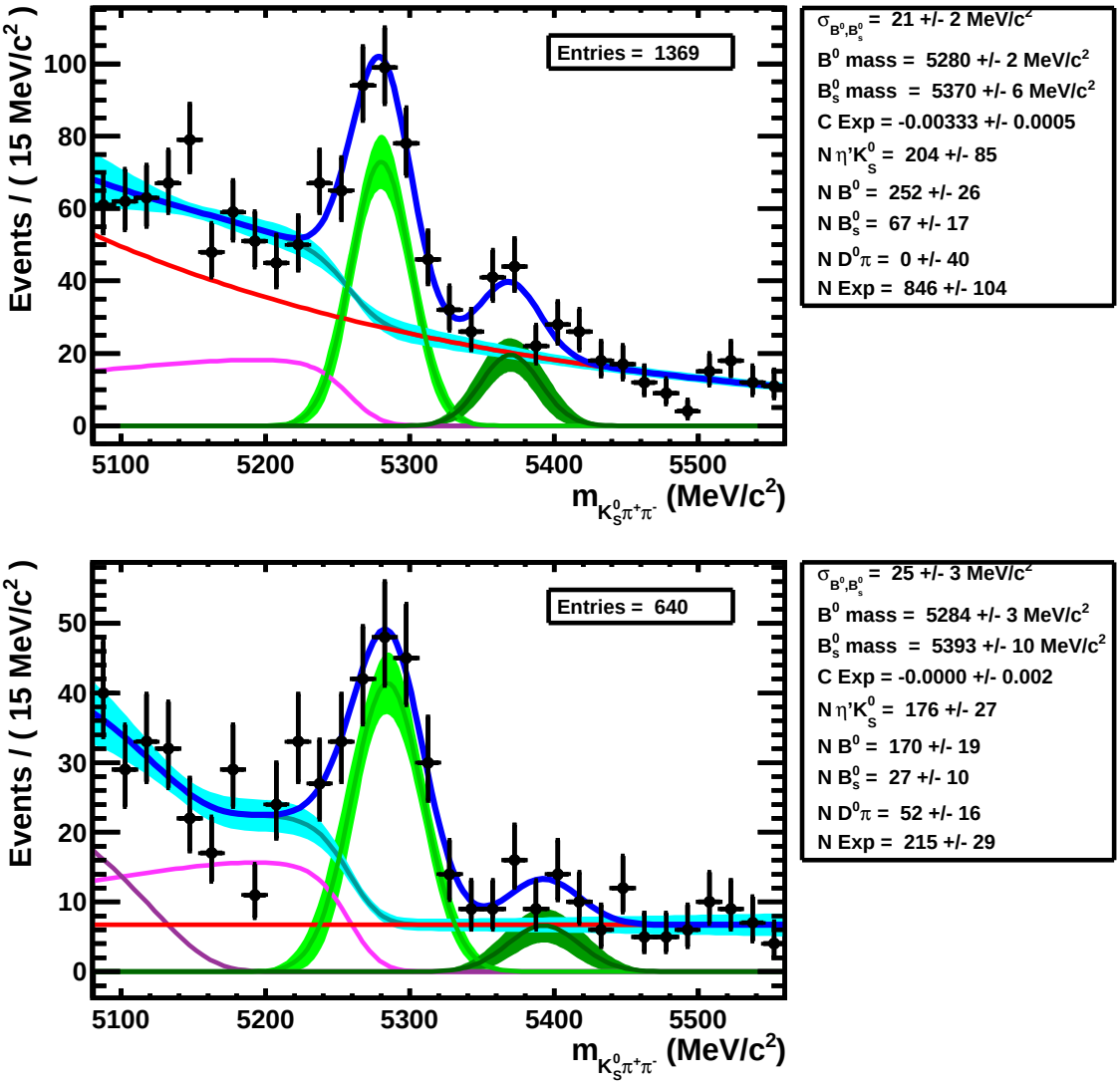

Figure 7.18: *Histograms of $K^0_S\pi\pi$ combination mass, obtained with the selection optimised for $B^0 \to K^0_S\pi\pi$, applied to the 2011 data. Top: DD K^0_S candidates; bottom: LL K^0_S candidates. Blue line – the fit model. Light green – B^0 signal shape (line) and $\pm1\sigma$ band. Dark green – B^0_s signal shape (line) and $\pm1\sigma$ band. Red line – combinatorial background. Magenta line – $\eta' K^0_S$ background. Violet line – $D\pi$ partially reconstructed background. Cyan – all background types combined (line) with $\pm1\sigma$ band.*

The yields for DD K^0_S are: 252 ± 26 for B^0, and 67 ± 17 for B^0_s. For LL K^0_S they are: 170 ± 19 for B^0, and 27 ± 10 for B^0_s. Again in agreement with the expectations as far as $B^0 \to K^0_S\pi\pi$ is concerned. Adding together the yields from DD and LL for the hypothesis of $B^0_s \to K^0_S\pi\pi$, and summing the uncertainties from the fits in quadrature, we obtain the number of $B^0_s \to K^0_S\pi\pi$ equal to: 94 ± 20. The significance of this signal is 4.7σ. However, the yields are contaminated by systematic, model dependent uncertainties, which are not addressed here, as the final fit model will be different.

7.10 $K^0_S K\pi$ channel

For $K^0_S K\pi$ combinations, the selection with cut designed for $B^0_s \to K^0_S K\pi$ is applied. We can expect that the number of events in this modes should be larger than for $B^0 \to K^0_S K\pi$, as in terms of diagrams these are the sister-modes to the decays $B^0 \to K^0_S\pi\pi$, and $B^0_s \to K^0_S\pi\pi$ respectively.

The cut on particle identification log likelihood applied to kaons selects K, but also a significant fraction of protons. It is possible to remove the protons with the cut: $PIDK - PIDp > 5$. The efficiency of the proton identification has been not yet precisely investigated, hence this method of purifying the sample can be used temporarily only. It will be dropped, once the shapes of baryonic background types from Monte Carlo are extracted.

The fit model is modified in the parts which represent the partially reconstructed, MC modelled background. As the contribution of $B^0_s \to K^0_S K\pi$ is expected to dominate, for the time being we neglect the partially reconstructed background from B^0. On the other hand, we add the partially reconstructed background for B^0_s, by shifting the MC distributions obtained for B^0 by the mass difference between B^0_s and B^0. The results of the fits, together with the histograms, are presented in the figure 7.19.

Again, the combinatorial background shape was chosen differently in DD from LL K^0_S. The model appears to not follow perfectly the histogram points for the masses lower than B^0 mass, which suggests that there are missing contributions in the partially reconstructed backgrounds. The yields: K^0_S DD, for B^0 it is 24 ± 17, while for B^0_s it is 62 ± 12. In case of K^0_S LL, for B^0 we obtain 15 ± 5, and 22 ± 6 for B^0_s. Summing up the statistics from both types of K^0_S, we obtain the number of $B^0_s \to K^0_S K\pi$ events estimated from the fits equal to 84 ± 13. The number of signal events in this case is not much dependent on the background shape (whether it contains more or less exponential character, and whether it has more or less partially reconstructed background events). The amount of background is low, and the differences between PDF shapes under B^0_s peak are not significant, respectively to the signal significance. Concluding, with these results we can claim the first observation of the decay mode $B^0_s \to K^0_S K\pi$. The next step is to measure the branching fraction.

7.11 $K^0_S KK$ channel

In this part we repeat the steps made in the case of $K^0_S\pi\pi$, but we apply the selection optimised for $B^0 \to K^0_S\pi\pi$ to the combinations of $K^0_S KK$ (figure 7.20). The yields

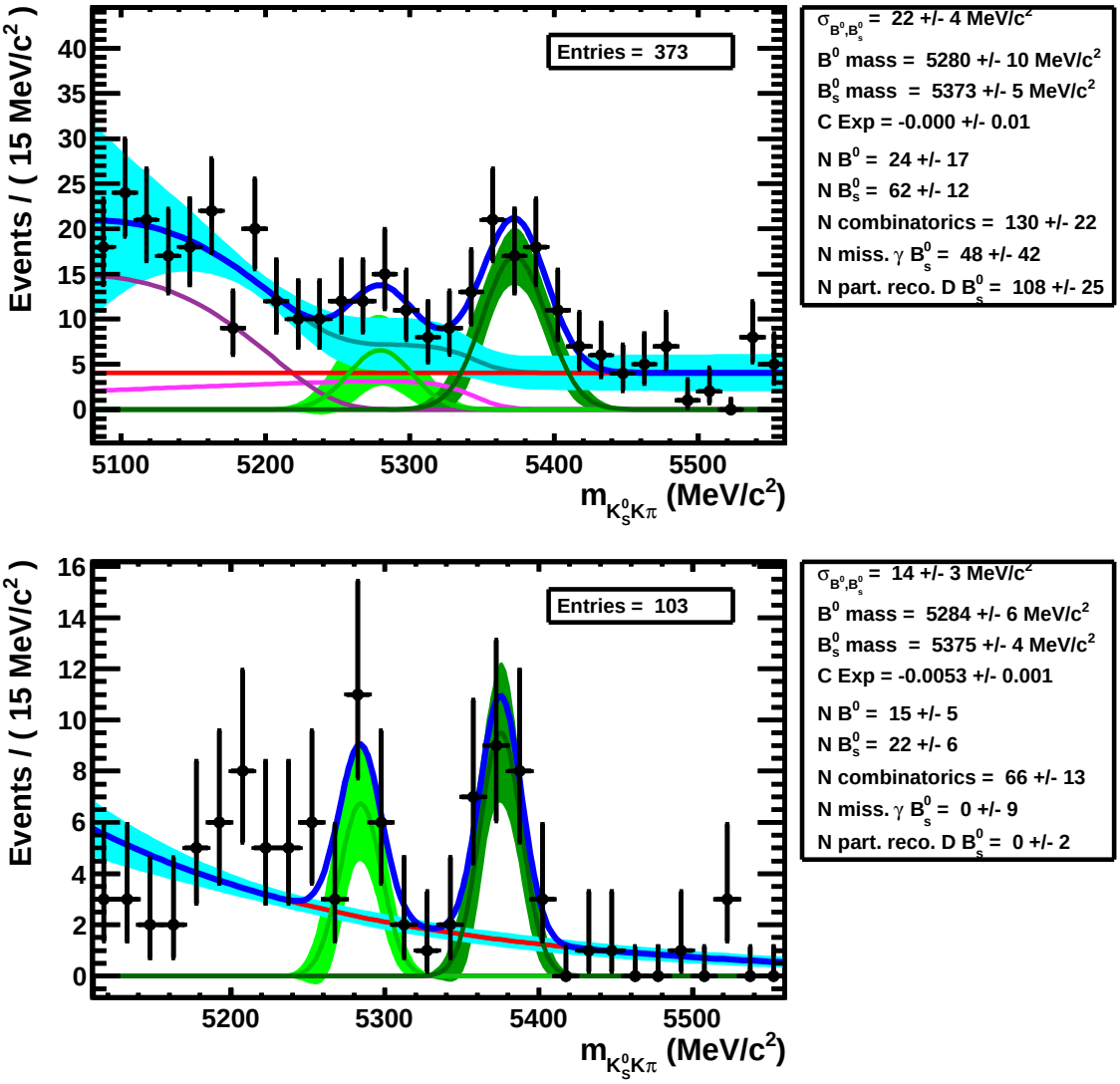

Figure 7.19: *Histograms of $K^0_S K\pi$ combination mass, obtained with the selection optimised for $B^0_s \to K^0_S K\pi$, applied to the 2011 data. Additional PID cut applied to K: $PIDK - PIDp > 5$. Top: DD K^0_S candidates; bottom: LL K^0_S candidates. Blue line – the fit model. Light green – B^0 signal shape (line) and $\pm 1\sigma$ band. Dark green – B^0_s signal shape (line) and $\pm 1\sigma$ band. Red line – combinatorial background. Magenta line – B^0_s radiative partially reconstructed background. Violet line – B^0_s partially reconstructed background with D. Cyan – all background types combined (line) with $\pm 1\sigma$ band.*

from the fit for DD K^0_S are equal to: 96 ± 14 and 31 ± 9, for B^0 and B^0_S respectively. For LL K^0_S, they are equal to: 62 ± 13 and 7 ± 7.

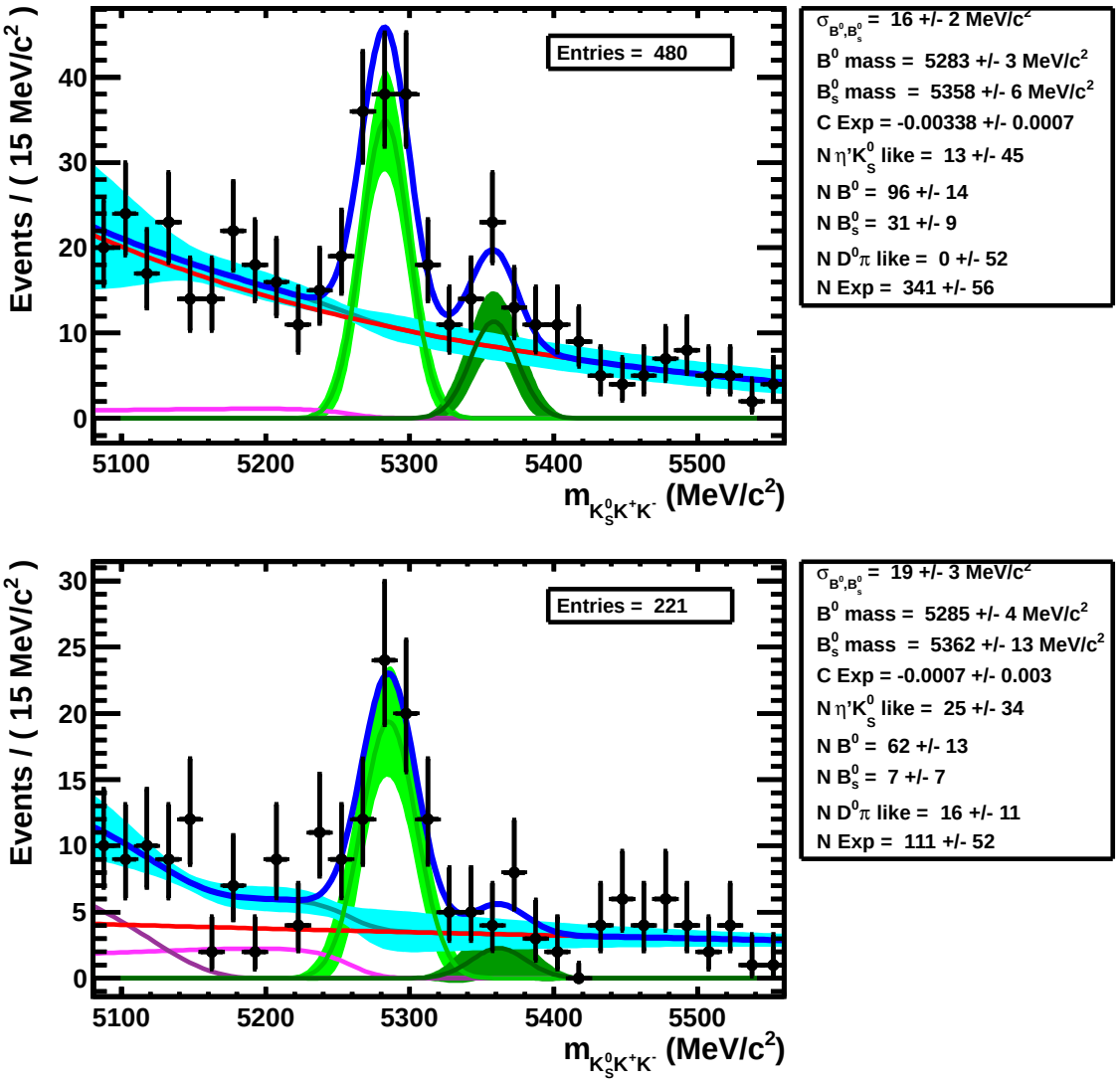

Figure 7.20: *Histograms of $K^0_S KK$ combination mass, obtained with the selection optimised for $B^0 \to K^0_S \pi\pi$, applied to the 2011 data. Top: DD K^0_S candidates; bottom: LL K^0_S candidates. Blue line – the fit model. Light green – B^0 signal shape (line) and $\pm 1\sigma$ band. Dark green – B^0_s signal shape (line) and $\pm 1\sigma$ band. Red line – combinatorial background. Magenta line – B^0 radiative partially reconstructed background. Violet line –B^0 partially reconstructed background with D. Cyan – all background types combined (line) with $\pm 1\sigma$ band.*

7.12 Perspectives

The first signal shapes with 230 pb^{-1} from 2011 data were established. The yields are summarised in the table 7.11. The decay mode $B^0_s \to K^0_S K\pi$ has been observed (6.5σ).

There are evidences of the decay modes $B_s^0 \to K_S^0\pi\pi$ (4.7σ) and $B_s^0 \to K_S^0KK$ (3.5σ). With the whole 2011 statistics, these modes should be observed. This means that the branching fraction measurements can be performed, starting from the decay of $B_s^0 \to K_S^0K\pi$. Let us focus on this mode for the sake of the example.

Mode	DD K_S^0	LL K_S^0	Combined K_S^0	significance
$B^0 \to K_S^0\pi\pi$	252 ± 26	170 ± 19	422 ± 32	13σ
$B_s^0 \to K_S^0\pi\pi$	67 ± 17	27 ± 10	94 ± 20	4.7σ
$B^0 \to K_S^0K\pi$	24 ± 17	15 ± 5	39 ± 18	2.2σ
$B_s^0 \to K_S^0K\pi$	62 ± 12	22 ± 6	84 ± 13	6.5σ
$B^0 \to K_S^0KK$	96 ± 14	62 ± 13	158 ± 19	8.3σ
$B_s^0 \to K_S^0KK$	31 ± 9	7 ± 7	38 ± 11	3.5σ

Table 7.11: *Signal yields for* 230 pb^{-1} *of 2011 data.*

This will be a relative branching fraction measurement, and the reference will be the decay mode of $B^0 \to K_S^0\pi\pi$. The formula, which describes it, can be written as:

$$\mathcal{B}(B_s \to K_SK\pi) = \mathcal{B}(B_d \to K_S\pi\pi) \times \frac{\epsilon^{\text{sel}}_{B_d\to K_S\pi\pi}}{\epsilon^{\text{sel}}_{B_s\to K_SK\pi}} \times \frac{\epsilon^{\text{PID}}_{B_d\to K_S\pi\pi}}{\epsilon^{\text{PID}}_{B_s\to K_SK\pi}} \times \frac{N_{B_s\to K_SK\pi}}{N_{B_d\to K_S\pi\pi}} \times \frac{f_d}{f_s}, \quad (7.1)$$

where ϵ_X^{sel} is the efficiency to reconstruct the decay mode X including the geometrical acceptance, trigger, stripping and selection steps and N_X is the number of reconstructed events in this mode. ϵ_X^{PID} is the PID efficiency. The values of ϵ_X^{sel} are obtained from the Monte Carlo. The values of ϵ_X^{PID} are data driven. The hadronisation fraction ratio f_d/f_s is taken from the LHCb measurement. From this equation, the next steps towards the measurement can be concluded:

- The trigger, stripping and selection efficiencies calculation. The simplified version was presented in the beginning of this chapter for *Stripping*12*b* and 2010 trigger configuration. This has to be done on the Monte Carlo samples for both signal modes stripped with *Stripping*15. Systematic uncertainties have to be estimated as well. With sufficient statistics, in the future, one would also introduce here a representation of different resonant structures of the Dalitz planes in both decays, and hence different efficiencies.

- The yields have to be extracted from the simultaneous unbinned fits of the models to the data. The models have to be extended by addition of baryonic background shapes, and partially reconstructed background shapes extracted from the simulation. The model related systematic uncertainties have to be addressed. Additionally, the results have to be corrected for reflections of one signal mode to the other. Finally, a proper procedure of dealing with multiple candidates per event has to be applied. It means, that only one, randomly chosen candidate per event is used.

- The yields have to be checked for stability against different selection working points. Similarly for different PID cuts, and mass vetoes of D and $\lambda_{b,c}$.

- Finally, the yields have to be reweighed accordingly to the PID efficiency maps obtained from the real data. Again, a proper treatment of the uncertainties is crucial.

All these steps are undergoing work with the Warwick group, and we are close to completion for the branching fractions measurement.

The exploratory work presented in this chapter on 2010 and a fraction of 2011 data served the commissioning of the complete analysis on ~ 5 times the statistics used here. We have, following the conclusions of this work, enough information supporting the first observation of the three $B_s \to K^0_S hh$ modes in 2011 data.

Summary

The analysis of charmless three-body decays of neutral B mesons may be very interesting. All CKM triangle angles can be accessed with a proper amplitudes decomposition for the transitions through different intermediate resonances. The amplitudes themselves can be extracted from the data with Dalitz analysis. An example of theoretical introduction to such kind of analysis was given in the first chapter . That was the γ angle extraction method from the B^0 and B_s^0 decays. In case of B^0 decays, a non-negligible contribution from electroweak penguin diagrams has to be taken into account. On the other hand, this contribution in case of B_s^0 is negligible, resulting in theoretical uncertainty below 1°. The other interesting analysis is the β angle extraction, which uses K_S^0hh final states. It is probably the first objective which will be reached by the analysis of charmless three-body decays of neutral B mesons.

This document described an exploratory work conducted in the spectrum region of $hh\pi^0$ and K_S^0hh decays. The first case is challenging, because neutral pion reconstruction is a difficult task. In case of B decays, the distance between two photons from a π^0 decay is comparable to the calorimeter cell longitudinal diameter. This means that high energy π^0 particles from B mesons are typically reconstructed as merged π^0. During the scrutiny of the data recorded in 2010 we observed that merged π^0 containers can be highly polluted by high energy photons. We decided to use multivariate analysis to separate π^0 from γ. We extended the pre-existing tool by adding the preshower information. The tool was trained on the Monte Carlo samples of π^0 and γ from B decays. The discriminative tool was successfully used to purify subsample of 2011 statistics.

The next step is to select the final set of variables used in the tool by removing the least powerful variables. Then, the evaluation of the efficiency of the tool on the data will take place. Charm decays $D^0 \to K\pi\pi^0$ will be used for this purpose. The evaluation will be performed for different momentum and transverse momentum regions. Once this efficiency map is prepared, the tool will be completely ready to be applied for the analyses.

The preshower of the electromagnetic calorimeter is used as one of the inputs in the reconstruction of neutral pions. Hence, the performance of the reconstruction relies on the calibration of the preshower. The largest part of this document was dedicated to the subject of the preshower calibration. The procedure of calibration based on minimum ionising particles was prepared. Different systematic effects were taken into account. The procedure was tested on the Monte Carlo and applied to the data. As the result, the detector was calibrated for 2010 and 2011 at the required level. Additionally, the detector alignment respect to the tracking system was discussed. The method of measuring the misalignment was introduced and it was applied to (re-)align

the preshower for 2010 and 2011 data taking. Certainly, the algorithms described in this document will be used in the following years to maintain the detector calibration.

Finally, the charmless three-body decays of B^0 and B_s^0 into K_S^0hh finals states were discussed. The first observation of $B_s^0 \to K_S^0 K\pi$ was presented. The exploratory work described here, which includes signal selection, signal and background modeling, and the efficiency studies is the introduction to the complete analysis of the data. The branching fraction measurements of the unobserved modes is the first objective to be reached. The first results obtained with the whole statistics recorded in 2011 will be ready in the beginning of 2012.

Appendix A

Photomultiplier β parameter determination

To set the new values of high voltage properly, it is first required to measure the β values for all boards. The measurement is done with LED calibration system. The same constant for each photomultiplier high voltages are applied. For each setting, a set of measurements is taken. The process of the measurements is similar to normal data taking with the exception that light signal from LED flashes is used. The LED calibration PRS system has been designed such that the LED flashes are constant within few percent [85]. For each high voltage setting and each channel of multianode photomultiplier a histogram of integrated charge by a photomultiplier for each LED flash event is prepared. Then, the average charge per channel $\overline{Q_{ch}(U)}$ and the root mean square $\sigma_{ch}(U)$ are calculated. The results of $\overline{Q_{ch}^{U}}$ and $(\sigma_{ch}^{U})^2/\overline{Q_{ch}(U)}$ as a function of $\overline{Q_{ch}(U)}$ are presented in the figure A.1. For the further analysis, only the working points which lie in a certain range of $\sigma_{ch}^2(U)/\overline{Q_{ch}(U)}$. The range is marked on the plot with a red band. The basis of that is the fact that the value of $\sigma_{ch}^2(U)/\overline{Q_{ch}(U)}$ should be constant and simply related to the photostatistics of the photomultiplier. The rejection of the points which are far from the mean value removes unstable channels or channels for which the statistics is polluted by flashes other than LED flashes.

The next step is the fit of the law to the LED data. Only the channels for which at least three working points with different high voltages settings are valid are fit. The fit is done on the plot of $\overline{Q_{ch}(U)}$ as a function of U, in logarithmic scales for both axises. The fit function is a first order polynomial. The slope of the fit is β_{ch} accordingly to the (4.4). The results of the fit for an exemplary board are presented in the figure A.2. For each fit the residuals are calculated. The distribution of the residuals is shown in the figure A.3. The cut on the residuals is made by asking to keep the fits with the value lower than 0.5% only. The cut removes the channels which do not comply with the law (4.4). The distribution of β for each channel before and after the residual cut can be found in the figure A.3.

The last step is the construction of the average $\overline{\beta}$ for each board from all valid channels. The results are presented in the figure A.4. One can find in the figure dashed areas – these are the boards for which the shortcut in the power supply of the LED system made the measurement impossible. Additionally the number of valid channels used for the averaging respect to the number of all channels in the board in

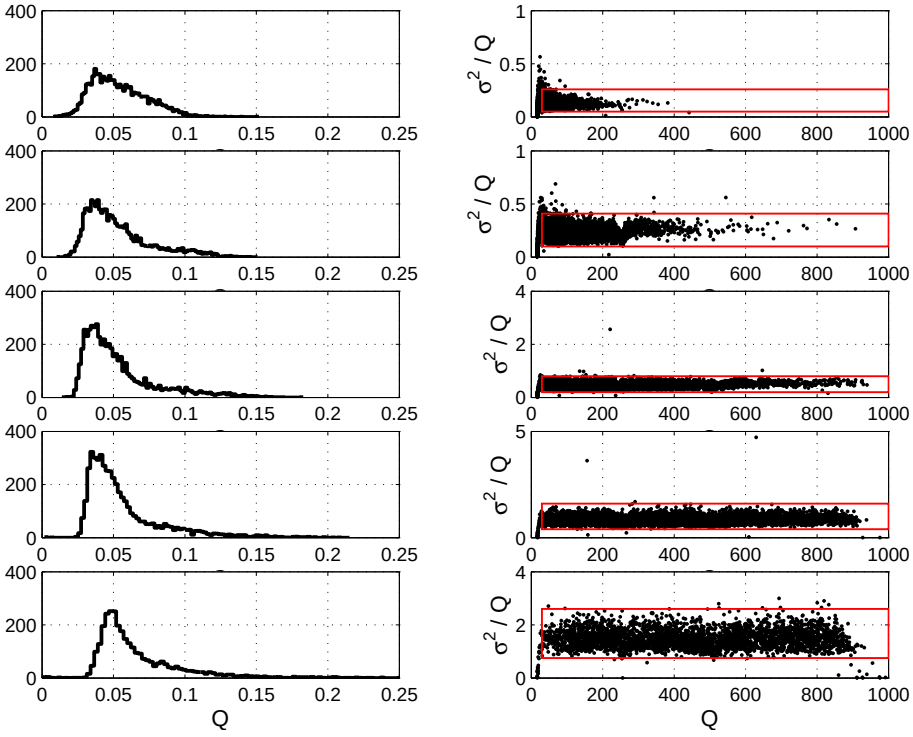

Figure A.1: *Left plot: Distributions of the average charge integrated from LED calibration flashes. One entry per channel. Charge are in a relative unit respect to a fixed value. One plot per one high voltage setting. The voltage value rises from the top to the bottom. Right plot:* $\sigma^2_{ch}(U)/\overline{Q_{ch}(U)}$ *as a function of* $\overline{Q_{ch}(U)}$*. One entry per channel. One plot per one high voltage setting. The voltage value rises from the top to the bottom. Area marked with red shows the working points selected for the extraction of* β*.*

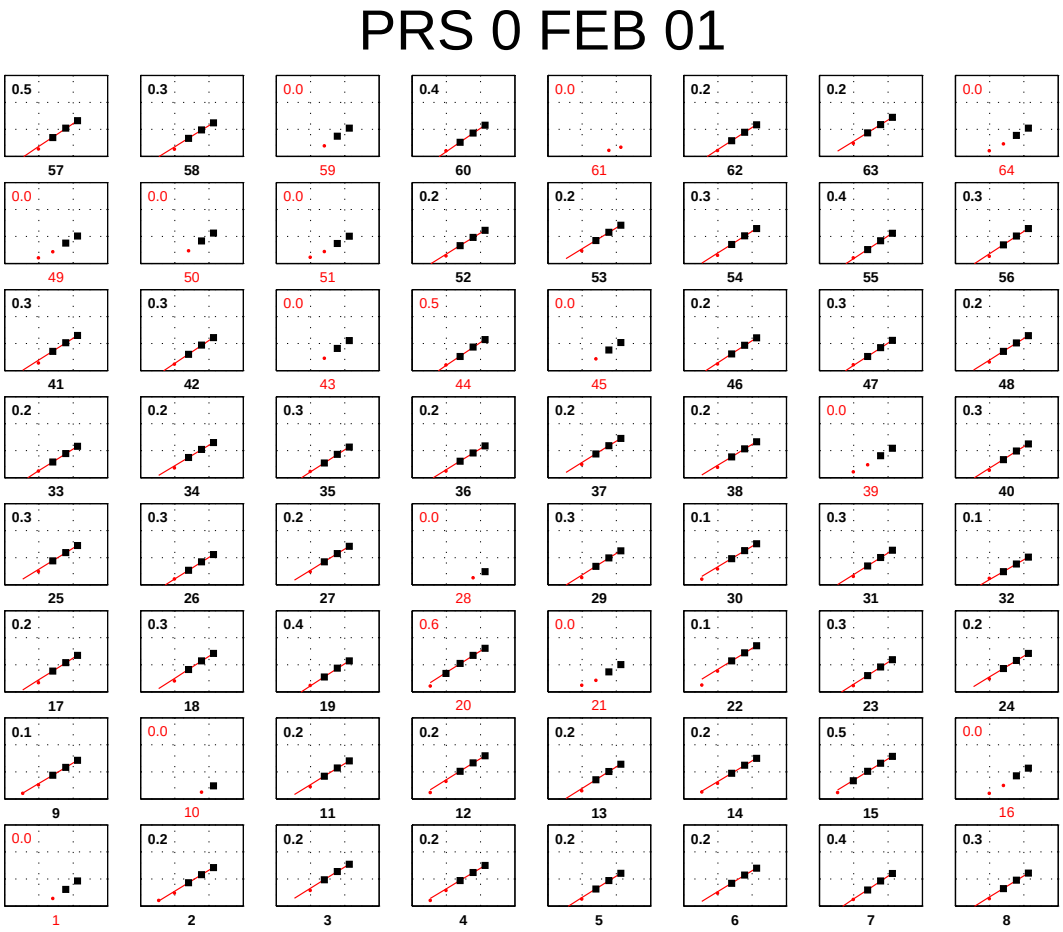

Figure A.2: *Results of the fits of the equation (4.4) law to the LED data for one board of the PRS detector. One histogram per one FEB channel. Both axes are in logarithmic scale. On the horizontal axis the high voltage is presented. On the vertical axis the average charge collected by the photomultiplier is shown. Black points represent points which passed* $\sigma^2_{ch}(U)/\overline{Q_{ch}(U)}$ *cut. Red small points represent rejected points. Red lines are the linear fits in log-log scale. The slope values of the fits are the* β *values of the channels.*

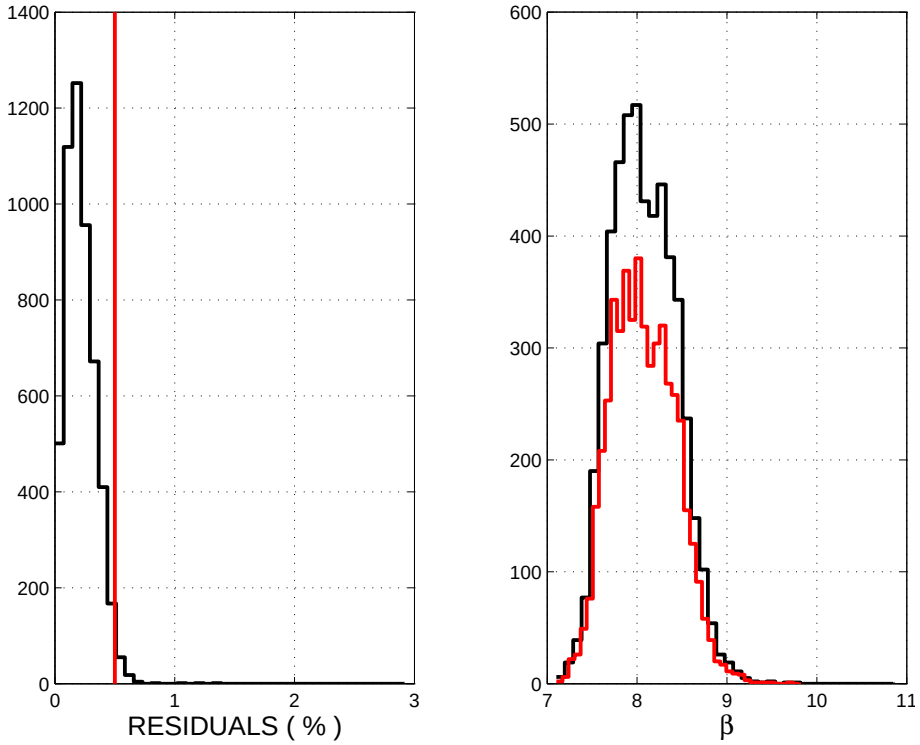

Figure A.3: *Left plot: Distribution of the value of residuals of fits of the equation (4.4) to the LED data. One entry per channel. Red line shows the cut value used for the selection of valid channels. Right plot: The result of the fits of β parameters. With black colour all PRS channels are marked. Red colour represents only the channels which passed the selection based on the residuals.*

percents is presented. For all boards with working LED system that value is larger than 50%. For the PRS 0 that ratio is a bit lower then for the other regions. If the PRS 0 is excluded, then more than 90% of channels was good in terms of calculating the average values of $\overline{\beta}$.

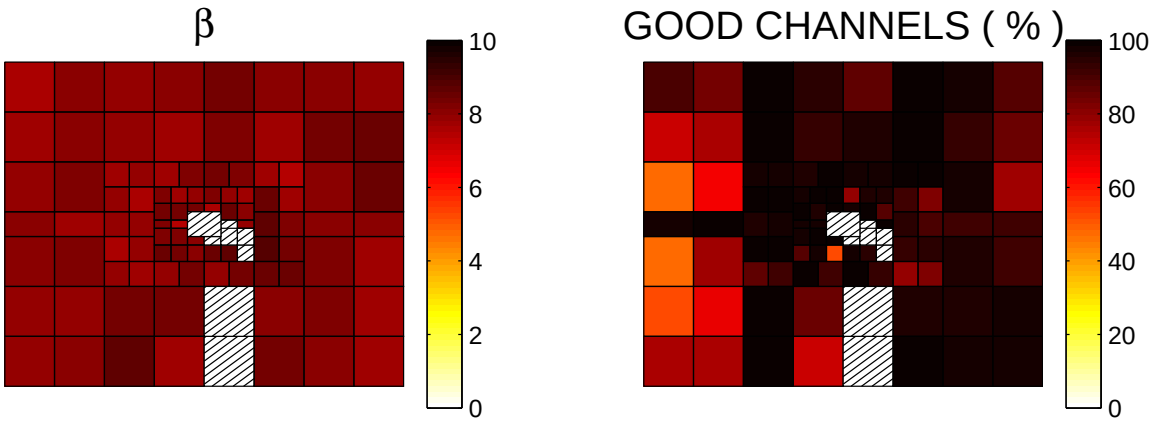

Figure A.4: *Left plot: The $\overline{\beta}$ parameter for different boards of the preshower detector. Dashed areas represent boards with the shortcut in the LED power supply system for which the measurement was impossible. Right plot: Ratio of channels used for the extraction of the $\overline{\beta}$ parameter for each cell (called "good channels") to all channels for each front-end board. The "good channels" are the channels which have passed the criteria of: $\sigma^2_{ch}(U)/\overline{Q_{ch}(U)}$ and residuals cuts.*

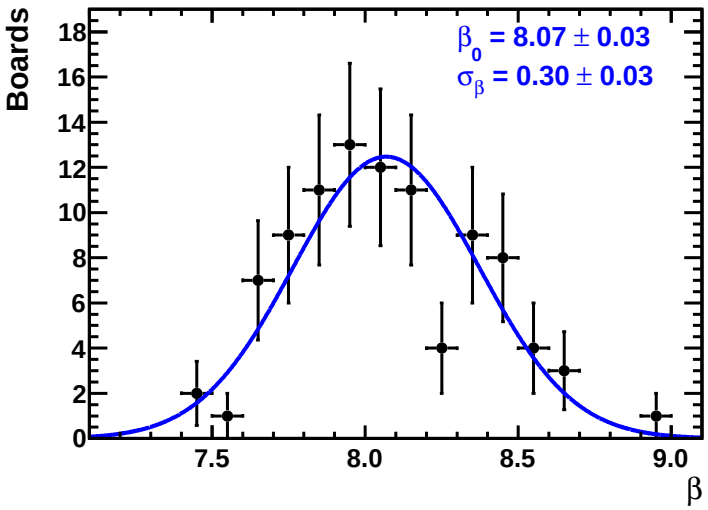

Figure A.5: *Distribution of the $\overline{\beta}$ parameter of the preshower boards. The fit is done assuming that the parameter is distributed according to the normal distribution.*

For the boards with LED power supply system shortcut an average $\beta = 8.07$ was used, calculated from all boards for which the calculation of it was possible. A

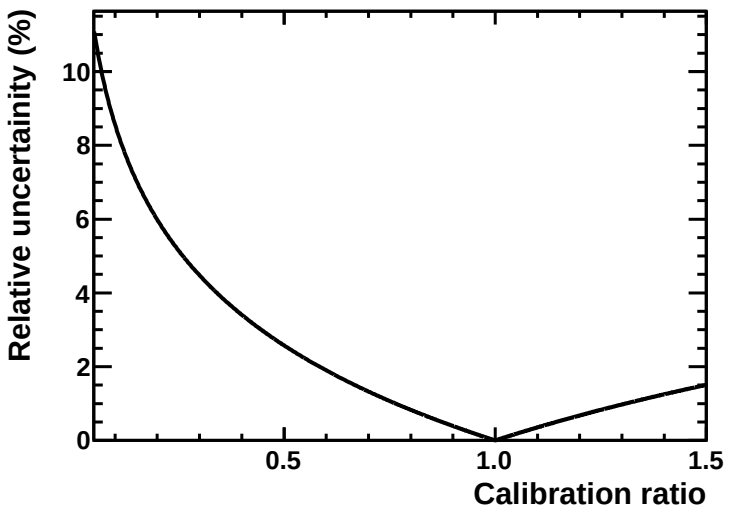

Figure A.6: *Relative uncertainty of the calibration with high voltage manipulation as a function of the requested calibration ratio for the boards with the shortcut in the LED power supply. If the MPV value of MIP from the fit for the board is μ_{fit} and a requested MPV after the high voltage change is μ_{req} then the calibration ratio is μ_{req}/μ_{fit}. The relative uncertainty is $\sigma_{\mu_{req}}/\mu_{req}$. Relative uncertainty equal to 0 for the calibration ratio equal to 1 is explained then as the result of no change to the high voltage settings and so it means no calibration. The relative uncertainty is calculated from the $\overline{\beta}$ distribution fit presented in the figure A.5.*

histogram with β values for all boards with working LED systems is presented in the figure A.5. Assuming that the β parameter is distributed accordingly to the normal distribution, a fit to the histogram was performed. The results are: $\beta_0 = 8.07 \pm 0.03$ with $\sigma_\beta = 0.30 \pm 0.03$. An estimation of the impact of the wrong assignment of beta values for the boards with shortcut in the LED system on the calibration was prepared. The results are shown in the figure A.6. As the plot in the figure is an universal one it can be used also for any further calibration with high voltage changes.

Appendix B

Track momentum maps

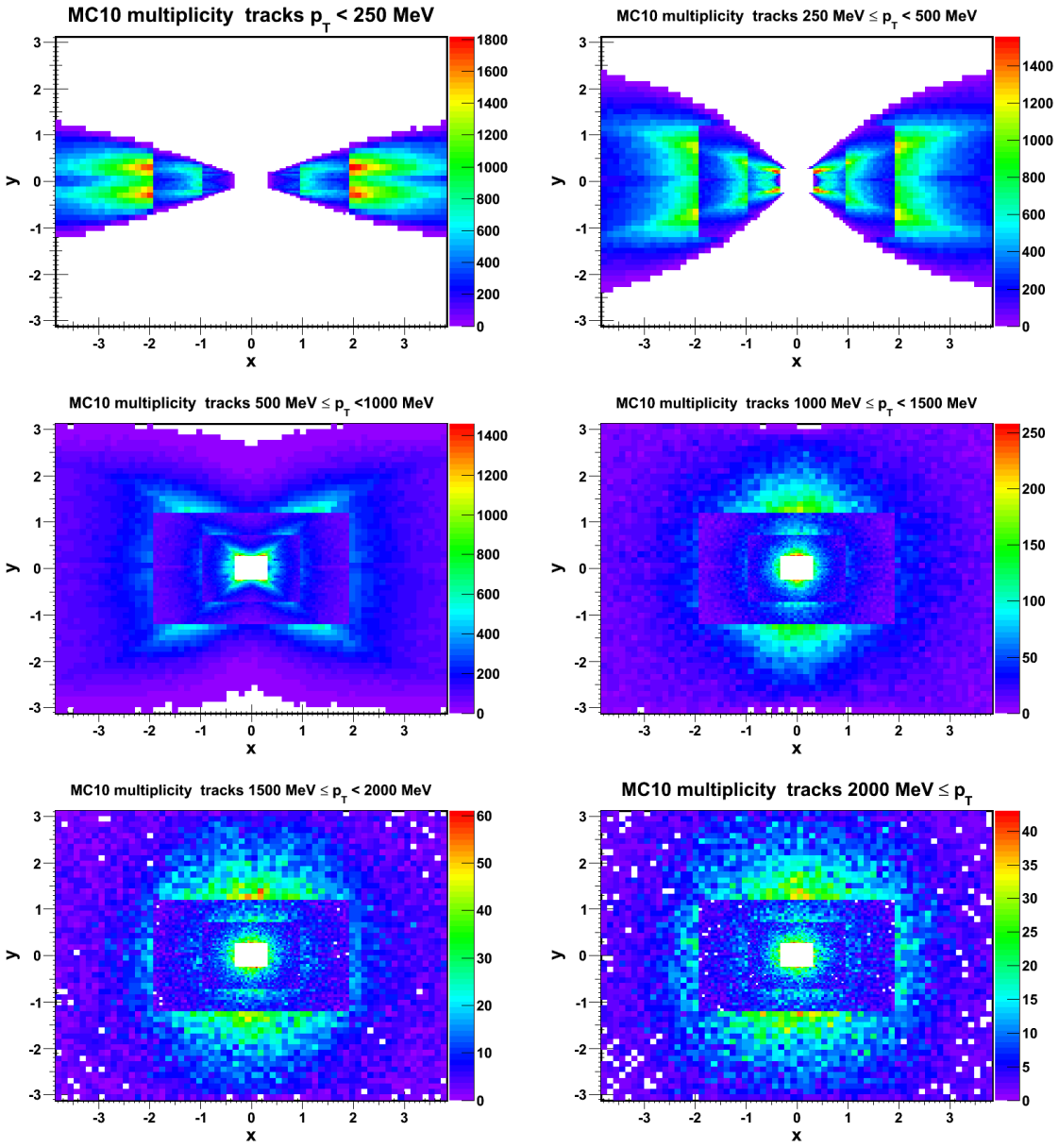

Figure B.1: *Track multiplicity map for different transverse momentum ranges with a MC10 minimum bias sample.*

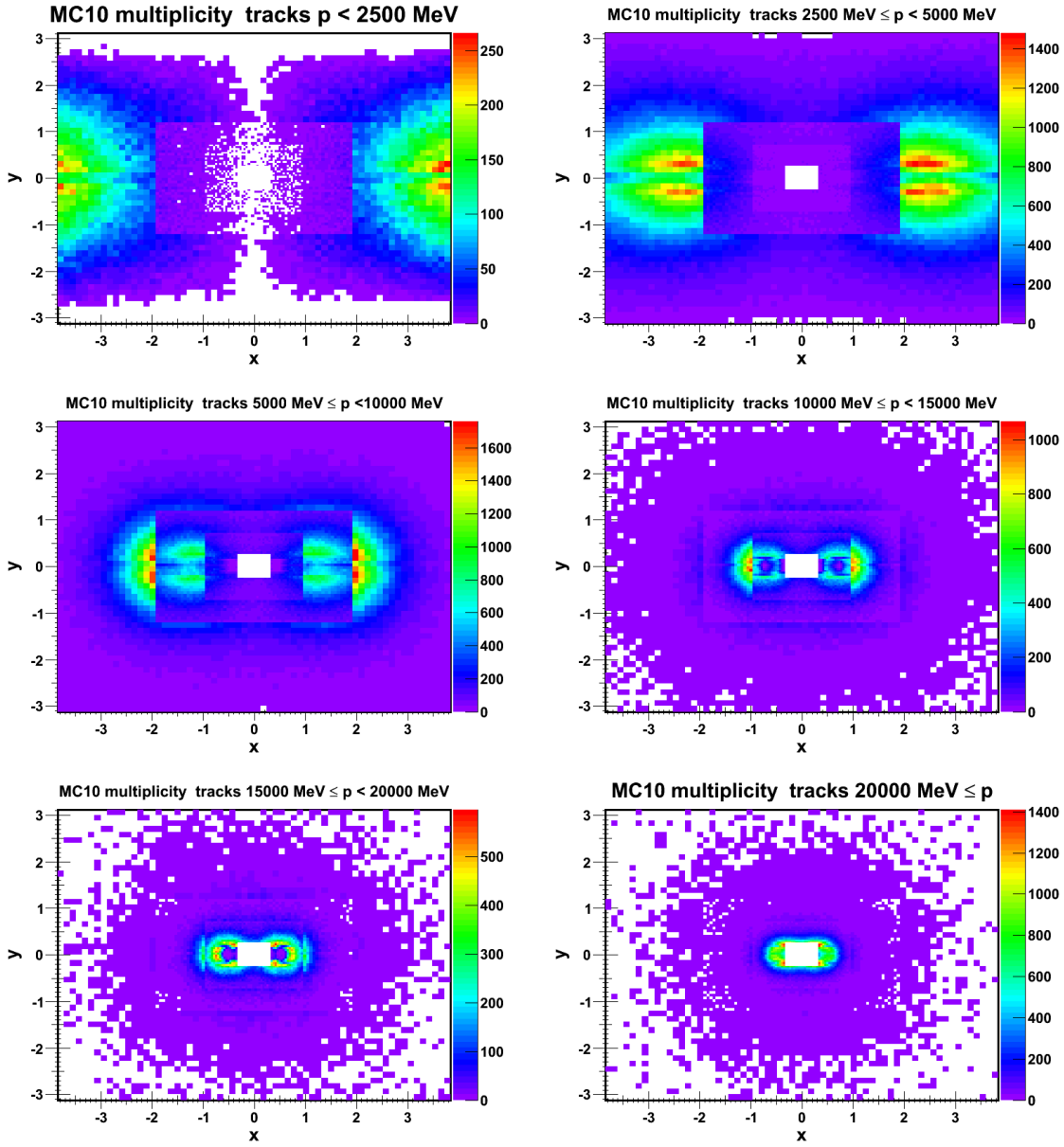

Figure B.2: *Track multiplicity map for different momentum ranges with a MC10 minimum bias sample.*

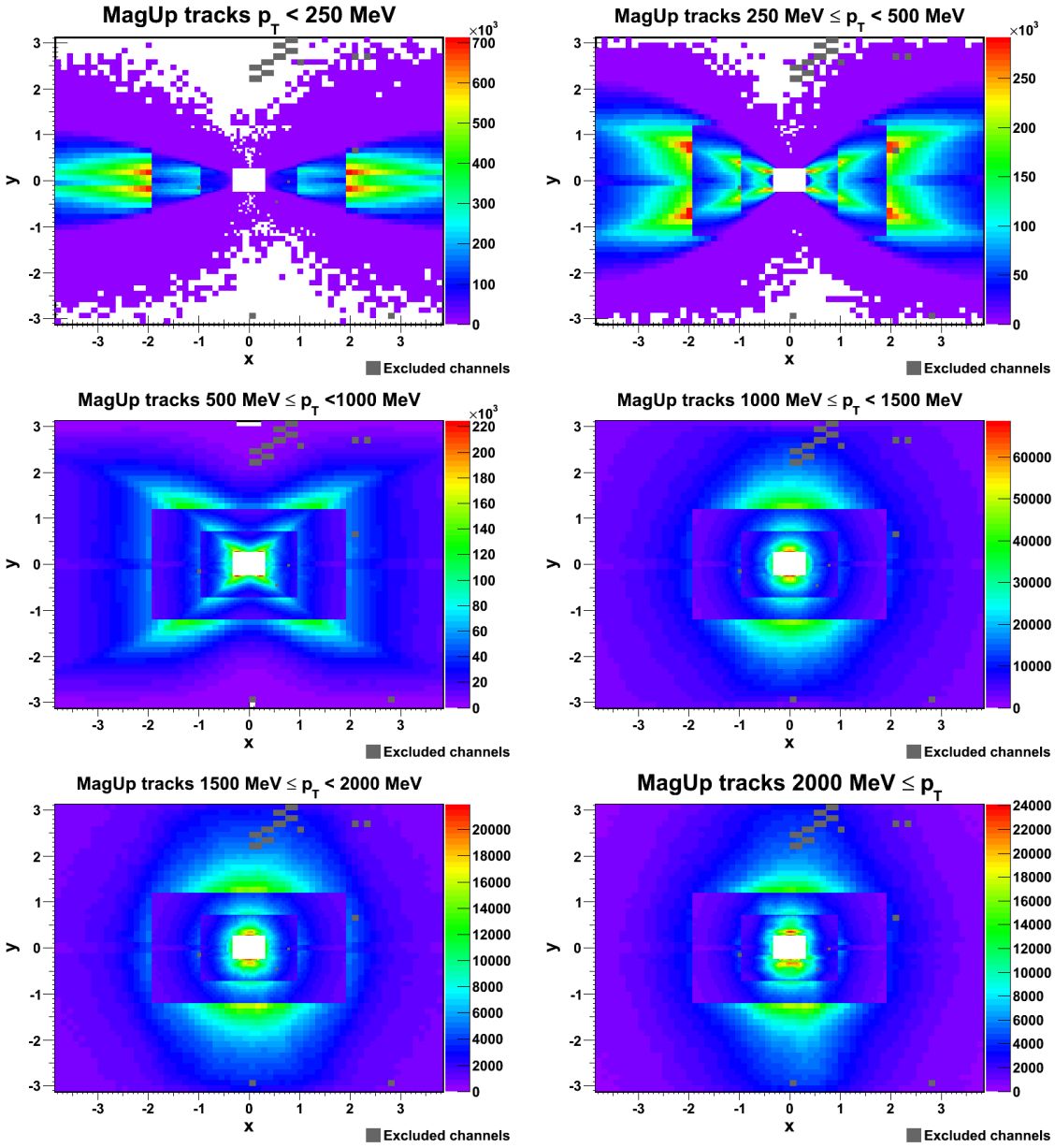

Figure B.3: *Track multiplicity map for different transverse momentum ranges with a sample of the real data minimum bias from 2011 at 7 TeV.*

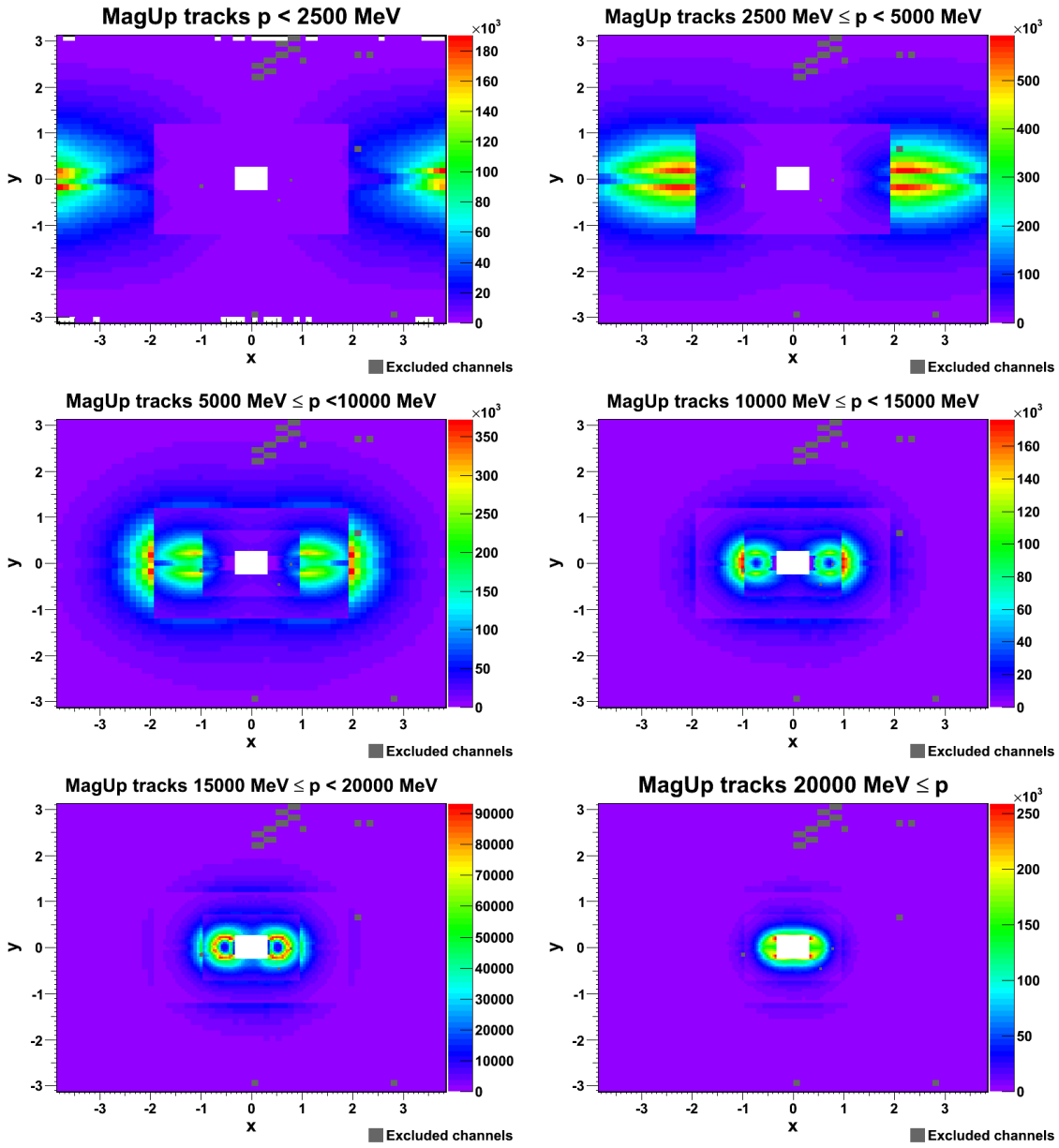

Figure B.4: *Track multiplicity map for different momentum ranges with a sample of the real data minimum bias from 2011 at 7 TeV.*

Appendix C

B2HHPi0 stripping control plots

C.1 Merged π^0

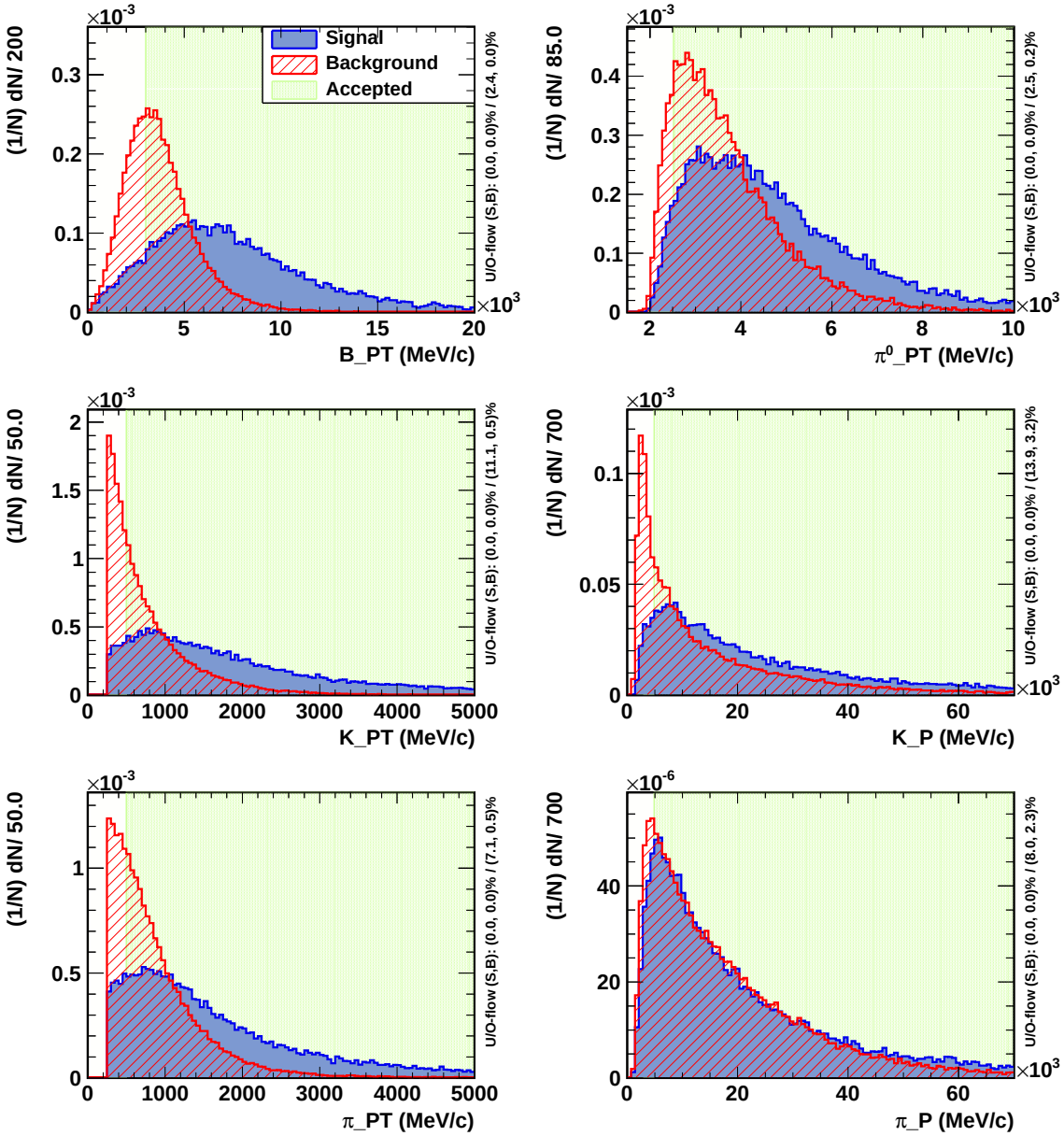

Figure C.1: *Kinematic properties of the* $\mathrm{K}\pi\pi^0$ *candidates made with merged* π^0*. Two MC10 samples are presented:* ${\mathrm{B_s}}^0 \to \mathrm{K}\pi\pi^0$ *(Signal) and* $b\bar{b}$ *inclusive (Background). The green ranges (Accepted) mark the stripping cuts.*

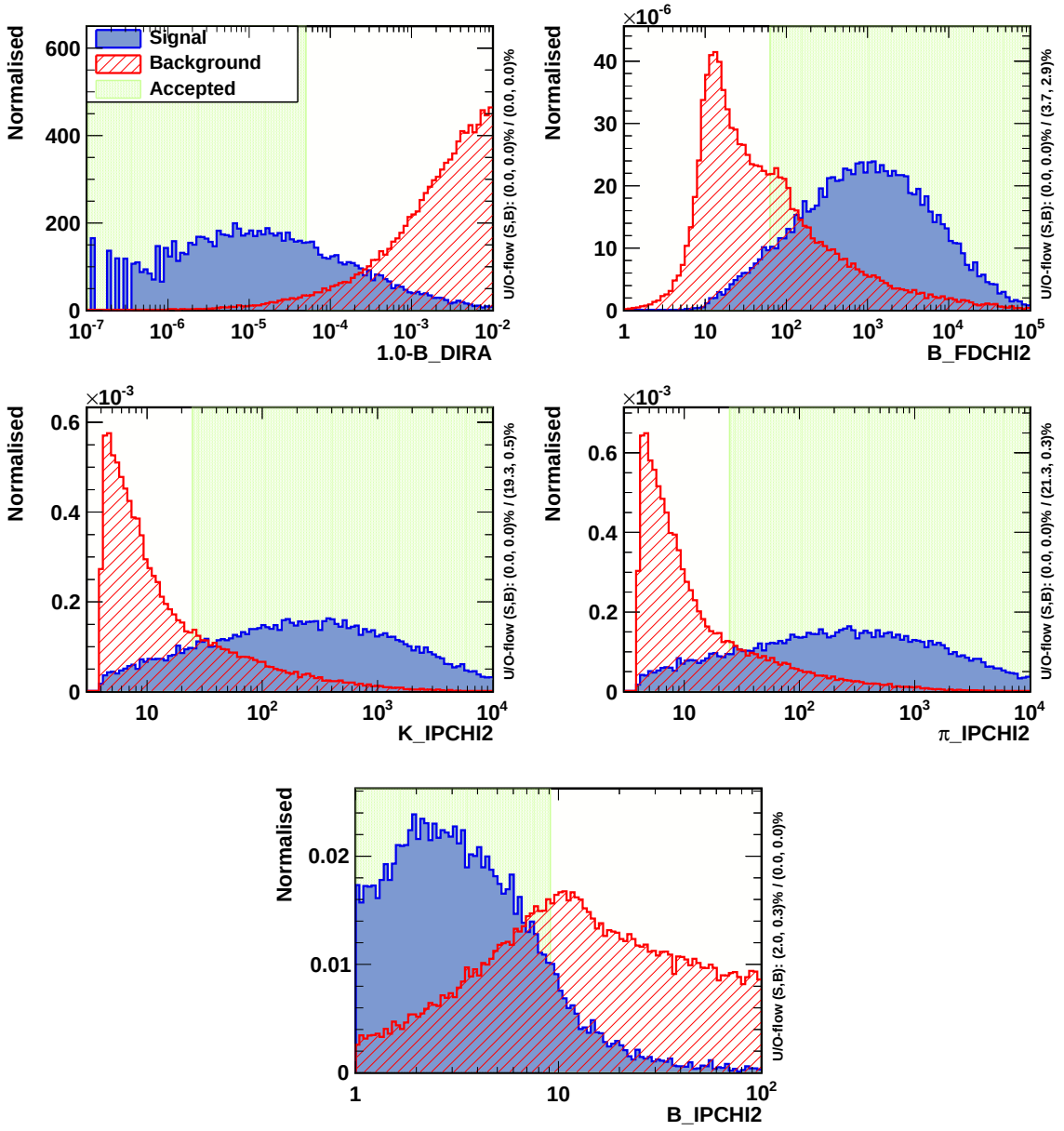

Figure C.2: *Topological properties of the* $\mathrm{K}\pi\pi^0$ *candidates made with merged* π^0*. Two MC10 samples are presented:* $\mathrm{B_s}^0 \to \mathrm{K}\pi\pi^0$ *(Signal) and* $b\bar{b}$ *inclusive (Background). The green ranges (Accepted) mark the stripping cuts.*

C.2 Resolved π^0

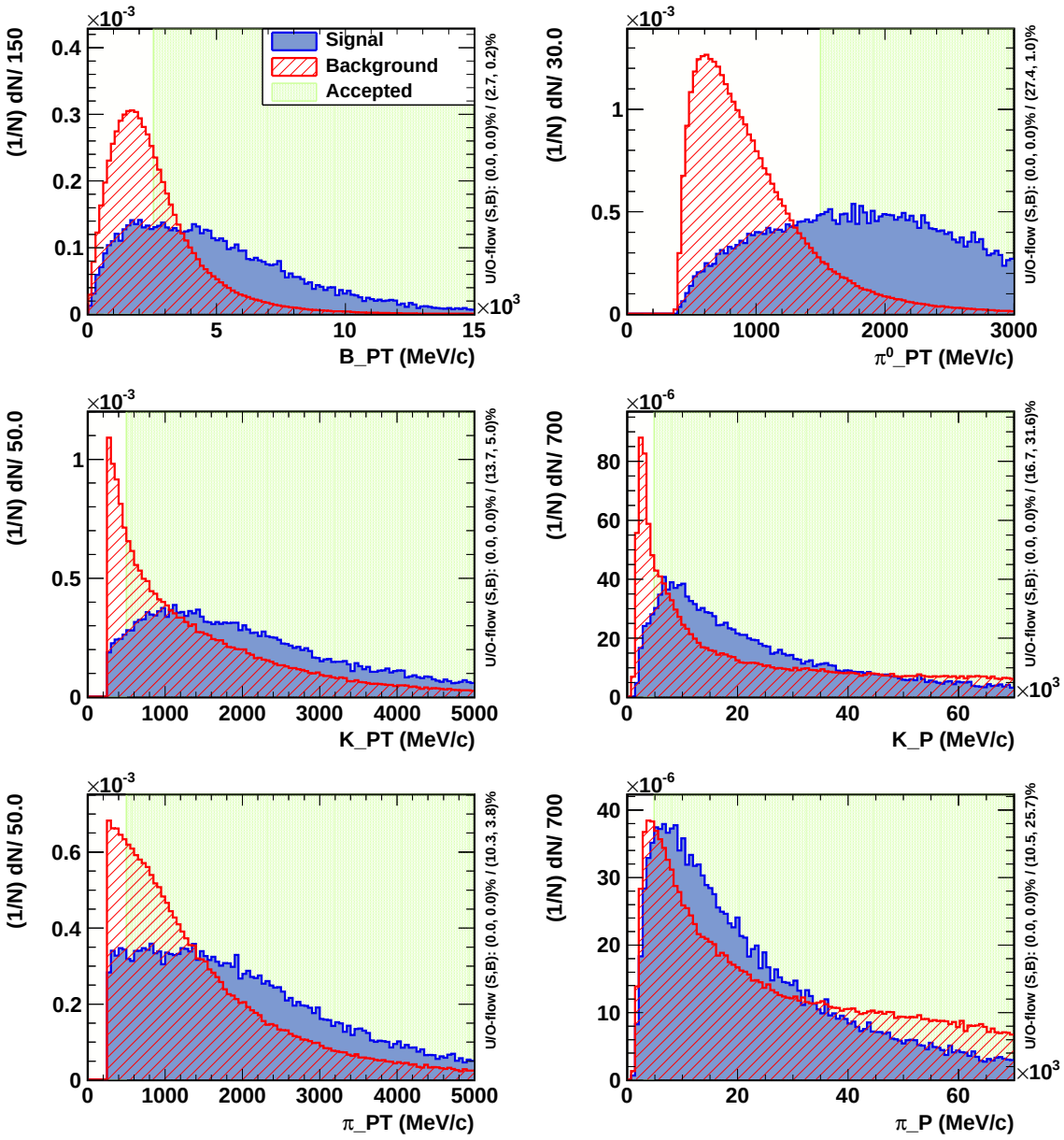

Figure C.3: *Kinematic properties of the* $K\pi\pi^0$ *candidates made with resolved* π^0*. Two MC10 samples are presented:* $B_s{}^0 \to K\pi\pi^0$ *(Signal) and* $b\bar{b}$ *inclusive (Background). The green ranges (Accepted) mark the stripping cuts.*

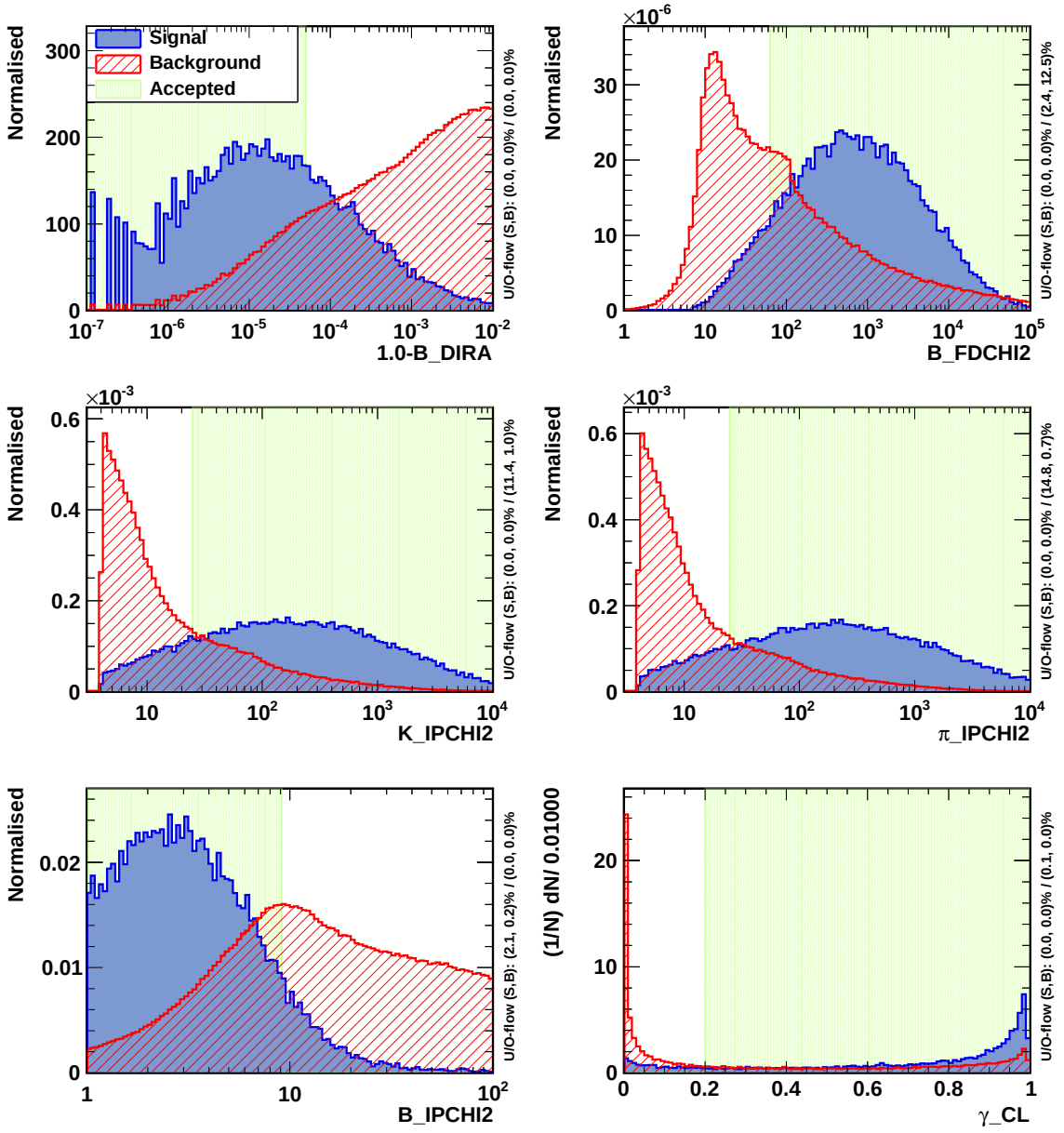

Figure C.4: *Topological properties of the* $\mathrm{K}\pi\pi^0$ *candidates made with resolved* π^0*. Two MC10 samples are presented:* $\mathrm{B_s}^0 \to \mathrm{K}\pi\pi^0$ *(Signal) and* $b\bar{b}$ *inclusive (Background). The green ranges (Accepted) mark the stripping cuts.*

C.3 Merged π^0, $\mu_1 = 0.6$, 10 TeV and $\mu_2 = 2.3$, 7 TeV comparison

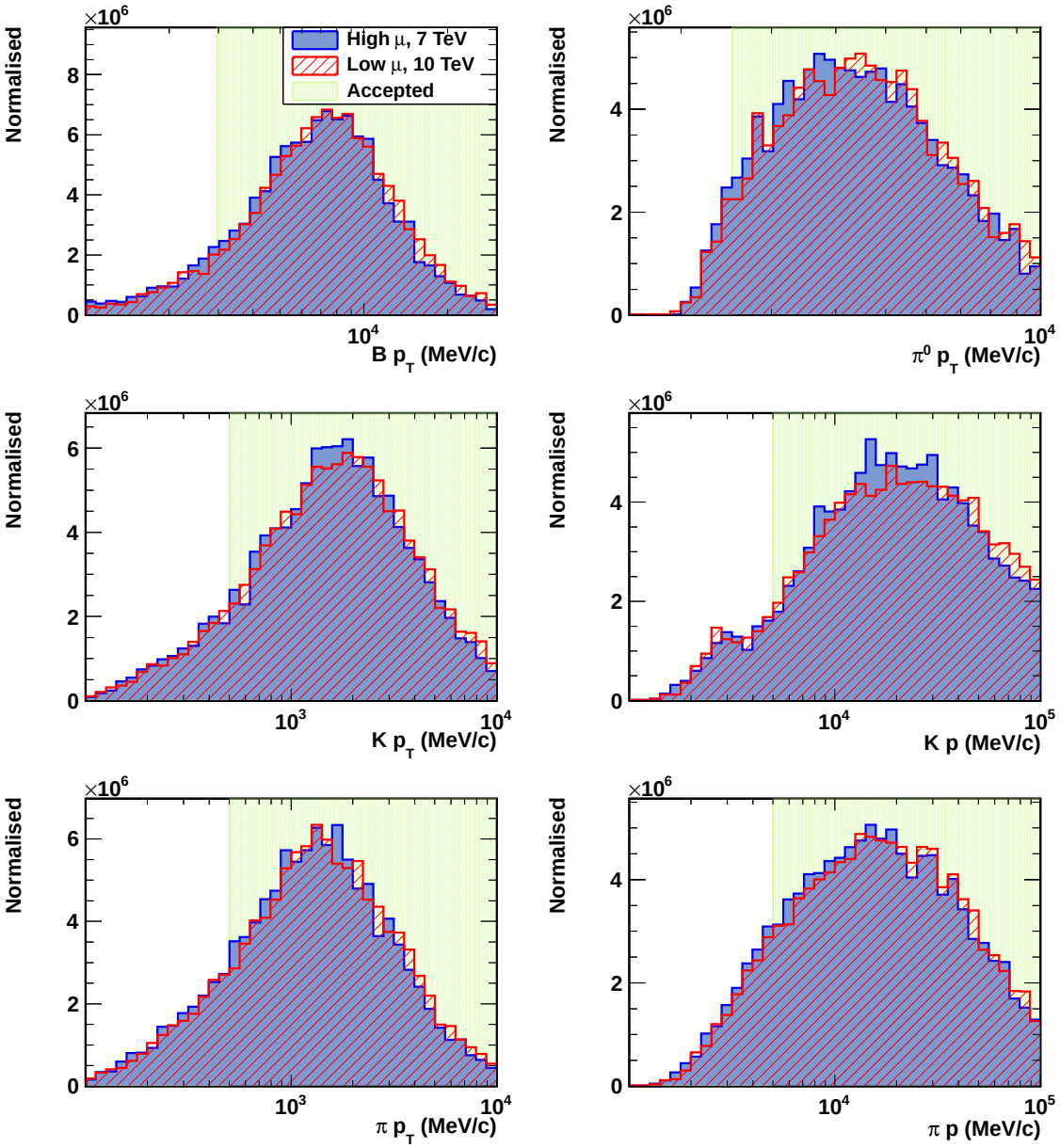

Figure C.5: *Comparison of kinematic distributions for merged π^0 for two MC09 samples: $\mu_1 = 0.6$, 10 TeV and $\mu_2 = 2.3$, 7 TeV. Stripping cuts (Accepted) are marked with green colour.*

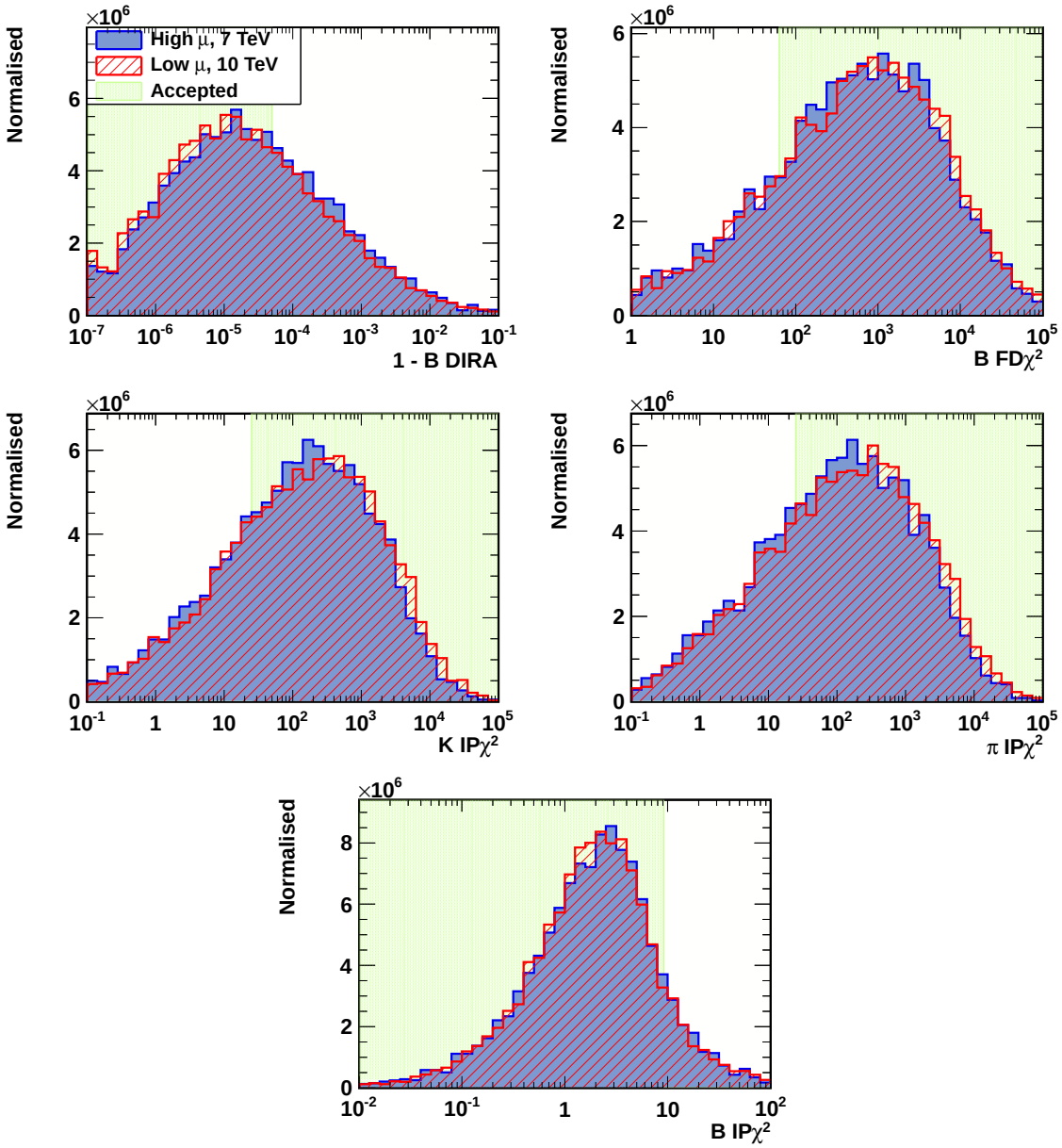

Figure C.6: *Comparison of topological distributions for merged π^0 for two MC09 samples: $\mu_1 = 0.6$, 10 TeV and $\mu_2 = 2.3$, 7 TeV. Stripping cuts (Accepted) are marked with green colour.*

C.4 Resolved π^0, $\mu_1 = 0.6$, 10 TeV and $\mu_2 = 2.3$, 7 TeV comparison

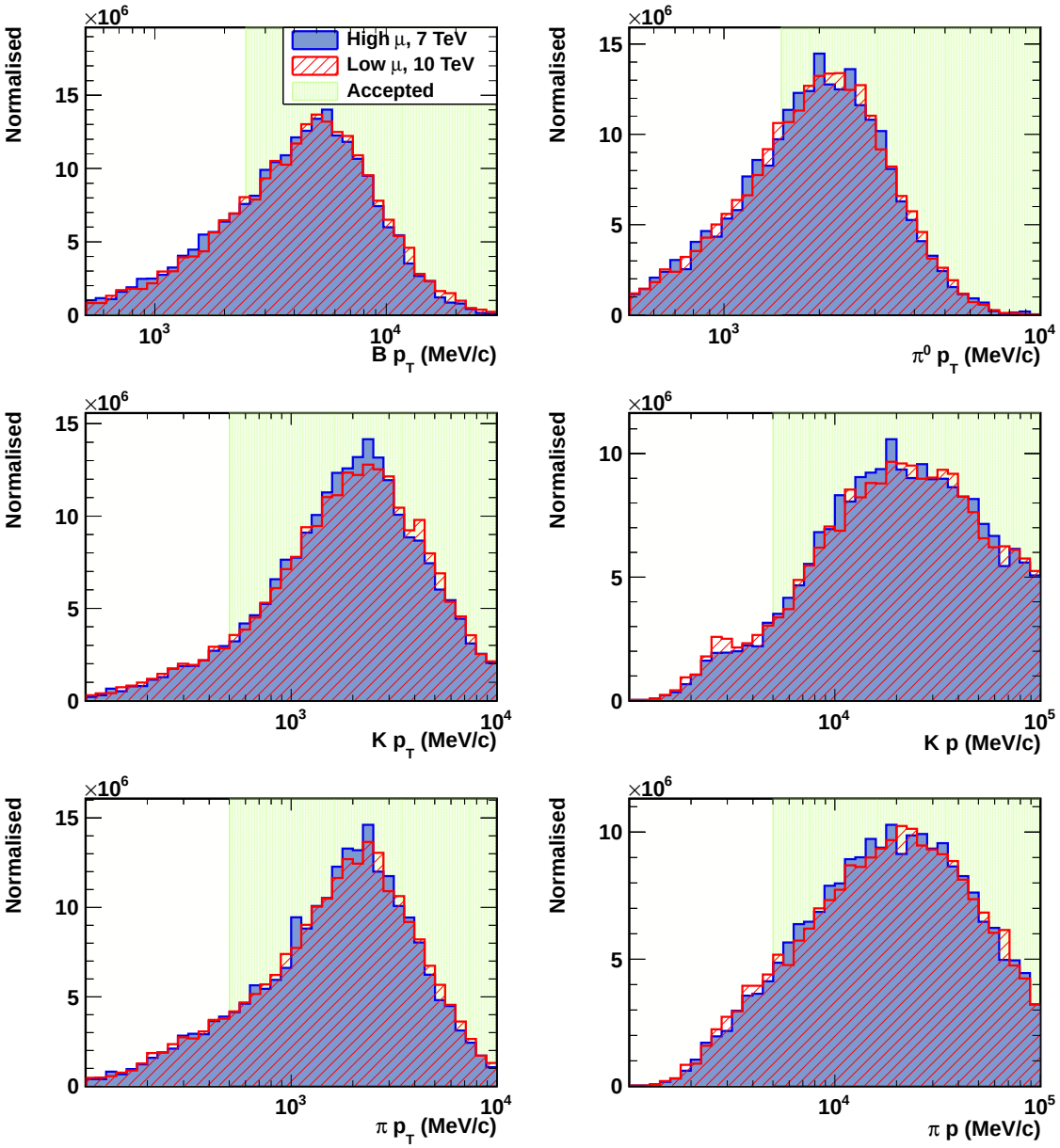

Figure C.7: *Comparison of kinematic distributions for resolved π^0 for two MC09 samples: $\mu_1 = 0.6$, 10 TeV and $\mu_2 = 2.3$, 7 TeV. Stripping cuts (Accepted) are marked with green colour.*

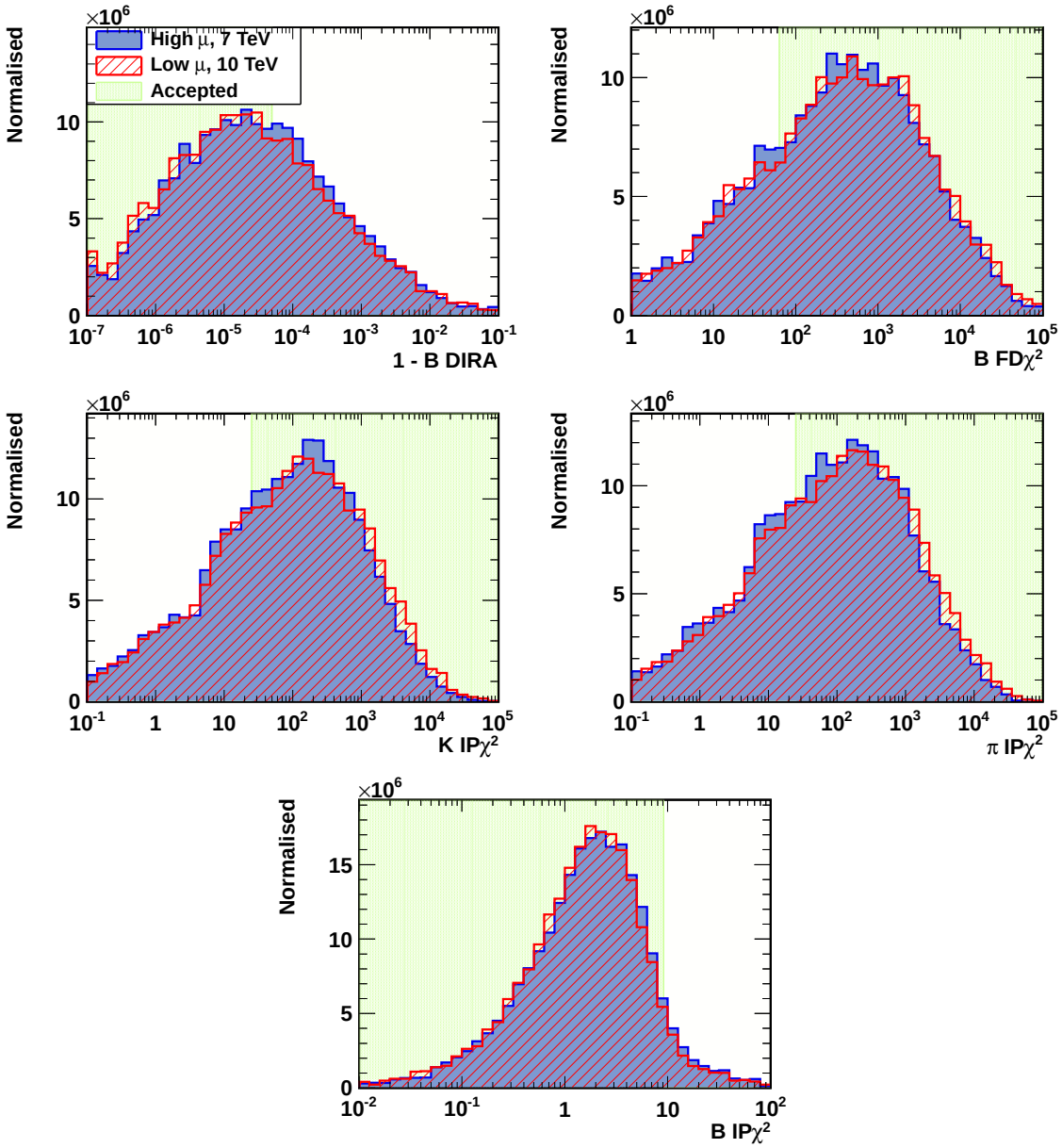

Figure C.8: *Comparison of topological distributions for resolved π^0 for two MC09 samples: $\mu_1 = 0.6$, 10 TeV and $\mu_2 = 2.3$, 7 TeV. Stripping cuts (Accepted) are marked with green colour.*

Appendix D

π^0/γ discriminant optimisation control plots

D.1 Inner distributions

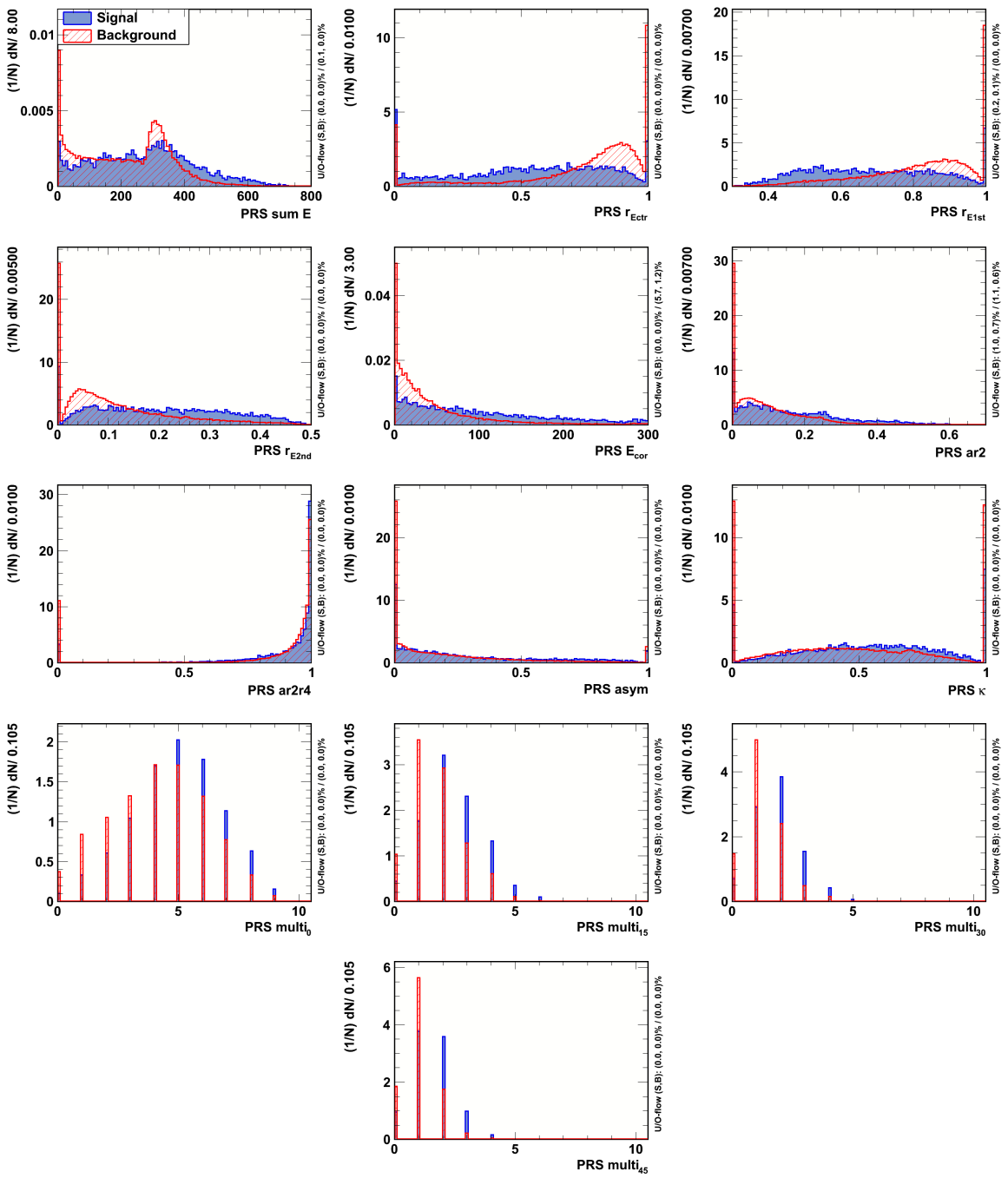

Figure D.1: *Inner cluster PRS variables for π^0 (signal) and γ (background).*

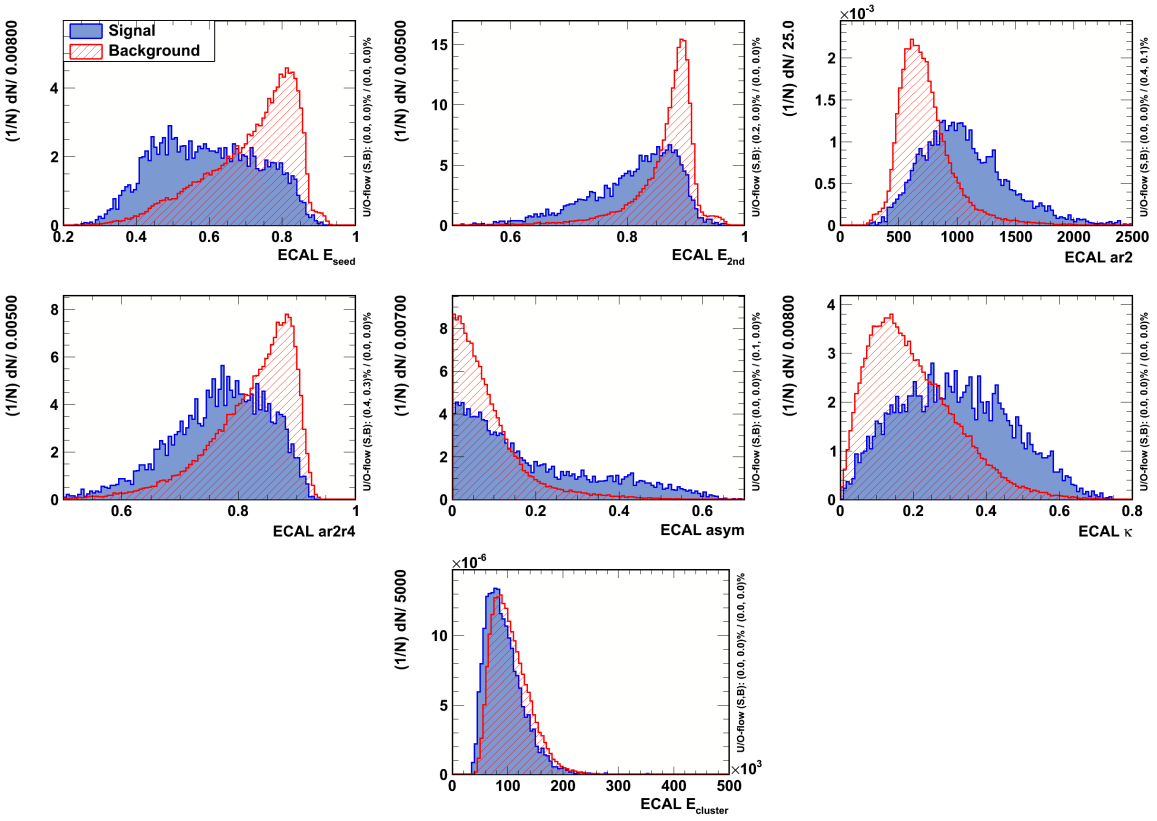

Figure D.2: *Inner cluster ECAL variables for π^0 (signal) and γ (background).*

D.2 Middle distributions

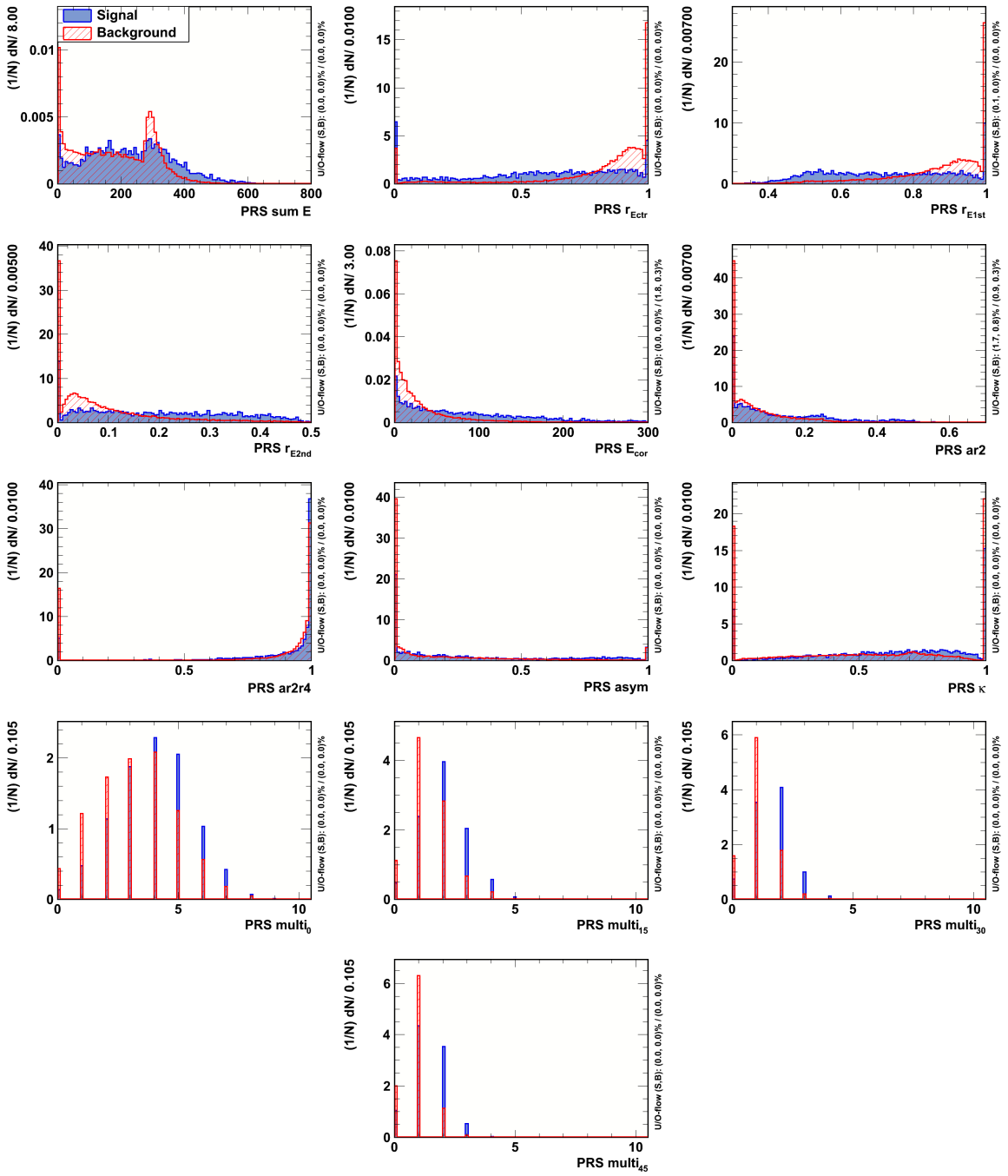

Figure D.3: *Middle cluster PRS variables for π^0 (signal) and γ (background).*

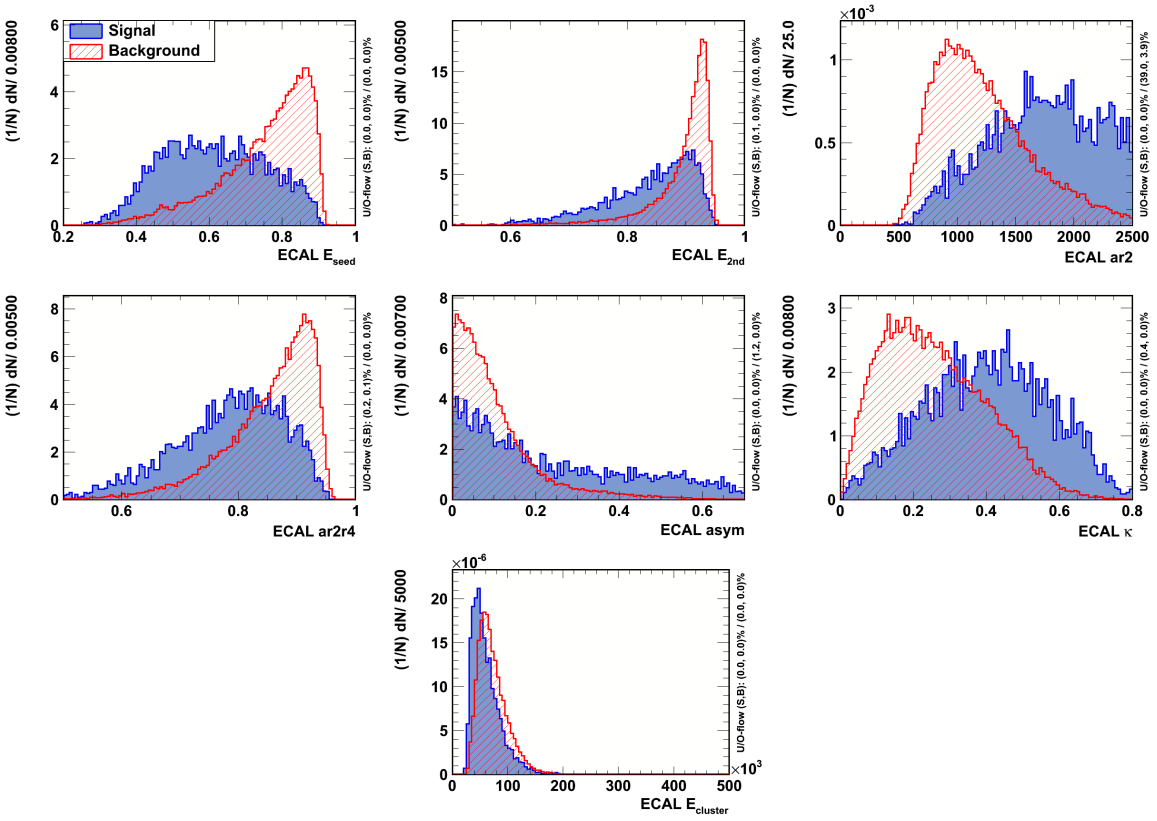

Figure D.4: *Middle cluster ECAL variables for π^0 (signal) and γ (background).*

D.3 Outer distributions

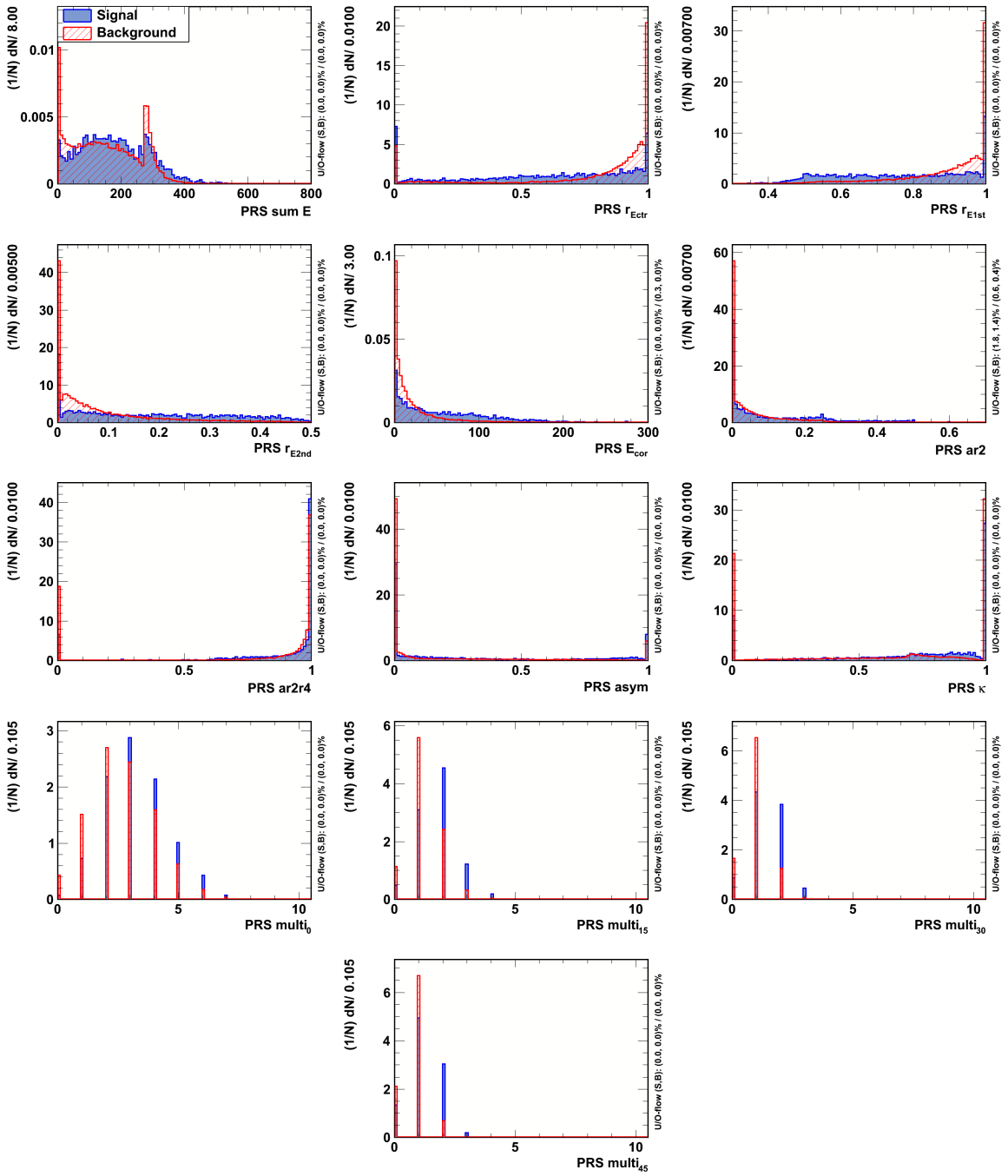

Figure D.5: *Outer cluster PRS variables for π^0 (signal) and γ (background).*

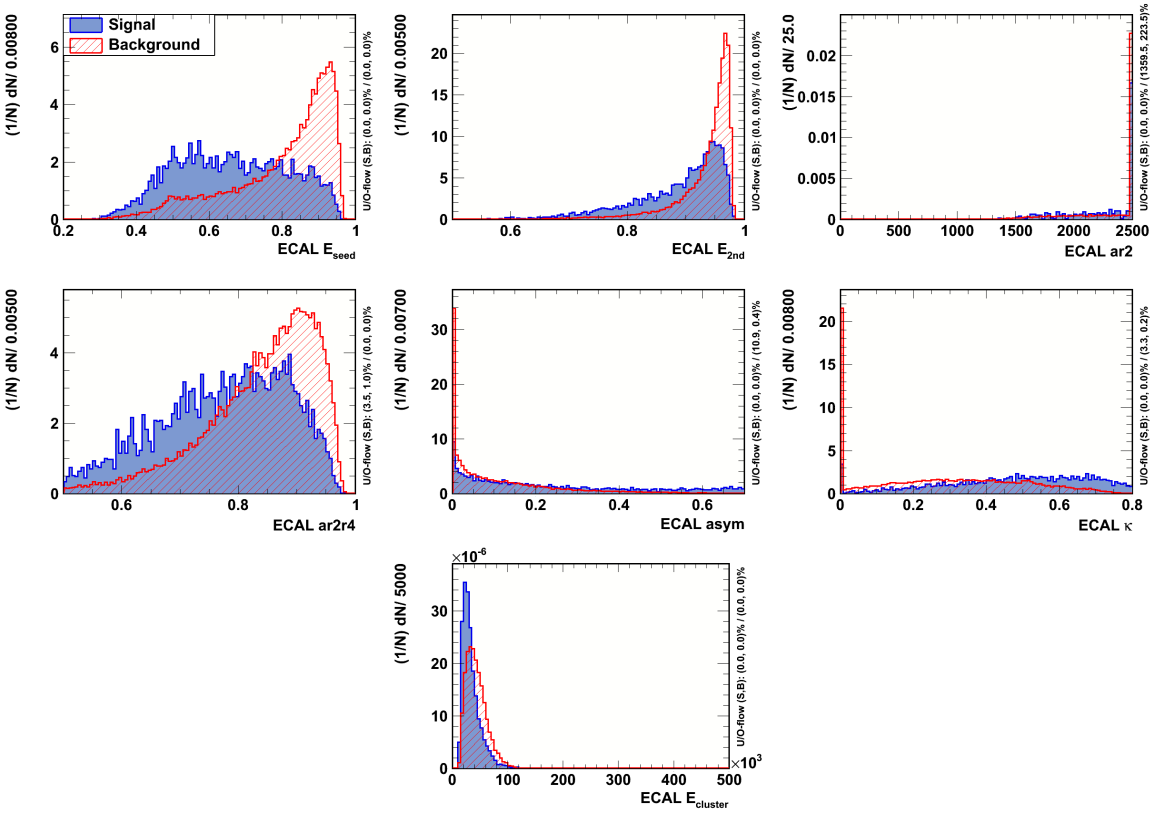

Figure D.6: *Outer cluster ECAL variables for π^0 (signal) and γ (background).*

D.4 ECAL optimisation

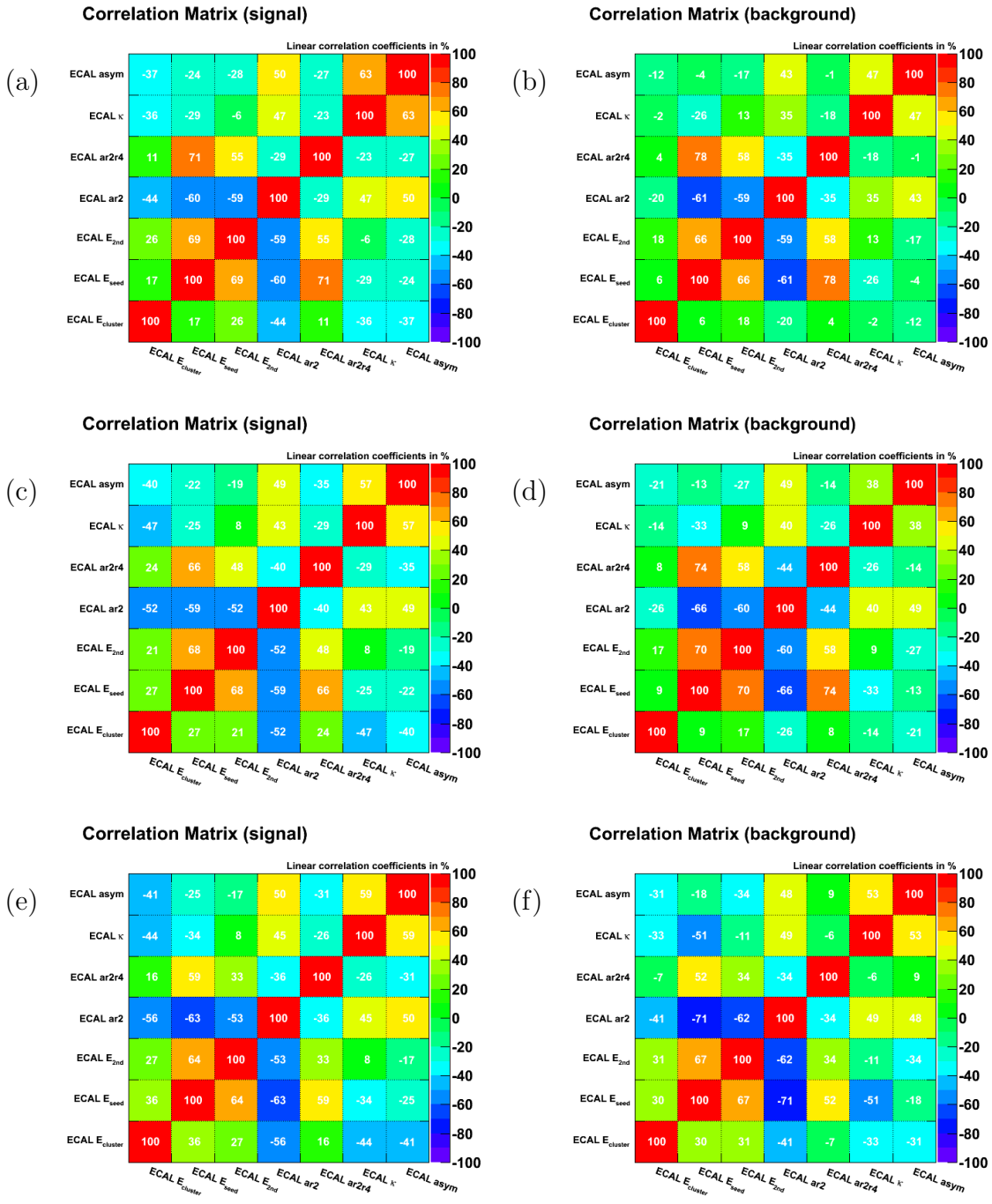

Figure D.7: *Correlations between ECAL variables for π^0 sample (signal) and γ sample (background).*

(a)

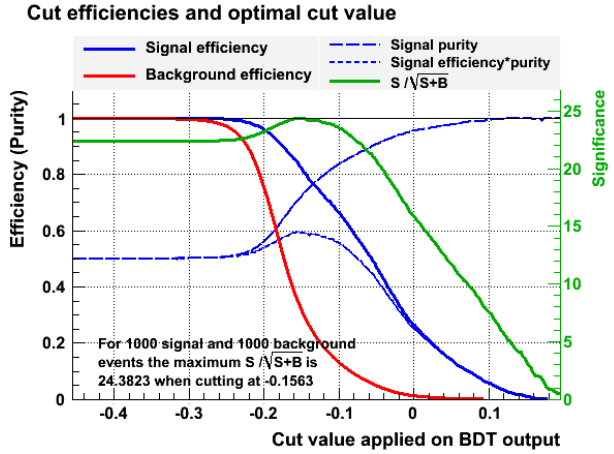

(b)

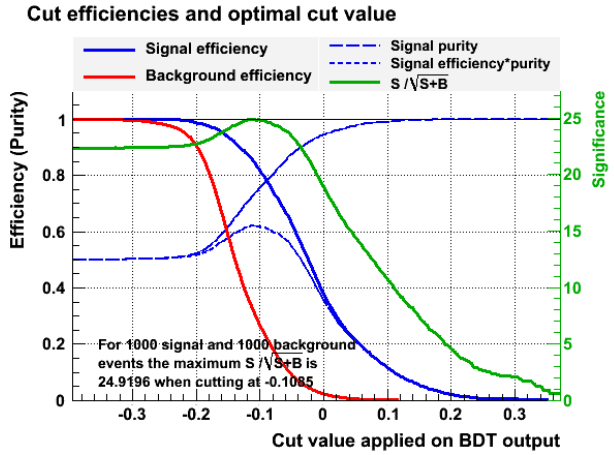

(c)

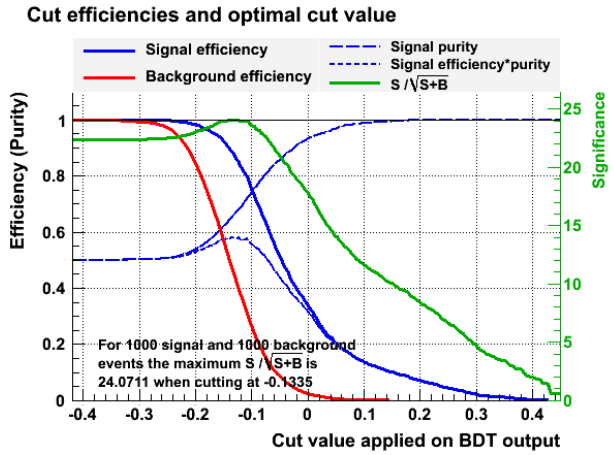

Figure D.8: *Efficiencies for optimisation based on the ECAL variables only for the inner (a), the middle (b), and the outer (c).*

D.5 PRS optimisation

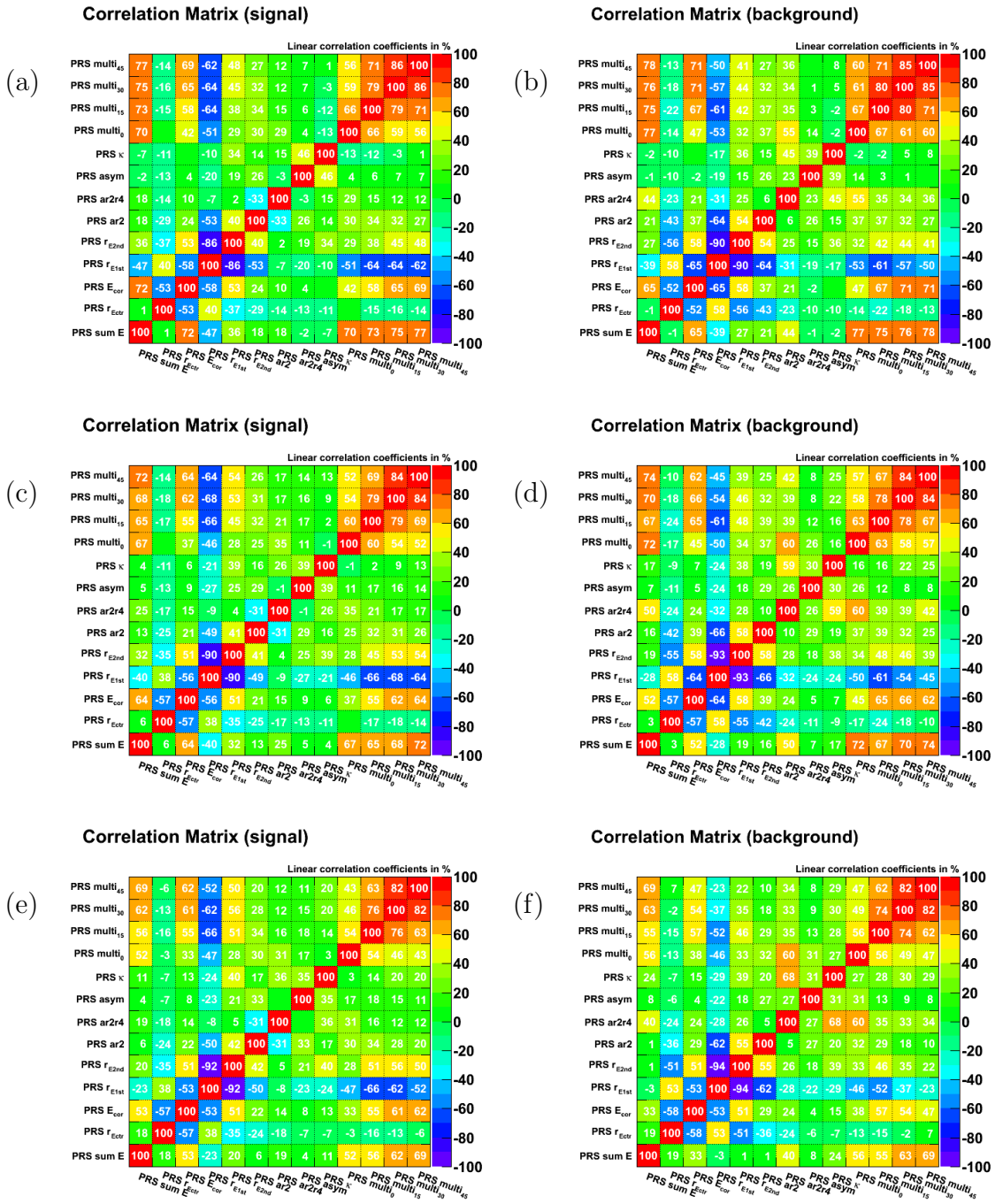

Figure D.9: *Correlations between PRS variables for π^0 sample (signal) and γ sample (background).*

(a)

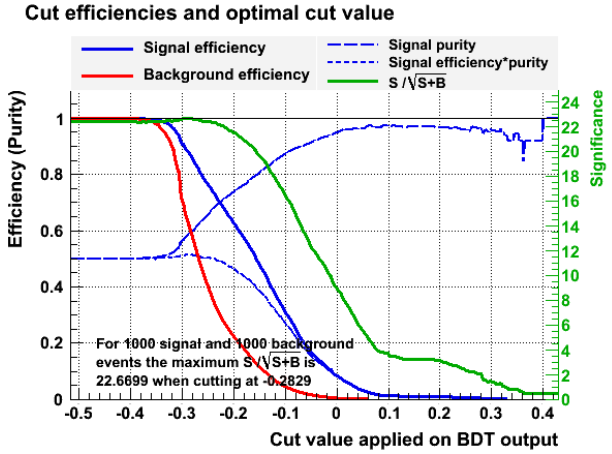

(b)

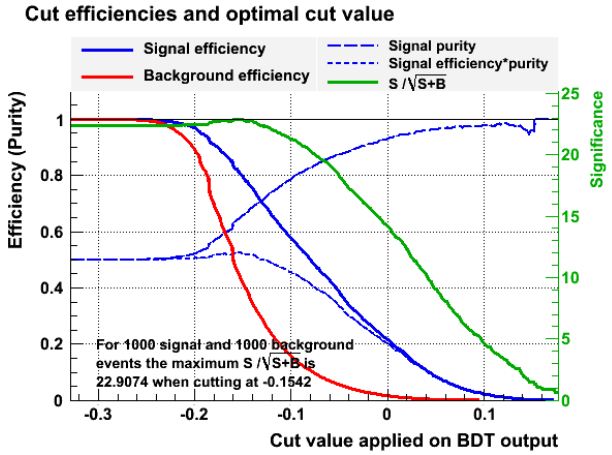

(c)

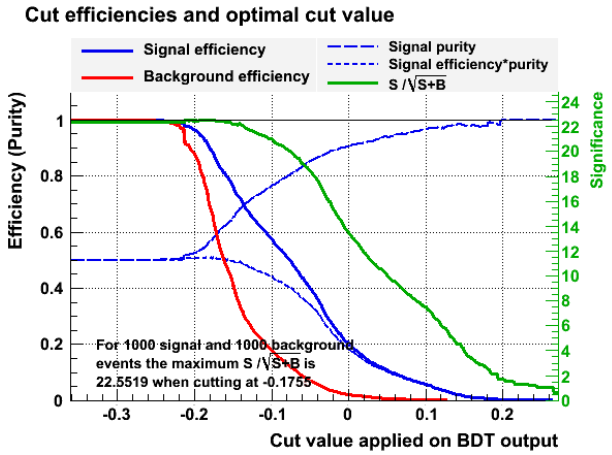

Figure D.10: *Efficiencies for optimisation based on the PRS variables only for the inner (a), the middle (b), and the outer (c).*

D.6 ECAL + PRS optimisation

(a)

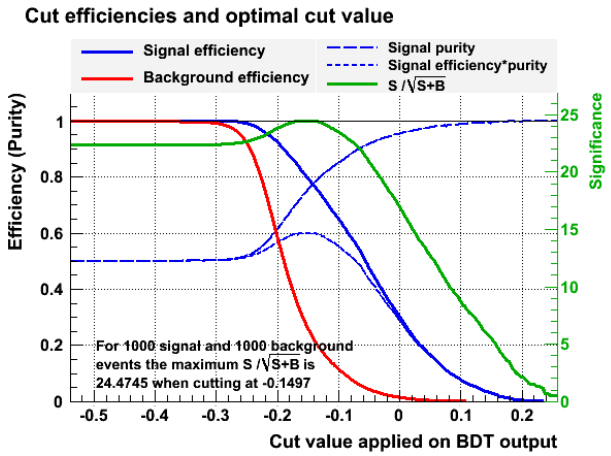

(b)

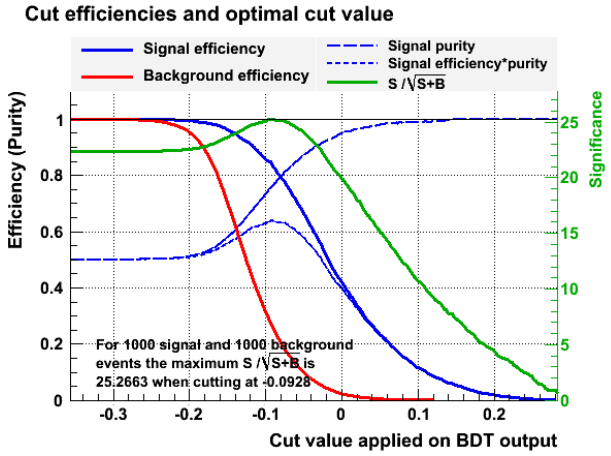

(c)

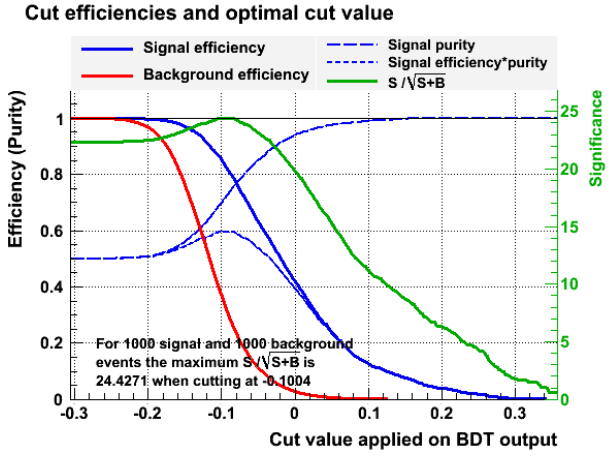

Figure D.11: *Efficiencies for optimisation based on the ECAL and PRS variables for the inner (a), the middle (b), and the outer (c).*

Appendix E

$K^0_S hh$ additional plots

E.1 K_S^0 DD

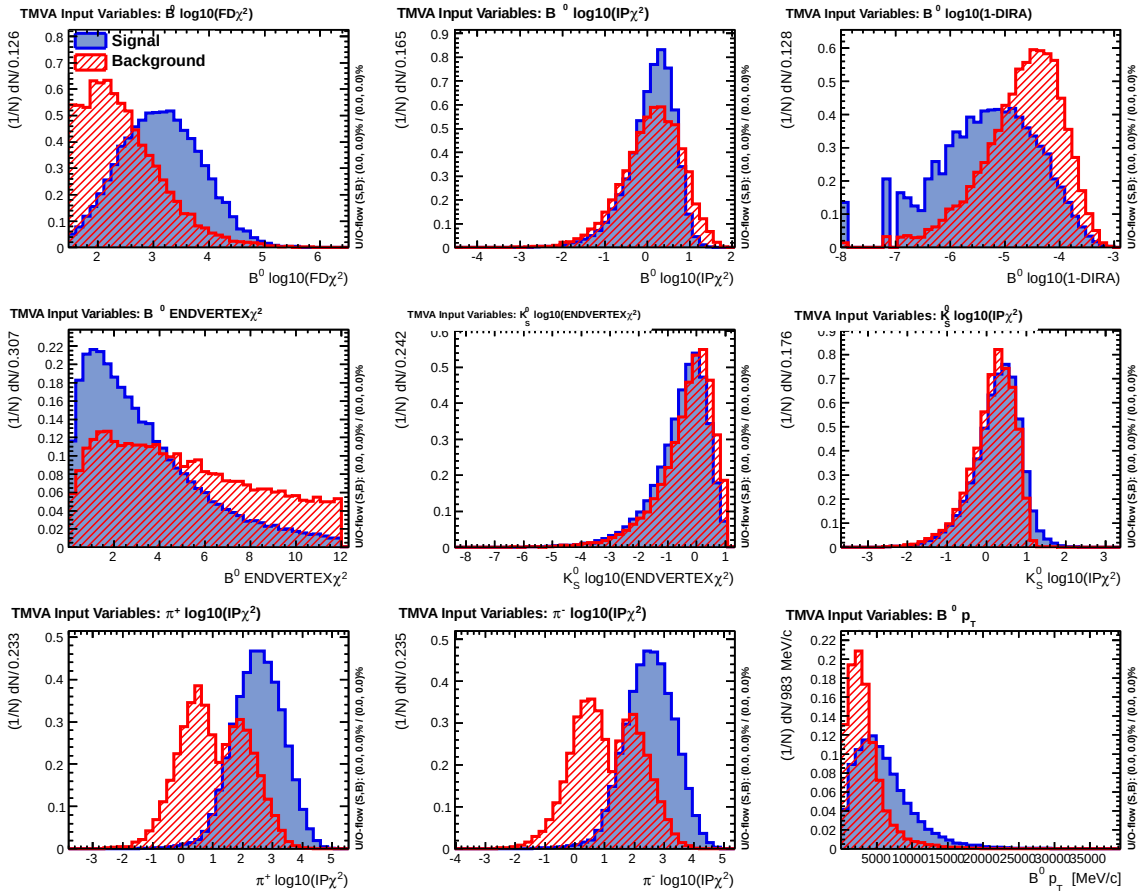

Figure E.1: *Variables used in the optimisation of the BDT discriminant. K_S^0 DD.*

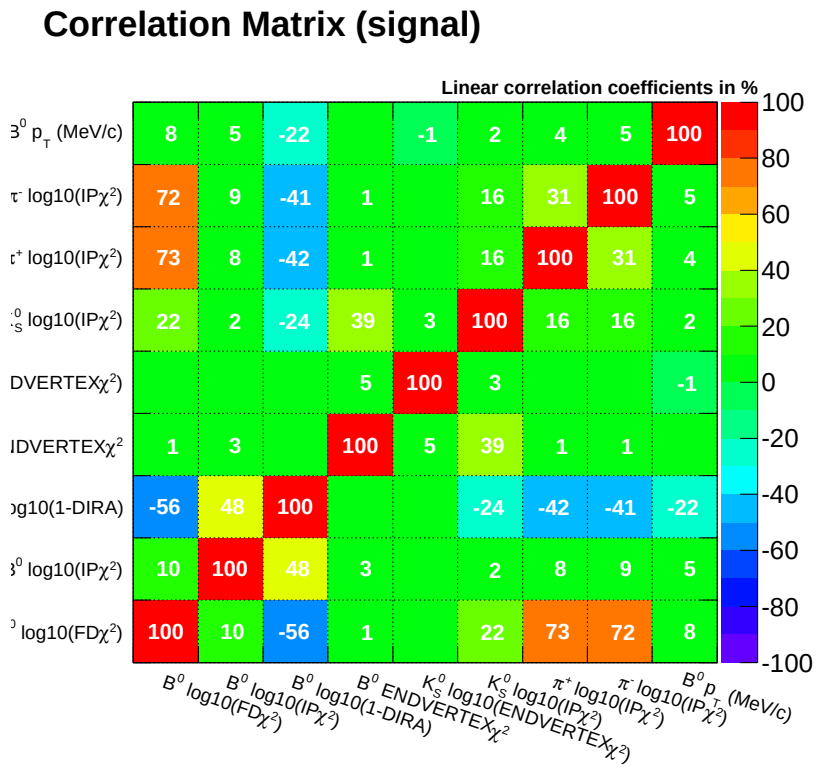

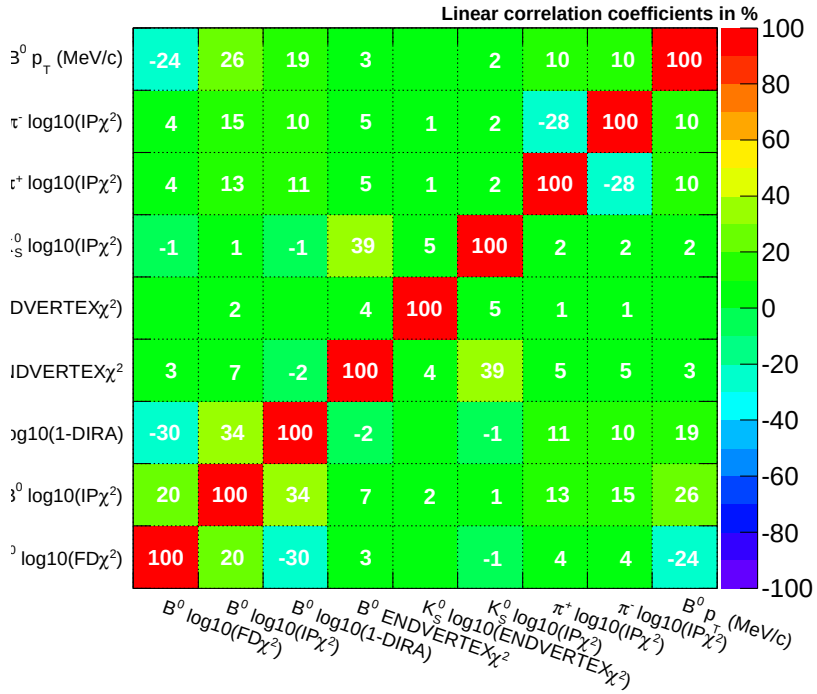

Figure E.2: *Linear correlations between the variables used in the optimisation of the BDT. K^0_S DD.*

E.2 K_S^0 LL

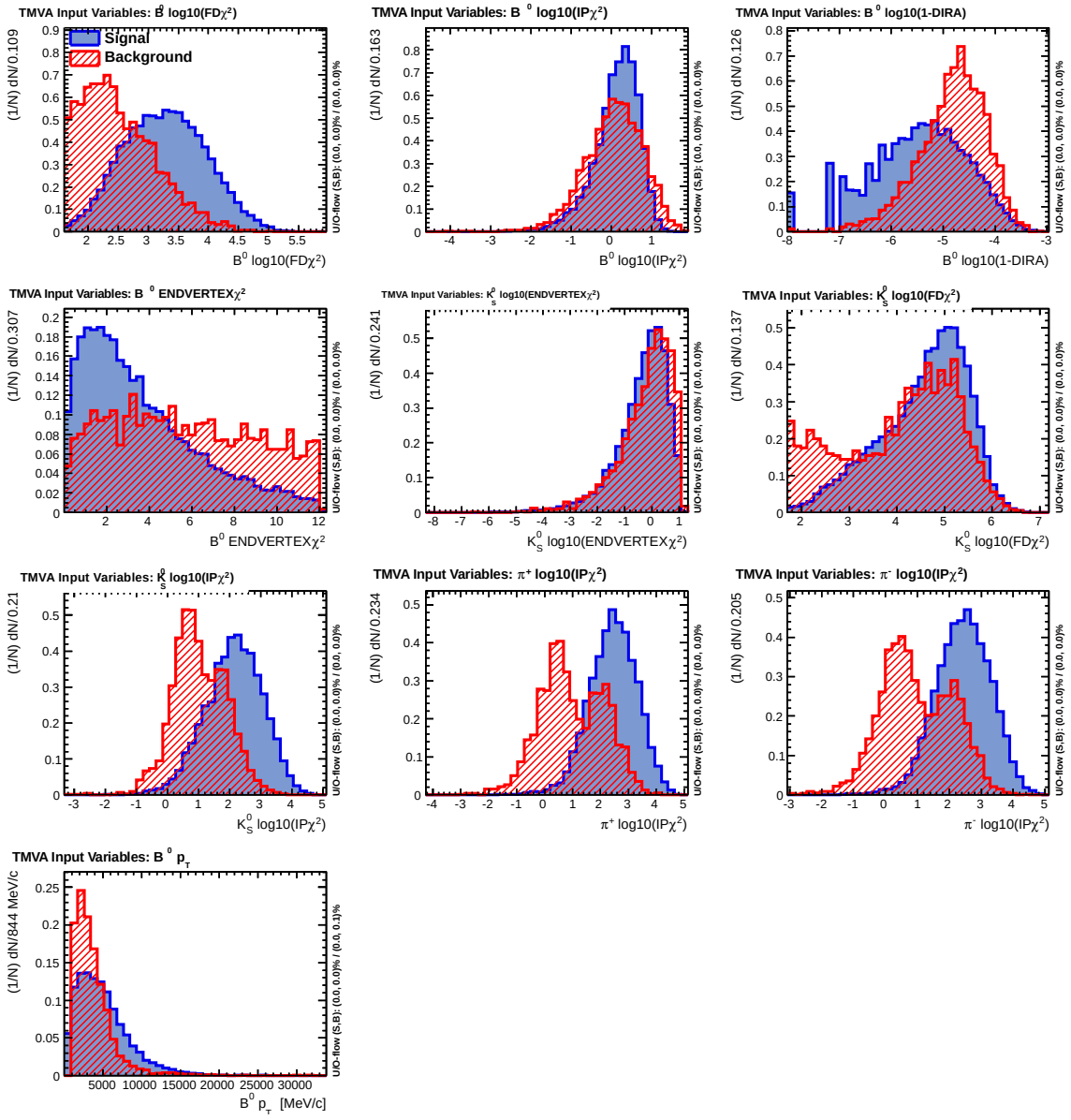

Figure E.3: *Variables used in the optimisation of the BDT discriminant.* K_S^0 *LL.*

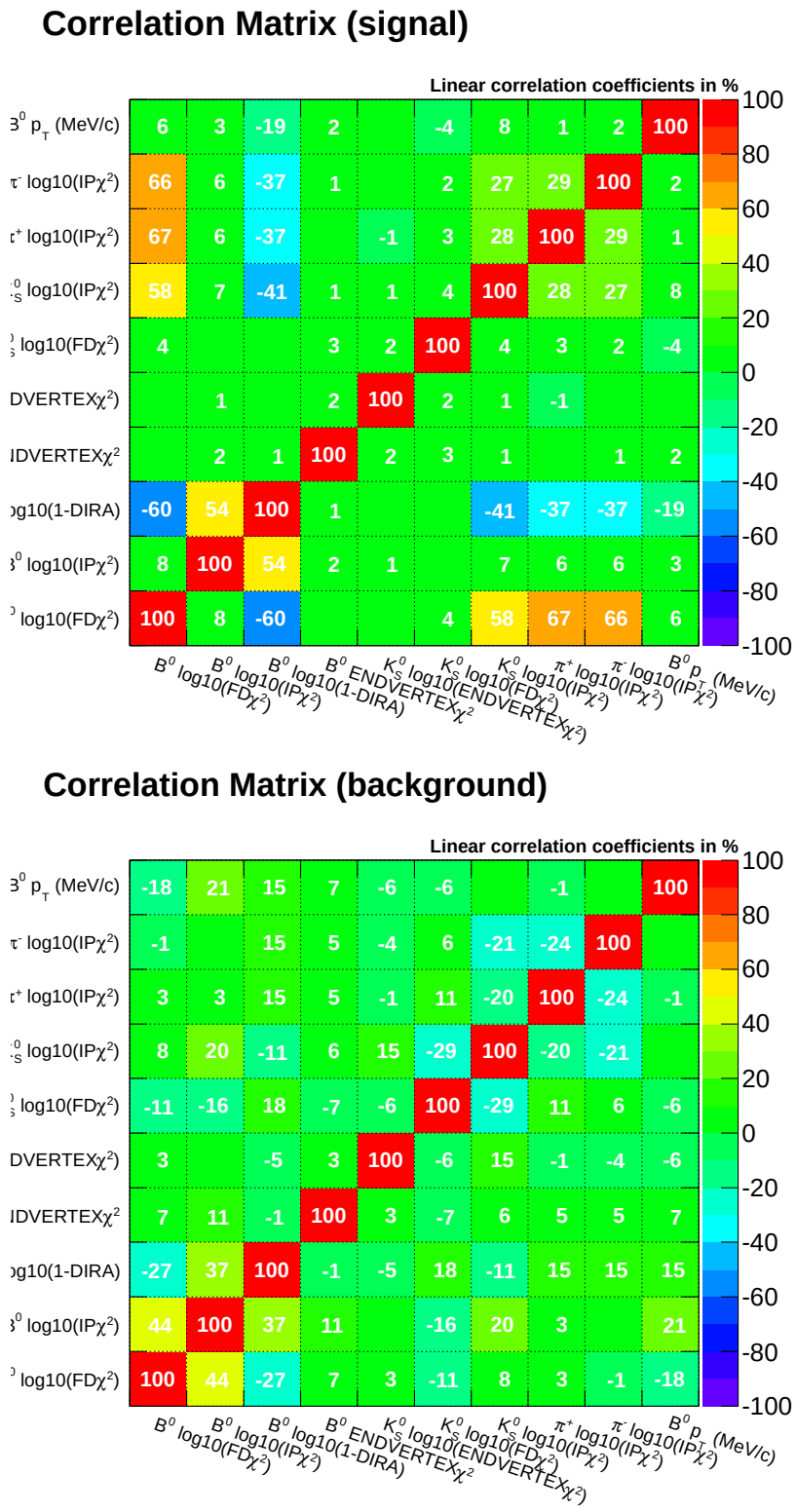

Figure E.4: *Linear correlations between the variables used in the optimisation of the BDT. K^0_S LL.*

Bibliography

[1] M. Kobayashi and T. Maskawa, Prog. Theor. Phys. **49** (1973) 652.

[2] K. Nakamura et al. (Particle Data Group), J. Phys. G 37, 075021 (2010).

[3] S. L. Glashow, Nucl. Phys. **22** (1961) 579;
A. Salam, Phys. Rev. **127** (1962) 331;
S. Weinberg, Phys. Rev. Lett. **19** (1967) 1264.

[4] G. 't Hooft and M.Veltman, Nucl. Phys. **B44**, (1972).

[5] F. Englert and R. Brout, Phys. Rev. Lett. 13 (1964) 321;
P. Higgs, Phys. Lett. **B12** (1964) 132;
P. Higgs, Phys. Rev. Lett. 13, (1964) 508.

[6] L. L. Chau and W. Y. Keung, Phys. Rev. Lett. **53** (1984) 1802.

[7] L. Wolfenstein, Phys. Rev. Lett. **51** (1983) 1945.

[8] J. Charles *et al.*, Phys. Rev. D **84** (2011) 033005 [arXiv:1106.4041 [hep-ph]].

[9] C. Jarlskog, in *CP Violation*, C. Jarlskog ed., World Scientific, Singapore (1988).

[10] J. C. Hardy and I. S. Towner, Phys. Rev. C **79** (2009) 055502 [arXiv:0812.1202 [nucl-ex]].

[11] M. Antonelli *et al.* [FlaviaNet Working Group on Kaon Decays], arXiv:0801.1817 [hep-ph].

[12] L. Widhalm *et al.* [Belle Collaboration], Phys. Rev. Lett. **97** (2006) 061804 [hep-ex/0604049].

[13] P. Vilain *et al.* [CHARM II Collaboration], Eur. Phys. J. C **11** (1999) 19.

[14] P. Abreu *et al.* [DELPHI Collaboration], Phys. Lett. B **439** (1998) 209.

[15] R. Kowalewski [BaBar Collaboration], PoSFPCP **2010** (2010) 028.

[16] *http://www.slac.stanford.edu/xorg/hfag/index.html*

D. Asner *et al.* [Heavy Flavor Averaging Group], arXiv:1010.1589 [hep-ex].

[17] T. E. W. Group [CDF and D0 Collaboration], arXiv:0908.2171 [hep-ex].

[18] A. Hocker, H. Lacker, S. Laplace and F. Le Diberder, Eur. Phys. J. C **21** (2001) 225 [hep-ph/0104062].

[19] Y. Li, "Prospects for gamma measurements at LHCb", arXiv:0905.4869v1 [hep-ex].

[20] The LHCb Collaboration, "Roadmap for selected key measurements of LHCb," arXiv:0912.4179.

[21] M. Antonelli *et al.*, Phys. Rept. **494** (2010) 197 [arXiv:0907.5386 [hep-ph]].

[22] M. Artuso, B. Meadows and A. A. Petrov, Ann. Rev. Nucl. Part. Sci. **58** (2008) 249 [arXiv:0802.2934 [hep-ph]].

[23] M. Gronau and D. London, Phys. Lett. B **253** (1991) 483.

[24] D. Atwood, I. Dunietz and A. Soni, Phys. Rev. Lett. **78** (1997) 3257 [arXiv:hep-ph/9612433];
D. Atwood, I. Dunietz and A. Soni, Phys. Rev. D **63** (2001) 036005 [arXiv:hep-ph/0008090].

[25] A. Giri, Y. Grossman, A. Soffer and J. Zupan, Phys. Rev. D **68** (2003) 054018 [arXiv:hep-ph/0303187].

[26] A. Bondar, Proceedings of BINP Special Analysis Meeting on Dalitz Analysis, 24-26 Sep. 2002, unpublished.

[27] R. Aleksan, I. Dunietz and B. Kayser, Z. Phys. C **54** (1992) 653.

[28] I. Dunietz and R. G. Sachs, Phys. Rev. D **37** (1988) 3186 [Erratum-ibid. D **39** (1989) 3515] [Phys. Rev. D **39** (1989) 3515].

[29] R. Fleischer, Phys. Lett. B **459** (1999) 306 [arXiv:hep-ph/9903456].

[30] R. Fleischer, Eur. Phys. J. C **52** (2007) 267 [arXiv:0705.1121 [hep-ph]].

[31] A. Soni and D. A. Suprun, Phys. Rev. D **75** (2007) 054006 [arXiv:hep-ph/0609089].

[32] H. J. Lipkin, Y. Nir, H. R. Quinn and A. Snyder, Phys. Rev. D **44** (1991) 1454.

[33] N. G. Deshpande, N. Sinha, R. Sinha, Phys. Rev. Lett. **90** (2003) 061802. [hep-ph/0207257].

[34] M. Neubert and J. L. Rosner, Phys. Lett. B **441** (1998) 403 [arXiv:hep-ph/9808493].

[35] M. Gronau, D. Pirjol and T. M. Yan, Phys. Rev. D **60** (1999) 034021 [Erratum-ibid. D **69** (2004) 119901] [arXiv:hep-ph/9810482].

[36] M. Gronau, Phys. Rev. Lett. **91** (2003) 139101. [hep-ph/0305144].

[37] M. Imbeault, N. L. Lorier and D. London, arXiv:1011.4973 [hep-ph].

[38] I. Bediaga, G. Guerrer and J. M. de Miranda, arXiv:hep-ph/0608268.

[39] M. Ciuchini, M. Pierini, L. Silvestrini, Phys. Rev. **D74** (2006) 051301. [hep-ph/0601233].

[40] M. Gronau, D. Pirjol, A. Soni and J. Zupan, Phys. Rev. D **75** (2007) 014002 [arXiv:hep-ph/0608243].

[41] D. -s. Du, H. -j. Gong, J. -f. Sun, D. -s. Yang, G. -h. Zhu, Phys. Rev. **D65** (2002) 094025. [hep-ph/0201253].

[42] J. M. Blatt and V. F. Weisskopf, "Theoretical Nuclear Physics", Wiley, New York, p. 361 (1952).

[43] G. Buchalla, A. J. Buras and M. E. Lautenbacher, Rev. Mod. Phys. **68** (1996) 1125 [arXiv:hep-ph/9512380].

[44] M. Ciuchini, M. Pierini, L. Silvestrini, Phys. Lett. **B645** (2007) 201-203. [hep-ph/0602207].

[45] *http://lhc-machine-outreach.web.cern.ch/lhc-machine-outreach/*

[46] Collaboration ATLAS, *Technical Proposal,* CERN-LHCC/94-43.

[47] Collaboration CMS, *Technical Proposal,* CERN-LHCC/94-38.

[48] Collaboration ALICE, *Technical Proposal,* CERN-LHCC/95-71.

[49] Collaboration ALICE, *Technical Proposal,* Addendum 1 CERN-LHCC/96-32.

[50] Collaboration TOTEM, *Technical Proposal,* CERN-LHCC/99-7.

[51] Collaboration TOTEM, *Technical Design Report,* CERN-LHCC/2004-02.

[52] LHCf collaboration, J. Instrum. 3 (2008) S08006.

[53] LHC Study Group, "The Large Hadron Collider : Conceptual design", CERN-AC-95-05-LHC.

[54] M. Lamont, "LHC from commissioning to operations", presentation at IPAC11, 2011.

[55] LHCb collaboration, *Technical Proposal,* CERN-LHCC-98-004

[56] R. Aaij *et al.* [LHCb Collaboration], arXiv:1106.4435 [hep-ex].

[57] D. Asner *et al.* [Heavy Flavor Averaging Group Collaboration], [arXiv:1010.1589 [hep-ex]].

[58] M. Needham and T. Ruf, "Estimation of the material budget of the LHCb detector", Note LHCb 2007-025.

[59] Juan Knaster, "Technical Specification for a Beryllium or Aluminium-Beryllium Beam Pipe for LHCb", LHC-VC8-CI-0001.

[60] LHCb collaboration, "LHCb vertex locator technical design report", CERN-LHCC-2001-011.

[61] LHCb collaboration, "RICH Technical Design Report", CERN-LHCC-2000-037.

[62] LHCb Collaboration, "Measurement of direct CP violation in charmless charged two-body B decays at LHCb", LHCb-CONF-2011-011.

[63] S. Barsuk et al., "Design and construction of the electromagnetic calorimeter for the LHCb experiment", Note LHCb 2000-043.

[64] A.G. Buckley, "A study of $B \to K\pi$ decays with the LHCb experiment", CERN-THESIS-2005-058

[65] E. Tarkovsky, Nucl. Instrum. Meth. **A 379** (1996) 515.

[66] A. Bazilevsky et al, IEEE Trans. Nucl. Sci. **43 no.3** (1996) 1.

[67] J. Badier et al., Nucl. Instrum. Meth. **A 348** (1994) 74.

[68] S. Monteil, "Mesures de precision electrofaibles", Habilitation a diriger des recherches, Université Blaise Pascal, HDR 280.

[69] LHCb collaboration, "Muon System Technical Design Report", CERN-LHCC-2001-010.

[70] The LHCb Collaboration, "LHCb Trigger System Technical Design Report", CERN-LHCC-2003-031.

[71] E. van Herwijnen, "LHCb trigger system", CERN-LHCb-PROC-2010-055.

[72] V.V. Gligorov, C. Thomas, M. Williams, "The HLT inclusive B triggers", LHCb-PUB-2011-016.

[73] R. Lefevre, Private Information

[74] S. N. Filippov *et al.*., "Design and construction of the LHCb Scintillator-Pad/Preshower Detector", Note LHCb 2000-042.

[75] S. N. Filippov *et al.*, "Experimental performance of PS/SPD prototypes", Note LHCb 2000-031.

[76] G. Böhner *et al.*, "Very Front-End Electronics for LHCb Preshower", Note LHCb 2000-047.

[77] Hamamatsu, Multianode Photomultiplier Tube Asembly H7546A, H7546B

[78] *https://lbtwiki.cern.ch/bin/view/CALO/LHCbCaloReadout*

[79] L. Landau, J. Phys. (USSR) **8** (1944) 201.

[80] H. Bichsel, Rev. Mod. Phys. **60** (1988) 663.

[81] N. Globus, D. Allard and E. Parizot, arXiv:0709.1541 [astro-ph].

[82] W. M.Yao et al. (Particle Data Group), J. Phys. G 33, 1 (2006) and 2007 partial update for the 2008 edition.

[83] Y. Wang, *J. Phys. Conf. Ser. 293 (2011) nonconsec. pag*

[84] *http://roofit.sourceforge.net*

[85] LHCb Collaboration, "LHCb calorimeters Technical Design Report", CERN-LHCC-2000-036.

[86] G. Böhner, R. Bonnefoy, C. Cârloganu, R. Cornat, M .Crouau, O. Deschamps, S. Monteil, J. Lecoq, R. Lefévre, P. Perret, "Ageing measurements for the Ps multianode photomultipliers tubes", *Internal note*, LHCb-2003-044.

[87] J. Lefrançois, F. Machefert, A. Martens, "Calibration of the LHCb calorimeters with energy flow", *Internal note*, LHCb-INT-2010-021.

[88] A. Martens, PhD Thesis

[89] A. Martens, Private information.

[90] A. Ryd, *et al.*, "EvtGen: A Monte Carlo Generator for B-Physics", EVTGEN-V00-11-07 (2005).

[91] F. Machefert, P. Robbe, MH. Schune, O. Deschamps, A. Robert, "$B^0 \to \pi^+\pi^-\pi^0$ reconstruction with the re-optimized LHCb detector", LHCb-2003-077, 2003.

[92] *http://marwww.in2p3.fr/ legac/LHCb/TCKs*

[93] R. Aaij *et al.* [LHCb Collaboration], Phys. Lett. B **694** (2010) 209 [arXiv:1009.2731 [hep-ex]].

[94] *http://tmva.sourceforge.net/*

[95] S. W. Bosch and G. Buchalla, JHEP **0501** (2005) 035 [arXiv:hep-ph/0408231].

[96] T. Hurth, T. Mannel, AIP Conf. Proc. **602** (2001) 212-219. [hep-ph/0109041].

[97] K. Kiers, A. Soni and G. H. Wu, Phys. Rev. D **62** (2000) 116004 [arXiv:hep-ph/0006280].

[98] A. Soni, arXiv:hep-ph/0509180.

[99] F. Soomro, "Radiative decays of B mesons at LHCb", CERN-THESIS-2011-035.

[100] O. Deschamps, F.P. Machefert, M.H. and Schune, and G. Pakhlova, and I. Belyaev, "Photon and neutral pion reconstruction", LHCb-2003-091.

[101] S. Barsuk, Private Information.

[102] M. Calvo, Private Information.

[103] T. Gershon, T. Latham, D. Dosset, The University of Warwick

[104] W. Verkerke, D. Kirkby, "RooFit Users Manual v2.07"

[105] B. Aubert *et al.* [BABAR Collaboration], Phys. Rev. Lett. **87** (2001) 091801 [arXiv:hep-ex/0107013].

[106] K. Abe *et al.* [Belle Collaboration], Phys. Rev. Lett. **87** (2001) 091802 [arXiv:hep-ex/0107061].

[107] LHCb collaboration, "Search for CP violation in $B^0 \to J/\psi K^0_S$ decays with first LHCb data", LHCb-ANA-2011-004.